DEVELOPMENT AND CHARACTERIZATION OF COMPOSITE NICKEL ELECTRODE FOR NICKEL-IRON BATTERY BASED ENERGY STORAGE

By

Dorcas Zide

A thesis submitted in fulfilment of the requirements for the degree

Doctor of Philosophy in Analytical Chemistry

Faculty of Applied Science

At the Cape Peninsula University of Technology

Supervisor: Dr Tobie Oosthuysen (CPUT)

Supervisor (Ext.) Prof Bernard Jan Bladergroen (SAIAMC)

Bellville

Date submitted: September 2021

ABSTRACT

In this study, a β-$Ni(OH)_2$ material was synthesized using the co-precipitation method followed by hydrothermal treatment. The effect of stirring, ageing and hydrothermal treatment step during the synthesis of the $Ni(OH)_2$ material were evaluated. Secondly, the impact of carbon black as a conductive network for $Ni(OH)_2$ active material was gauged. Thirdly, the effect of the partial substitution of Cu^{2+} for β-$Ni(OH)_2$ material, Co^{2+} for β-$Ni(OH)_2$ material, Al^{3+} for β-$Ni(OH)_2$ material, Mg^{2+} for β-$Ni(OH)_2$ material, Mn^{2+} for β-$Ni(OH)_2$ material, was then optimised and evaluated for electrochemical performance. Four weight percentages (5 wt.%, 10 wt.%, 25 wt.%, and 50 wt.%) of additives (Cu^{2+}, Co^{2+}, Al^{3+}, Mg^{2+}, Mn^{2+}) were partial substitutions for the β-$Ni(OH)_2$ material. XRD, FTIR, TG-DTA, and SEM were used to measure the morphologies of the material. SEM/EDS and ICP-OES were used to confirm the composition of the material. Lastly, a novel bipolar battery cell prepared using $Ni_{0.75}Cu_{0.25}(OH)_2$ as the active cathode material was evaluated for Ni-Fe battery applications. The physical characterization performed for β-$Ni(OH)_2$ material concluded that the hydrothermal treatment step was vital for this study to produce the expected $Ni(OH)_2$-based materials. The addition of 5 wt.%, carbon black powder improves the utilization of the active material; however, it leads to a decrease in the stability of the electrode. For example, the specific discharge capacity (after 20 cycle activation) was increased by 74% compared to 0 wt.% carbon black added to the positive nickel electrode. However, a drastic decrease in specific discharge capacity was observed after an additional 60 cycles. The specific discharge capacity of the synthesized $Ni(OH)_2$ with 5 wt.% carbon black electrode decreased by 66%, while the synthesized $Ni(OH)_2$ with 0 wt.% carbon black decreased by only 18% after the 80 cycles. In addition, the partial substitution of Cu^{2+} for β-$Ni(OH)_2$ significantly improves the coulombic efficiency of the β-$Ni(OH)_2$ active material. It also increases the specific discharge capacity and enhances the stability of the electrode. Lastly, a novel bipolar battery cell was prepared and evaluated its discharge capacities for the Ni-Fe battery applications. The $Ni_{0.75}Cu_{0.25}(OH)_2$ material was first deposited onto both a graphite composite and Ni-mesh substrates to form the monopolar electrodes. The bipolar-based Ni-Fe battery cell demonstrated a discharge capacity of 158 mAh/g after the 100^{th} cycle, corresponding to a coloumbic efficiency of 72%. A cost evaluation of the typical battery plant for a bipolar based Ni-Fe was estimated, and it was found that the bipolar design reduces the production cost by 33% from R12/Wh to R8/Wh.

DECLARATION

I, Dorcas Zide, declare that:

(i) These findings reported in this write-up is my original work, excluding where otherwise specified or accredited.

(ii) I acknowledge this dissertation has not been submitted entirely or in part for any degree or examination to any other university.

(iii) This thesis does not comprise other persons' data, images, diagrams, or supplementary data except specifically accredited as being sourced from other persons.

(iv) This thesis does not comprehend other persons' scripts except accredited as being obtained from other investigators. Where additional written sources have been recited, then:

a) Their disputes have been re-phrased; nonetheless, the general information ascribed to them has been referenced.

b) Their script has been placed inside quotation marks and referenced where precise words have been cited.

(v) This study does not comprise typo-script, graphics or tables copied and pasted from the internet unless accredited. The source is detailed in the thesis and the References sections.

(vi) Furthermore, this work represents my sentiments and not necessarily those of the Cape Peninsula University of Technology (CPUT) or South African Institute for Advanced Materials Chemistry (SAIAMC).

September 2021

Signed **Date**

ACKNOWLEDGMENT

- My appreciation goes to God, the master planner and master builder of my life in whom I find joy and peace, for seeing me through the period of this work.
- My father, Mzikayise and mother, Constant, for your parental care, love, prayer, and moral and financial support during this study. I will forever be grateful to you.
- My supervisors, Dr T. Oosthuysen and Prof. B.J Bladergroen, your advice, assistance, encouragement, patience, financial and academic guidance during this research work are highly appreciated. You have been so wonderful for the success of this research work.
- My gratitude goes to my God's gifted siblings (Lindiwe, Gcobani, Sakhiwo); I am fortunate to have a family like you.
- My nephews and niece, Songezo, Sisonke, Zubenathi, Athenkosi, Anovuyo, Anathi, Ayakha, Athule, Lihle, Lindilizwi, Awonke I cannot name you all but, you always knew how to keep your aunt happy.
- Sinto's family (Ntombovuyo, Mzolisi and Anele), thank you so much for being there for me.
- The technical staff (Mrs. Zandile Mthembu, Ms Phumza Stemella from CPUT, and Mr Stanford Chidziva (SAIAMC- UWC), your support did not go unnoticed.
- Mrs Denise Davids (SAIAMC-UWC) for ensuring all my administrative documents were dealt with timeously and to Dr C. Felix (SAIAMC-UWC) for lending me an ear when needed.
- Many others are too numerous to mention, including my laboratory colleagues (Mohamed Ali and Tendai Tawonezvi), station mates, office mates, friends, and the Wesgro Strategic Project team (Mrs Jacyntha Twynam and Ms. Fiona Lunda). I thank you all.

BIOGRAPHICAL SKETCH

I, Dorcas Zide, completed my PhD in Chemistry in 2021 at Cape Peninsula University of Technology (CPUT) in collaboration with the South African Institute for Advanced Materials Chemistry (SAIMAC) department at the University of the Western Cape (UWC). My research focused on the chemistry materials to improve the performance of nickel-iron batteries. The key focus was to develop a positive Ni-electrode for the bipolar-based Ni-Fe battery application. This study produced **four** research papers published in accredited international journals.

I also completed my Master's Degree in Chemistry in 2017 through CPUT. The project focused on the synthesis of hydrotalcite nanomaterials and zeolites from coal fly ash. I used the synthesized materials for the adsorption of pharmaceutical pollutants (antibiotics) from aqueous water. I have authored and published a full research article titled "Zeolite 'adsorption' capacities in aqueous acidic media; The role of acid choice and quantification method on ciprofloxacin removal. I completed my BTech Degree in Chemistry in 2014 and National Diploma in Analytical Chemistry in 2012 through the same University.

In 2020, I started working as a Retention Officer (RO) at the Chemistry department at CPUT. I liaise with First-Year Experience (FYE) Coordinators, departmental lecturers, and students (first-year students, Teacher Assistants (TA), tutors and mentors). The key deliverable is to assure that no student is left behind and assist the first-year in managing their academic studies under the pandemic's stress (Covid-19).

From 2017 to 2019, I joined Wesgro (Tourism, Trade and Investment Agency of the Western Cape). In my time at Wesgro, I was the Assistant Manager of the Cape Health Technology Park (CHTP) project. CHTP plays a role in establishing a health technologies innovation and manufacturing hub in South Africa and the Western Cape. The CHTP focuses on five sub-health industries: pharmaceuticals, medical devices, digital health, biotechnology, and indigenous medicines. I was also seconded at the Technology Transfer and Industrial Linkages (TTO), a unit within CPUT that acts as an instrumental in identifying, protecting, and commercialization of intellectual property (IP). In my time at the TTO, I was exposed to the intellectual property rights act (IPR), assessing and evaluating disclosures and market analysis.

From 2014 – 2016, I spent 3-years at the Fundani Centre for Higher Education Development at CPUT as a Chemistry Facilitator, worked for 4-months at Proxa Water Treatment Plant as a Specialist Lab Analyst. In 2012, I served for 1 year at Pretoria Portland Cement (PPC) as a Trainee Analyst.

DEDICATION

Without God's presence in everything, we touch there will be no success. I want to devote this thesis to my God firstly. He has proven to me numerous times that there is nothing impossible for Him. All this was successful because of His grace. Lastly, to the two magnificent, loving, supporting and caring women in my life, my mother, Mrs Zide Constance, and Dr Afrika Nthabiseng (my sister from another mother), there are not enough words to thank you, but allow me to devote this thesis to you.

PREFACE

Experimental Work: The research contained in this thesis was completed by the candidate in the Department of Chemistry at Cape Peninsula University of Technology (CPUT), Bellville Campus, Cape Town, South Africa, in collaboration with the South African Institute for Advanced Materials Chemistry (SAIAMC) department at the University of the Western Cape (UWC), Cape Town, South Africa. The work was conducted under the supervision of Doctor Tobie Oosthuysen (CPUT) and Professor Bernard Jan Bladergroen (UWC).

Research Funding: The research was financially supported by the Department of Science and Innovation of South Africa; Eskom Holdings SOC Ltd Reg no 2002/015527/30 (Eskom Research, Testing, and Development Business Unit); and the National Research Foundation of South Africa (Grant Number: 121413, 130409).

Chapter Division: This thesis consists of seven chapters. Chapter 1 presents the introduction, problem statement, aim and objectives, and the significance of the research study. Chapter 2 contains a comprehensive literature review. Chapter 3 to Chapter 6 covers the research results obtained during this research study. The results are presented in an article form according to the journal's specific writing style, and the CPUT reference style was adopted. Chapter 7 presents a general discussion and conclusion of the obtained findings.

Publication Declaration: I, Dorcas Zide, declares that I planned, executed and wrote the initial draft of the following manuscript:

(i) **Manuscript 1:** This work has been presented in CHAPTER 3 of this thesis. It was published at Elsevier, under the Journal of Electroanalytical Chemistry (impact factor 3.807). It can be accessed online: https://doi.org/10.1016/j.jelechem.2020.114539. The work should be cited as: Zide, D., Felix, C., Oosthuysen, T. and Bladergroen, B.J., 2020. The influence of copper and carbon black on electrochemical behavior of nickel positive electrode. *Journal of Electroanalytical Chemistry*, 878, p.114539.

(ii) **Manuscript 2:** This work has been presented in CHAPTER 4 of this thesis. It was published at Wiley, under the Journal of Electroanalysis (impact factor 2.507). It can be accessed online: https://doi.org/10.1002/elan.202060202. The work should be cited as: Zide, D., Felix, C., Oosthuysen, T. and Bladergroen, B.J., 2020. Electrochemical studies of the nickel-based hydroxide electrode for the oxygen evolution reaction and coulombic efficiency of the electrode. *Electroanalysis*, 32(12), p.2703-2712.

(iii) **Manuscript 3:** This work has been presented in CHAPTER 5 of this thesis. It was published at Elsevier, under the Journal of Electroanalytical Chemistry (impact factor 3.807). It can be

accessed online: https://doi.org/10.1016/j.jelechem.2021.115418. The work should be cited as: Zide, D., Felix, C., Oosthuysen, T. and Bladergroen, B.J., 2021. Synthesis, structural characterization, and electrochemical properties of the Mg and Mn doped-$Ni(OH)_2$ for use as active cathode materials in NiFe batteries. *Journal of Electroanalytical Chemistry*, p.115418.

(iv) **Manuscript 4:** This work has been presented in CHAPTER 6 of this thesis. It was published to Elsevier, the Journal of Energy Storage (impact factor 6.5). It can be accessed online: https://doi.org/10.1016/j.est.2021.103719. The work should be cites as: Zide, D., Felix, C., Oosthuysen, T., Burfeind, J., Grevé, A. and Bladergroen, B.J., 2022. Towards the development of a novel bipolar-based battery in aqueous electrolyte: Evaluation of the electrochemical properties of NiCu based hydroxide electrodes fabricated on Ni–mesh and graphite composite current collectors. Journal of Energy Storage, 45, p.103719.

TABLE OF CONTENTS

LIST OF FIGURES

LIST OF TABLES

LIST OF EQUATIONS

CHAPTER 1

1 Introduction and Background

1.1 Background

Non-renewable sources of energy such as fossil fuels, coal, petroleum, nuclear fission and shale gas currently play a vital role in meeting the economic energy demands of the world. Fossil fuels supply nearly 86% of worldwide primary energy demand. Oil, gas and coal currently share 36%, 27%, and 23%, respectively, of the global energy mix and nuclear power with a 6% share. Solar, wind, geothermal, and biomass contribute 8% (Abas *et al.*, 2015). The downside of fossil fuel use is carbon dioxide (CO_2) emissions which have been identified as a significant global environmental threat due to their contribution to climate change (Perera, 2017; Riahi *et al.*, 2017). The life cycle costs and public health effects of coal are projected to be $74.6 billion annually due to water and air contamination released by coal and natural gas plants, associated with breathing difficulties, nerve damage, heart attacks, cancer, early death, and many more (Ellabban *et al.*, 2014).

At present, there is a growing interest in using alternative and maintainable renewable energy resources due to the expedited growing demand for energy and the rising concerns over environmental pollution (IPCC, 2014). Renewable energy sources can alleviate climate change by eliminating greenhouse gas emissions from fossil fuel-based power generation. Renewable energy sources need to be sustainable to deliver its full potential and meet our future energy demands (Owusu and Asumadu-Sarkodie, 2016).

Wind and solar power are two suitable solutions to the upsurge in energy security, electricity supply and environmental issues (Sarrias-Mena *et al.*, 2014; Warren, 2014; Oseghale *et al.*, 2016). However, the challenge is amplified with the highly concentrated demand peaks in the early morning and early evening when solar generation is minimal. Therefore, the energy generated from wind or solar systems is subject to stochastic wind profiles and the seasonal availability of resources (Nejat *et al.*, 2015).

In order to construct a more robust energy infrastructure and low-cost utility systems for consumers, various energy storage solutions (ESS) are being evaluated worldwide (Liberatore *et al.*, 2012; Breytenbach, 2015; Panos *et al.*, 2016; Bresser *et al.*, 2018; Nadeem *et al.*, 2018; Sarbu and Sebarchievici, 2018). These ESSs includes but are not limited to electrical, mechanical, thermal, chemical, and electrochemical energy storage techniques and these are discussed briefly.

1.1.1 Electrical Energy Storage

Electrical energy storage units provide several benefits to a power system, which include but are not limited to peak reduction and load flattening. Renewable energy sources such as wind and solar power are "dispatchable" power sources and reliable backup. Advantages of renewable energy sources include spinning reserve, improved efficiency of generation, regulation and stabilisation, and reduced emissions

(Hadian and Madani, 2015). In an electrical storage system, the energy is stored unswervingly as electricity in the form of an electric field by separating charges or magnetic field by flux (Hannan *et al.*, 2017). The main characteristics of an electric storage system are the amount of energy it can store and the rate at which the electric energy storage unit can accept and release power. The service lifetime and fault current are often significant considerations and concerns (Ellabban *et al.*, 2014).

1.1.2 Mechanical Energy Storage

Mechanical energy storage systems are the most frequently employed system to generate electricity worldwide (Hannan *et al.*, 2017). Pumped hydro, compressed air and flywheel energy storage are the main types researched. Briefly, pumped hydro storage is used in pumped hydroelectric power plants and contributes approximately 99% of the world's electrical storage capacity, which is around 3% of the global electricity generation capacity (Panos *et al.*, 2016). In comparison, compressed air energy storage is applicable for large capacity electricity production. It is diversified with natural gas expanded and further transformed into modified gas to feed to a gas turbine shafted with a generator to produce electricity (Hadian and Madani, 2015). Flywheel systems are suitable for electric vehicles (EVs) and power systems because of advances in power electronics and material engineering. The efficiency and rated power of flywheel systems fall within the range of 90 – 95% and 0 – 50 megawatts (MW), respectively (Zhao *et al.*, 2015). The main advantages of this system are high energy and power density, theoretically infinite charge and discharge cycles, low cost, long life, and no depth of discharge effect. Their drawback is high self-discharging features because of the bearing friction losses (Hannan *et al.*, 2017).

1.1.3 Thermal Energy Storage

Thermal energy storage is attained with extensively divergent technologies. Depending on the specific technology, it allows excess thermal energy to be stored for later use. The storage media include the following: (i) water or ice-slush tanks, (ii) masses of native earth or bedrock accessed with heat exchangers utilising boreholes, (iii) deep aquifers contained between impermeable strata, (iv) shallow, (v) lined pits filled with gravel and water and insulated at the top, as well as eutectic solutions and phase-change materials. The energy stored using a thermal energy storage system may last for a limited time because of losses by radiation, convection, and conduction (Sarbu and Sebarchievici, 2018).

1.1.4 Chemical Energy Storage

The chemical energy is stored in the chemical bonds of atoms and molecules, which can only be observed when released in a chemical reaction. Chemical fuels are the dominant form of energy storage in electrical generation and energy transportation (Guney and Tepe, 2017). The most commonly used chemical fuels processed are coal, gasoline, diesel fuel, natural gas, liquefied petroleum gas, propane, butane, ethanol, biodiesel, and hydrogen. The chemicals mentioned above are freely converted to thermal and mechanical energy and then to electrical power using heat engines as the prime mover

(Guney and Tepe, 2017). Additionally, the stored chemical energy can be released through electron transfer reactions for the direct production of electricity. Chemical storage focuses mainly on generating hydrogen through electrolysis, also called power-to-gas technology. Power-to-gas technology was conceived as a way to use the existing gas grid to store renewable electricity. Benefits of power-to-gas include but are not limited to "greening" the end-uses of natural gas, such as heat generation. Power-to-gas improves the flexibility of the energy system by pooling the gas and power infrastructures (Nadeem *et al.*, 2018).

1.1.5 Electrochemical Energy Storage

Contrary to the other energy storages mentioned, electrochemical energy storage systems play a crucial role in the energy sector owing to the worldwide demand to overcome the current energy issues, including but not limited to the increasing demand for energy and rising concerns over environmental pollution (El Kharbachi *et al.*, 2020). Electrochemical energy involves the conversion of chemical energy into electrical power. This energy is expressed as electric current at a defined voltage and time (Linden, 1995; Guney and Tepe, 2017). Electrochemical batteries and electrochemical capacitors are two major branches of electrochemical storage technologies. The existing electrochemical storage systems vary according to the nature of the chemical reaction, structural features, and design (Guney and Tepe, 2017). Electrochemical cells and batteries can be classified into four categories such as primary cell or battery, secondary cell or battery, reserve cell, and fuel cell (Linden and Linden, 1984; Linden, 1995; Huang, Kui *et al.*, 2011; Galushkin *et al.*, 2013; Jensen, 2013; Bernard and Lippert, 2015; Falahati *et al.*, 2015; Guney and Tepe, 2017; Henao and Martinez-Gomez, 2017; Holmberg, 2017; Casas-Cabanas *et al.*, 2018; Chen, Wei *et al.*, 2018) based on the principle of operation.

In recent years there has been significant exploration and development hype in the battery technology sector. Mainly in the rechargeable batteries, also known as secondary cells, and as a result, breakthrough technologies are being knowledgeable and used worldwide (Huang, Kui *et al.*, 2011; Galushkin *et al.*, 2013; Jensen, 2013; Bernard and Lippert, 2015; Falahati *et al.*, 2015; Henao and Martinez-Gomez, 2017; Holmberg, 2017; Casas-Cabanas *et al.*, 2018; Chen, Wei *et al.*, 2018). Rechargeable batteries came into existence due to the need to store generated electrical energy. The battery market is experiencing rapid growth due to the urgent demand for mobile devices, electric vehicles, and energy storage systems, conveying the current energy transition (El Kharbachi *et al.*, 2020). Rechargeable batteries are critical enabling technologies for renewable energy; energy management, conservation storage, pollution control or monitoring; and greenhouse gas reduction (Badwal *et al.*, 2014). The most commonly used rechargeable batteries are (i) lead-based, (ii) lithium-based, and (iii) nickel-based batteries. These systems are continuously optimised, focusing on their cost, lifetime, and performance, leading to continued expansion into existing and emerging market sectors.

1.2 Statement of Research Problem

Access to high-quality, uninterrupted and clean electricity is of national interest and directly impacts the country's economic stability and economic growth potential. The need to liberate modern society from its dependence on fossil fuels is urgent by the growing demand for clean and sustainable energy and concerns over climate change due to burning fossil fuels. The need for independence from fossil fuels is further compounded by the increasing cost of extraction and distribution of fossil fuels and the uneven distribution of finite fossil fuel stores, leading to conflict between and within nations.

Electrochemical technologies offer the interconversion of electrical and chemical energy on a minute or shorter time scale without polluting gas emissions compared to other renewables. Ni-Fe batteries are experiencing a rebirth for renewable energy applications among the studied technologies due to their incredibly long life and robust and durable qualities (Abdalla *et al.*, 2016; Posada and Hall, 2016; Chen, Wei *et al.*, 2018). Yet, the Ni-Fe battery suffers from severe drawbacks, induced mainly by the nickel-electrode, which impels low efficiency (50% - 60%) and low specific energy. Furthermore, nickel-electrode exhibits poor performance, which results from:

(i) The evolution of oxygen tends to interfere with the oxidation of the active material (Wang, Xianyou *et al.*, 2004; Begum *et al.*, 2009).
(ii) The reduced charge acceptance of nickel-electrode is suspected to be related to a relatively long distance between $Ni(OH)_2$ particles and the nearest portion of the substrate(Begum *et al.*, 2009).
(iii) The practical capacity of nickel-electrode is also said to depend on how well the $Ni(OH)_2$ particles are embedded within a conductive electron network allowing electrons to move between particles and the current collector (Begum *et al.*, 2009).

These current limitations of the nickel-electrode generated the opportunity and potential for this present study. Accordingly, this study focused on improving the performance of the nickel-electrode while reducing the overall cost of the Ni-Fe battery.

1.3 Research Aim and Objectives

This study aimed to develop a composite nickel-electrode suitable for a bipolar-based nickel-iron battery in response to the global demand for a cost-effective energy storage system.

Specific Objectives:

I. Synthesization of $Ni(OH)_2$ active material using the modified existing chemical precipitation method followed by hydrothermal treatment.
II. To chemically modify the $Ni(OH)_2$ using the selected divalent and trivalent modifiers (Cu, Co, Mg, Mn, and Al) following the existing modified method (I).

III. To physically characterised the synthesised $Ni(OH)_2$-based materials (I) and (II) using XRD, FTIR, ICP, and SEM/EDS.

IV. To screen the synthesised materials (I) and (II) by assessing their electrochemical properties.

V. To evaluate the best synthesised $Ni(OH)_2$-based material (IV) towards developing a Ni-electrode for a bipolar Ni-Fe battery.

1.4 Delineations

This study exclusively focused on developing and characterising the composite nickel-based electrode (cathode) to improve the overall performance of a nickel-iron battery. The development of the Fe negative electrode and the actual assembling of a full bipolar Ni-Fe battery was not on this study's scope.

1.5 Significance of Research

Although renewable energy resources hold great promise to provide energy while overcoming Africa's infrastructural challenges, the generated energy still need to be efficiently and economically stored. Hence low-cost batteries could be a game-changer for Africa. Storing the energy during times of low load demand and then releasing it during peak demand not only overcomes the infeasibility of the power generated from wind and solar systems but also reduces the energy wastage from various industries. Battery-based technologies can reduce greenhouse gas emissions while offering a practical way of reducing the dependence on fossil fuels; however, lead-acid and nickel-cadmium batteries are heavy and contain toxic elements such as lead and cadmium. In the current study $Ni(OH)_2$ material used for positive material of Ni-Fe battery was synthesized and modified using less hazardous and cost-effective divalent and trivalent elements. Fundamental interest is to contribute towards producing an advanced Ni-Fe battery with high levels of reliability, safety, and low maintenance requirements, which can outperform other electrochemical energy storage devices.

1.6 Thesis Layout

The current report is a thesis by publication made out of four full research papers. Three papers have been published and available online. The fourth manuscript has been sent out to Elsevier, the Journal of Energy Storage, for consideration, and it is currently under review.

This thesis consists of seven chapters, and the outline is given below:

Chapter 1 - Introduction: This is an introductory chapter that provides an insight into the research with an overview of background information on the non-renewable and renewable sources of energy that have been investigated and are currently under investigation. This chapter also provides challenges that led to executing the current study, including the intended outcomes with specific objectives of the study.

Chapter 2 - Literature Review: The literature review shelters all the theoretical background required to understand the fundamental chemistry principles applied in this research. A historical overview of batteries and their classification with a primary focus on Ni-Fe batteries is provided in this chapter. Developing a nickel-electrode for Ni-Fe battery is the main focus of this study; therefore, an extensive overview of $Ni(OH)_2$ material electrode is provided.

Chapter 3 – Chapter 6: Presents all the results and findings obtained during this study. All the presented works have been published.

Chapter 3: The article's title is "influence of copper and carbon black on electrochemical behavior of nickel positive electrode". This article was published in 2020 at Elsevier, Journal of Electroanalytical Chemistry.

Chapter 4: The article's title is "electrochemical studies of the nickel-based hydroxide electrode for the oxygen evolution reaction and coulombic efficiency of the electrode". This article was published in 2020 at Wiley, Journal of Electroanalysis.

Chapter 5: The article's title is "synthesis, structural characterisation, and electrochemical properties of the Mg and Mn doped-$Ni(OH)_2$ for use as active cathode materials in Ni-Fe batteries". This article was published in 2021 at Elsevier, Journal of Electroanalytical Chemistry.

Chapter 6: The article's title is " Towards the development of a novel bipolar-based battery in aqueous electrolyte: Evaluation of the electrochemical properties of NiCu based hydroxide electrodes fabricated on Ni–mesh and graphite composite current collectors." This article was published in 2021 to Elsevier, the Journal of Energy Storage.

Chapter 7: General conclusion and recommendations

1.7 References

Abas, N., Kalair, A. and Khan, N. (2015). Review of fossil fuels and future energy technologies. Futures 69: 31-49.

Abdalla, A. H., Oseghale, C. I., Posada, J. O. G. and Hall, P. J. (2016). Rechargeable nickel-iron batteries for large-scale energy storage. Institution of Engineering and Technology Renewable Power Generation 10(10): 1529-1534.

Badwal, S. P., Giddey, S. S., Munnings, C., Bhatt, A. I. and Hollenkamp, A. F. (2014). Emerging electrochemical energy conversion and storage technologies. Frontiers in Chemistry 2: 79.

Begum, S. N., Muralidharan, V. and Basha, C. A. (2009). The influences of some additives on electrochemical behaviour of nickel electrodes. International Journal of Hydrogen Energy 34(3): 1548-1555.

Bernard, P. and Lippert, M. (2015). Nickel-cadmium and nickel-metal hydride battery energy storage. Electrochemical Energy storage for Renewable Sources and Grid Balancing, Elsevier: 223-251.

Bresser, D., Buchholz, D., Moretti, A., Varzi, A. and Passerini, S. (2018). Alternative binders for sustainable electrochemical energy storage–the transition to aqueous electrode processing and bio-derived polymers. Energy and Environmental Science 11(11): 3096-3127.

Breytenbach, K. (2015). How renewable energy has empowered South Africa. South African International Renewable Energy Conference (SAIREC).

Casas-Cabanas, M., Radin, M. D., Kim, J., Grey, C. P., Van der Ven, A. and Palacín, M. R. (2018). The nickel battery positive electrode revisited: stability and structure of the β-NiOOH phase. Journal of Materials Chemistry A 6(39): 19256-19265.

Chen, W., Jin, Y., Zhao, J., Liu, N. and Cui, Y. (2018). Nickel-hydrogen batteries for large-scale energy storage. Proceedings of the National Academy of Sciences 115(46): 11694-11699.

El Kharbachi, A., Zavorotynska, O., Latroche, M., Cuevas, F., Yartys, V. and Fichtner, M. (2020). Exploits, advances and challenges benefiting beyond Li-ion battery technologies. Journal of Alloys and Compounds 817: 153261.

Ellabban, O., Abu-Rub, H. and Blaabjerg, F. (2014). Renewable energy resources: Current status, future prospects and their enabling technology. Renewable and Sustainable Energy Reviews 39: 748-764.

Falahati, H., Kim, E. and Barz, D. P. (2015). Fabrication and characterization of thin film nickel hydroxide electrodes for micropower applications. American Chemical Society: Applied Materials and Interfaces 7(23): 12797-12808.

Galushkin, N., Yazvinskaya, N. and Galushkin, D. (2013). Ni-Cd batteries as hydrogen storage units of high-capacity. ECS Electrochemistry Letters 2(1): A1-A2.

Guney, M. S. and Tepe, Y. (2017). Classification and assessment of energy storage systems. Renewable and Sustainable Energy Reviews 75: 1187-1197.

Hadian, S. and Madani, K. (2015). A system of systems approach to energy sustainability assessment: Are all renewables really green? Ecological Indicators 52: 194-206.

Hannan, M., Hoque, M., Mohamed, A. and Ayob, A. (2017). Review of energy storage systems for electric vehicle applications: Issues and challenges. Renewable and Sustainable Energy Reviews 69: 771-789.

Henao, J. and Martinez-Gomez, L. (2017). on rare-earth perovskite-type negative electrodes in nickel-hydride (Ni/H) secondary batteries. Materials for Renewable and Sustainable Energy 6(2): 7.

Holmberg, F. (2017). Recycling of nickel metal hydride (NiMH) batteries. Chalmers University of Technology.

Huang, K., Li, J. and Xu, Z. (2011). Enhancement of the recycling of waste Ni-Cd and Ni-MH batteries by mechanical treatment. Journal of Waste Management 31(6): 1292-1299.

IPCC (2014). Summary for policymakers. IIn: Climate Change 2014: Mitigation of Climate Change. Contribution of Working Group III to the Fifth Assessment Report of the Intergovernmental Panel on Climate Change [Edenhofer, O., R. Pichs-Madruga, Y. Sokona, E. Farahani, S. Kadner, K. Seyboth, A. Adler, I. Baum, S. Brunner, P. Eickemeier, B. Kriemann, J. Savolainen, S. Schlömer, C. von Stechow, T. Zwickel and J.C. Minx (eds.)]. International Institute for Applied Systems Analysis (IIASA), Cambridge University Press, Cambridge, United Kingdom and New York, NY, USA.

Jensen, W. B. (2013). The Edison nickel-iron alkaline storage cell: notes from the Oesper collections, No. 21, July/August 2013. Oesper Collections in the History of Chemistry.

Liberatore, R., Lanchi, M., Giaconia, A. and Tarquini, P. (2012). Energy and economic assessment of an industrial plant for the hydrogen production by water-splitting through the sulfur-iodine thermochemical cycle powered by concentrated solar energy. International Journal of Hydrogen Energy 37(12): 9550-9565.

Linden, D. (1995). Handbook of batteries. Fuel and Energy Abstracts.

Linden, D. and Linden, D. (1984). Handbook of batteries and fuel cells: McGraw-Hill New York et al.

Nadeem, F., Hussain, S. S., Tiwari, P. K., Goswami, A. K. and Ustun, T. S. (2018). Comparative review of energy storage systems, their roles, and impacts on future power systems. Institute of Electrical and Electronics Engineers (IEEE) Access 7: 4555-4585.

Nejat, P., Jomehzadeh, F., Taheri, M. M., Gohari, M. and Majid, M. Z. A. (2015). A global review of energy consumption, CO_2 emissions and policy in the residential sector (with an overview of the top ten CO_2 emitting countries). Renewable and Sustainable Energy Reviews 43: 843-862.

Oseghale, C., Abdalla, A., Posada, J. and Hall, P. (2016). A new synthesis route for sustainable gold copper utilization in direct formic acid fuel cells. International Journal of Hydrogen Energy 41(37): 16394-16401.

Owusu, P. A. and Asumadu-Sarkodie, S. (2016). A review of renewable energy sources, sustainability issues and climate change mitigation. Cogent Engineering 3(1): 1167990.

Panos, E., Densing, M. and Volkart, K. (2016). Access to electricity in the World Energy Council's global energy scenarios: An outlook for developing regions until 2030. Energy Strategy Reviews 9: 28-49.

Perera, F. (2017). Pollution from fossil-fuel combustion is the leading environmental threat to global pediatric health and equity: Solutions exist. Environmental Research and Public Health 15(1): 16.

Posada, J. O. G. and Hall, P. J. (2016). Towards the development of safe and commercially viable nickel-iron batteries: improvements to coulombic efficiency at high iron sulphide electrode formulations. Applied Electrochemistry 46(4): 451-458.

Riahi, K., Van Vuuren, D. P., Kriegler, E., Edmonds, J., O'neill, B. C., Fujimori, S., Bauer, N., Calvin, K., Dellink, R. and Fricko, O. (2017). The shared socioeconomic pathways and their energy, land use, and greenhouse gas emissions implications: an overview. Global Environmental Change 42: 153-168.

Sarbu, I. and Sebarchievici, C. (2018). A comprehensive review of thermal energy storage. Sustainability 10(1): 191.

Sarrias-Mena, R., Fernández-Ramírez, L. M., García-Vázquez, C. A. and Jurado, F. (2014). Improving grid integration of wind turbines by using secondary batteries. Renewable and Sustainable Energy Reviews 34: 194-207.

Wang, X., Luo, H., Yang, H., Sebastian, P. and Gamboa, S. (2004). Oxygen catalytic evolution reaction on nickel hydroxide electrode modified by electroless cobalt coating. International Journal of Hydrogen Energy 29(9): 967-972.

Warren, P. (2014). A review of demand-side management policy in the UK. Renewable and Sustainable Energy Reviews 29: 941-951.

Zhao, H., Wu, Q., Hu, S., Xu, H. and Rasmussen, C. N. (2015). Review of energy storage system for wind power integration support. Journal of Applied Energy 137: 545-553.

CHAPTER 2:

2 Literature Review

2.1 Background of Batteries

The term "battery" was first coined by Benjamin Franklin back in 1748 to describe an array of a charged glass plates. Between the years 1780 to 1800, Luigi Galvani and Alessandro Volta discovered the first electrochemical cell (Schipper and Aurbach, 2016; Placke *et al.*, 2017). According to Galvani's observation, the legs of frogs suspended on brass or iron hooks would twitch when prodded with a probe made of another type of metal. Galvani believed that this response was due to electricity within the frogs' tissues and named it "animal electricity".

While Galvani believed that animals could generate electricity, Volta recognised that the muscle contraction was due to the voltage generated by the two different metals. Based on these considerations, Volta developed the first electrochemical cell, currently known as a voltaic pile (Placke *et al.*, 2017). The voltaic stack comprises zinc and copper plates separated by cardboard or leather spacers soaked with an acidic electrolyte. The voltaic pile produces electrical voltage as the zinc discs give off electrons, creating an excess of electrons and thus a negative charge. The copper, nonetheless, absorbs the zinc electrons, making a shortage of electrons and a positive charge. The voltaic pile was the first electrical battery that could continuously provide an electric current to a circuit. The voltaic pile then enabled a rapid series of other discoveries, and up-to-date, many batteries still work on the voltaic pile-based principle, such as small-scale hearing aid batteries.

In 1802, the German physicist Johann Wilhelm Ritter developed a cell that consisted of a glass tube filled with a saline solution and closed by corks on both sides, each equipped with gold wires. Ritter used Volta's battery to charge his cell. Ritter's observation was the generation of gas bubbles (oxygen and hydrogen gassing) at both wires when a current was applied through the glass tube. Ritter further discovered that the electrolysis of water took place during charge, and the recombination of oxygen and hydrogen to water occurred during discharge. In addition, Ritter designed the first galvanic cell that comprises a redox reaction of H_2 with O_2, which can be considered the fuel cell's forerunner (Placke *et al.*, 2017). Since then, a number of primary and secondary based-battery technologies using aqueous electrolytes were discovered. Wilhelm Josef Sinsteden invented the rechargeable lead-acid battery in 1854. In 1859, Gaston Raimond Planté developed an improved construction leading to the first commercially viable and today well-known lead-acid battery, which nowadays still dominates the sector of starter and backup batteries, despite its relatively low practical specific energy (20 - 40 Wh kg^{-1}) (Thackeray *et al.*, 2012; Placke *et al.*, 2017).

Nickel-based systems constitute another essential type of rechargeable battery technology. Among the Ni-based batteries, the nickel-cadmium battery invention was credited to Waldemar Jungner in 1899, and the nickel-iron battery invention was ascribed to Thomas Edison in 1901. Both systems were the forerunners of the nickel-metal hydride battery, which was commercialised in 1989 and showed an improved practical, specific energy (70 – 100 Wh kg^{-1}) compared to the nickel-cadmium and nickel-iron batteries (20 – 50 Wh kg^{-1}) (Huang, Kui *et al.*, 2011; Galushkin *et al.*, 2013; Holmberg, 2017; Placke *et al.*, 2017). The nickel-metal hydride battery was primarily used to power small-scale consumer electronics and was also applied as the system of choice for many of Toyota's hybrid electric vehicles, such as the Toyota Prius (Thackeray *et al.*, 2012; Schipper and Aurbach, 2016; Holmberg, 2017; Placke *et al.*, 2017).

2.2 Classification of Batteries

Battery chemistries differ depending on the arrangement and material used to fabricate the anode, cathode, and electrolyte. The material used to manufacture a battery allows batteries to be classified into various categories and types. The classification of a battery is based on its chemical composition, size, form factor, and applications. There are two major battery types: (i) primary batteries and (ii) secondary batteries. There are also four categories of significant cells. Both the battery and the cell are used to store chemical energy and then transform the stored chemical energy into electrical power. A cell is referred to as a single unit, whereas a battery is a group of cells. Some comparison between a cell and a battery is presented in Table 2-1.

Table 2-1: A comparison chart of cells and battery (Thurner, 2016).

Basis for Comparison	**Cell**	**Battery**
Definition	The single-unit device, which converts the chemical energy into electrical energy	It is the collection of electrochemical cells which either connect in series or parallel
Symbol	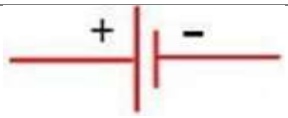	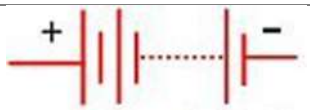
Types	Dry cell, wet cell, reserve cell, and fuel cell.	Primary battery and secondary battery.
Specification	Light and compact	Heavy
Power	Supply power for a short time.	Supply power for a long time.
Applications	Clocks, lamps, radio, remote control devices, etc.	Automobiles, inverter, emergency light, etc.
Cost	Cheap	Expensive

Primary batteries are batteries that cannot be recharged once depleted. Primary batteries are made of electrochemical cells whose electrochemical reactions cannot be reversed. These batteries exist in different forms ranging from coin cells to AA batteries. Primary batteries are commonly used in standalone applications where recharging is impractical or impossible. Most primary cells utilise electrolytes that are contained within absorbent material or a separator (i.e., no free or liquid electrolyte) and are thus termed dry-cells. Primary batteries are mainly categorised based on electrolyte type, such as aqueous or non-aqueous electrolytes. Examples of aqueous-based electrolytes include but are not limited to leclanche zinc-carbon and zinc-chloride, alkaline zinc–manganese dioxide, zinc-air, zinc–silver oxide, and zinc–mercuric oxide. Nonaqueous-based electrolytes include lithium–thionyl chloride, lithium–sulfuryl chloride and lithium–sulphur dioxide, lithium–manganese dioxide, lithium–carbon monofluoride, lithium–iron disulfide, lithium-iodine, lithium–silver vanadium oxide, lithium–copper oxide, to name a few.

Secondary batteries are rechargeable batteries where the chemical reactions can be reversed by applying a specific voltage to the battery in the reversed direction. The most commonly used rechargeable batteries are (i) lead-based, (ii) lithium-based, and (iii) nickel-based batteries. A general classification of these rechargeable batteries with their subcategories is given in Figure 2-1. Since the interest of this study was on the NiFe battery-based energy storage technology, different types of nickel-based batteries are briefly discussed in section 2.3 below.

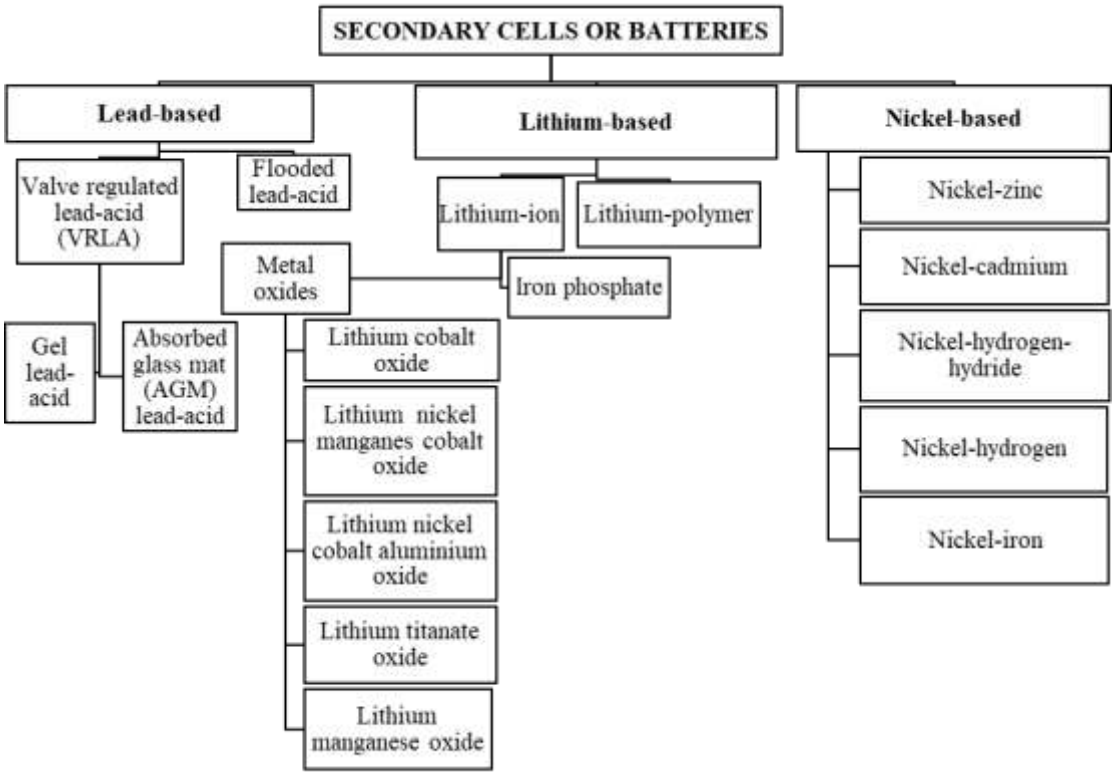

Figure 2-1: Classification of most common secondary batteries (Liu, Kailong *et al.*, 2019).

2.3 Nickel-Based Batteries

Nickel-based batteries are alkaline secondary batteries whose chemical reactions are based on nickel hydroxide electrodes as the positive plates in the system but differ in their performance and application in the energy storage market. Nickel-based batteries include but are not limited to nickel-zinc (Ni-Zn), nickel-cadmium (Ni-Cd), nickel-hydrogen (Ni-H), nickel-metal-hydride (NiMH), and nickel-iron (Ni-Fe). These batteries primarily utilise alkaline solutions such as potassium hydroxide, sodium hydroxide, or lithiated potassium hydroxide as electrolytes; hence they are named alkaline secondary batteries. A brief background of the aforementioned nickel-based batteries is provided in Sections 2.3.1 to 2.3.5.

Ni-Fe batteries stand out from the rest of previous rechargeable batteries because of their durability and robustness. NiFe batteries continue to occupy a niche in the battery market where ultra-reliability and long cycle life are required (Dougherty *et al.*, 1995). Their service life can be 20 to 25 years (Chakkaravarthy *et al.*, 1991), and there are examples of Ni-Fe batteries lasting for 40 years (Barton *et al.*, 2020). The rest of the review literature will dwell mainly on NiFe batteries with a tremendous interest in understanding the chemistry and the properties of the nickel-electrode for Ni-Fe batteries.

2.3.1 Nickel-Zinc Battery

Nickel-zinc (Ni-Zn) batteries are based on the reversible electrochemical reactions (Equation 2-1) of nickel and zinc in a potassium hydroxide electrolyte. Ni-Zn battery was first patented in the late 1890s to early 1900s by Michalowski from Germany. However, it was not commercialised until the 1930s, when an Irish chemist, Drumm, used it in electric trains. Ni-Zn batteries remained of particular interest owing to their high-output voltage of approximately 1.8V compared to other aqueous batteries (mostly $\leq$ 1.2V). Their high voltage empowered the development of high-energy, safe and cost-effective energy storage devices that shows great potential for various applications (Liu *et al.*, 2016).

Equation 2-1: Overall cell redox reaction in the Ni-Zn batteries

$$2NiOOH + Zn + H_2O \rightleftharpoons 2Ni(OH)_2 + Zn(OH)_2$$

The commercialisation of Ni-Zn batteries is usually limited by their cycling lifetime due to zinc-electrode (negative-electrode or anode) (Zhang, L *et al.*, 2008). The disadvantage of zinc-electrode includes but are not limited to dendrite formation at the zinc-electrode during the electrochemical reaction leading to a redistribution of zinc material to cause a shape change that results in high polarisation and significant loss of capacity (Yan, Zhao *et al.*, 2015). In addition, the use of heavy metal foil or metal supports is likely to reduce the energy density and flexibility of the entire device (Lee, Sang Heon *et al.*, 2011; Hu *et al.*, 2015).

2.3.2 Nickel-Cadmium Batteries

The electrochemical chemistry of nickel-cadmium (Ni-Cd) batteries is based on nickel-electrode as a positive terminal (cathode) and cadmium as a negative terminal (cathode). Ni-Cd batteries were first

developed in 1899 by Walder Junger and were exclusively utilised in portable devices due to their robustness and low maintenance. Their advantages also include but are not limited to their resistance to electrical abuse, high cycle lives, reliability and versatility. During discharge (Equation 2-2), the NiOOH combines with H_2O to produce divalent $Ni(OH)_2$ and a hydroxide ion. Metallic cadmium is oxidised to produce cadmium hydroxide at the negative electrode.

Equation 2-2: Overall cell redox reaction in the Ni-Cd batteries

$$2NiOOH + 2H_2O + Cd \underset{\text{charge}}{\overset{\text{discharge}}{\rightleftharpoons}} 2Ni(OH)_2 + Cd(OH)_2$$

The process is reversed during charging, but oxygen can be released at the positive electrode, and hydrogen can be formed at the negative electrode. The downside of Ni-Cd batteries is a negative electrode that is based on Cd active material, and Cd is classified as a toxic element. Ni-Cd batteries suffer from the so-called memory effect. They are less commercialised mainly due to their considerable costs (approximately $979/kWh) at about 10-times that of lead-acid batteries (Huang, Kui *et al.*, 2011).

2.3.3 Nickel-Metal-Hydride

Nickel-metal-hydride (NiMH) batteries were invented in 1967 and largely replaced Ni-Cd as the default battery for most electronic devices that uses AA or AAA sized batteries. NiMH batteries apply hydride of metal alloys such as nickel and lanthanum alloy as the negative electrode in an alkaline bath of potassium hydroxide. The overall cell charge-discharge redox reaction performance based on the reversible electrochemical reactions of nickel and metal hybrid is provided in Equation 2-3.

Equation 2-3: Overall cell redox reaction in the NiMH batteries

$$\beta - NiOOH.2H_2O + MH \underset{\text{charge}}{\overset{\text{discharge}}{\rightleftharpoons}} Ni(OH)_2 + M + H_2O$$

The metal hydride electrode has a theoretical capacity that is 40% higher compared to the Cd-electrode in a Ni-Cd couple battery. Nickel-metal-hydrides also provide energy densities that are 20% greater than the equivalent Ni-Cd battery. NiMH batteries have a reduced memory effect and are less damaging to the environment than Ni-Cd (Piłatowicz *et al.*, 2015). The flat discharge characteristic, excellent high rate, long cycle life, and abuse tolerance have made NiMH batteries the first choice for hybrid electric vehicles (HEVs) (Young, Kwo-hsiung and Yasuoka, 2016). However, the significant barrier for Nickel-metal-hydrides batteries is the high rate of self-discharge and losing 5% – 20% of its capacity within the first 24h after fully charging.

2.3.4 Nickel-Hydrogen Batteries

Nickel-hydrogen (Ni-H_2) batteries were later introduced due to the limitations of NiMH batteries (Section 2.3.3). The Ni-H_2 batteries were solely used for aerospace applications such as satellites because of their long service life, high gravimetric energy density, high power density, and remarkable temperature performance of –28°C to 54°C. Nevertheless, low-specific energy and high cost worked against this endeavour (Henao and Martinez-Gomez, 2017; Chen, Wei *et al.*, 2018). Also, the inherent problems, such as low-volumetric energy density due to gaseous hydrogen and high self-discharge rate, wedged the extensive use of Ni-H_2 batteries. Their chemical reaction can be expressed as it is shown in Equation 2-4. During discharge, NiOOH is reduced to $Ni(OH)_2$, and H_2 is consumed.

Equation 2-4: Redox reaction in the Ni-H_2 batteries

$$2NiOOH + H_2 \rightleftharpoons 2Ni(OH)_2$$

2.3.5 Nickel-Iron Battery

The nickel-iron (Ni-Fe) battery was patented and commercialised in 1901 by Thomas Edison in the United States. Since the advancement of Ni-Fe batteries, Edison has had several patents, including but not limited to U.S. Patent 678,722/1901, U.S. Patent 692,507/1902, and German patent No 157.290/1901 (Jensen, 2013). According to Edison's claim, the Ni-Fe were far superior to batteries using lead plates and acids. Yet, the invention went in vain when gasoline-powered cars took over, and the auto-industry did not adopt the Ni-Fe batteries. Edison's batteries also performed poorly at low temperatures and were more expensive than the lead-acid batteries in use at the time (Novakovskii *et al.*, 1973). Since then, many scientists have continued to innovate. Currently, Ni-Fe batteries are experiencing a rebirth for renewable energy applications due to their incredibly long life and robust and durable qualities.

2.4 Characteristics of Nickel-Iron Batteries

2.4.1 Electrochemistry and Availability of Ni-Fe Batteries

The electrochemical chemistry of Ni-Fe batteries is based on the Fe-electrode as the negative terminal (anode), Ni-electrode as the positive terminal (cathode) and alkaline electrolytes such as potassium hydroxide. Ni-Fe cells are typically charged using a galvanostatic method and should not be charged using a constant voltage supply since the cells can be damaged by thermal runaway. Thermal runaway occurs due to a drop in cell voltage as gassing begins due to overcharging, high cell temperature and high current drawn from a constant potential source. A typical galvanic cell of a Ni-Fe cell is presented in Figure 2-2.

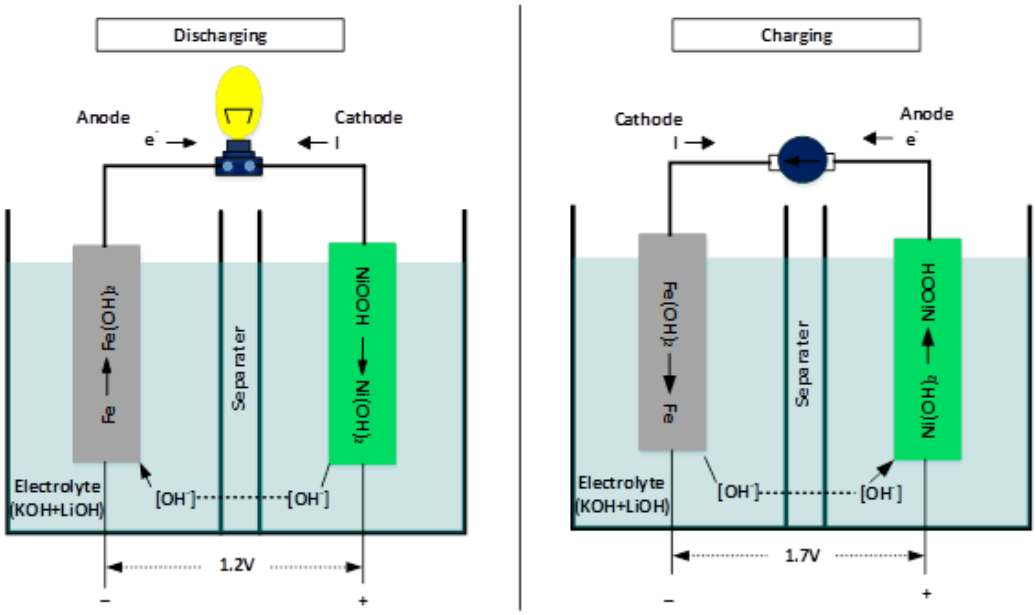

Figure 2-2: Illustration of a galvanic cell (Ni-Fe cell) (Thurner, 2016).

The electrochemistry of a typical Ni-Fe battery is based on a chemical reaction within the battery known as electrolysis. Electrolysis is defined as the chemical reaction taking place when there is current flow, and it can be both the source and the result of the chemical reaction. The overall cell reaction is presented in Equation 2-5.

Equation 2-5: Overall reaction of Ni-Fe cell

$$3Fe + 8NiOOH + 4H_2O \underset{\text{charge}}{\overset{\text{discharge}}{\rightleftharpoons}} 8Ni(OH)_2 + Fe_3O_4$$

During a typical Ni-Fe battery charge-discharge process, the reduction of NiOOH and the oxidization of Fe (Equation 2-6) occurs (Hariprakash *et al.*, 2005; Omar *et al.*, 2014; Lei *et al.*, 2016). Upon further charging-discharging process, a redox reaction (Equation 2-7) of lower potential (~ 1.05V) with a negative limited configuration leading to the formation of an overall Ni-Fe redox reaction (Equation 2-5) may be expected (Hariprakash *et al.*, 2005). In practical Ni-Fe batteries, the appearance of the charge-discharge Ni-Fe cell reaction presented in Equation 2-7 is mainly avoided. However, preventing this reaction entails adding a lot of extra iron (Jackovitz and Bayles, 2002). The charge-discharge overall response of the Ni-Fe cell (Equation 2-5) results in the transfer of oxygen from one electrode to the other (Jackovitz and Bayles, 2002).

Equation 2-6: First plateau reaction of charge-discharge reaction of Ni-Fe battery electrode

$$2NiOOH + 2H_2O + Fe \underset{\text{charge}}{\overset{\text{discharge}}{\rightleftharpoons}} 2Ni(OH)_2 + Fe(OH)_2 \qquad (E° = 1.37V)$$

Equation 2-7: Second plateau of charge-discharge reaction of Ni-Fe battery electrode

$$3Fe(OH)_2 + 2NiOOH \underset{\text{Charge}}{\overset{\text{Discharge}}{\rightleftharpoons}} 2Ni(OH)_2 + Fe_3O_4 + 2H_2O \qquad (E° = 1.05V)$$

The Ni-Fe battery is a very robust battery tolerant of abuse (overcharge, over-discharge, and short-circuiting) and can have a very long service life. Ni-Fe batteries are primarily used in backup applications where they can be continuously charged and may last for more than 20 years. Ni-Fe batteries are commercially available from different supplies, such as IRON EDISON BATTERY COMPANY, which provides Ni-Fe batteries for off-grid solar and battery backups, IRONCORE BATTERIES. Ni-Fe batteries are used in various technologies such as London underground electric locomotives, New York City Subway car (R62A), forklift trucks, and motorised hand trucks. Around the 1980s, Ni-Fe batteries were used in Peugeot 205 electric vehicles, allowing a range of 200km (Omar *et al.*, 2014).

2.4.2 Components of Nickel-Iron Battery

As mentioned previously, Ni-Fe batteries are composed of three major components which are ionically conducting electrolytes (usually an aqueous alkaline solution), metallic iron for a negative electrode, and nickel hydroxide for a nickel-electrode. The capability of a typical Ni-Fe battery to endure frequent cycling owes to the low solubility of the reactants in the electrolyte. For example, the formation of metallic iron during charge is slow due to the low solubility of the reaction product ferrous hydroxide. While the slow build of iron crystals preserves the electrodes, it also limits the high-rate performance. A generic discussion of electrolytes, Fe-electrode, and Ni-electrode is briefly provided in Section 2.4.2.1, Section 2.4.2.2, and Section 2.4.2.3, respectively.

There are also minor components that complete the design of a Ni-Fe battery. However, these components exhibit little to no influence on the overall electrochemical performance of the battery. The minor features involved in the battery construction include but are not limited to the following:

- ✓ **Case**: a closed vessel that houses all the battery components and electrolyte solution.
- ✓ **Cover**: permanent or removable seal (for ease of battery maintenance) at the top of the battery case. Its design constitutes outlets for battery terminals and gas vents.
- ✓ **Plates**: contains the active materials for anode and cathode; standard batteries constitute more than one plate to produce more energy.
- ✓ **Separators**: are commonly made of thin and porous ion-permeable membranes. They are positioned in-between anode and cathode plates to avoid short-circuiting resulting from direct contact of polarised plates of the battery. The membranes are typically microporous layers

composed of polyethylene and polypropylene, which are designed to allow the passage of the ions (Omar *et al.*, 2014; Posada *et al.*, 2016; Posada and Hall, 2016). Moreover, separators ensure that electrons can only shuttle from the anode to the cathode through the external circuit.

- ✓ **Vent Caps**: allow regulated expulsion of hydrogen gas produced during charging and the electrolyte level during battery maintenance.
- ✓ **Terminals** are current collectors connected to the upper or top of a battery cell's positive and negative electrical contact.

2.4.2.1 Electrolyte

Electrolytes should ideally exhibit high ionic conductivity, low to zero electrical conductivity, and non-reactive with active electrode materials. Electrolytes should also be safe to handle, cost-effective and show suitable thermal properties (Kao *et al.*, 2011). The most commonly used electrolyte is potassium hydroxide (KOH), typically in the range of 30 - 32 weight percentage (Jackovitz and Bayles, 2002). The KOH is preferred owing to its cost-effectiveness, higher conductivity, and low freezing point. The electrolyte solution acts as a medium for unrestricted migration of ions (at optimal levels) between the Fe-electrode and Ni- electrode and prevents short circuits. In addition, the electrolyte provides an ion transfer channel linking the Fe-plate and Ni-plate to generate an electrical pressure (voltage). Lithium hydroxide (LiOH) is commonly added to the KOH electrolyte solution to stabilise the battery's capacity during charging mode (Chakkaravarthy *et al.*, 1991; Casas-Cabanas *et al.*, 2018).

2.4.2.2 Fe-Anode Electrode

The Fe-electrode, composed of metallic iron, is the anode where oxidation occurs during the charging process. The Fe-based active electrode material enables the movement of electric current through the external circuit while activating reversible absorption of electrons absorbed by the anode (Linden and Linden, 1984). Moreover, a Fe-based electrode releases electrons to the external circuit and oxidises elemental iron (Fe) to ferrous iron (Fe^{2+}) during the electrochemical reaction. Similarly, the reduction of ferrous ion (Fe^{2+}) to essential iron (Fe) occurs during the charging of the same electrode. Two redox reactions may transpire during a typical charge-discharge of a Fe-based electrode (Equation 2-9 and Equation 2-10). The redox reaction in Equation 2-8 with higher electrode potential (E° = -0.877 V) is considered reversible. In contrast, the second redox reaction (Equation 2-9) with a lower potential (E° = -0.560 V) do not readily accept a charge (Chakkaravarthy *et al.*, 1991).

Equation 2-8:First redox reaction of Fe-based electrode

$$Fe + 2OH^- \underset{\text{Charge}}{\overset{\text{Discharge}}{\rightleftharpoons}} Fe(OH)_2 + 2e^- \qquad E^\circ = -0.877\ V$$

Equation 2-9: Second redox reaction of Fe-based electrode

$$Fe(OH)_2 + OH^- \underset{\text{Charge}}{\overset{\text{Discharge}}{\rightleftharpoons}} FeOOH + H_2O + e^- \qquad E^\circ = -0.560\ V$$

A common drawback of a typical Fe-electrode is premature passivation of the Fe surface. Thus, Fe-electrodes whose active mass consists of pure Fe become passivated after a limited number of cycles. The passivation step is due to iron oxides forming on the electrode surface, inhibiting the charging process. In recent years, several additives such as nickel-sulfate or ferrous-sulfide are customarily added to the active material of the Fe-electrode to inhabit the passivation stage (Chakkaravarthy *et al.*, 1991; Shukla *et al.*, 1994; Linden, 1995). Sulfur or sulfide addition changes the electro-crystallisation kinetics and makes the Fe-electrode reaction more reversible. Sulfide is also known to absorb the Fe electrode, raising the overpotential for the hydrogen evolution reaction during charging. A shortcoming of a typical sulfur-modified Fe-based electrode is a possibility of a loss of sulfide over time due to the dissolution of sulfide into the electrolyte and resultant oxidation to sulfate ineffective, providing long-lasting activation of the iron electrode.

2.4.2.3 Nickel-Cathode Electrode

The nickel-electrode is the cathode and is composed of nickel hydroxide ($Ni(OH)_2$). $Ni(OH)_2$ has been used as a Ni-electrode material in commercial alkaline secondary batteries for more than 100 years. $Ni(OH)_2$ materials are chosen because of their excellent high rate discharge ability performance, vast operation and storage temperature range, and relatively low cost (Young, Kwo-Hsiung *et al.*, 2017). Structurally, $Ni(OH)_2$ has two polymorphic forms (α- and β-phases) of layered material (Lee, Jeong Woo *et al.*, 2011). α-$Ni(OH)_2$ is the metastable phase and displays a higher theoretical capacity (462 - 480 mAh/g) (Young, Kwo-Hsiung *et al.*, 2017). The β-$Ni(OH)_2$ has a relatively low theoretical capacity, limited to 289 mAh/g (Yang, LJ *et al.*, 2007; Begum *et al.*, 2009; Huang, Jichun *et al.*, 2013). This specific capacity corresponds to the exchange of one electron ($1e^-$) per Ni atom. In practice, the particular capability of β-Ni $(OH)_2$ material is below the said theoretical value (Begum *et al.*, 2009). Although the capacity of α-$Ni(OH)_2$ (462 - 480 mAh/g) is higher than that in the β-$Ni(OH)_2$ (289 mAh/g), the α-$Ni(OH)_2$ tends to convert to β-$Ni(OH)_2$ in alkaline solution or when subjected to charge-discharge cycles (Lee, Jeong Woo *et al.*, 2011). Owing to the instability of the α-$Ni(OH)_2$, β-$Ni(OH)_2$ is often selected as a discharged-state active material in the preparation of nickel-electrodes (Hall *et al.*, 2015; Posada and Hall, 2016; Zide *et al.*, 2020b, a).

During electrochemical cycling of a typical nickel-electrode, redox reactions of $Ni(OH)_2$/NiOOH active materials are detected. In addition, side reaction owing to oxygen evolution is usually observed in a standard nickel-electrode battery. While charging, self-discharge occurs through a couple involving the

reduction of NiOOH and the oxidation of water to oxygen. The self-discharge process could make it difficult to experimentally determine the reversibility potential of the $Ni(OH)_2$/NiOOH material. The reaction process involved may be explained according to Equation 2-10 to Equation 2-12 (Carbonio *et al.*, 1982; Zimmerman and Effa, 1984).

Equation 2-10: Formation of protons at the electrode/electrolyte interface

$$H_2O \rightleftharpoons OH^-(aq) + H^+(s)$$

Equation 2-11: Formation of protons at the electrode/electrolyte interface

$$H^+(s) \rightleftharpoons H^+(s`)$$

Equation 2-12: Charge transfer process involving redox reaction of NiOOH active material in the lattice

$$H^+(s`) + NiOOH(s`) + e^-(s`) \rightleftharpoons Ni(OH)_2(s`)$$

According to the authors, Equation 2-10 represents the formation of a proton at catalytic site (s) at the electrode/electrolyte interface. Equation 2-11 involves the diffusion of the proton from the site (s) into the electrode to the charge transfer site (s'). Equation 2-12 is the charge transfer process involving the reduction of NiOOH active material in the lattice. Furthermore, Equation 2-10 appears to be consistent with diffusion of OH^- between the bulk electrolyte and the active material surface as the rate-limiting step for high-rate electrode operation, particularly at reduced concentrations of OH^-. Equation 2-11, proton diffusion, is generally regarded as controlling the rate of nickel electrode discharge at the potential and current densities typically used in battery operation. Equation 2-12 is viewed as a none rate-limiting under the operating conditions of the nickel electrode because it would not account for the observed diffusion kinetics (Carbonio *et al.*, 1982; Zimmerman and Effa, 1984). The proton diffusion rate and proton concentration are predicted to depend on the phase composition of the NiOOH and the presence of additives in the lattice structure (Zimmerman and Effa, 1984). In addition to the $Ni(OH)_2$/NiOOH electrode reaction, parasitic reactions such as the corrosion of nickel current collector materials and the oxidation of organic materials from separators are predictable.

These limiting or side reactions are typically minimised or even avoided by partial substitution or incorporation of foreign ions such as magnesium, cobalt, and zinc during the synthesis and production of active electrode material (Young, Kwo-Hsiung *et al.*, 2017; Liu, Ling *et al.*, 2019). However, incorporating a foreign ion could lead to the structural disorder of $Ni(OH)_2$ active material. The relationship between structural condition and the measured electrochemical properties is not always clear; however, a well-crystallised β-$Ni(OH)_2$ is reported to lower electrochemical activity than disordered β-$Ni(OH)_2$ materials (Hall *et al.*, 2015).

A comprehensive review of nickel hydroxide-based materials is discussed in Section 2.5 to Section 2.9. The emphasis is on the chemistry (2.5), material production (2.6), electrode production (2.7), and the analytical techniques used in this study to characterize the physical (2.8) and electrochemical (2.9) properties of the $Ni(OH)_2$ materials.

2.5 Chemistry of $Ni(OH)_2$

The $Ni(OH)_2$ material has been widely studied (Falahati *et al.*, 2015; Hall *et al.*, 2015; Holmberg, 2017; Bresser *et al.*, 2018; Young, Kwo *et al.*, 2018) and the most significant advances in the understanding of the overall reaction of the $Ni(OH)_2$ material. The electrochemical behaviour of $Ni(OH)_2$ electrode material was first proposed by Bode and co-workers in 1966 (Bode *et al.*, 1966). According to the authors, $Ni(OH)_2$ could exist in a β-form or α-form. The β-form is anhydrous and has a layered brucite, $Mg(OH)_2$ or $Co(OH)_2$ structure, while the α-form is hydrated and has intercalated water between brucite-like layers. Oxidation of β-$Ni(OH)_2$ on charge produces β-NiOOH, which discharge to yield β-$Ni(OH)_2$ and if overcharged, the β-$Ni(OH)_2$ could be converted to γ-NiOOH. The overall transformation is shown in Equation 2-13.

Equation 2-13: Beta-Two (β(II))) to Beta-Three (β(III)) then Gamma (γ(III)) on overcharge

$$\beta - Ni(OH)_2 \underset{Discharge}{\overset{Charge}{\rightleftharpoons}} \beta - NiOOH + H^+ + e^- \overset{Overcharge}{\rightarrow} \gamma - NiOOH + H^+ + e^-$$

The β-$Ni(OH)_2$ is stable in strong alkaline electrolytes and has good reversibility when charged to β-NiOOH. The β-NiOOH has a similar structure with a lattice constant of inter-sheet (4.85Å); thus, the volume expansion associated with cycling is less than any other form. However, the formation of γ-NiOOH when β-$Ni(OH)_2$ is overcharge contains Ni^{4+} (Yang, LJ *et al.*, 2007; Hall *et al.*, 2015) with an average nickel oxidation state of 3.3−3.7 (Yang, LJ *et al.*, 2007). The conversion of β-$Ni(OH)_2$ to γ-NiOOH is accompanied by a large volumetric change, and this may result in loss of contact between the active material and the conductive substrate, thus causing fast capacity fading during charge-discharge cycling (Hall *et al.*, 2015).

The oxidation of α-$Ni(OH)_2$ on charge produces γ-NiOOH, which discharged to form α-$Ni(OH)_2$ (Equation 2-14). In general, α-$Ni(OH)_2$ is unstable and can be transformed to β-$Ni(OH)_2$ in a neutral or KOH aqueous solution. Primarily α-$Ni(OH)_2$ is dissolved in the aqueous solution slowly and then re-nucleated to form β-$Ni(OH)_2$ (Equation 2-15) (Hall *et al.*, 2015).

Equation 2-14: Alpha (α) to Gamma (γ) form

$$\alpha - \mathrm{Ni(OH)_2} \underset{Discharge}{\overset{Charge}{\rightleftharpoons}} \gamma - \mathrm{NiOOH} + \mathrm{H^+} + \mathrm{e^-}$$

Equation 2-15: Alpha (α) to Beta (β) form

$$\alpha - Ni(OH)_2 \underset{Aging}{\overset{Dehydrate}{\rightarrow}} \beta - Ni(OH)_2$$

The α - γ transformation may involve more than one electron transfer per Ni atom (up to 1.6 to 1.67 electrons) (Young, Kwo-Hsiung *et al.*, 2017). This owes to the non-integral average oxidation states of the α and γ phases that occur because of the presence of anions (NO_3^-, CO_3^{2-}, SO_4^{2-}, Cl^-, etc.) and cations (Li^+, Na^+, K^+, etc.) in the water layers in α-$Ni(OH)_2$ and γ-NiOOH, respectively (Hall *et al.*, 2015). The general scheme diagram initially proposed by Bode *et al.* (Bode *et al.*, 1966) and currently validated by many researchers (Bresser et al., 2018, Falahati et al., 2015, Hall et al., 2015, Holmberg, 2017, Young et al., 2018) is shown in Figure 2-3.

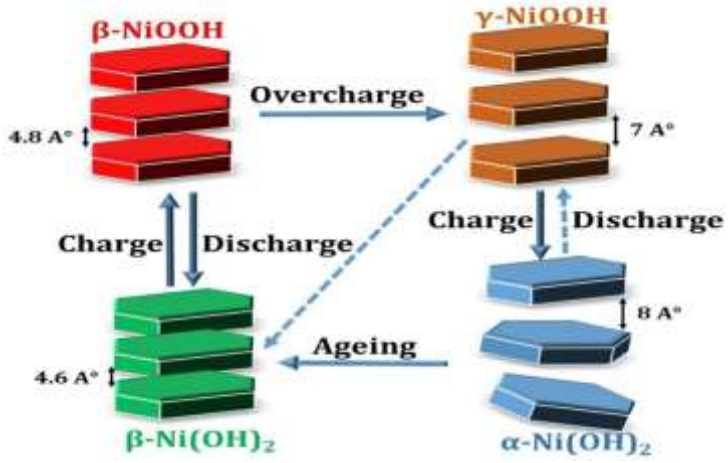

Figure 2-3: Illustration of the Bode's diagram for the Ni(II)/Ni(III) reduction-oxidation transition in the $Ni(OH)_2$ layers. Source: (Falahati *et al.*, 2015).

The Ni(II)/Ni(III) redox transition is generally referred to as β/β and α/γ reaction. The β-form can exist in hydrated and un-hydrated forms. Hydrated β-$Ni(OH)_2$ material is vital for electrochemical applications as it can improve electrochemical properties such as charge capacity. At the same time, thermal dehydration reduces the charge capacity of β-$Ni(OH)_2$ battery electrodes by approximately 10-14% (KOBER, 1967; Hall *et al.*, 2015). The hydrated form of β-$Ni(OH)_2$ is designated as $[Ni(H_2O)_x](OH)_2$, where $0.1 \leq x \leq 0.4$ (Dennstedt and Löser, 1971; Hall *et al.*, 2015); and the water molecules are weakly associated with the nickel cations and do not form hydrogen bonds with the lattice hydroxide (KOBER, 1967). While the α-$Ni(OH)_2$ xH_2O materials are constantly hydrated because water

is intrinsic to their structure. The degree of hydration in α-$Ni(OH)_2$ xH_2O materials differs within the composition $0.41 \leq x \leq 0.7$ (Daniel and Besenhard, 2012; Hall *et al.*, 2015).

Moreover, a typically mixed phase of α- and β-form have been reported. The presence of an α- and β-form in the exact composition of the structural material is designated as 'interstratified phases consisting of α- and β-type structural motifs' and not simple mixtures of α- and β-$Ni(OH)_2$ crystals (Delmas *et al.*, 1992; Guerlou-Demourgues *et al.*, 1994; Rajamathi *et al.*, 2000; Hall *et al.*, 2015). Instead, the presence of interstratification allows α- and β-$Ni(OH)_2$ domains to coexist within a single crystal. The α-$Ni(OH)_2$, β-$Ni(OH)_2$, β-NiOOH, γ-NiOOH, and α/β-interstratification $Ni(OH)_2$ are briefly discussed below.

2.5.1 β-$Ni(OH)_2$

β-form of $Ni(OH)_2$ has a hexagonal structure and can be adopted by the hydroxides of bivalent atoms such as Ca, Mg, and Co, and is usually denoted as the brucite, $Mg(OH)_2$) or C6-type structure. It occurs naturally as the mineral theophrastite, and it has been represented by the formula β-$Ni(OH)_2$. A typical structural representative is shown in Figure 2-4, where the medium size (grey) spheres are denoting Ni^{2+}; the large (red) spheres are symbolising O^{2-}, and the small (pink) spheres are signifying H^+ (Hall *et al.*, 2015). According to Hall and co-workers, the atoms have fractional coordinates of (0, 0, 0), (1/3, 2/3, u or 2/3, 1/3, ū), and (1/3, 2/3, v or 2/3, 1/3, v̄) where, u = 0.2221 to 0.24, and v = 0.4275 to 0.47 for nickel, oxygen, and hydrogen atoms, respectively.

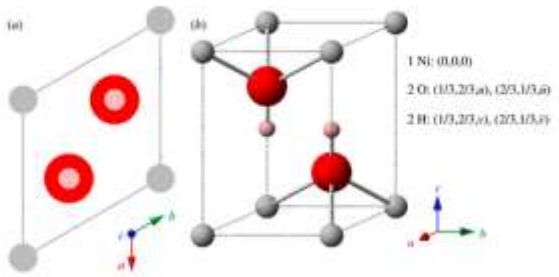

Figure 2-4: Illustration of a typical crystal structure of β-$Ni(OH)_2$. Sourced (Hall *et al.*, 2015).

The O-H bonds in isomorphous molecules such as $Mg(OH)_2$ lie parallel to the c axis where the hydrogen atoms are on opposite sides of the oxygen layer, and the O - O distance is 3.3Å. For this reason, the possibility of hydrogen bonding was ruled out (Hall *et al.*, 2015). Six central oxygen atoms surround Nickel-metal, three lying above the plane of the nickel and three below.

2.5.2 α-$Ni(OH)_2$

α-$Ni(OH)_2$ is highly hydrated and represented by the formula α-$Ni(OH)_2 \cdot xH_2O$, where x varies between 0.5 and 0.7. Although the material is fundamentally hydrated, the water molecule is usually omitted from the written formula, i.e., the material is denoted α-$Ni(OH)_2$. The hydrous α-$Ni(OH)_2$ (Figure 2-5)

differs from the anhydrous hydroxide by the presence of water molecules situated above and below some Ni atoms along the trigonal axis and thereby increases the c axis length to about 8Å.

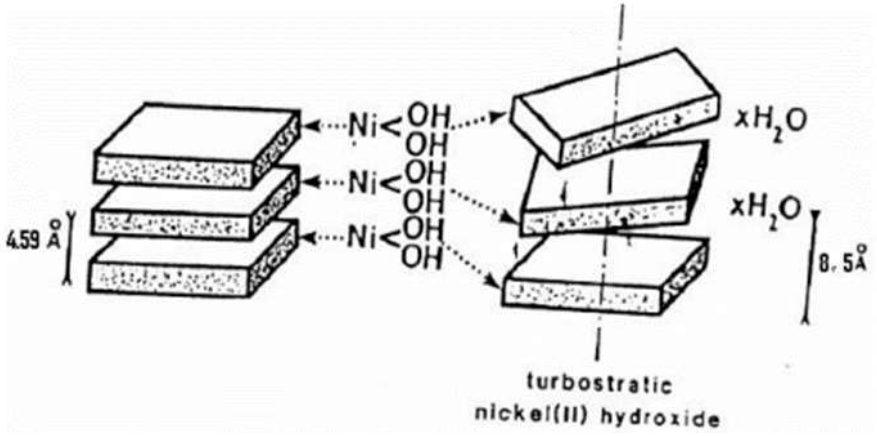

Figure 2-5: Hydrated form of nickel(II) hydroxide: The idealised crystal structure of α-$Ni(OH)_2$ xH_2O. Sourced from (McEwen, 1971).

2.5.3 β-NiOOH

Nickel oxy-hydroxide (β-NiOOH) has a relatively amorphous distorted brucite structure-like demonstrating a hexagonal lattice. The β-NiOOH is a mainly used inorganic catalyst for water oxidation reaction and energy conversion. The investigational band-gap for β-NiOOH is estimated between 1.7 eV -1.8 eV (Tkalych *et al.*, 2015). The magnitudes of unit cell transformation of β-$Ni(OH)_2$ is from a = 3.13Å to 2.82Å and from c = 4.60Å to 4.85Å (Figure 2-6).

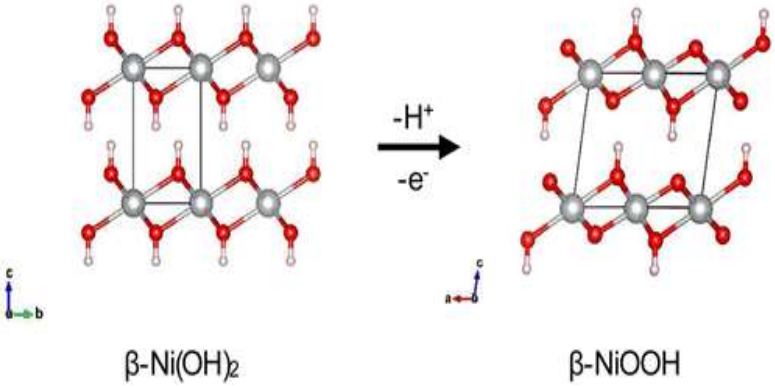

Figure 2-6: Transformation of β-$Ni(OH)_2$ to β-NiOOH structure. Sourced from (Tkalych *et al.*, 2015).

There is no clear establishment of whether the β-NiOOH exhibit n-type semiconductor or p-type semiconductor. In an n-type semiconductor, the donor impurity contributes free electrons, thereby increasing the conductivity of the intrinsic semiconductor. While in p-type semiconductors, the acceptor impurity (intrinsic semiconductor) creates deficiencies of valence electrons, called "holes". Some studies have reported the β-NiOOH as an n-type semiconductor (Tkalych *et al.*, 2015; Dhaka and Toroker, 2019), while others elucidated it as a p-type semiconductor (Madou and McKubre, 1983).

Moreover, the IR spectral analysis of this material indicates that NiOOH is a hydrogen-bonded structure with no free OH^- groups (Dhaka and Toroker, 2019).

2.5.4 γ-NiOOH

The gamma nickel oxy-hydroxide (γ–NiOOH) phase is typically transformed during the overcharge of β-$Ni(OH)_2$ and the charge of α-$Ni(OH)_2$. The transformation of β(II)-$Ni(OH)_2$ to β(III)-NiOOH results in the extraction of one electron per Ni ion cycled. However, more than one electron per Ni can be cycled if γ-form participates in the couple. For example, the transformation of β-$Ni(OH)_2$ to γ-NiOOH and α-$Ni(OH)_2$ to γ-NiOOH. Oxidation of γ-form has, nevertheless, been limited to a supreme oxidation state for Ni of +3.66. Moreover, the spacing between the Ni layers is 7.2Å, but it depends on the insertion of alkali cations and water molecules. Therefore, the transition of β-$Ni(OH)_2$ to γ-NiOOH results in swelling due to significant volume expansion.

2.5.5 α/β-Interstratification materials physical properties and analytical characterizations

The α/β-interstratification comprises of a single grain or crystal of $Ni(OH)_2$ in which some of the layers are detached by incorporated water (α) and some of the layers by a β-form (Hall *et al.*, 2015). A schematic diagram of α/β-interstratification, adapted from Hall and co-workers (Hall *et al.*, 2015), in which both phases coexist within a single crystal, is shown in Figure 2-7.

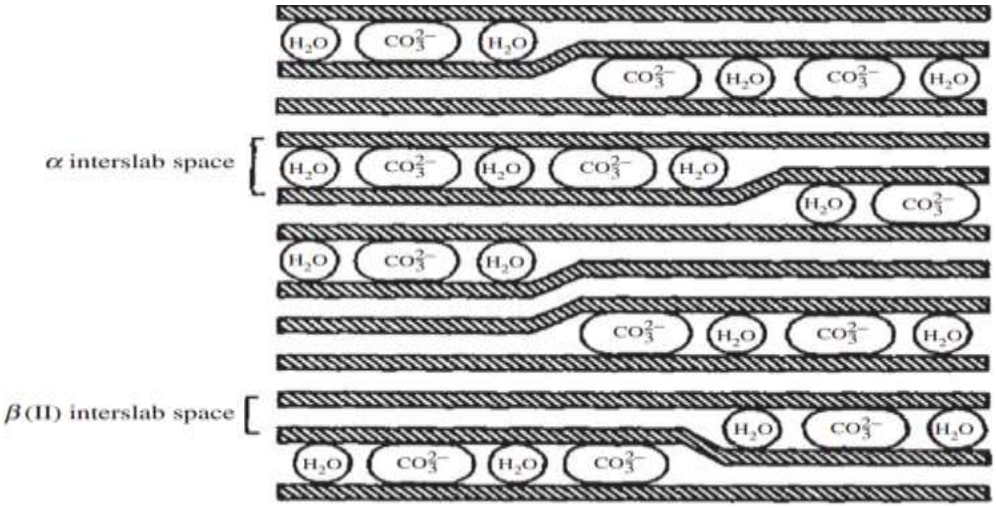

Figure 2-7: Schematic of α/β-interstratification, in which both phases coexist within a single crystal. Sourced from (Hall *et al.*, 2015).

These spheres may be massive or as diminutive as a solitary layer. Usually, the evaluated XRD pattern of materials exhibiting primarily one phase (i.e., when the interstratification is negligible) is quite similar to that of the pure material. For mixed samples such as the α/β-$Ni(OH)_2$ (Figure 2-7), the diffraction lines appear shifted and broadened. This is because the long-range structural order essential for diffraction quantities is diminished in interstratified materials (Hall *et al.*, 2015). If each layer is

solely α- or β-phase, the disorder is only oriented along the c-axis, and the (hkl), $l \neq 0$, XRD lines will be selectively broadened or even absent from the rhythmic pattern (Hall *et al.*, 2015). However, it is also possible to have both phases within a single layer, as shown in Figure 2-7, in which case the structural disorder will be more generalized.

2.6 Synthesis of $Ni(OH)_2$

2.6.1 Synthesis of unmodified $Ni(OH)_2$

Generally, $Ni(OH)_2$ particles are prepared by reacting an inorganic nickel salt with an alkali metal hydroxide in a liquid medium maintained at a pH and temperature at which conversion of the nickel salt to insoluble $Ni(OH)_2$ occurs. The commonly used inorganic nickel salts are (i) $NiSO_4.6H_2O$, (ii) $Ni(NO_3)_2$, or (iii) $NiCl_2$, and the alkali metal hydroxides are (i) NaOH, (ii) KOH, or (iii) LiOH. In the past years, various methods such as chemical precipitation, impregnation-precipitation, electrochemical deposition, sol-gel, chemical ageing, and hydrothermal processes, to name a few, have been used to synthesise the $Ni(OH)_2$ with various morphologies and crystal structures (Yang, Guang-Wu *et al.*, 2008; Jiang *et al.*, 2011; Giri and Sarkar, 2016; Gonçalves *et al.*, 2018).

2.6.2 Ionic substitution and foreign ion incorporation

Despite the encouraging progress, among the drawback mentioned above for $Ni(OH)_2$ as electrode materials is its poor conductivity ($\sim 10^{-17}$ S/cm) (Motori *et al.*, 1994; Sun and Lu, 2012). Therefore, additives are often required for $Ni(OH)_2$ to form composites to improve the performance (Shangguan *et al.*, 2010; Wang, Hailiang *et al.*, 2012; Miao *et al.*, 2015; Xie *et al.*, 2016). These materials are commonly known as the modified or doped $Ni(OH)_2$ materials.

The preparation of the modified materials involves the partial substitution of Ni in $Ni(OH)_2$ with a different metal ion. Numerous cationic substitutions of $Ni(OH)_2$ have been prepared from divalent metal cations and are given the general formula $Ni_{1-x}M_x(OH)_2$, where M is the substituted metal atom. The modified $Ni(OH)_2$ material may be produced by mixing a conductive material with the nickel ion solution to form a suspension. The caustic (NaOH) solution can be then mixed with the suspension to precipitate the $Ni(OH)_2$ material onto the conductive particles, thereby forming the deposit. As the $Ni(OH)_2$ deposits onto the conductive particle, the conductive particle becomes at least partially embedded in the $Ni(OH)_2$ material. The conductive material acts as a nucleation site for the $Ni(OH)_2$ material precipitation.

Modified $Ni(OH)_2$ may contain one or more modifiers selected from the group consisting of Co, Cd, Ag, V, Sb, Ca , Mg, A1, Bi , Cr, Cu, Fe, In , rare earths, Mn, Ru, Sn, Ti, Ba, Si, Sr and Zn (Young, Kwo *et al.*, 2018). In addition, the conductive material may comprise one or more additives selected from the group consisting of carbon, graphite, copper oxide, and cobalt oxide.

2.6.3 Prior works on the production of $Ni(OH)_2$

Table 2-2 summarises prior works on producing α-$Ni(OH)_2$ and mixed α/β-$Ni(OH)_2$ for electrochemical applications. EP, CP, and ECI denote electrochemical precipitation, chemical precipitation, and electrochemical impregnation, respectively. In addition, α-$Ni(OH)_2$ and β-$Ni(OH)_2$ are represented by α and β, respectively. The concentration of the primary dopant in molar percentage is listed in the main dopant column. These methods can also be used to produce β-$Ni(OH)_2$ (Yang, Guang-Wu *et al.*, 2008; Jiang *et al.*, 2011; Giri and Sarkar, 2016; Gonçalves *et al.*, 2018).

Table 2-2: Summaries of prior works on producing α-$Ni(OH)_2$ and mixed α/β-$Ni(OH)_2$ for electrochemical applications. Sourced from (Young, Kwo-Hsiung *et al.*, 2017).

Main Dopant	Preparation Method	Main Findings
Co (6%, 45%, 75%)	EP	• First used with Co to stabilize α and γ
Co (20%, 55%)	CP	• Co stabilizes α up to 50 cycles with 345 mAh/g
Fe (10%, 20%, 30%)	CP	• First used with Fe to stabilize α up to 60 cycles with 232 mAh/g
Al, Fe, Cr, Mn (25%)	EP	• First used with other trivalent cations to promote • Al shows the highest columbic efficiency
Al (10%–25%)	CP from nitrates	• The discharge capacity of 240 mAh/g • Lower resistance and a high self-discharge rate found on α
Al (20%)	CP from nitrates	• α has a higher self-discharge than β
None	Sintering	• The discharge capacity of 225 mAh/g • The first use of a non-precipitation method
Mn (20%–40%)	CP	• Mn stabilizes α up to 120 cycles
Al (20%)	CP from sulfates	• The discharge capacity of 343 mAh/g • Better reversibility of α
Al (30%)	Sintering	• The discharge capacity of ca. 450 mAh/g
Al (25%)	CP from nitrates	• The discharge capacity of 381 mAh/g
Al (5%–20%)	CP	• The discharge capacity of 260 mAh/g
Fe (0%–40%)	CP	• 20% Fe is needed to stabilize α
None	CP from nitrates	• The capacity of 180 mAh/g for an α/β mixture • Ageing process from α to β
Y (1%–10%)	CP from nitrates	• Tap density of 1.6 $g.cc^{-1}$ and 330 mAh/g

Al (8.8%–25.4%)	CP from nitrates	• Al stabilizes α up to 100 cycles
Mn, Zn, Co (13%, 4.5%, 3%)	CP	• α/β mixture showing high tap density and capacity of 375 mAh/g
Al (10%–30%)	CP from nitrates	• The discharge capacity of ca. 350 mAh/g with 10 at % Al
Al (10%, 15%)	ECI	• The discharge capacity of 230 - 240 mAh/g after 200 cycles
Al (20%)	Solid-state synthesis	• The discharge capacity of 336 mAh/g
Al (13.2%–19.5%)	CP from nitrates	• The discharge capacity of 360 mAh/g after 300 cycles
Al (10%, 25%), Co	CP from nitrates	• Al and Co together improve rate capability
Al (10%, 25%)	Sintering	• 25% Al is better than 10% Al for battery application
La (3.26%–9.19%)	CP from nitrates	• La increases the plateau voltage and cycle stability
Ti (11%)	CP from sulfates	• 1.22 electron transfer per Ni • _ Good for high temperature (80 °C)
Al (10%)	CP from nitrates	• The discharge capacity of 380-400 mAh/g • Low tap density
Co, Zn, Mn (10%–20%)	CP	• Mn improves the conductivity and reversibility
Al (20%)	CP	• Nitrate is better than sulfate as raw material • Performance controlled by bulk diffusion
Al (10%), Y (5%), Nd (5%)	CP from sulfates	• Y and Nd improve the hydrogen diffusion
Al (10%), Y (5%)	CP from sulfates	• The discharge capacity of 388 mAh/g
Al (20%)	CP from nitrates	• Capacity degradation due to Al-migration onto surface
None	Rapid freezing micro-emulsion	• The discharge capacity of 340 mAh/g after 35 cycles
Al (15%), Y (4%)	CP from sulfates	• Discharge capacity of 351 mAh/g due to high defect density
Co (20%), Cd (3%)	Ultrasound radiation	• Lower the oxidation potential to avoid oxygen evolution during charge
Al (10%), Ce (5%)	CP + rapid freezing	• Discharge capacity of 363.2 mAh/g
Al (10%)	CP from nitrates	• Capacity, high-rate, and high temperature performance improved by addition of metallic Co or $Y(OH)_3$

None	Liquid phase deposition	• α carbon composite was made
Al (20%)	CP from nitrates	• Nitrate shows better results than sulfate
La (4.3%), Zn (2.4%)	CP from sulfates	• La and Zr improve the high rate, cycle stability, and capacity (373 mAh/g)
Al (15%), Mg (5%)	CP from nitrates	• Mg increases defect density and capacity (359 mAh/g)
Al	Conversely migrates	• Nanowire for capacitor use
Al, Co, Zn, Y (16%)	Supersonic CP	• Capacity of 346 mAh/g due to synergetic effect
Y (16%)	Supersonic CP	• Y increases the capacity to 358 mAh/g
Co (50%)	CP from chlorides CP from chlorides	• Hexamethylenetetramine is a better hydrolytic agent than urea
Zn (5%–20%)	ECI	• Increased surface area for supercapacitor application
Al (9%)	CP from nitrates	• α/β mixture showing high tap density and capacity of 325 mAh/g @ 200 mA/g
Co, Al, Mn, Ca	CP	• β formation is the main failure mode
Cu (9%–23%)	Supersonic CP	• Cu improves both capacity (310 mAh/g) and cycle stability
Al (3% - 7%)	CP from nitrates	• Al improves both capacity (324.5 mAh/g) and cycle stability
Al (17.2%)	Coating with β	• β coating improves both capacity and cycle stability
Y (17%)	CP from chlorides	• Influence from the buffer Na_2CO_3 was studied
Al (20%)	Drying and hydrothermal	• High tap density: 1.84 $g.c^{-1}$
Al (20%)	Anion exchange from chloride	• High tap density: 1.89 $g.c^{-1}$
Al (20%)	Drying	• Cl^- improves both high rate and cycle stability
Al (9%), Mn (4.5%), Yb (9%)	Supersonic CP	• Capacity of 309 mAh/g due to synergetic effects
None	Hydrothermal plus calcination	• Large capacitance for capacitor application
Co (11.1%)	Hydrothermal	• Large capacitance for capacitor application
Sn (2%–17%)	Supersonic CP	• Sn improves capacity, cycle stability, reaction reversibility, and bulk diffusion

Transition metal hydroxides are one of the most promising candidates for battery electrode materials. However, transition metal hydroxides usually suffer from quick decay in capacity during cycling. This

is mainly caused by the decrease of the electroactive surface area, which results from the instability of structural morphology upon fast and repeated charging/ discharging (Xie *et al.*, 2016). Also, the phase control of metal-based-incorporated $Ni(OH)_2$ hybridization remains a challenge on the way toward perfect metal-based-incorporated $Ni(OH)_2$ systems (Yuan *et al.*, 2016).

The current study reports a β-$Ni(OH)_2$ material prepared by co-precipitation method followed by hydrothermal treatment with Cu, Mg, Co, Al, and Mn as the effective dopants. Contrary to this study, Yuan and co-workers (Yuan *et al.*, 2016) reports the electrochemical properties of a prepared porous pompon-like Mg-incorporated α-$Ni(OH)_2$ using a facile chemical co-precipitation method. The α-$Ni(OH)_2$ tends to convert to β-$Ni(OH)_2$ in an alkaline solution or when subjected to charge-discharge cycles (Lee, Jeong Woo *et al.*, 2011). Moreover, the metals are chosen as additives due to their low cost, safety and stability.

2.7 Electrode Production

Nickel electrodes are fabricated using different methods depending on various components or processes such as a (i) selection of material modifiers, (ii) a preparation process conditions and methods, (iii) material additives, (iv) binders or different processing conditions of an electrode, which are annealing, electrodeless plating, surface coating by physical vapour deposition or wet chemical dipping, radiation and electrochemical pressing conditions (Oshitani *et al.*, 1984; Liang *et al.*, 2010; Su *et al.*, 2014; Thurner, 2016; Xu *et al.*, 2017; Bresser *et al.*, 2018; Barton *et al.*, 2020; Kong *et al.*, 2020). Sintered, pressed and tubular or pocket are the mainly used methods for producing nickel-based electrode. These three methods are briefly highlighted below.

2.7.1 Sintered Electrodes

Sintering is a thermal deposition process in which loose active particles are transmuted into a thin coherent porous matrix by heating in an inert atmosphere below the melting point of the active material. The electrode material usually is deposited on an ideal current collector and sintered in an inert atmosphere at approximately 1115K to formulate a porous matrix (Ferrando *et al.*,1984). Chakkaravarthy *et al*. (1991) stated that the inert atmosphere could be either hydrogen, argon, nitrogen or a mixture of either of the gases. The substrate (current conductor) may be Ni mesh or Ni-plated mild or stainless-steel mesh, perforated Ni foil or Ni-plated, perforated mild or stainless-steel foil, Ni-fibre mat or Ni-plated steel-fibre mat.

Bilateral embedding of the electrode material on an ideal current collector process is performed using a graphite mould (under dry conditions) before sintering. This process is titled ‘loose sintering’ or ‘dry powder sintering’. ‘Wet slurry sintering’ is another process wherein an active material slurry of ideal consistency is rooted on a suitable substrate before sintering. These progressions produce physically stable electrode plates of actual thickness and 70 - 90% porosity (Shukla *et al*., 1994). Sintered

electrodes may generate a high electrical conductivity due to the crystal binding between the active material in combination with high mechanical strength. On the downside, sintered electrodes possess a relatively high inactive/active weight ratio and suffer high production costs (Bernard & Lippert, 2015; Chakkaravarthy *et al*. 1991).

2.7.2 Tubular or Pocket Plate Electrodes

The Pocket-plate design was developed between 1897-1903 when the first electrode design for Ni-Fe batteries was created (Chakkaravarthy *et al*., 1991). Pre-perforated Ni-plated steel sheets or thin Ni sheets are filled with palletized active material powder blended with conductive additive, mostly graphite and other suitable additives. The particles are then pressed and hold together as pockets with folded strips along the edges. The Ni pockets act as the small particles and current collector (Bernard & Lippert, 2015). Chakkaravarthy *et al*. (1991) highlighted that the current collector at the electrode/ electrolyte interface would accelerate the overpotential hydrogen evolution reaction. Nickel electrodes formulated using a pocket method would increase overpotential due to inevitable diffusion through the perforated steel and pressed palletized active material. Therefore, this design is chiefly suitable for low-current density applications. Nevertheless, the pocket plate technology is still widely applied, presumably due to its robust design.

2.7.3 Paste Type Electrodes

The active material with sufficient additives is blended with an aqueous polymeric binder such as poly(tetrafluoroethylene) (PTFE) or poly(ethylene) (PE). The resulting mixture (paste) is pasted on a porous Ni-foam sheet to produce a plate of the desired thickness. Finally, the wet electrode is dried for 24-48 hours in a vacuum oven (Huang & Chou, 2007; Kao *et al*., 2011). This design of flat paste type negative electrodes exhibits better performance than its counterparts (pocket type and sintered type electrodes) in terms of specific energy, volumetric capacity, ampere-hour capacity and Fe active material (Caldas *et al*., 1998). In addition, "paste plate" type electrodes production entails much lower costs, therefore, are more attractive than sintered electrodes counterparts (Manohar *et al*., 2012; Kao & Chou, 2010).

2.7.4 Pressed or Roll Compacted Electrodes

Ni-based active material composite mixture coupled with graphite powder and other additives in appropriate proportions is incorporated with a binder to formulate an electrode composite mix (PTFE, CA or PVDF) (Chakkaravarthy *et al*., 1991). The electrode composite material is hot pressed on an ideal electro-conducting mesh (usually Ni-mesh) or fed into a rolling machine along with the mesh (Caldas *et al*., 1998; Mrha *et al*., 1979). The thickness of the electrode plate is typically regulated by the applied pressure and the gap between the press plates (Chakkaravarthy *et al*., 1991). Chakkaravarthy *et al*. (1991) and Caldas *et al*. (1998) stressed that sometimes, pore-formers such as minute NaCl or $(NH_4)_2CO_2$ particles are utilised to induce sufficient porosity. Pressed electrodes incur low-cost

production and exhibit good charge characteristics and durability under optimal current drains (C/5-10).

2.8 Physical Properties and Analytical Techniques Applied in this Study

Various analytical instrumentation has been used for the characterisation of typical $Ni(OH)_2$ based materials. The most emphasis is on understanding the chemical and the structural properties of these materials. For example, the crystalline phase of the active materials and their unit cell dimension were identified using X-Ray Powder Diffraction (XRD). The present functional groups were determined using Fourier Transform Infrared Spectroscopy (FTIR). The active material's thermal stability and its fraction of volatile components were monitored using Thermal Gravimetric Analysis (TGA) equipped with Differential Thermal Analysis (DTA). Specific surface area and pore size were analysed using Brunauer-Emmett-Teller (BET) nitrogen adsorption isotherms and Barrett-Joyner-Halenda (BJH), respectively. The elemental compositions present were confirmed using Inductively Coupled Plasma Optical Emission Spectroscopy (ICP-OES) and Scanning Electron Microscope – Elemental Dispersive Spectrometer (SEM-EDS). SEM images were also collected, and Transmission Electron Microscopy (TEM) was used to determine the morphological changes of the best composition material after application.

A brief overview of each technique and its relevance application in $Ni(OH)_2$, where it is applicable, as cited in the literature, is provided below.

2.8.1 X-Ray Diffraction (XRD)

X-ray powder diffraction (XRD) is a rapid analytical technique primarily used to phase identification of a crystalline material and provide information on unit cell dimensions. The analysed material is finely ground, homogenized, and the average bulk composition is determined. Max von Laue, in 1912, discovered that crystalline substances act as three-dimensional diffraction gratings for X-ray wavelengths similar to the spacing of planes in a crystal lattice. X-ray diffraction is now a common technique for studying crystal structures and atomic spacing (Guinier, 1994).

2.8.1.1 XRD characterization of $Ni(OH)_2$ based material

A representative diffractogram of a β- and α-form of $Ni(OH)_2$ films layered on Ni substrates composed using a CuKα X-ray source are demonstrated in Figure 2-8. Figure 2-8 was adapted from Hall and co-workers (Hall *et al.*, 2015). According to the authors, the β-$Ni(OH)_2$ (Figure 2-8a) demonstrated a discerning line broadening of the peaks that contain the crystallographic c-axis. While the α-$Ni(OH)_2$ (Figure 2-8b) showed low XRD intensities owing to high general structural disorder.

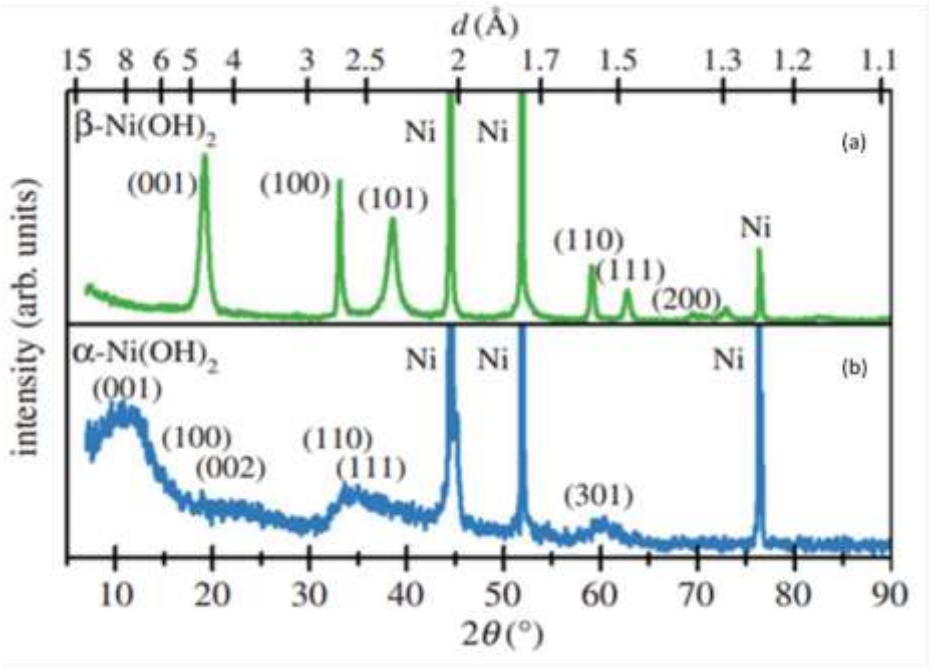

Figure 2-8: Typical schematic diffractogram of $Ni(OH)_2$ on Ni substrates collected using a CuKα X-ray source. (a) β-$Ni(OH)_2$ and (b) α-$Ni(OH)_2$ sourced from (Hall *et al.*, 2015).

The d_{Ni-Ni} may be compared directly with the a-parameter of β-$Ni(OH)_2$ (Table 2-3); and the a-parameter depends on how the unit cell is defined, which is determined by the degree of hydration. Furthermore, the c-parameter is more significant if the interlayer space contains anionic impurities.

Table 2-3: Unit cell parameters for the two fundamental phases of $Ni(OH)_2$ (Hall *et al.*, 2015).

	β-$Ni(OH)_2$	**β-$Ni(OD)_2$**		**α-$Ni(OH)_2$ xH_2O**
Space group	D^3_3d / $P\bar{3}m1$/No.164			D13d / $P\bar{3}m1$ /No.162a
α = β	90°			90°
γ	120°			120°
a = b	3.126 Å	3.126 Å	d_{Ni-Ni}	3.08 Å
c	4.605 Å	4.593 Å		8.0 Å

In addition to β- and α-form of $Ni(OH)_2$ phases, there are several structural disorders of $Ni(OH)_2$ that are reported in the literature (Delmas *et al.*, 1992; Guerlou-Demourgues *et al.*, 1994; Huang, Jichun *et al.*, 2013; Hall *et al.*, 2015). For example, the mixture of the β- and α-form of $Ni(OH)_2$ previously expressed as α/β-interstratification has been reported in the literature (Hall *et al.*, 2015). In addition, the formation of internal mechanical stress during the synthesis of the α-derived structures has been reported by Hall and co-workers. A representative XRD diffraction pattern source from (Hall *et al.*, 2015) is presented in Figure 2-9.

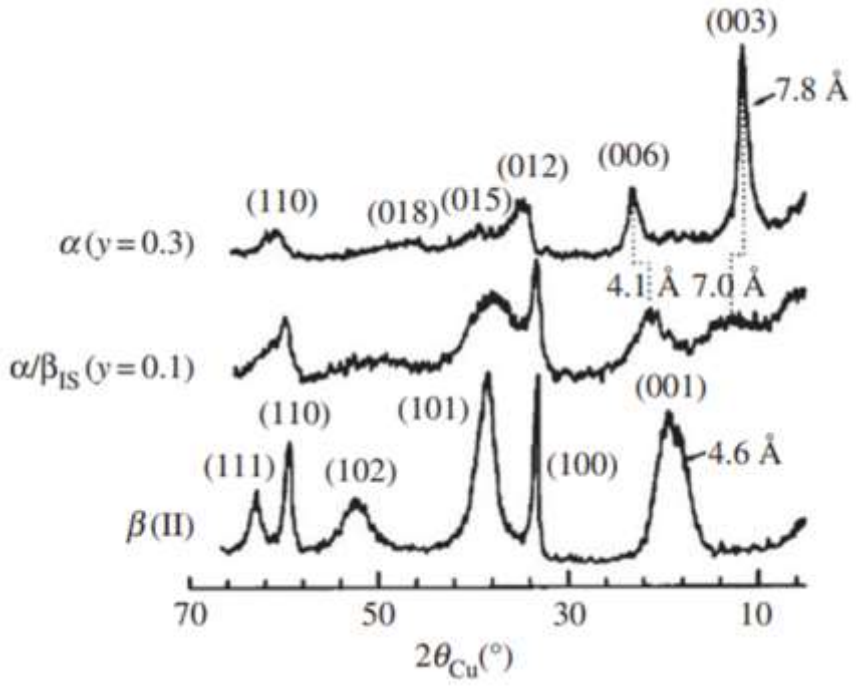

Figure 2-9: A typical XRD patterns collected from α-$Ni_{0.7}Mn_{0.3}(OH)_2$, α/$β_{IS}$-$Ni_{0.9}Mn_{0.1}(OH)_2$, and β-$Ni(OH)_2$ using a CuKα X-ray. Sourced from (Hall *et al.*, 2015).

No one umbrella fits the causes of the structural disorder. However, it has been reported that the insertion of large polyatomic anions, such as nitrate, into the lattice sites or the intercalation space of α-$Ni(OH)_2$ is expected to introduce mechanical stress (Hall *et al.*, 2015). According to Hall and co-workers, during the chemical ageing of α- to β-$Ni(OH)_2$, the internal stress may occur due to changing the unit cell c-parameter (8.0 – 4.6 Å). The transformation of α- to β-$Ni(OH)_2$ results in compressive and tensile forces along the c-direction of the α- to β-forms, respectively (Hall *et al.*, 2014).

Also, in dried $Ni(OH)_2$ samples and redox cycling of $Ni(OH)_2$ electrodes in batteries, mechanical stress is generally observed due to variations in densities of $Ni(OH)_2$ and NiOOH (Oliva *et al.*, 1982). In dried $Ni(OH)_2$, the lattice vibrational modes are shifted when the $Ni(OH)_2$ films are fractured, illustrating that the elimination of water changes the density of the materials and causes internal stresses (Hall *et al.*, 2012). The α-derived structures are the α-form related materials that do not truly belong to the α-$Ni(OH)_2$ form but often represented as "α"-form owing to structural similarities. Fundamentally, this proposes two likely elucidations of the 'α' label: (i) brucite-like $Ni(OH)_2$ sheets with incorporated water or (ii) brucite-like $Ni(OH)_2$ sheets with any introduced species.

According to the authors, the vibrational spectra collected from interstratified materials contain the characteristic O-H internal stretching modes of the α- and β-phase materials. Other possible interstratification and structural disorder such as the mixed metals, carbonate-intercalated of α/$β_{IS}$-$Ni_{0.9}Mn_{0.1}(OH)_2$ (Guerlou-Demourgues *et al.*, 1994), α/$β_{IS}$-$Ni_{1-x}Co_x(OH)_2$ in (Delmas *et al.*, 1992), and α/$β_{IS}$-$Ni_{1-x}Al_x(OH)_2$ (Huang, Jichun *et al.*, 2013) materials have been reported. Guerlou-Demourgues

and co-workers (Guerlou-Demourgues *et al.*, 1994) commend that the minimal quantity of carbonate in their samples was inadequate to dispense within the interlayer space, which produced segregation evenly.

Huang and co-workers (Huang, Jichun *et al.*, 2013) partially substituted Al for Ni in β-$Ni(OH)_2$ material. The authors observed that with the increase of Al content in β-$Ni(OH)_2$, the diffraction intensity of α-form was more pronounced, while the β-phase was minimal. Also, the authors observed that the diffraction peak position of Al-incorporated $Ni(OH)_2$ samples shifted to the left with an increase in Al content. The observed shift in diffraction peak position was due to variation of metal ionic radius between Al and Ni metal. Huang and co-workers (Huang, Jichun *et al.*, 2013) concluded that their findings demonstrated that both α/β-form was due to the addition of Al.

2.8.2 Fourier-Transform Infrared Spectroscopy (FTIR)

Fourier-transform infrared spectroscopy (FTIR) exploits molecules that absorb specific frequencies from the electromagnetic spectrum (EMS) characteristic of their structure. The absorbed frequencies are directly proportional to vibrational energies and dependent on Hooke's law (Equation 2-16). Where ν, c, k, and μ is a vibrational frequency, speed of light, force/spring constant and reduced mass of bonding atoms, respectively (Phillippi and Mazdiyasni, 1971; Mirabella, 1992). Factors that influence the exact IR absorption band of a covalent bond are the shape of the molecular potential energy surface, the mass of absorbing atoms and associated vibrational coupling.

Equation 2-16: Vibrational frequency equation

$$\nu = \frac{1}{2\pi c}\sqrt{\frac{k}{\mu}}$$

Where ν is the vibrational frequency, c is the speed constancy (c = $3x10^{10}$ cm/sec), k is the molecular force constant, and μ is the reduced mass given by Equation 2-17. Where m_A and m_B is the atomic mass A and mass B, respectively.

Equation 2-17: Reduced mass of bonding atoms equation

$$\mu = \frac{m_A m_B}{m_A + m_B}$$

When a sample interacts with infrared light, selected IR vibrational frequencies are absorbed. Examination of transmitted light reveals how much energy is absorbed in each frequency. The technique is commonly used for the analysis of samples containing covalent bonds (non-metals) (Phillippi and Mazdiyasni, 1971; Mirabella, 1992). IR absorption occurs when the incoming light frequency matches the bond's vibrational frequency, enabling the researchers to identify specific functional groups in molecules in the sample. When the bond is strong, the frequency where atoms vibrate becomes stronger

(shorter the wavelength, higher the energy). Light can be detected through transmission (%T) - the amount of light that passes through the sample. It can also be seen by reflection - the amount of light that bounces off the sample. High transmittance at a frequency means few bonds absorb that "colour" light in the sample. Low transmittance means a high population of bonds have vibrational energies corresponding to the incident light.

Although incident radiation can be scattered, absorbed, reflected or transmitted in battery materials such as $Ni(OH)_2$, transmittance (%T) has more physical meaning than absorbance (Abs). Therefore, %T is preferred chiefly for qualitative analysis, while absorbance (Abs.) is used quantitatively. The most observed infrared-active vibrational modes of $Ni(OH)_2$ observed in literature are presented below.

2.8.2.1 FTIR characterization of $Ni(OH)_2$ based material

The β and α-phases are mostly considered when identifying functional groups of the material, although different types and degrees of disorder exist as mentioned in the section below (Bantignies *et al.*, 2008; Martins *et al.*, 2014; Gonçalves *et al.*, 2018). Bantignies and co-workers (Bantignies *et al.*, 2008), reported only four IR lattice modes in a range of 332 - 354, 440 - 475, 510 - 553 and 3630 - 3650 cm^{-1} for a β-$Ni(OH)_2$. Since then, several peak bands have been reported. A weak feature at approximately 1600 cm^{-1} superimposed with a soft peak at around 1630 cm^{-1} attributed to the O-H bend of H_2O that has adsorbed on the material surface or has been trapped within the material has been detected. The existence of water in β-$Ni(OH)_2$ is weakly associated with the nickel cations and does not form hydrogen bonds with the lattice hydroxide (Begum *et al.*, 2009; Hall *et al.*, 2014; Hall *et al.*, 2015; Posada and Hall, 2016). The minimal present amount of H_2O in β-$Ni(OH)_2$ has the potential to elucidate the electrochemical properties of the battery electrode (Begum *et al.*, 2009). The peaks at roughly 3380 cm^{-1} and about 3450 cm^{-1} are from the O-H stretch of the H_2O. A shoulder at 3601 cm^{-1} corresponds to the in-phase O-H stretch of disordered β-$Ni(OH)_2$ has also been reported. β-$Ni(OH)_2$ materials often contain stacking faults, incorporated during preparation. Moreover, different degrees of hydration can occur, observed by large H_2O bands in the Raman and IR spectra. Finally, other factors such as crystallite size, point defects, stacking faults, etc., are expected to affect the spectroscopic properties of the materials.

The α-phase of $Ni(OH)_2$ is turbostratic, where adjacent layers are separated by amorphous H_2O. The anions in the Ni^{2+} salt used for sample preparation often incorporate into this interlayer region. There are three IR-active α-$Ni(OH)_2$ modes at 380 - 400, 460 - 480 and 625 - 670 cm^{-1} mostly reported (Begum *et al.*, 2009; Hall *et al.*, 2014; Su *et al.*, 2014; Li *et al.*, 2015; Shanaj and John, 2016; Yan, Zhenhua *et al.*, 2018; Liu, Ling *et al.*, 2019; Wiston and Ashok, 2019). Weakly visible combination bands are observed at 835 and 1055 cm^{-1} (Begum *et al.*, 2009; Shanaj and John, 2016). The latter is not visible in the spectra of nitrate-intercalated α-$Ni(OH)_2$ samples because it is obscured by nitrate bands (Begum *et*

al., 2009; Shanaj and John, 2016). Two peaks from the O-H bending modes of lattice OH are observed at 1380 - 1390 and 1480 - 1490 cm^{-1} (Begum *et al.*, 2009; Hall *et al.*, 2015; Shanaj and John, 2016). These peaks vary slightly between samples because of structural disorder and the mechanical stress induced when the materials are dried. The O-H bending mode from intercalated H_2O is measured at 1600 cm^{-1} (Begum *et al.*, 2009; Hall *et al.*, 2015). Broad features from free H_2O are estimated at 3220 - 3515 cm^{-1}, and peaks corresponding to lattice OH and inter-sheet H_2O are observed at 3570 - 3640 cm^{-1} (Begum *et al.*, 2009).

The most common FTIR attribution bands present in the $Ni(OH)_2$ based materials that have been reported in the literature are listed in Table 2-4.

Table 2-4: FTIR attributions of absorption bands for $Ni(OH)_2$

Wavenumber (cm^{-1})	**Attribution of absorption bands**	**References**
3600	Vibrational stretching of a hydroxyl group in the nickel hydroxide lattice	(Begum *et al.*, 2009; Shanaj and John, 2016)
3400	Vibrational stretching of the adsorbed water	(Begum *et al.*, 2009; Shanaj and John, 2016)
2000	CO_2 present in the air	(Begum *et al.*, 2009)
1600	Water angular deformation	(Begum *et al.*, 2009; Shanaj and John, 2016)
1400, 1300, 1100	Carbon, nitrates, and sulphates anions vibration stretching	(Begum *et al.*, 2009; Shanaj and John, 2016)
500	Water angular deformation in a plan	(Begum *et al.*, 2009)
400	Ni-O vibrational stretching	(Begum *et al.*, 2009; Shanaj and John, 2016)

2.8.3 Thermogravimetric Analysis (TGA) and Differential Thermal Analysis (DTA)

Thermogravimetric analysis or thermal gravimetric analysis (TGA) is among the frequently used techniques to assess the amount of hydration for $Ni(OH)_2$ (Dennstedt and Löser, 1971; Begum *et al.*, 2009; Hall *et al.*, 2015; Shanaj and John, 2016). Thermogravimetric analysis (TGA) is a thermal analysis technique involving determining the change in weight of a sample as a function of temperature and/or time of heating. TGA is performed either in an inert nitrogen environment or in an oxidative environment (air). The TG component measures temperatures where decomposition, reduction or oxidation occurs. It simultaneously measures the weight changes associated with decomposition, oxidation, and any other physical or chemical changes that result in sample weight loss or gain.

The differential thermal analysis (DTA) is a technique that measures the difference between the sample temperature (Ts) and the temperature of a reference (Tr). A plot of (Ts – Tr) over a programmed

temperature range will show a series of peaks or step changes that map the temperatures where thermal events occur. The DTA component shows whether decomposition processes are endothermic or exothermic. The DTA also measures temperatures corresponding to phase changes where no mass loss occurs, such as melting, crystallization and glass transitions.

TG/DTA is a simultaneous thermal analyzer that can characterize multiple thermal properties of a sample in a single experiment. However, the amount of heat absorbed or released by the sample as it undergoes temperature changes cannot be accurately quantified by the TG/DTA instrument (Hall *et al.*, 2015; Shanaj and John, 2016).

2.8.4 Brunauer-Emmett-Teller (BET) Theory

The Brunauer-Emmett-Teller (BET) technique is commonly used to measure the specific surface area of materials. The BET theory is related to the adsorption of a gas on the material's surface. BET theory is used in systems of counter-layer adsorption and typically employs inquisitive gases. The boiling temperature of nitrogen gas is the commonly used gas because N_2 does not chemically respond with material surfaces as adsorbates to compute the specific surface area (Che and Védrine, 2012; Lowell *et al.*, 2012; Park, 2012; Hiemenz and Rajagopalan, 2016). Specific surface area is a scale-dependent property, with no single actual value of a particular surface area definable. Thus quantities of a specific surface area determined through BET theory may depend on the adsorbate molecule utilized and its adsorption cross-section (Nasrollahzadeh *et al.*, 2019).

Six BET isotherms (Figure 2-10) have been reported in the literature (Park, 2012; Garcia-Martinez and Li, 2015; Thommes *et al.*, 2015). A Type I isotherm (Figure 2-10(Ia-Ib)) is concave to the P/P° axis and the amount adsorbed approaches a limiting value. This limiting uptake is governed by the accessible micropore volume rather than by the internal surface area. A steep uptake at very low P/P° is due to enhanced adsorbent-adsorptive interactions in narrow micropores (micropores of molecular dimensions), resulting in micropore filling at very low P/P°. Reversible type I isotherm, which is typical for microporous solids, has two patterns. For nitrogen and argon adsorption at 77 K and 87 K, Type I(a) isotherms (Figure 2-10 Ia) are microporous materials and mainly composed of narrow micropores (of width $<\sim$ 1 nm). The pore size distributions of Type I(b) isotherms (Figure 2-10 Ib) are narrow mesopores ($< \sim$ 2.5 nm) and wider micropores (Park, 2012; Thommes *et al.*, 2015).

Reversible type II isotherm (Figure 2-10 II) represents mono-porous and microporous materials. The gradual change in curvature demonstrates the multilayer adoption (monolayer coverage overlaps). In contrast, if the monolayer coverage (Point B on the isotherm) is elucidated, the difference in curvature will be sharp. Type III isotherm (Figure 2-10 III) indicates weak interaction between the adsorbent and adsorbate. Type IVa isotherm (Figure 2-10 IVa) depends on the size of the width and the critical width. For example, suppose the width's size width is larger than the required width corresponding to the material's adsorption characteristics and temperature, Type IVa isotherm (Figure 2-10 IVa). In

comparison, Type IVb isotherm (Figure 2-10 IVb) is only obtained for mesopores materials of smaller widths. Type V isotherm (Figure 2-10 V) can be detected at lower P/P° ranges and has a similar shape as Type III isotherms, which may be credited to the weak adsorbent-adsorbate relations. However, hysteresis, such as obtained in Type IV(a), can be detected at higher P/P° ranges due to pores filled by molecular clustering. Type VI isotherm (Figure 2-10 VI) represents multilayer adsorption materials with highly uniform nonporous surfaces. The stepwise curve of the isotherm depends on the material, gas, and the temperature at which it is operated.

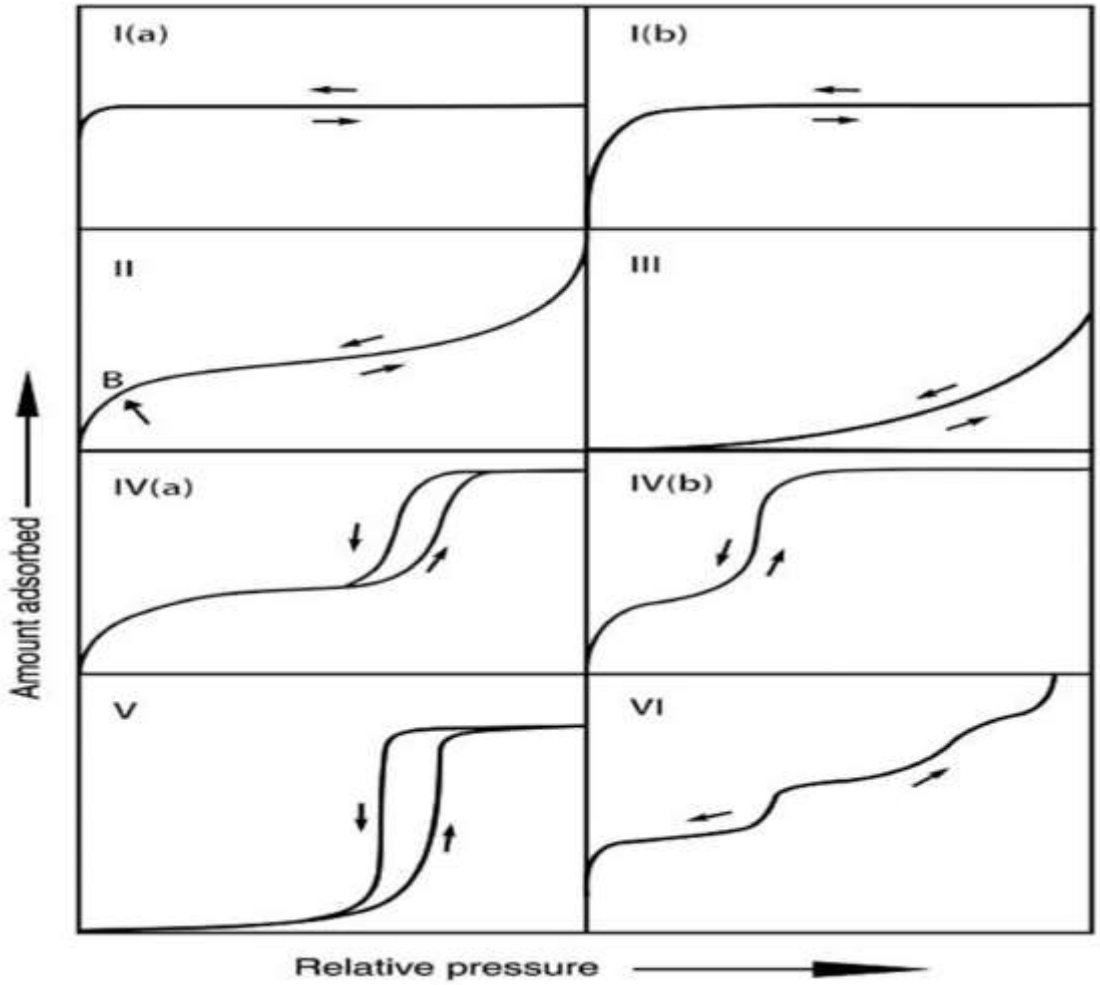

Figure 2-10: International Union of Pure and Applied Chemistry (IUPAC) classification of BET isotherms (Thommes *et al.*, 2015).

Five types of hysteresis loops (Figure 2-11) are reported in the original IUPAC classification of 1985, which is now extended in light of more recent findings. Each of these five distinct types is reasonably closely related to particular pore structure features and underlying adsorption mechanisms. The Type H1 loop is found in materials that exhibit a narrow range of uniform mesopores (Thommes and Cychosz, 2014)). Hysteresis loops of Type H2 are given by more complex pore structures in which network

effects are significant. The very steep desorption branch, which is a characteristic feature of H2(a) loops, can be attributed either to pore-blocking/percolation in a narrow range of pore necks cavitation-induced evaporation. The Type H2(b) loop is also associated with pore blocking, but the size distribution of neck widths is now much more prominent. There are two distinctive features of the Type H3 loop: (i) the adsorption branch resembles a Type II isotherm (ii) the lower limit of the desorption branch usually is located at the cavitation-induced P/P°. For the H4 loop, the adsorption branch is a composite of Types I and II, the more pronounced uptake at low P/P° being associated with the filling of micropores. Type H5 loop is unusual, but it has a distinctive form related to specific pore structures containing both open and partially blocked mesopores.

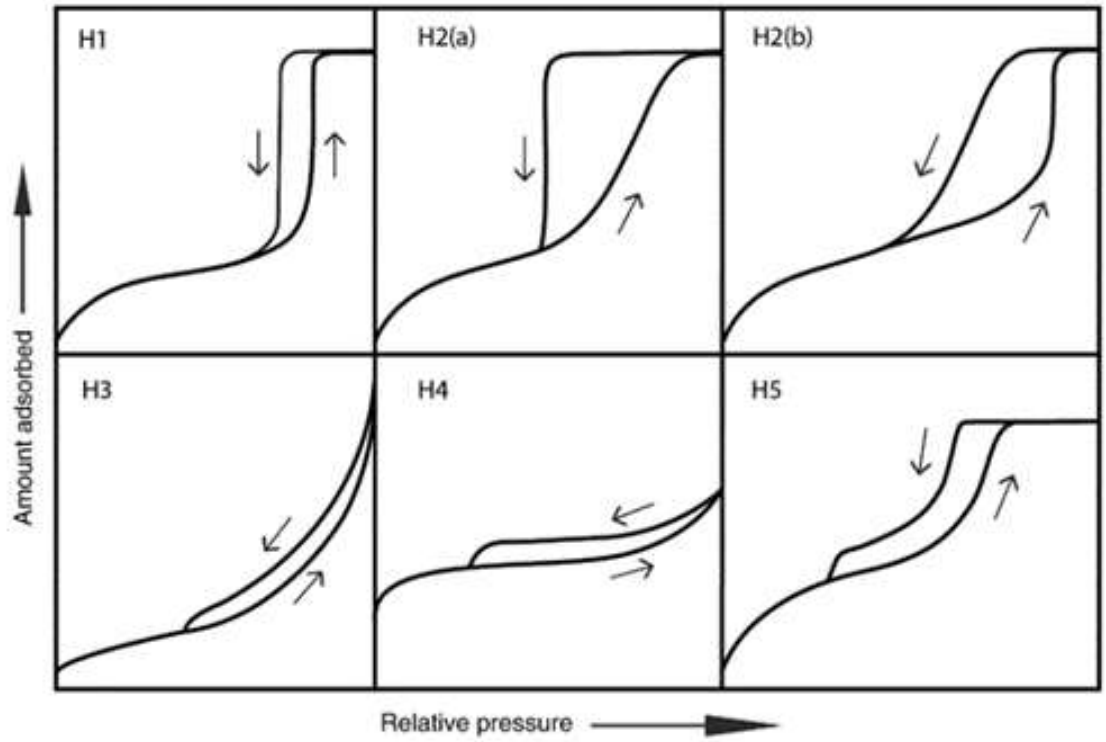

Figure 2-11: Classification of hysteresis loops (Thommes *et al.*, 2015).

2.8.4.1 BET characterization of $Ni(OH)_2$ based material

The Brunauer Emmett Teller (BET) specific surface area, Barrett-Joyner-Halenda (BJH) average pore size and Brunauer-Deming-Deming-Teller (BDDT) classification of nickel-based hydroxide materials has been previously reported in the literature. Table 2-5 briefly listed some of the findings and the references.

Table 2-5: Brunauer-Emmett-Teller (BET) specific surface area, Barrett-Joyner-Halenda (BJH) average pore size and Brunauer-Deming-Deming-Teller (BDDT) classification

Material	BET specific surface area (m^2/g)	BJH average pore size(nm)	BDDT classification	Reference
α-$Ni(OH)_2$	169.94	range of 2–20 nm centred at 3.5 nm	Type IV N_2 adsorption/desorption isotherms with a noticeable H3 type hysteresis loop at the relative pressure (P/P0) range between 0.5 and 1.0 reveals its mesoporous characteristic.	(Yu *et al.*, 2019)
β-$Ni(OH)_2$	56.40	Range of 4–20 nm	Narrow distribution of mesopores	(Dubal *et al.*, 2012)
NiO nanoflowers	62.30	Centred at 6.06 nm	Type IV isotherms with H1-type hysteresis loops, confirming the presence of porosity structure.	(Wang, Xiangyan *et al.*, 2011)
NiO nanodiscs	70.00	Centred at 5.39 nm	Type IV isotherms with H1-type hysteresis loops, confirming the presence of porosity structure.	(Wang, Xiangyan *et al.*, 2011)

Despite the work done using the BET method, many authors have discussed the limitations that are fundamentally related when applied for the surface area determination of microporous materials. The drawbacks in the BET method are mainly related to monolayers owing to gas adsorption. For instance, (i) the legitimacy of n_m (the BET monolayer capacity) is challenging, (ii) the monolayer structure is not the same on all surfaces, mainly when N_2 isotherms are used since the molecule is quadrupolar, and (iii) at shallow pressure ranges (P/P_0) strong adsorption can include localized monolayer coverage and primary micropore filling in the pores of molecular dimensions (Sing, 2001). In addition, several parameters such as temperature, pressure, and characteristics of the material, to name a few, may influence the BET process (Crittenden and Thomas, 1998; Cai, 2011).

2.8.5 Scanning Electron Microscope (SEM)

The scanning electron microscope (SEM) was developed in the early 1950s. The SEM is a microscope that uses electrons instead of light to form an image. It also describes the physics of electron-probe formation and electron-specimen interactions. Prints are produced by scanning the beam while

displaying the signal from an electron detector on a computer monitor. By choosing the appropriate detection mode, information about the sample, such as external morphology (texture), chemical composition, and crystalline structure and orientation of materials that make up the sample, can be obtained (Reimer, 2013). The 'composition' here refers to the mean atomic number, as the individual elements cannot be distinguished.

2.8.6 Inductively Coupled Plasma

Inductively Coupled Plasma (ICP) is an optical emission spectrometry method. When plasma energy is given to an analysis sample from outside, the component elements (atoms) are excited. When the excited atoms return to a low energy position, emission rays (spectrum rays) are released, and the emission rays that correspond to the photon wavelength are measured. The element type is determined based on the photon rays' position, and each element's content is determined based on the rays' intensity.

2.9 Electrochemical Properties and Electrochemical Techniques Applied in this Study

2.9.1 Cyclic Voltammetry (CV)

Cyclic voltammetry is a direct current (DC) electrochemical technique that records the current response. At the same time, a potential scan is applied to the working electrode at a constant scan rate in the forward and reverse directions, once or several times (Bard *et al.*, 1980). Depending upon the information required, the experiment can be performed for several cycles. The resulting response is plotted as current (A) versus potential (V), called cyclic voltammogram. This is a convenient method for the characterization of both double-layer and pseudo-capacitance behaviour of super-capacitors.

The pseudo-capacitance behaviour (Figure 2-12a) shows an anodic peak and a cathodic peak in mirror-image symmetry during a reversible process.

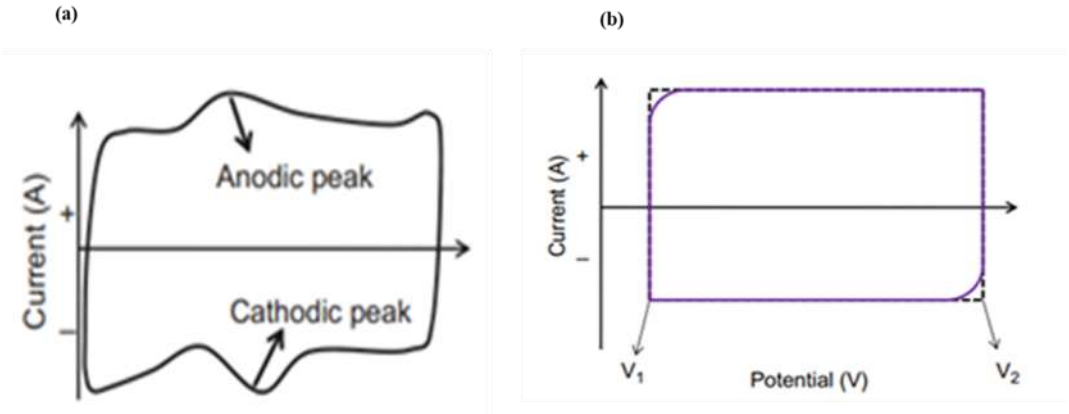

Figure 2-12: CV response (a) pseudo-capacitance behaviour of super-capacitor, (b) between potential difference V1 and V2 of the ideal double-layer capacitor (Elgrishi *et al.*, 2018)

The electrochemical double-layer CV response shows rectangular behaviour (*Figure 2-12*b) without any peaks for the ideal super-capacitor because no redox reaction occurs at the electrode-electrolyte

interface (Ching *et al.*, 1994). The double-layer response expected for a reversible redox couple during a single potential cycle is presented in Figure 2-13. In this typical cyclic voltammogram, it is assumed that only the oxidized form of the active material is present initially (Motlagh *et al.*, 2011; Ma *et al.*, 2015; Miao *et al.*, 2015; Gonçalves *et al.*, 2018; Yin *et al.*, 2019).

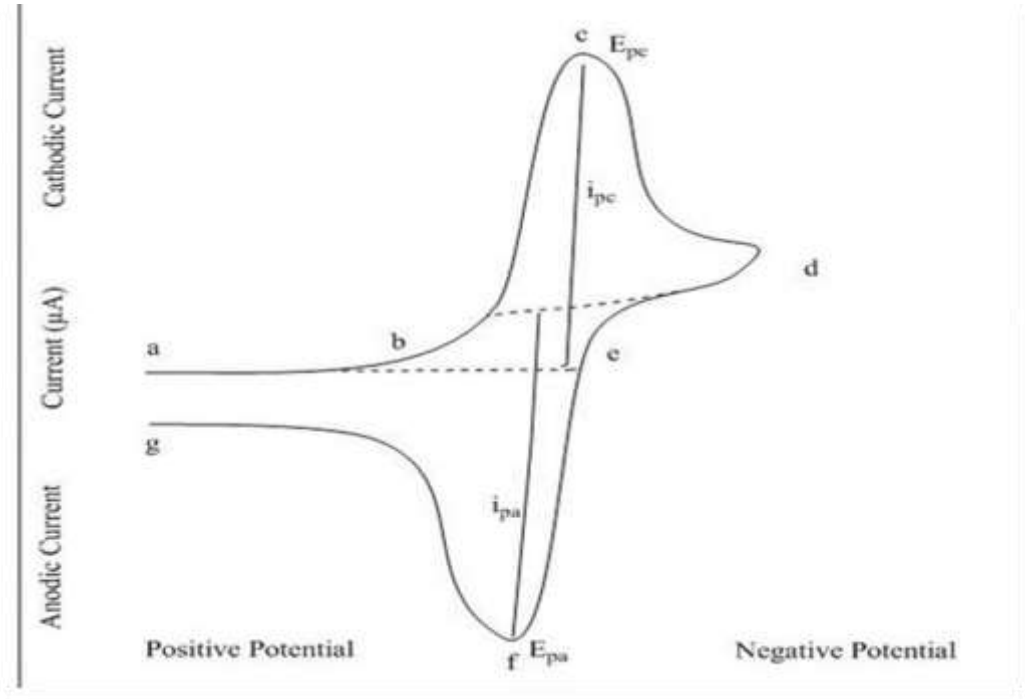

Figure 2-13: Typical cyclic voltammogram for the active material reduction-oxidation assuming that only the oxidized form of the analyte is taking place (Elgrishi *et al.*, 2018)

As demonstrated in Figure 2-13, point (a) to point (b) illustrates a background caused by a capacitated current. Point (b) to point (c) represents a faradaic current, which is the analyte results in the electrochemical reaction. Fundamentally, the reduction process transpires from (a) the initial potential to (d) the switching potential. In this region (a-d), the potential is scanned negatively to cause a reduction of the active material. The resulting current is called cathodic current (i_{pc}). The corresponding peak potential occurs at (c) and is called the cathodic peak potential (E_{pc}). The E_{pc} is reached when all of the substrates at the surface of the electrode have been reduced. After the switching potential has been reached (d), the potential scans positively from (d) to (g). This results in anodic current (i_{pa}) and oxidation of the active material. The peak potential at (f) is called the anodic peak potential (E_{pa}) and is reached when all of the substrates at the surface of the electrode have been oxidized.

2.9.1.1 Cyclic voltammetry characterization of $Ni(OH)_2$ based material

Recently, the potentiodynamic characteristic of the model interface M/$Ni(OH)_2$ (where M could be a Pt or vitreous/glassy carbon) is extensively studied (Shinomiya *et al.*, 2006; Li *et al.*, 2015; Lu and Zhao, 2015; Young, Kwo-hsiung and Yasuoka, 2016; Xu *et al.*, 2017; Liu, Ling *et al.*, 2019; Wiston and Ashok, 2019). For Ni electrode, the applied potential window normal ranges from 0V to 0.8V depending

on the point where the side reaction (oxygen evolution) occurs (Motlagh *et al.*, 2011; Ma *et al.*, 2015; Miao *et al.*, 2015; Gonçalves *et al.*, 2018; Yin *et al.*, 2019). A typical cyclic voltammogram of $Ni(OH)_2$ is demonstrated in Figure 2-14 (Lyons and Brandon, 2008).

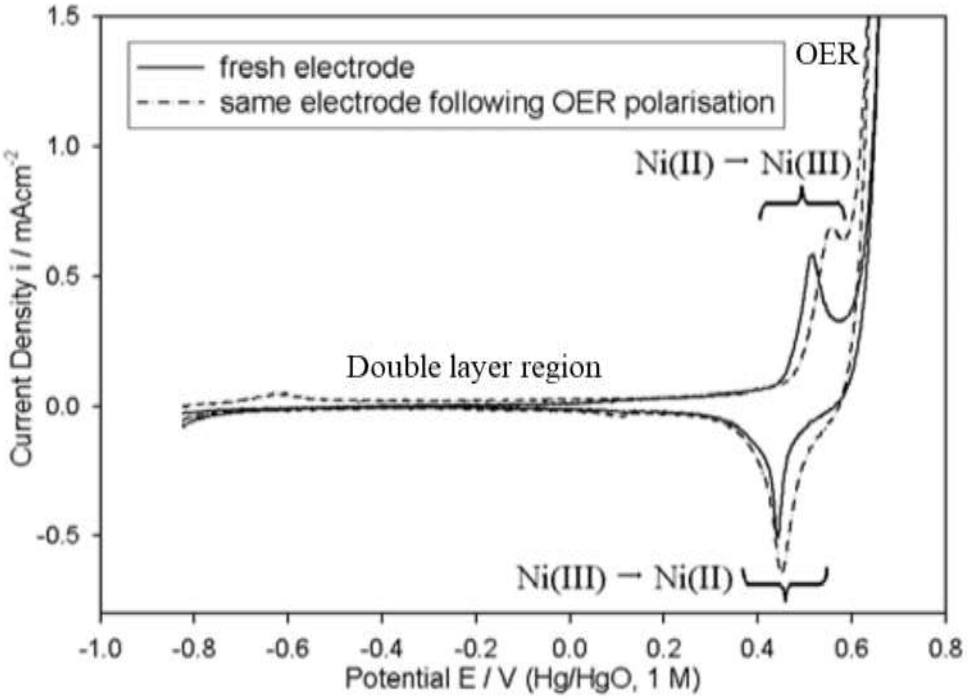

Figure 2-14: Typical cyclic voltammogram of $Ni(OH)_2$ recorded in 1 M NaOH at a sweep rate of 40 mV/s, sourced from (Lyons and Brandon, 2008).

Generally, in cyclic voltammogram of $Ni(OH)_2$ materials, the respective anodic and cathodic peaks for the α/γ couple occur at 0.43 V, and 0.34 V. For the β/β couple, the cathodic and anodic peaks occur at 0.50V and 0.37V. The reversible potentials of the β/β couple are essentially invariant with KOH concentration. In contrast, the α/γ couple varies with OH^- concentration and ageing of α-Ni(OH), reduces the OH- dependence of the reversible potential (Young, Kwo-hsiung and Yasuoka, 2016; Young, Kwo *et al.*, 2018) owing to the conversion to the β/β couple. The β-NiOOH could oxidize α-$Ni(OH)_2$ to α-NiOOH (Daniel and Besenhard, 2012). This reaction is possible while performing cyclic voltammetry on α-$Ni(OH)_2$ thin-film electrodes in the KOH electrolyte. During the cyclic process, some of the α-material gets transformed to the β-form, which could account for the negative drift customarily observed in the anodic peaks in the early stages of cycling (Daniel and Besenhard, 2012). Reactions of this type can introduce distortions; and features in cyclic voltammograms that are difficult to interpret.

2.9.2 Chrono-Charge Discharge Galvanostatic (CCDG)

The chrono-charge discharge galvanostatic (CCDG) sweep involves exposing a working electrode to a constant current where the potential is measured against the potential of a reference electrode as a

function of time. The applied start current is usually lower than the limiting current; moreover, the voltage is rapidly declining due to the ohmic drop (I*R loss). The concentration of the reactants may also decrease at the electrode surface, leading to overpotential due to mass transport limitation. When the applied current is higher than the current limiting current, the diffusion mechanism may not expedite the needed current flow; thus, the electrode potential may keep accelerating until it reaches the next reaction potential. Furthermore, the redox reaction occurs at a constant rate during the galvanostatic cycling, following the anodic/cathodic applied current. The electrode potential evolves with time as the concentration of the reactant species and product species changes at the electrode surface. When the reactant concentration at the electrode surface is almost equal to zero, the amount of the reactant can be insufficient to accommodate all the electrons generated by the constant current flux. Therefore, the voltage will move to more anodic or cathodic values.

Additionally, a typical discharge-charge curve of a commercial Ni-Fe battery is shown in Figure 2-15. The battery's open-circuit voltage is 1.4V. It has a nominal voltage of 1.2V, and on a charge, the maximum voltage between 1.7 to 1.8V is commonly used. The charge cut off voltage widely enrolled to limit gassing of oxygen and hydrogen evolution is approximately 1.6 V_{dc}/cell. The cut-off voltage during discharge depends on the battery's application and the desired cycle life but is conventionally between 0.6 and 1 V_{dc}/cell (Oshitani *et al.*, 1984).

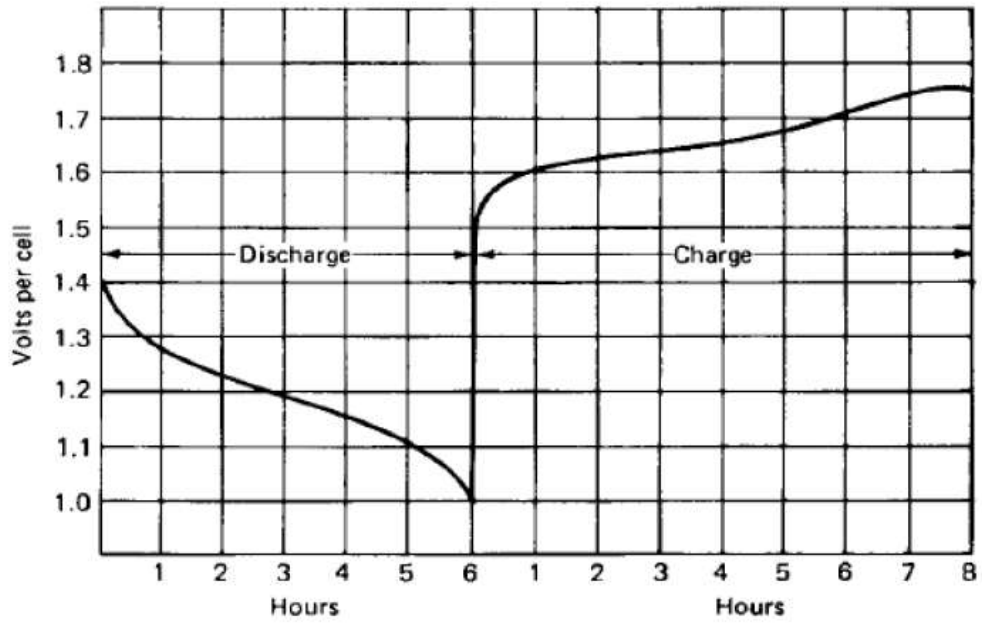

Figure 2-15: The typical voltage characteristics during constant-rate discharge and charge. Sourced from (Oshitani *et al.*, 1984).

2.9.2.1 Galvanostatic of characterization of $Ni(OH)_2$ based material

The β/β couples had open circuit potentials in the range of 0.44V to 0.47V vs Hg/HgO, whereas the α/γ couples had values in the range of 0.39V to 0.44V (Daniel and Besenhard, 2012). The open-circuit

potentials depended on pre-treatments such as formation cycles and ageing in concentrated KOH electrolytes. This open-circuit potential is a mixed-potential, not a true equilibrium potential (Oshitani *et al.*, 1984; Zimmerman and Effa, 1984; Daniel and Besenhard, 2012) that are due to the discharge of NiOOH and oxygen evolution. A typical nickel electrode potential change during charge is presented in Figure 2-16.

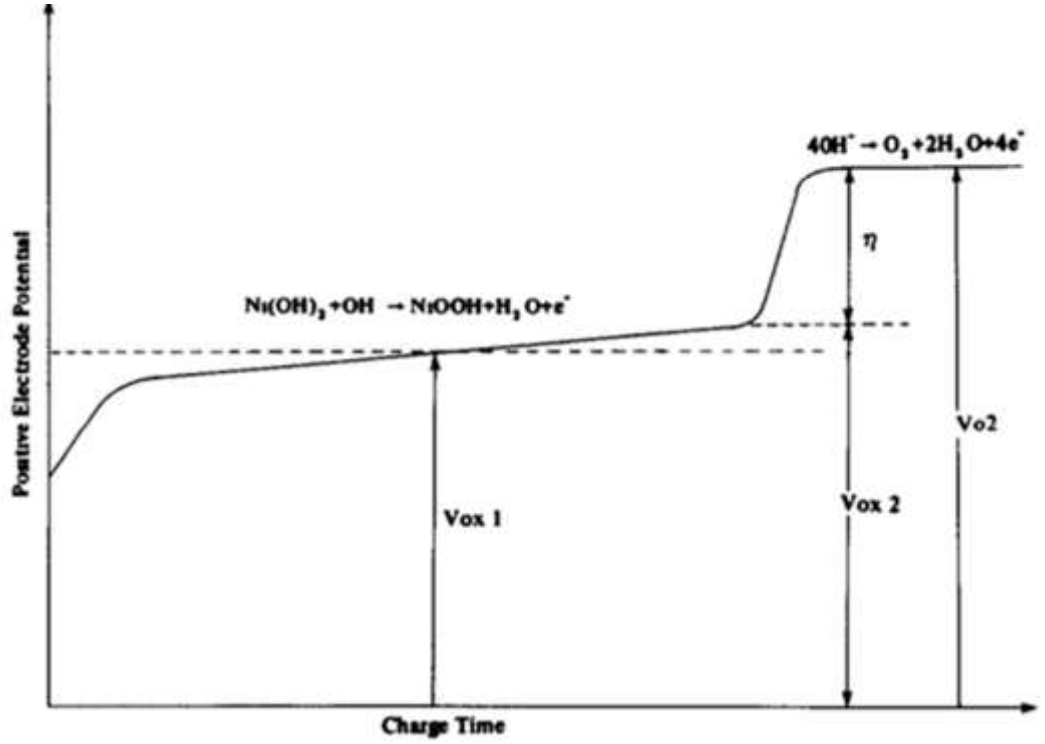

Figure 2-16: A typical nickel electrode potential change during charge (Vox 1 charge potential after 5 hours in charging at 0.1C rate). Sourced from (Oshitani *et al.*, 1984).

The illustrated diagram is based on the assumption that the insufficient capacities of the nickel electrodes after charging at a low rate under average or high temperature are attributable to a low charge efficiency resulting from the competitive reactions of the oxidation of active material and the evolution of oxygen (Oshitani *et al.*, 1984). The illustration is based on a typical discharged state of nickel electrodes charged at a 0.1C rate at 25°C to obtain their charge voltage curves.

The received voltage curves are defined as follow, $V_{OX}1$ is the median oxidation potential (median potential to oxygen evolution). V_O2 is the oxygen evolution potential, and η is the voltage difference between oxygen evolution potential (V_O2) and the maximum oxidation potential ($V_{OX}2$) - the oxidation potential just before oxygen evolution starts. The partial substitution of Ni in $Ni(OH)_2$ with additives such as Co, Al, Zn etc., could potentially lower the median oxidation potential $V_{OX}1$ and shift the oxygen evolution V_O2 to a more noble potential.

2.10 Battery Construction Architecture

Battery architectures may be categorised as a singly design, monopolar or bipolar, depending on how the cell units are electrically connected in a single module. A number of designed structures have been considered, including cylindrical cell, prismatic cell, monopolar, and bipolar batteries(Rota *et al.*, 1995; Saakes *et al.*, 2005; Piłatowicz *et al.*, 2015; Schipper and Aurbach, 2016; Thurner, 2016; Zuo *et al.*, 2017; Liu, Kailong *et al.*, 2019; Liu, Tiefeng *et al.*, 2020).

In cylindrical batteries, electrodes are coiled together with a separator in a swiss roll similar format to the cylindrical battery design. However, this design is not extensively implemented due to its complex design entailed with high costs(Ruetschi, 2004; Omar *et al.*, 2014; Kong *et al.*, 2020).

In prismatic batteries design, the electrodes are cut into rectangular, triangular or circular plates of desired dimensions and assembled into cells by interspacing the negative and positive electrode plates. The advantage of prismatic designed batteries is a high purity material with unique particle characteristics for enhanced electrochemical performance (Schipper and Aurbach, 2016; Thurner, 2016; Zuo *et al.*, 2017; Hao *et al.*, 2018). The prismatic design is the most common design due to its simple yet rugged design synonymous with outstanding electrochemical performance (Zuo *et al.*, 2017; Hao *et al.*, 2018; Liu, Kailong *et al.*, 2019).

Thus, the development of advanced rechargeable batteries provides an excellent opportunity for basic and applied researchers to collectively overcome challenging scientific and technological barriers that directly address a critical need for energy storage. In addition to novel battery chemistries often scientifically reviewed, advanced battery structures via technological innovations that boost battery performance are also worthy of attention. In this context, bipolar electrodes can improve the specific power, simplify cell components, and reduce manufacturing costs for rechargeable batteries. By focusing on the fundamentals and applications of bipolar electrodes in rechargeable batteries, the rational utilization of bipolar electrodes from an academic perspective is considered. Due to the recent interest in bipolar electrodes, the monopolar and bipolar is briefly discussed in the study below.

2.10.1 Monopolar architecture

The monopolar battery designed comprises an electrolyte and multiple cells connected in a series using conductive external wiring. The main futures of a monopolar design are (i) current collector that acts as either a positive or a negative pole, which is denoted as a monopolar plate (MP plate). (ii) electrodes, the active material of the positive electrode and negative electrode are coated separately on one side of each monopolar plate. (iii) unit cell, assembled with the positive electrode (PE/MP), the electrolyte solution, and the negative electrode (NE/MP). It is then sealed and packaged. (iv) Module, a conductive wire (strap/tab) extending from the negative plate of one cell to a positive tab on the next cell. (v) Electron pathway in the module, here during discharge, the electrons move from negative electrode through the in-plane direction of the monopolar toward negative tap. Then, via the external wire towards

the positive tab of the next, and in the in-plane direction of the monopolar plate to enter the positive electrode. A typical schematic diagram of a monopolar design (Jung *et al.*, 2019) is provided in Figure 2-17. The essential requirement for producing a stuck monopolar design (the series connection between a liquid electrode-based cell) is to prevent internal short-circuiting due to electrolyte leakage when sealing and packaging an individual's cells.

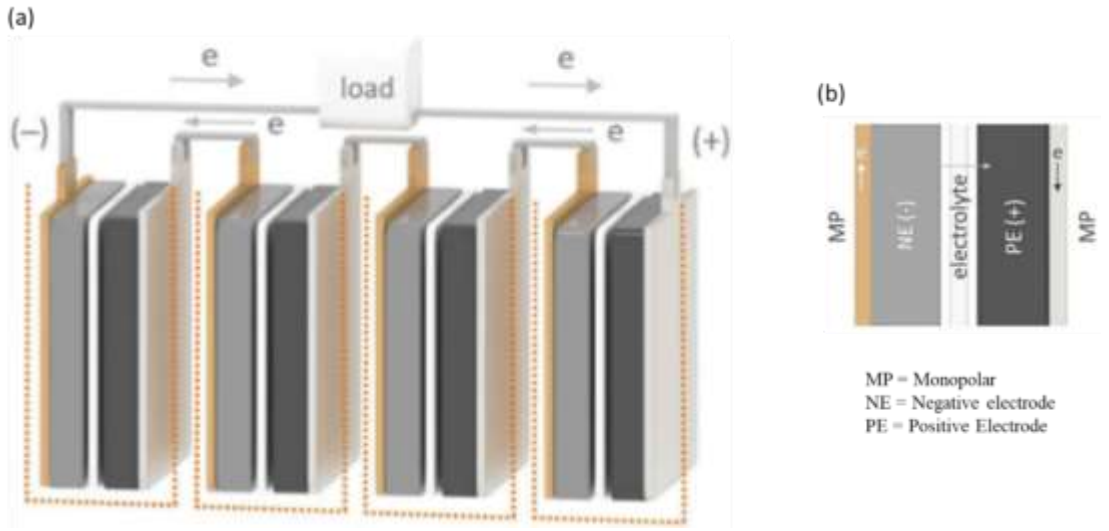

Figure 2-17: Schematic diagram of a) monopolar design with liquid electrolytes and (b) Single unit of a monopolar design cell. Both are sourced from (Jung *et al.*, 2019).

The advantage of the monopolar design is the simple assembly of unit cells with liquid electrolytes. However, monopolar design may not be the right fit for high voltage and high-power applications. For example, battery systems for electric vehicles, since the external electrical connections inevitably increase the resistive losses due to long electron pathways (Shen and Halpert, 1993; Karami *et al.*, 2003; Gambe *et al.*, 2015; Janek and Zeier, 2016; Yoshima *et al.*, 2016). In addition, the required number of monopolar plates, separate cell packaging, and external wiring reduces the volumetric and gravimetric energy densities of the battery's module and increases the material cost of the battery.

2.10.2 Bipolar architecture

On the contrary to monopolar design, bipolar electrodes can improve the specific power, simplify cell components and reduce manufacturing costs for rechargeable batteries (Liu, Tiefeng *et al.*, 2020). In bipolar design, the active materials for the cathode and the functional materials for the anode are applied to a common electrode carrier, which means the positive and the negative slurries are separately coated on both sides of the substrate. Electron transfer between the cathode and the anode occurs through this substrate without an external connector, resulting in a short electron transfer for lower ohmic resistance and a homogeneous current distribution for lower heat production.

The core structures of the bipolar design may be summarized as follows: (i) Current collector, which acts as both positive and negative poles that are called bipolar. (ii) Electrode, made of a positive and a negative electrode equipped on each side of the bipolar plate. (iii) Unit cell, which does not require individual sealing and packaging. (iv) Module, whereby multiple unit cells are connected in series through bipolar plates without external wiring. Thus, a module is formed by sequential stacking or lamination of the positive electrode material on one side of a bipolar plate and the negative electrode on the other side of bipolar plate assemblies and electrolytes. (v) Electron pathway in the module, where electrodes of adjoining cells are on either side of the bipolar plate. Hence, an electron exiting the negative electrode of one cell travels in the through-plane direction of the bipolar plate to the positive electrode during discharge. A typical bipolar design is presented in Figure 2-18.

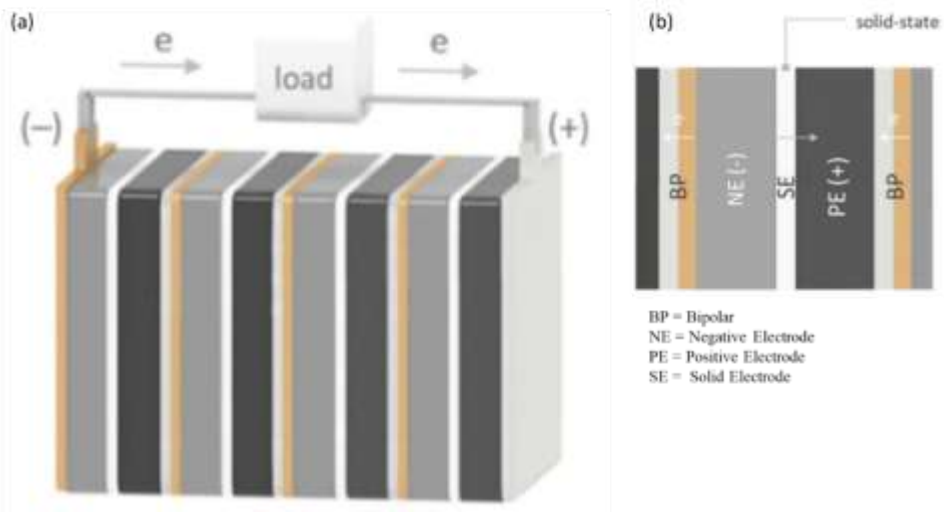

Figure 2-18: Schematic diagrams of a) bipolar stacked design equipped with solid electrolyte and (b) Single unit of a bipolar design cell. Both are sourced from (Jung *et al.*, 2019).

2.11 References

Bantignies, J. L., Deabate, S., Righi, A., Rols, S., Hermet, P., Sauvajol, J. L. and Henn, F. (2008). New insight into the vibrational behavior of nickel hydroxide and oxyhydroxide using inelastic neutron scattering, far/mid-infrared and Raman spectroscopies. The Journal of Physical Chemistry 112(6): 2193-2201.

Bard, A. J., Faulkner, L. R., Leddy, J. and Zoski, C. G. (1980). Electrochemical methods: fundamentals and applications: Wiley New York.

Barton, J., Gammon, R. and Rahil, A. (2020). Characterisation of a nickel-iron battolyser, an integrated battery and electrolyser. Frontiers in Energy Research 8: 509052.

Begum, S. N., Muralidharan, V. and Basha, C. A. (2009). The influences of some additives on electrochemical behaviour of nickel electrodes. International Journal of Hydrogen Energy 34(3): 1548-1555.

Bode, H., Dehmelt, K. and Witte, J. (1966). Theory of the nickel hydroxide electrode-I about the nickel (II)-hydroxidhydrat. Journal of Electrochimica Acta 11: 1079-1087.

Bresser, D., Buchholz, D., Moretti, A., Varzi, A. and Passerini, S. (2018). Alternative binders for sustainable electrochemical energy storage–the transition to aqueous electrode processing and bio-derived polymers. Energy and Environmental Science 11(11): 3096-3127.

Cai, M. (2011). Rock mechanics: achievements and ambitions: CRC Press.

Carbonio, R., Macagno, V., Giordano, M., Vilche, J. and Arvia, A. (1982). A transition in the kinetics of the $Ni(OH)_2$/NiOOH electrode reaction. Journal of the Electrochemical Society 129(5): 983-991.

Casas-Cabanas, M., Radin, M. D., Kim, J., Grey, C. P., Van der Ven, A. and Palacín, M. R. (2018). The nickel battery positive electrode revisited: stability and structure of the β-NiOOH phase. Journal of Materials Chemistry A 6(39): 19256-19265.

Chakkaravarthy, C., Periasamy, P., Jegannathan, S. and Vasu, K. (1991). The nickel/iron battery. Power Sources 35(1): 21-35.

Che, M. and Védrine, J. C. (2012). Characterization of solid materials and heterogeneous catalysts: From structure to surface reactivity: John Wiley & Sons.

Chen, W., Jin, Y., Zhao, J., Liu, N. and Cui, Y. (2018). Nickel-hydrogen batteries for large-scale energy storage. Proceedings of the National Academy of Sciences 115(46): 11694-11699.

Ching, S., Dudek, R. and Tabet, E. (1994). Cyclic voltammetry with ultramicroelectrodes. Chemical Education 71(7): 602.

Crittenden, B. and Thomas, W. J. (1998). Adsorption technology and design: Elsevier.

Daniel, C. and Besenhard, J. O. (2012). Handbook of battery materials: John Wiley & Sons.

Delmas, C., Faure, C. and Borthomieu, Y. (1992). The effect of cobalt on the chemical and electrochemical behaviour of the nickel hydroxide electrode. Materials Science and Engineering: B 13(2): 89-96.

Dennstedt, W. and Löser, W. (1971). Zur kenntnis der nickelhydroxid-elektrode—III. Thermogravimetrische untersuchungen an Nickel (II)-hydroxiden. Journal of Electrochimica Acta 16(3): 429-435.

Dhaka, K. and Toroker, M. C. (2019). Revealing the conducting character of the β-NiOOH catalyst through defect chemistry. The Journal of Physical Chemistry C 123(31): 18895-18904.

Dougherty, B. J., Tanzella, F. L. and Weaver, R. D. (1995). Some nickel-iron, and nickel-metal hydride, cell cycling results. Proceedings of the Tenth Annual Battery Conference on Applications and Advances, IEEE.

Dubal, D., Lee, S. and Kim, W. (2012). Sponge-like β-$Ni(OH)_2$ nanoparticles: synthesis, characterization and electrochemical properties. Journal of Materials Science 47(8): 3817-3821.

Elgrishi, N., Rountree, K. J., McCarthy, B. D., Rountree, E. S., Eisenhart, T. T. and Dempsey, J. L. (2018). A practical beginner's guide to cyclic voltammetry. Journal of chemical education 95(2): 197-206.

Falahati, H., Kim, E. and Barz, D. P. (2015). Fabrication and characterization of thin film nickel hydroxide electrodes for micropower applications. American Chemical Society: Applied Materials and Interfaces 7(23): 12797-12808.

Galushkin, N., Yazvinskaya, N. and Galushkin, D. (2013). Ni-Cd batteries as hydrogen storage units of high-capacity. ECS Electrochemistry Letters 2(1): A1-A2.

Gambe, Y., Sun, Y. and Honma, I. (2015). Development of bipolar all-solid-state lithium battery based on quasi-solid-state electrolyte containing tetraglyme-LiTFSA equimolar complex. Scientific Reports 5(1): 1-4.

Garcia-Martinez, J. and Li, K. (2015). Mesoporous zeolites: preparation, characterization and applications: Wiley-VCH.

Giri, S. D. and Sarkar, A. (2016). Electrochemical study of bulk and monolayer copper in alkaline solution. Journal of the Electrochemical Society 163(3): H252-H259.

Gonçalves, J. M., Alves, K. M., Gonzalez-Huila, M. F., Duarte, A., Martins, P. R. and Araki, K. (2018). Unexpected Stabilization of α-$Ni(OH)_2$ Nanoparticles in GO Nanocomposites. Journal of Nanomaterials 2018: 13.

Guerlou-Demourgues, L., Denage, C. and Delmas, C. (1994). New manganese-substituted nickel hydroxides: Part 1. Crystal chemistry and physical characterization. Power Sources 52(2): 269-274.

Guinier, A. (1994). X-ray diffraction in crystals, imperfect crystals, and amorphous bodies: Courier Corporation.

Hall, D. S., Lockwood, D. J., Bock, C. and MacDougall, B. R. (2015). Nickel hydroxides and related materials: a review of their structures, synthesis and properties. Proceedings of the Royal Society A: Mathematical, Physical and Engineering Sciences 471(2174): 20140792.

Hall, D. S., Lockwood, D. J., Poirier, S., Bock, C. and MacDougall, B. R. (2012). Raman and infrared spectroscopy of α and β phases of thin nickel hydroxide films electrochemically formed on nickel. The Journal of Physical Chemistry A 116(25): 6771-6784.

Hall, D. S., Lockwood, D. J., Poirier, S., Bock, C. and MacDougall, B. R. (2014). Applications of in situ Raman spectroscopy for identifying nickel hydroxide materials and surface layers during chemical aging. American Chemical Society: Applied Materials and Interfaces 6(5): 3141-3149.

Hao, F., Han, F., Liang, Y., Wang, C. and Yao, Y. (2018). Architectural design and fabrication approaches for solid-state batteries. MRS Bulletin 43(10): 775-781.

Hariprakash, B., Martha, S., Hegde, M. and Shukla, A. (2005). A sealed, starved-electrolyte nickel–iron battery. Applied Electrochemistry 35(1): 27-32.

Henao, J. and Martinez-Gomez, L. (2017). on rare-earth perovskite-type negative electrodes in nickel-hydride (Ni/H) secondary batteries. Materials for Renewable and Sustainable Energy 6(2): 7.

Hiemenz, P. C. and Rajagopalan, R. (2016). Principles of colloid and surface chemistry, revised and expanded: CRC Press.

Holmberg, F. (2017). Recycling of nickel metal hydride (NiMH) batteries. Chalmers University of Technology.

Hu, P., Wang, T., Zhao, J., Zhang, C., Ma, J., Du, H., Wang, X. and Cui, G. (2015). Ultrafast alkaline Ni/Zn battery based on Ni-foam-supported Ni_3S_2 nanosheets. American Chemical Society: Applied Materials & Interfaces 7(48): 26396-26399.

Huang, J., Cao, D., Lei, T., Yang, S., Zhou, X., Xu, P. and Wang, G. (2013). Structural and electrochemical performance of Al-substituted β-$Ni(OH)_2$ nanosheets electrodes for nickel metal hydride battery. Journal of Electrochimica Acta 111: 713-719.

Huang, K., Li, J. and Xu, Z. (2011). Enhancement of the recycling of waste Ni-Cd and Ni-MH batteries by mechanical treatment. Journal of Waste Management 31(6): 1292-1299.

Jackovitz, J. F. and Bayles, G. A. (2002). Iron electrode batteries. Handbook of batteries.

Janek, J. and Zeier, W. G. (2016). A solid future for battery development. Nature Energy 1(9): 1-4.

Jensen, W. B. (2013). The Edison nickel-iron alkaline storage cell: notes from the Oesper collections, No. 21, July/August 2013. Oesper Collections in the History of Chemistry.

Jiang, H., Zhao, T., Li, C. and Ma, J. (2011). Hierarchical self-assembly of ultrathin nickel hydroxide nanoflakes for high-performance supercapacitors. Journal of Materials Chemistry 21(11): 3818-3823.

Jung, K. N., Shin, H. S., Park, M. S. and Lee, J. W. (2019). Solid-state lithium batteries: bipolar design, fabrication, and electrochemistry. ChemElectroChem 6(15): 3842-3859.

Kao, C. Y., Tsai, Y. R. and Chou, K. S. (2011). Synthesis and characterization of the iron/copper composite as an electrode material for the rechargeable alkaline battery. Power Sources 196(13): 5746-5750.

Karami, H., Mousavi, M. F. and Shamsipur, M. (2003). A novel dry bipolar rechargeable battery based on polyaniline. Power Sources 124(1): 303-308.

KOBER, F. P. (1967). On the structure of electrochemically active hydrated nickel-oxide electrodes. Power Sources, Elsevier: 257-268.

Kong, D., Wang, Y., Huang, S., Zhang, B., Lim, Y. V., Sim, G. J., Valdivia y Alvarado, P., Ge, Q. and Yang, H. Y. (2020). 3D printed compressible quasi-solid-state nickel-iron battery. American Chemical Society Nano 14(8): 9675-9686.

Lee, J. W., Ko, J. M. and Kim, J.-D. (2011). Hierarchical microspheres based on α-Ni $(OH)_2$ nanosheets intercalated with different anions: synthesis, anion exchange, and effect of intercalated anions on electrochemical capacitance. The Journal of Physical Chemistry C 115(39): 19445-19454.

Lee, S. H., Yi, C. W. and Kim, K. (2011). Characteristics and electrochemical performance of the TiO_2-coated ZnO anode for Ni-Zn secondary batteries. The Journal of Physical Chemistry C 115(5): 2572-2577.

Lei, D., Lee, D. C., Magasinski, A., Zhao, E., Steingart, D. and Yushin, G. (2016). Performance enhancement and side reactions in rechargeable nickel–iron batteries with nanostructured electrodes. American Chemical Society: Applied Materials & Interfaces 8(3): 2088-2096.

Li, Z., Han, J., Fan, L., Wang, M., Tao, S. and Guo, R. (2015). The anion exchange strategy towards mesoporous α-$Ni(OH)_2$ nanowires with multinanocavities for high-performance supercapacitors. Chemical Communications 51(15): 3053-3056.

Liang, Y., Schwab, M. G., Zhi, L., Mugnaioli, E., Kolb, U., Feng, X. and Müllen, K. (2010). Direct access to metal or metal oxide nanocrystals integrated with one-dimensional nanoporous carbons for electrochemical energy storage. Journal of the American Chemical Society 132(42): 15030-15037.

Linden, D. (1995). Handbook of batteries. Fuel and Energy Abstracts.

Linden, D. and Linden, D. (1984). Handbook of batteries and fuel cells: McGraw-Hill New York et al.

Liu, J., Guan, C., Zhou, C., Fan, Z., Ke, Q., Zhang, G., Liu, C. and Wang, J. (2016). A flexible quasi-solid-state nickel–zinc battery with high energy and power densities based on 3D electrode design. Advanced Materials 28(39): 8732-8739.

Liu, K., Li, K., Peng, Q. and Zhang, C. (2019). A brief review on key technologies in the battery management system of electric vehicles. Frontiers of Mechanical Engineering 14(1): 47-64.

Liu, L., Hou, Y., Gao, Y., Yang, N., Liu, J. and Wang, X. (2019). Co doped α-$Ni(OH)_2$ multiple-dimensional structure electrode material. Journal of Electrochimica Acta 295: 340-346.

Liu, T., Yuan, Y., Tao, X., Lin, Z. and Lu, J. (2020). Bipolar electrodes for next-generation rechargeable batteries. Advanced Science 7(17): 2001207.

Lowell, S., Shields, J. E., Thomas, M. A. and Thommes, M. (2012). Characterization of porous solids and powders: surface area, pore size and density: Springer Science and Business Media.

Lu, X. and Zhao, C. (2015). Electrodeposition of hierarchically structured three-dimensional nickel–iron electrodes for efficient oxygen evolution at high current densities. Journal of Nature Communications 6(1): 1-7.

Lyons, M. E. and Brandon, M. P. (2008). The oxygen evolution reaction on passive oxide covered transition metal electrodes in aqueous alkaline solution. Part 1-nickel. International Journal of Electrochemical Science 3(12): 1386-1424.

Ma, X., Li, Y., Wen, Z., Gao, F., Liang, C. and Che, R. (2015). Ultrathin β-$Ni(OH)_2$ nanoplates vertically grown on nickel-coated carbon nanotubes as high-performance pseudocapacitor electrode materials. American Chemical Society: Applied Materials and Interfaces 7(1): 974-979.

Madou, M. J. and McKubre, M. C. (1983). Impedance measurements and photoeffects on Ni electrodes. Journal of The Electrochemical Society 130(5): 1056.

Martins, P. R., Ferreira, L. M. C., Araki, K. and Angnes, L. (2014). Influence of cobalt content on nanostructured alpha-phase-nickel hydroxide modified electrodes for electrocatalytic oxidation of isoniazid. Sensors and Actuators B: Chemical 192: 601-606.

McEwen, R. (1971). Crystallographic studies on nickel hydroxide and the higher nickel oxides. The Journal of Physical Chemistry 75(12): 1782-1789.

Miao, C., Zhu, Y., Zhao, T., Jian, X. and Li, W. (2015). Synthesis and electrochemical performance of mixed phase α/β nickel hydroxide by codoping with Ca^{2+} and PO_4^{3-}. Ionics 21(12): 3201-3208.

Mirabella, F. M. (1992). Internal reflection spectroscopy: Theory and applications: CRC Press.

Motlagh, M. K., Youzbashi, A. and Sabaghzadeh, L. (2011). Synthesis and characterization of nickel hydroxide/oxide nanoparticles by the complexation-precipitation method. International Journal of Physical Sciences 6(6): 1471-1476.

Motori, A., Sandrolini, F. and Davolio, G. (1994). Electrical properties of nickel hydroxide for alkaline cell systems. Power Sources 48(3): 361-370.

Nasrollahzadeh, M., Atarod, M., Sajjadi, M., Sajadi, S. M. and Issaabadi, Z. (2019). Plant-mediated green synthesis of nanostructures: mechanisms, characterization, and applications. Interface Science and Technology, Elsevier. 28: 199-322.

Novakovskii, A., Grushkina, S. and Kozlova, R. (1973). Influence of electrical conductivity of the active material on the behavior of the iron plate in an alkaline storage cell. J. Appl. Chem. USSR (Engl. Transl.);(United States) 46(9).

Oliva, P., Leonardi, J., Laurent, J., Delmas, C., Braconnier, J., Figlarz, M., Fievet, F. and Guibert, A. d. (1982). Review of the structure and the electrochemistry of nickel hydroxides and oxy-hydroxides. Power Sources 8: 229-255.

Omar, N., Firouz, Y., Monem, M., Samba, A., Gualous, H., Coosemans, T., Van den Bossche, P. and Van Mierlo, J. (2014). Analysis of nickel-based battery technologies for hybrid and electric vehicles.

Oshitani, M., Sasaki, Y. and Takashima, K. (1984). Development of a nickel electrode having stable performance at various charge and discharge rates over a wide temperature range. Power Sources 12(3-4): 219-231.

Park, J.-K. (2012). Principles and applications of lithium secondary batteries: John Wiley & Sons.

Phillippi, C. and Mazdiyasni, K. (1971). Infrared and raman spectra of zirconia polymorphs. Journal of the American Ceramic Society 54(5): 254-258.

Piłatowicz, G., Marongiu, A., Drillkens, J., Sinhuber, P. and Sauer, D. U. (2015). A critical overview of definitions and determination techniques of the internal resistance using lithium-ion, lead-acid, nickel metal-hydride batteries and electrochemical double-layer capacitors as examples. Power Sources 296: 365-376.

Placke, T., Kloepsch, R., Dühnen, S. and Winter, M. (2017). Lithium ion, lithium metal, and alternative rechargeable battery technologies: the odyssey for high energy density. Journal of Solid State Electrochemistry 21(7): 1939-1964.

Posada, J. O. G., Abdalla, A. H., Oseghale, C. I. and Hall, P. J. (2016). Multiple regression analysis in the development of NiFe cells as energy storage solutions for intermittent power sources such as wind or solar. International Journal of Hydrogen Energy 41(37): 16330-16337.

Posada, J. O. G. and Hall, P. J. (2016). Towards the development of safe and commercially viable nickel-iron batteries: improvements to coulombic efficiency at high iron sulphide electrode formulations. Applied Electrochemistry 46(4): 451-458.

Rajamathi, M., Kamath, P. V. and Seshadri, R. (2000). Polymorphism in nickel hydroxide: role of interstratification. Journal of Materials Chemistry 10(2): 503-506.

Reimer, L. (2013). Transmission electron microscopy: physics of image formation and microanalysis: Springer.

Rota, M., Comninellis, C., Moller, S., Holzer, F. and Haas, O. (1995). Bipolar Al/O_2 battery with planar electrodes in alkaline and acidic electrolytes. Applied Electrochemistry 25(2): 114-121.

Ruetschi, P. (2004). Aging mechanisms and service life of lead–acid batteries. Power Sources 127(1-2): 33-44.

Saakes, M., Woortmeijer, R. and Schmal, D. (2005). Bipolar lead–acid battery for hybrid vehicles. Power Sources 144(2): 536-545.

Schipper, F. and Aurbach, D. (2016). A brief review: past, present and future of lithium ion batteries. Russian Journal of Electrochemistry 52(12): 1095-1121.

Shanaj, B. and John, X. (2016). Effect of calcination time on structural, optical and antimicrobial properties of nickel oxide nanoparticles. Journal of Theoretical Computer Science 3(2).

Shangguan, E., Chang, Z., Tang, H., Yuan, X.-Z. and Wang, H. (2010). Synthesis and characterization of high-density non-spherical $Ni(OH)_2$ cathode material for Ni-MH batteries. International Journal of Hydrogen Energy 35(18): 9716-9724.

Shen, D. H. and Halpert, G. (1993). Design concepts of high power bipolar rechargeable lithium battery. Power Sources 43(1-3): 327-338.

Shinomiya, T., Gupta, V. and Miura, N. (2006). Effects of electrochemical-deposition method and microstructure on the capacitive characteristics of nano-sized manganese oxide. Journal of Electrochimica Acta 51(21): 4412-4419.

Shukla, A., Ravikumar, M. and Balasubramanian, T. (1994). Nickel/iron batteries. Power Sources 51(1-2): 29-36.

Sing, K. (2001). The use of nitrogen adsorption for the characterisation of porous materials. Colloids and Surfaces A: Physicochemical and Engineering Aspects 187: 3-9.

Su, Y.-Z., Xiao, K., Li, N., Liu, Z.-Q. and Qiao, S.-Z. (2014). Amorphous $Ni(OH)_2$ @ three-dimensional Ni core–shell nanostructures for high capacitance pseudocapacitors and asymmetric supercapacitors. Journal of Materials Chemistry A 2(34): 13845-13853.

Sun, Z. and Lu, X. (2012). A solid-state reaction route to anchoring $Ni(OH)_2$ nanoparticles on reduced graphene oxide sheets for supercapacitors. Industrial and Engineering Chemistry Research 51(30): 9973-9979.

Thackeray, M. M., Wolverton, C. and Isaacs, E. D. (2012). Electrical energy storage for transportation—approaching the limits of, and going beyond, lithium-ion batteries. Energy and Environmental Science 5(7): 7854-7863.

Thommes, M. and Cychosz, K. A. (2014). Physical adsorption characterization of nanoporous materials: progress and challenges. Adsorption 20(2-3): 233-250.

Thommes, M., Kaneko, K., Neimark, A. V., Olivier, J. P., Rodriguez-Reinoso, F., Rouquerol, J. and Sing, K. S. (2015). Physisorption of gases, with special reference to the evaluation of surface area and pore size distribution (IUPAC Technical Report). Pure and Applied Chemistry 87(9-10): 1051-1069.

Thurner, H. (2016). Battery storage systems for electricity technology, applications and economics of large projects in Central and Eastern Europe, Wien.

Tkalych, A. J., Yu, K. and Carter, E. A. (2015). Structural and electronic features of β-$Ni(OH)_2$ and β-NiOOH from first principles. The Journal of Physical Chemistry C 119(43): 24315-24322.

Wang, H., Liang, Y., Gong, M., Li, Y., Chang, W., Mefford, T., Zhou, J., Wang, J., Regier, T. and Wei, F. (2012). An ultrafast nickel–iron battery from strongly coupled inorganic nanoparticle/nanocarbon hybrid materials. Journal of Nature Communications 3: 917.

Wang, X., Wan, L., Yu, T., Zhou, Y., Guan, J., Yu, Z., Li, Z. and Zou, Z. (2011). Non-basic solution eco-routes to nano-scale NiO with different shapes: Synthesis and application. Materials Chemistry and Physics 126(3): 494-499.

Wiston, B. R. and Ashok, M. (2019). Electrochemical performance of hydrothermally synthesized flower-like α-nickel hydroxide. Vacuum 160: 12-17.

Xie, M., Duan, S., Shen, Y., Fang, K., Wang, Y., Lin, M. and Guo, X. (2016). In-situ-grown $Mg(OH)_2$-derived hybrid α-$Ni(OH)_2$ for highly stable supercapacitor. American Chemical Society: Energy Letters 1(4): 814-819.

Xu, W., Lan, R., Du, D., Humphreys, J., Walker, M., Wu, Z., Wang, H. and Tao, S. (2017). Directly growing hierarchical nickel-copper hydroxide nanowires on carbon fibre cloth for efficient electrooxidation of ammonia. Applied Catalysis B: Environmental 218: 470-479.

Yan, Z., Sun, H., Chen, X., Liu, H., Zhao, Y., Li, H., Xie, W., Cheng, F. and Chen, J. (2018). Anion insertion enhanced electrodeposition of robust metal hydroxide/oxide electrodes for oxygen evolution. Journal of Nature Communications 9(1): 1-9.

Yan, Z., Wang, E., Jiang, L. and Sun, G. (2015). Superior cycling stability and high rate capability of three-dimensional Zn/Cu foam electrodes for zinc-based alkaline batteries. Royal Society of Chemistry (RSC): Advances 5(102): 83781-83787.

Yang, G.-W., Xu, C.-L. and Li, H.-L. (2008). Electrodeposited nickel hydroxide on nickel foam with ultrahigh capacitance. Chemical Communications(48): 6537-6539.

Yang, L., Gao, X., Wu, Q., Zhu, H. and Pan, G. (2007). Phase distribution and electrochemical properties of Al-substituted nickel hydroxides. The Journal of Physical Chemistry C 111(12): 4614-4619.

Yin, J., Zhou, G., Gao, X., Chen, J., Zhang, L., Xu, J., Zhao, P. and Gao, F. (2019). α-and β-Phase Ni-Mg hydroxide for high performance hybrid supercapacitors. Nanomaterials 9(12): 1686.

Yoshima, K., Harada, Y. and Takami, N. (2016). Thin hybrid electrolyte based on garnet-type lithium-ion conductor $Li7La_3Zr_2O_{12}$ for 12V-class bipolar batteries. Power Sources 302: 283-290.

Young, K.-H., Wang, L., Yan, S., Liao, X., Meng, T., Shen, H. and Mays, W. (2017). Fabrications of high-capacity alpha-$Ni(OH)_2$. Batteries 3(1): 6.

Young, K.-h. and Yasuoka, S. (2016). Capacity degradation mechanisms in nickel/metal hydride batteries. Batteries 2(1): 3.

Young, K., Wang, L., Mays, W., Reichman, B., Chao-Ian, H., Wong, D. and Nei, J. (2018). Nickel hydroxide positive electrode for alkaline rechargeable battery, Google Patents.

Yu, J., Pan, S., Zhang, Y., Liu, Q. and Li, B. (2019). Facile synthesis of monodispersed α-$Ni(OH)_2$ microspheres assembled by ultrathin nanosheets and its performance for oxygen evolution reduction. Frontiers in Materials 6: 124.

Yuan, S., Wang, X., Lu, C. and Chen, C.-M. (2016). The fine control of porous pompon-like Mg-incorporated α-$Ni(OH)_2$ for enhanced supercapacities. Functional Materials Letters 9(05): 1650057.

Zhang, L., Huang, H., Zhang, W., Gan, Y. and Wang, C. (2008). Effects of conductive ceramic on the electrochemical performance of ZnO for Ni/Zn rechargeable battery. Journal of Electrochimica Acta 53(16): 5386-5390.

Zide, D., Felix, C., Oosthuysen, T. and Bladergroen, B. J. (2020a). Electrochemical studies of the nickel-based hydroxide electrode for the oxygen evolution reaction and coulombic efficiency of the electrode. Electroanalysis 32(12): 2703-2712.

Zide, D., Felix, C., Oosthuysen, T. and Bladergroen, B. J. (2020b). The influence of copper and carbon black on electrochemical behavior of nickel positive electrode. Journal of Electroanalytical Chemistry 878: 114539.

Zimmerman, A. and Effa, P. (1984). Discharge kinetics of the nickel electrode. Journal of the Electrochemical Society 131(4): 709-713.

Zuo, W., Li, R., Zhou, C., Li, Y., Xia, J. and Liu, J. (2017). Battery-supercapacitor hybrid devices: recent progress and future prospects. Advanced Science 4(7): 1600539.

CHAPTER 3

3 The Influence of Copper and Carbon Black on Electrochemical Behavior of Nickel Positive Electrode

THIS CHAPTER HAS BEEN PUBLISHED:

Zide, D., Felix, C., Oosthuysen, T. and Bladergroen, B.J., 2020. The influence of copper and carbon black on electrochemical behavior of nickel positive electrode. *Journal of Electroanalytical Chemistry*, 878, p.114539.

3.1 Abstract

Nickel hydroxide is used as active material in positive electrodes of secondary alkaline batteries. In alkaline batteries, the capacity of the negative electrode is greater than that of the positive electrode; hence the cell capacity is limited by the positive electrode. The practical capacity of the $Ni(OH)_2$ positive electrode depends on the efficiency of the conductive network connecting the $Ni(OH)_2$ particles with the current collector. In this study, hot-pressed-type electrodes were prepared using fibre-like β-$Ni(OH)_2$ powder as the active material on a nickel mesh as a current collector. The effect of carbon black as a conductive network for $Ni(OH)_2$ active material and the partial substitution of $Cu(OH)_2$ for β-$Ni(OH)_2$ material on the electrode performance are examined. The carbon black powder addition improves the utilization of the active material; however, it leads to a decrease in the stability of the electrode. The partial substitution of $Cu(OH)_2$ for β-$Ni(OH)_2$ significantly improves the coulombic efficiency of the β-$Ni(OH)_2$ active material, and it also increases the specific discharge capacity and enhances the stability of the electrode. These findings showed that the copper modified β-$Ni(OH)_2$ electrodes possessed an improved specific capacity and stability and thus may be recognized as a promising hybrid material for battery electrode applications.

Key Words: Beta nickel hydroxide; Beta nickel-copper hydroxide; Carbon black; Hot-pressed-type; Nickel positive electrode

3.2 Introduction

Non-renewable sources of energy such as fossil fuels, coal and nuclear fission currently play a vital role in meeting the economic energy demands of the world (Abas *et al.*, 2015). The downside of fossil fuel use is CO_2 emissions, which have been identified as a significant global environmental threat owing to its contribution to global warming (Perera, 2017; Riahi *et al.*, 2017). This has encouraged the development and use of alternative and sustainable renewable energy resources. Two alternatives that have emerged as a suitable solution to upsurge energy security and address environmental issues are wind and solar power (Sarrias-Mena *et al.*, 2014; Warren, 2014; Oseghale *et al.*, 2016). The challenge is amplified with the highly concentrated demand peaks in the early morning and early evening when solar generation is minimal. Therefore the energy generated from wind or solar systems is subject to stochastic wind profiles and seasonal availability of resources (Nejat *et al.*, 2015).

Over the years, several energy storage technologies such as mechanical, thermal, and electrochemical energy have been researched. Among the studied electrochemical-based technologies, nickel-iron (NiFe) batteries are commercially viable (Abdalla *et al.*, 2016; Posada and Hall, 2016; Chen, Wei *et al.*, 2018). Yet, there are still several research that hurdles to enhance further its performance which includes poor charging efficiency and low discharge capability (Abdalla *et al.*, 2016). The capacity of the

negative electrode is greater than that of the positive electrode, and hence the overall poor performance of the NiFe battery is observed (Begum *et al.*, 2009).

Nickel positive electrode is based on nickel hydroxide ($Ni(OH)_2$) as the active material for storage of electrochemical energy(Adekunle *et al.*, 2014; Kumar, AV Narendra *et al.*, 2014; Hall *et al.*, 2015). Structurally, two reduction phases, β-$Ni(OH)_2$ and α-$Ni(OH)_2$ and two phases of the oxidized material, β-NiOOH and γ-NiOOH have been reported for the $Ni(OH)_2$ materials (Chen, Wei *et al.*, 2018; Jin *et al.*, 2018). The oxidation of β-$Ni(OH)_2$ on charge produces β-NiOOH, on discharge, it yields a β-$Ni(OH)_2$, and on overcharge, it could be converted to γ-NiOOH. The oxidation of α-$Ni(OH)_2$ on charge produces γ-NiOOH, and on discharge, it forms an α-$Ni(OH)_2$. In general, α-$Ni(OH)_2$ is unstable and can be transformed to β-$Ni(OH)_2$ in a neutral or KOH aqueous solution. Primarily α-$Ni(OH)_2$ is dissolved in the aqueous solution slowly and then re-nucleated to form β-$Ni(OH)_2$(Kumar, Niraj and Panda, 2015; Young, Kwo-Hsiung *et al.*, 2017). Owing to the low stability of α-$Ni(OH)_2$ in alkaline media and the possibility of battery swelling during charge-discharge, the β-$Ni(OH)_2$ is usually the preferred precursor material used in alkaline batteries (Gonçalves *et al.*, 2018).

The theoretical specific capacity of β-$Ni(OH)_2$ material in the positive nickel electrode is 289 mAh/g. Still, in practice, the specific capacity of β-$Ni(OH)_2$ material is below the expected theoretical capacity. The practical capacity of the positive nickel electrode depends on the efficiency of the conductive network connecting the β-$Ni(OH)_2$ particles with the current collector (Begum *et al.*, 2009). Considering the poor conductivity of β-$Ni(OH)_2$ powder, it is advisable to incorporate conductive materials during electrode construction. It is also important to note that the quantity of β-$Ni(OH)_2$ material could strongly influence the overall capacity of the electrode. When the β-$Ni(OH)_2$ amount is too high, the electrode resistance becomes excessive, which could affect the exploitation of the material and thereby reduce the electrode material's capacity.

Many studies have revealed that the incorporation of divalent elements such as magnesium, cobalt and zinc can improve active material utilization and cycle life (Young, Kwo-Hsiung *et al.*, 2017; Liu, Ling *et al.*, 2019). In addition, the electrochemical studies of the alpha form of Cu/Ni composition have been reported (Alhebshi and Alshareef, 2015; Kim, Kyung Ho *et al.*, 2018). However, in theory, the alpha form of $Ni(OH)_2$ is associated with swelling of the battery during charge-discharge of the battery cell (Gonçalves *et al.*, 2018).

In the present study, the influence of carbon black and the partial substitution of $Cu(OH)_2$ for β-$Ni(OH)_2$ is investigated. The copper is chosen owing to the abundant active sites and synergistic effects between Ni and Cu (Giri and Sarkar, 2016; Xu *et al.*, 2017). Ni and Cu are adjacent to one another in the periodic table of elements with atomic numbers 28 and 29 and atomic masses 58.69amu and 63.55amu,

respectively. To the best of the author's knowledge, very little work has been done to assess the effect of carbon black and the partial substitution of $Cu(OH)_2$ for β-$Ni(OH)_2$.

3.3 Material and methods

3.3.1 Materials

Sodium carbonate (99%), sodium hydroxide (98%), nickel nitrate hexahydrate, and copper nitrate trihydrate (99%) were purchased from Sigma-Aldrich (South Africa). Carbon black was purchased from Alfa Aesar (United States), coatheylene was purchased from Axalta (United States), and nickel mesh was purchased from Q-Lite batteries (China).

3.3.2 Synthesis of nickel hydroxide active material

The nickel-based active material was prepared using a modified co-precipitation method followed by hydrothermal treatment at pH = 14 (Lassoued *et al.*, 2017). Briefly, two solutions were prepared; solution 1 contained NaOH and Na_2CO_3, and solution 2 had Ni^{2+} as $Ni(NO_3)_2{\cdot}6H_2O$ salt. The two solutions were mixed dropwise under vigorous stirring at room temperature. The slurry was further agitated at room temperature for 30min and thereafter subjected to hydrothermal treatment at 65°C for 18h. The resulting precipitates were cool at room temperature, then filtered and washed with Milli-Q water. Finally, the precipitated samples were dried at 110°C for 12h, milled and transferred into vials for later application.

3.3.3 Synthesis of $Ni_{1-x}Cu_x(OH)_2$ active material

The compositions of $Ni_{1-x}Cu_x(OH)_2$ were prepared using a modified co-precipitation method and followed by hydrothermal treatment at pH = 14 (Lassoued *et al.*, 2017). Where "x" is the weight percentage of Cu^{2+}, i.e., 5 wt.%, 10 wt.%, 25 wt.%, and 50 wt.%. Briefly, two solutions were prepared; solution 1 contained NaOH and Na_2CO_3, and solution 2 contained Ni^{2+} as $Ni(NO_3)_2{\cdot}6H_2O$ salt and Cu^{2+} as $Cu(NO_3)_2{\cdot}3H_2O$ salt. The two solutions were mixed dropwise under vigorous stirring at room temperature. The slurry was further agitated at room temperature for 30min and thereafter subjected to hydrothermal treatment at 65°C for 18h. The resulting precipitates were cool at room temperature, then filtered and washed with Milli-Q water. The precipitated samples were dried at 110°C for 12h. The dried powders were crushed and transferred into vials, and the samples were labelled as $Ni_{0.95}Cu_{0.05}(OH)_2$, $Ni_{0.9}Cu_{0.1}(OH)_2$, $Ni_{0.75}Cu_{0.25}(OH)_2$, and $Ni_{0.5}Cu_{0.5}(OH)_2$, for the partial substitution of 5wt% Cu^{2+}, 10wt% Cu^{2+}, 25wt% Cu^{2+}, and 50wt% Cu^{2+}, respectively.

3.3.4 Structural and morphological characterization of the materials

The diffraction patterns were recorded using a multi-purpose X-ray Diffractometer D8-Advance from BRUKER AXS (Germany). Measurements were operated in a continuous θ - θ scan in locked coupled mode with Cu-Kα radiation ($\lambda K\alpha_1$=1.5406Å) in the 2-theta ranged from 10° to 70°, in steps of 0.034° per second. The functional groups present in the materials were identified using Fourier Transform

Infra-Red Spectrum II spectrometer (UATR-FTIR, Llantrisant UK), operated using spectrum software, and the absorption bands were collected in the range of 4000 cm^{-1} - 400 cm^{-1}. The thermal analysis was studied using a Perkin-Elmer (6300 instrument) thermal gravimetric analysis (TGA) coupled with differential thermal analysis (TGA-DTA). Measurements were performed under argon gas using a heating rate of 5˚C min^{-1} with a flow rate of 20 ml min^{-1} from 30˚C to 1000˚C temperature range. Their surface areas were analyzed using Brunauer-Emmett-Teller (BET) nitrogen adsorption isotherms and adsorption pore size using Barrett-Joyner-Halenda (BHJ). The compositions were determined using inductively coupled plasma optical emission spectroscopy (ICP-OES). The crystal structures of the synthesized materials were confirmed using transmission electron microscopy (TEM).

3.3.5 Fabrication of electrodes

The nickel electrodes were prepared by mixing 90 wt.% active material and 10 wt.% coathylene binder thoroughly. The mixture was poured onto a nickel mesh and hot-pressed at 80˚C at 6MPa using a custom-designed hydraulic press for 5min to assure good electrical contact between the nickel mesh and the active material. Electrode dimensions were kept at 1cm × 1cm for all the samples. For further characterization and optimization studies, 85 wt.% active material and 5 wt.% carbon black, 80 wt.% active material and 10 wt.% carbon black, and 70 wt.% active material and 20 wt.% carbon black, respectively, were mixed thoroughly with 10 wt.% coathylene. Each mixture was dispensed onto a nickel mesh and hot-pressed, as mentioned above.

3.3.6 Electrochemical characterization

The as-prepared nickel electrodes were soaked in 4M KOH prior to the electrochemical measurements for 2h. The cyclic voltammetry (CV) was used to identify redox couples and Chrono charge-discharge galvanostatic (CCDG) for capacities of the active materials. Electrochemical characterizations were performed using the Metrohm Auto-Lab PGSTAT302N connected to a three-electrode set-up using 4M KOH as the electrolyte. A graphite sheet (3cm x 4cm) and Hg/HgO/4M KOH were used as counter and reference electrodes, respectively.

3.4 Results and Discussion

3.4.1 Influence of Cu^{2+} on the structure and morphology of the synthesized $Ni(OH)_2$ material

3.4.1.1 Structural characterization of synthesized $Ni(OH)_2$

The crystalline phase of the synthesized $Ni(OH)_2$ was confirmed using XRD and indexed with the closest JCP2 standards. Further compared with the commercial $Ni(OH)_2$ and cross-referenced with published literature. Figure 3-1 depicts the diffractogram of the synthesized $Ni(OH)_2$ after 30 min mixing at room temperature (Figure 3-1a), aged at room temperature for 18 h (Figure 3-1b), hydrothermally treated for 18h (Figure 3-1c), and commercial $Ni(OH)_2$ (Figure 3-1d).

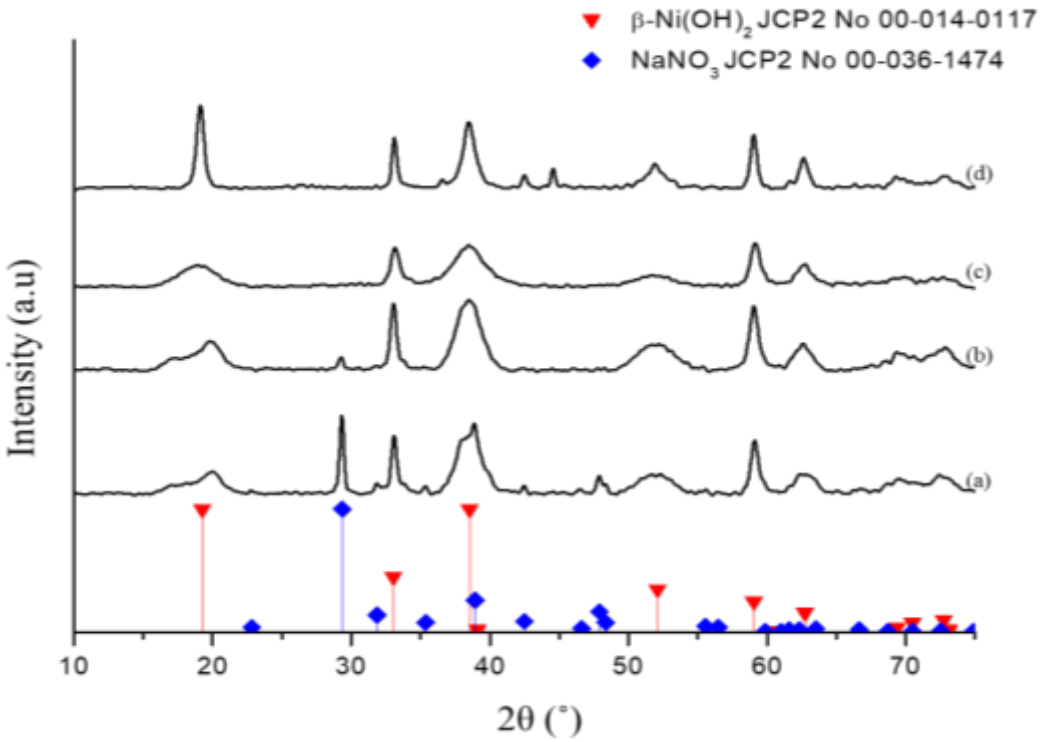

Figure 3-1: Diffractograms of the synthesized $Ni(OH)_2$ (a) stirred for 30min (b) aged for 18h at room temperature (c) hydrothermal treated for 18h, and (d) commercial $Ni(OH)_2$

The obtained diffractogram in Figure 3-1a shows a significant presence of nitratine ($NaNO_3$) (JCP2 No 00-036-1474) at around 29˚, 32˚, 35˚, 42˚, 46˚ and 48˚. As the sample was further aged at room temperature for 18h (Figure 3-1b), the presence of $NaNO_3$ was minimal. The peak at 29˚ started to compact as compared to Figure 3-1a; however, it can be noted that the rest of the peaks at around 32˚, 35˚, 42˚, 46˚ and 48˚ that corresponded to $NaNO_3$ were not present. The double peak bump between 17.189˚ and 20.189˚ (Figure 3-1a-b) may be owing to the formation of a mixture of $NaNO_3$ (JCP2 No 00-036-1474) and β-$Ni(OH)_2$ (JCP2 No 00-014-0117).

The obtained patterns of the hydrothermal treated $Ni(OH)_2$ (Figure 3-1c) were indexed to the pure hexagonal phase of β-$Ni(OH)_2$ standard (JCP2 No 00-014-0117). Similar diffractograms were reported in the literature (Wang, Hailiang *et al.*, 2012; Hall *et al.*, 2015; Young, Kwo *et al.*, 2018). Furthermore, the hydrothermal treated $Ni(OH)_2$ presented in Figure 3-1c exhibited no marked significant differences when compared to the observed crystallite of the commercial $Ni(OH)_2$ (Figure 3-1d). However, an additional three peaks at 2θ equal to 36.53°, 42.58°, and 44.70° for the commercial $Ni(OH)_2$ were observed. These peaks may be the result of an added modifier, conducting material and/or impurities that were closely fitted to zincite (ZnO) (JCP2 No 00-036-1451), $NaNO_3$ (JCP2 No 00-036-1474) and Ni-metal (JCP2 No 00-004-0850), respectively.

The crystallite sizes of the materials were calculated from the two major peaks (001), and (101) using the Debye-Scherer formula presented in Equation 3-1 and the results are shown in Table 3-1.

Equation 3-1: Debye-Scherer equation

$$D = \frac{K\lambda}{\beta Cos\theta})$$

Where D is the crystallite size, K is the Scherer constant (K = 0.9), β is the full width of half maximum (FWHM), and θ is the maximum diffraction angle (˚). As shown in Table 3-1, a decrease in crystallite size was observed as the synthesized samples were further treated. The crystallite sizes of the commercial $Ni(OH)_2$ were higher as compared to the synthesized $Ni(OH)_2$ samples.

Table 3-1: Crystallite size of the synthesized $Ni(OH)_2$ stirred for 30min, aged for 18h at room temperature, hydrothermally treated for 18h, and the commercial $Ni(OH)_2$

	(001)	**(101)**
Sample name	**Crystallite size (nm)**	**Crystallite size (nm)**
30min mixing: $Ni(OH)_2$	4,05	5,31
18h ageing: $Ni(OH)_2$	3,88	4,19
18h hydrothermal: $Ni(OH)_2$	2,59	3,35
Commercial $Ni(OH)_2$	14,36	9,36

The unit cell parameters “a” and “c” were calculated using the formulae $a = 2d_{110}$, and $c = d_{001}$; where d_{001} and d_{110} are the basal spacing at a miller index (hkl) of (001) and (110) which were obtained using Bragg’s law equation (Equation 3-2), assuming hexagonal stacking (Wiston and Ashok, 2019). The obtained results are presented in Table 3-2.

Equation 3-2: Bragg’s law

$$n\lambda = 2d \sin\theta$$

Where n is the order number, λ is the wavelength (1.54098 Å), d is the basal spacing (Å), and θ is the diffraction angle (˚). As presented in Table 3-2, the lattice parameter “a” for all the synthesized samples (Figure 3-1a-c) were the same (3.12Å). However, the parameter, “c” increases as samples were further treated with the calculated c-parameters of 4.39Å, 4.43Å, and 4.62Å, respectively. It can be noted that the hydrothermal treated sample had the same “a”-parameter and “c”-parameter values as the commercial $Ni(OH)_2$ (a = 3.12Å, $c = d_{001}$ = 4,62 Å), which both corresponded to the β-$Ni(OH)_2$ (JCP2 No 00-014-0117).

Table 3-2: XRD lattice parameter "a", "c" and "d-spacing" of the commercial and synthesized $Ni(OH)_2$

Sample name	(001) reflection 2θ (˚)	d001 (Å)	(110) reflection 2θ (˚)	d110 (Å)	a (Å)	c (Å)
30min mixing: $Ni(OH)_2$	20,19	4,39	59,11	1,56	3,12	4,39
18h ageing: $Ni(OH)_2$	20,04	4,43	59,11	1,56	3,12	4,43
18h hydrothermal: $Ni(OH)_2$	19,21	4,62	59,11	1,56	3,12	4,62
Commercial $Ni(OH)_2$	19,21	4,62	59,11	1,56	3,12	4,62
Standard $Ni(OH)_2$ (JCP2 No 00-041-0117)	19.26	4.60	59.05	1.56	3.13	4.60

Figure 3-2 depicts the FTIR spectra of the synthesized samples. The presence of sharp peaks at around 3636.92 cm^{-1}, 3635.33 cm^{-1}, 3638.26 cm^{-1} and 3633.42 cm^{-1} in Figure 3-2 (a-d), respectively is the confirmation of $Ni(OH)_2$ (Motlagh *et al.*, 2011; Shanaj and John, 2016). These absorption bands are assigned to O-H stretching vibrations (Begum *et al.*, 2009; Su *et al.*, 2014; Hall *et al.*, 2015; Shanaj and John, 2016).

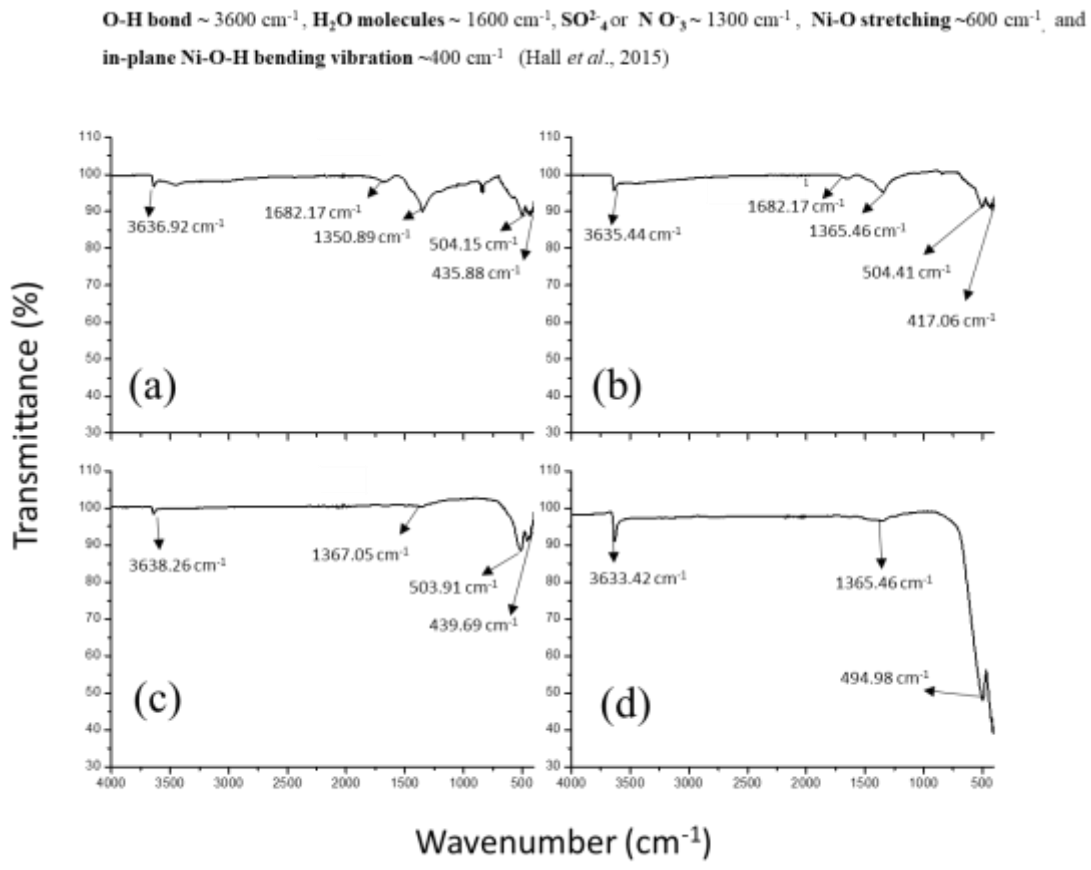

Figure 3-2: FTIR spectra of the synthesized $Ni(OH)_2$ (a) stirred for 30min (b) age for 18h at room temperature (c) hydrothermal treated for 18h, and (d) commercial $Ni(OH)_2$

The peaks at around 1682.17 cm^{-1} on both the synthesized $Ni(OH)_2$ stirred for 30min (Figure 3-2a) and aged for 18h at room temperature (Figure 3-2b) is attributed to the bending vibration mode of H_2O

molecules. The absorption bands at around 1300 cm^{-1}, 500 cm^{-1} and 400 cm^{-1} in Figure 3-2 (a-d) are attributed to the existence of interlayer nitrate anions (NO^{-}_{3}), Ni-O stretching vibrations and an in-plane Ni-O-H bending vibration respectively (Begum *et al.*, 2009; Su *et al.*, 2014; Hall *et al.*, 2015; Shanaj and John, 2016).

Figure 3-3 shows the thermal behaviour of the synthesized $Ni(OH)_2$ samples. The DTA curve of the synthesized $Ni(OH)_2$ stirred for 30min (Figure 3-3a) showed six exothermic peaks with temperatures at 44°C, 77°C, 236°C, 290°C, 734°C and 817°C indicating continuous degradation of the sample and continuous sample mass loss. The first two peaks (44°C and 77°C) may be due to the evaporation of residual water in the dried sample (Shanaj and John, 2016) resulting in the initial weight loss of 9.59 % (TGA curve). The other sharp peak located at 236˚C (DTA curve) may be the indicative of the removal of the OH group during the transformation of $Ni(OH)_2$ to NiO (Shanaj and John, 2016; Kovalenko *et al.*, 2017), resulting in a second weight loss of 8.32 %. A gradual weight loss of 3.29% between 230°C and 290°C was observed, owing to crystallization within the sample. This loss continues at a slow rate up to 734°C to yield another weight loss of 15.77% and further 5.43% at 817°C.

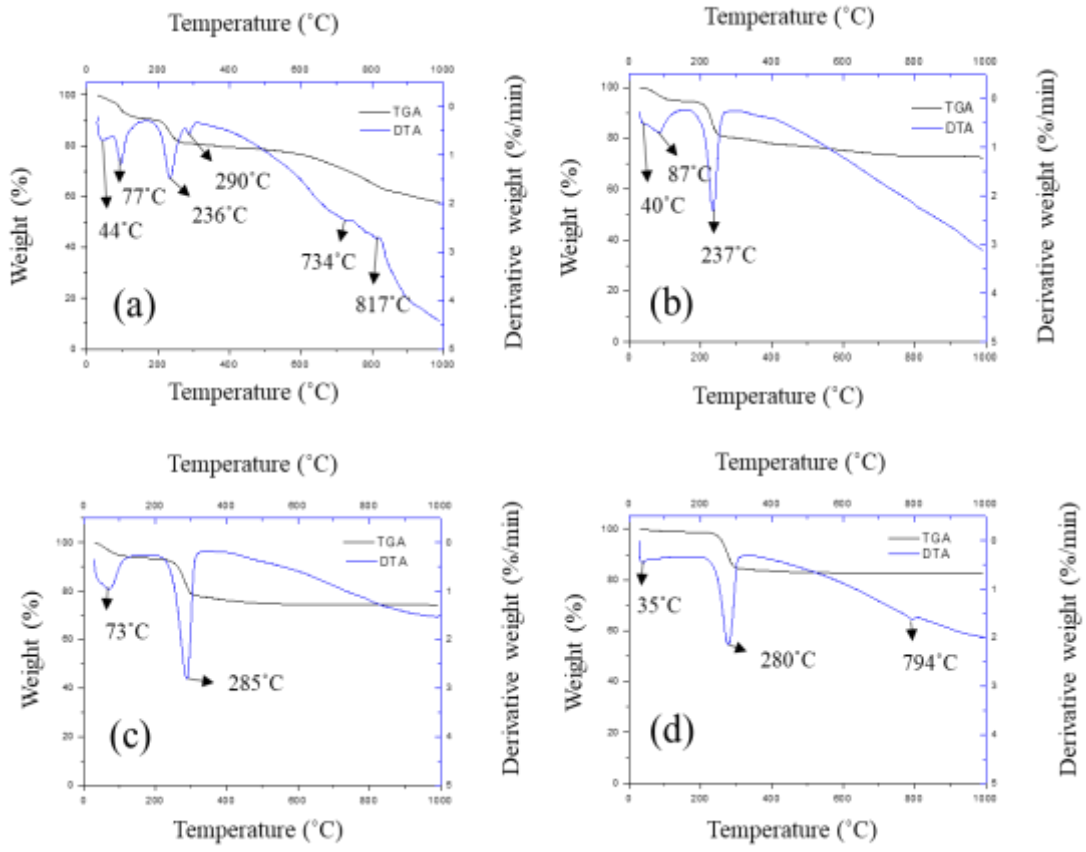

Figure 3-3: TG-DTA curves of the synthesized $Ni(OH)_2$ (a) stirred for 30min (b) age for 18h at room temperature (c) hydrothermal treated for 18h, and (d) commercial $Ni(OH)_2$

Figure 3-3b showed three exothermic peaks with temperatures at 40°C, 87°C and 237°C. The first two peaks (40°C and 87°C) may be due to the evaporation of residual water in the dried sample (Shanaj and John, 2016), resulting in the initial weight loss of 5.0 %. The other sharp peak located at 237˚C may be indicative of the removal of an OH^- group during the transformation of $Ni(OH)_2$ to NiO (Shanaj and John, 2016; Kovalenko *et al.*, 2017), corresponding to a total weight loss of 13.28 % followed by a weight loss of 8.32% that may be due to structural changes within the sample. It can be noted that the sample showed less reduction as compared to the sample presented in Figure 3-3a. Only two weight losses at 73°C and 285°C corresponding to weight losses of 5.20% and 8.32%, respectively, were observed on the hydrothermally treated sample (Figure 3-3c). These weight losses may be due to the evaporation of residual water in the dried sample (Shanaj and John, 2016) and decomposition of $Ni(OH)_2$ to NiO, respectively (Shanaj and John, 2016; Kovalenko *et al.*, 2017). In addition, a further weight loss of 3.94% due to structural changes within the sample was observed. Figure 3-3d showed a small peak at 35°C resulting in a weight loss of 0.87%. A radical weight loss of 14.09% was observed at 280°C, and as the sample slowly crystallized, a weight loss of 1.27% was calculated, followed by a further weight loss of 0.8% corresponding to a small peak at 794°C was obtained. The thermal behaviour of $Ni(OH)_2$ based material using TG-DTA has been reported in the literature. Shanaj and John (2016) reported three weight losses corresponding to DTA curves at 55°C, 89°C and 290°C. The general proposed thermal dehydration and decomposition reactions are presented in Equation 3-3 and Equation 3-4, respectively.

Equation 3-3: Thermal dehydration composition reaction of $Ni(OH)_2$

$$Ni(OH)_2 \cdot xH_2O \rightarrow Ni(OH)_2 + xH_2O$$

Equation 3-4: Thermal decomposition reaction of $Ni(OH)_2$

$$Ni(OH)_2 \overset{300^{\circ}C}{\rightarrow} NiO + H_2O$$

The Brunauer-Emmett-Teller (BET) specific surface areas (Table 3-3) increase as further treatments were performed. A lower surface area of 8.74 m^2/g and 44.48 m^2/g for the synthesized $Ni(OH)_2$ stirred for 30min and $Ni(OH)_2$ aged for 18h at room temperature, respectively were observed. While the BET surface area of the commercial $Ni(OH)_2$ was found to be 9.27m^2/g. Such lower surface areas have been reported (Du *et al.*, 2016; Zhai *et al.*, 2019). The hydrothermal treated sample demonstrated a higher surface area (361.92 m^2/g) and this finding corresponded with the BET specific surface area of $Ni(OH)_2$ (384 m^2/g and 343 m^2/g) reported in literature (Abbas *et al.*, 2019).

The average pore size distribution obtained from the adsorption branch of the isotherms by the Barrett-Joyner-Halenda (BJH) method (Table 3-3) further confirms a mesoporous structure within a size range

of 6–22 nm. As shown in Table 3-3, the average pore sizes of the synthesized samples decrease as the samples were further subjected to treatment.

Table 3-3: BET surface area and BJH adsorption average pore size of the synthesized $Ni(OH)_2$ after 30 min mixing, 18 h ageing and 18h hydrothermal treatment and the commercial $Ni(OH)_2$

Sample name	**BET Surface area (m^2/g)**	**Pore size (nm)**
30min mixing: $Ni(OH)_2$	8.74	22.12
18h ageing: $Ni(OH)_2$	44.48	11.62
18h hydrothermal: $Ni(OH)_2$	361.92	6.29
Commercial $Ni(OH)_2$	9.27	14.66

The nitrogen adsorption-desorption isotherms of the synthesized $Ni(OH)_2$ and the commercial $Ni(OH)_2$ are presented in Figure 3-4. The samples can be classified as type IV isotherm with a distinct hysteresis loop, indicating the presence of mesoporous structures at the relative pressure (P/P°) range between 0.48 and 1.0 (Figure 3-4a, b, d) and 0.7 and 1.0 (Figure 3-4c), which could be revealing the presence of mesoporous characteristics. These findings were in agreement with the results reported in literature (Coudun *et al.*, 2006; Zheng *et al.*, 2017; Yu *et al.*, 2019).

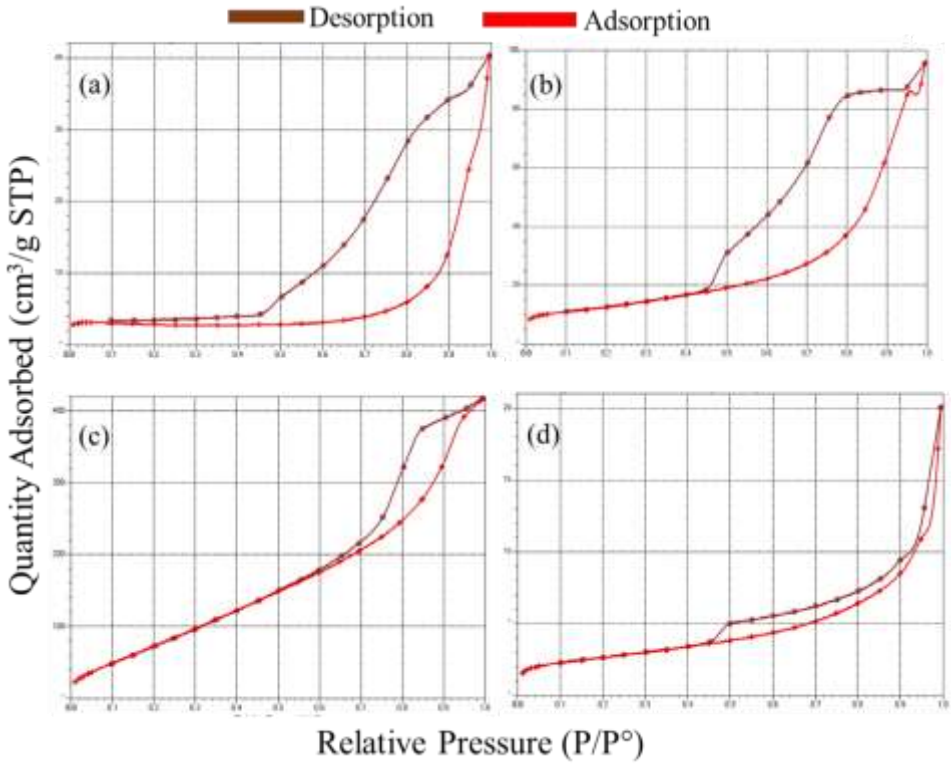

Figure 3-4: Nitrogen adsorption – desorption isotherm of the synthesized $Ni(OH)_2$ (a) stirred for 30min (b) age for 18h at room temperature (c) hydrothermal treated for 18h, and (d) commercial $Ni(OH)_2$

3.4.1.2 Structural characterization of $Ni_{1-x}Cu_x(OH)_2$

The obtained XRD patterns of $Ni_{1-x}Cu_x(OH)_2$ composition (where x is equal to 5 wt.%, 10 wt.%, 25 wt.%, and 50 wt.%) are reported in Figure 3-5(a-d). Common peaks in the diffractograms of $Ni_{0.95}Cu_{0.05}(OH)_2$ (Figure 3-5a), $Ni_{0.9}Cu_{0.1}(OH)_2$ (Figure 3-5b), $Ni_{0.75}Cu_{0.25}(OH)_2$ (Figure 3-5c) and $Ni_{0.5}Cu_{0.5}(OH)_2$ (Figure 3-5d) at diffraction angles 32.964˚, 38.43˚, 51.769˚, and 59.106˚, were observed. These peaks corresponded to $Ni(OH)_2$ (JCP2 No 00-014-0117) and $Cu(OH)_2$ (JCP2 No 00-013-0420).

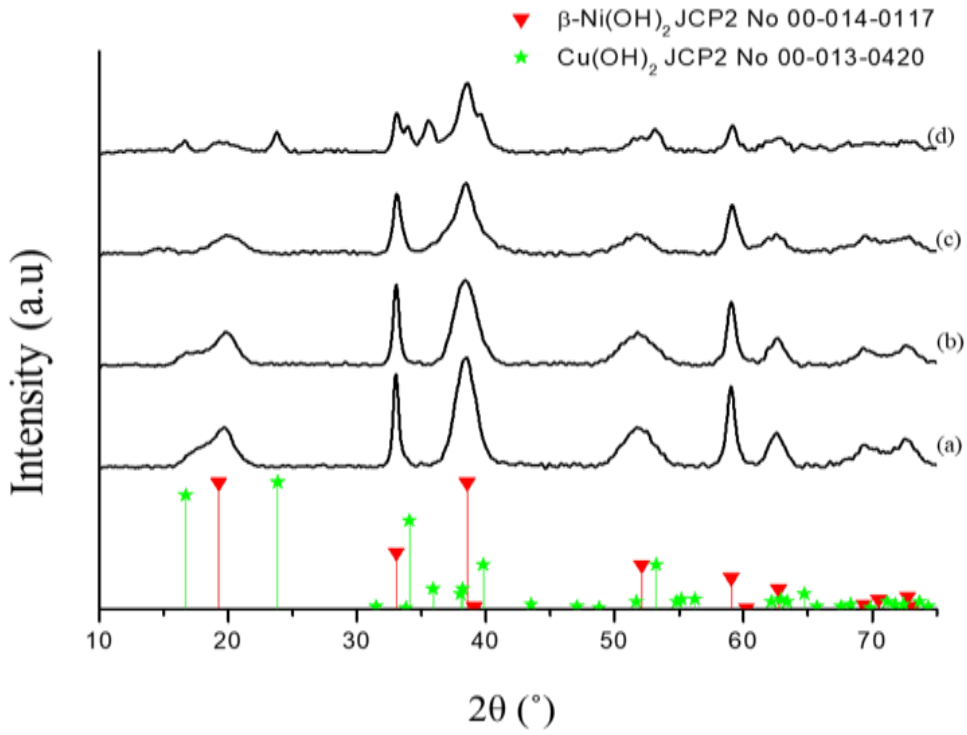

Figure 3-5: Diffractograms of (a) $Ni_{0.95}Cu_{0.05}(OH)_2$, (b) $Ni_{0.9}Cu_{0.1}(OH)_2$ (c) $Ni_{0.75}Cu_{0.25}(OH)_2$, and (d) $Ni_{0.5}Cu_{0.5}(OH)_2$.

The calculated crystallite sizes using Debye-Scherer formula (Equation 1) from the two major peaks, (001) and (101) index, ranged from 2 nm to 3 nm depending on the sample composition. Furthermore, the calculated unit cell parameters "a" were found to be 3.124Å for all the diffractograms presented in Figure 3-5a-d, and this value was in agreement with the JCP2 No 00-014-0117 standard $Ni(OH)_2$ (3.126Å). The lattice constant, "c" increases with an increase in Cu^{2+} addition, 4.460Å (Figure 3-5a-b), 4.486Å (Figure 3-5c), and 4.582Å (Figure 3-5d). This may be signifying the presence of foreign atoms at the Ni lattice points, which may be either larger or smaller than the host atom (Ni).

Figure 3-6, depicts the FTIR spectra of the as-prepared samples. The O-H bond was observed at around 3638.12 cm^{-1}, 3637.43 cm^{-1}, 3633.58 cm^{-1} and 3571.96 cm^{-1} for Figure 3-6a-d, respectively. It can be noted that the bands slightly shifted to a lower wavenumber as the amount of copper substituent was

increased during the synthesis. Furthermore, absorption bands due to NO^-_3 anion were observed at a wavenumber of 1349.96 cm^{-1} (Figure 3-6a), 1354.54 cm^{-1} (Figure 3-6b), 1356.13 cm^{-1} (Figure 3-6c) and 1372.04 cm^{-1}(Figure 3-6d), respectively.

O-H bond ~ 3600 cm^{-1} , **H_2O molecules** ~ 1600 cm^{-1}, **SO^{2-}_4** or **NO^-_3** ~ 1300 cm^{-1} , **Ni-O stretching** ~600 cm^{-1}, and **in-plane Ni-O-H bending vibration** ~400 cm^{-1} (Hall *et al.*, 2012).

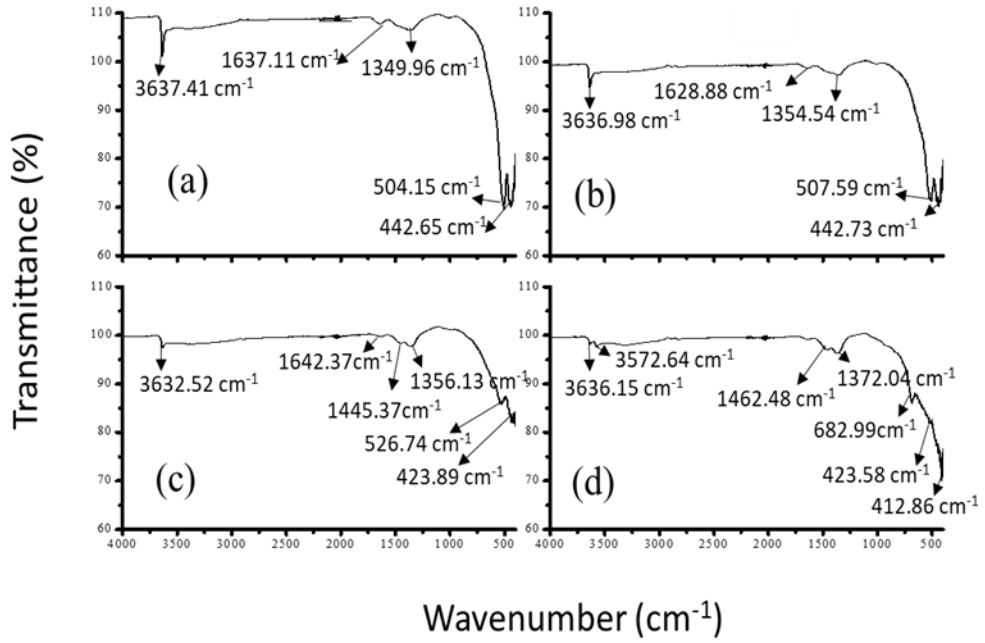

Figure 3-6: FTIR spectra of (a) $Ni_{0.95}Cu_{0.05}(OH)_2$, (b) $Ni_{0.9}Cu_{0.1}(OH)_2$, (c) $Ni_{0.75}Cu_{0.25}(OH)_2$, and (d) $Ni_{0.5}Cu_{0.5}(OH)_2$

The thermal behaviour of $Ni_{1-x}Cu_x(OH)_2$ were also investigated, and the obtained TG-DTA curves are presented in Figure 3-7. Figure 3-7a-c demonstrates two distinct weight losses; the initial weight losses of 7.12 wt.% (Figure 3-7a), 6.5 wt.% (Figure 3-7b) and 8.37 wt.% (Figure 3-7c) corresponded to small endothermic peaks at 72˚C, 64˚C and 73˚C respectively. The melting point of $Cu(OH)_2$ and $Ni(OH)_2$ are expected to occur at 80˚C and 230˚C, respectively. In general, the degradation of the dried sample is likely to appear before its melting point (Hall *et al.*, 2015). It can be said that these initial weight losses are due to the evaporation of residual water in the dried $Ni_{1-x}Cu_x(OH)_2$ samples. The second sharp peaks located at 290˚C, 285˚C and 285˚C corresponding to a weight loss of 18.41 wt.% (Figure 3-7a), 18.22 wt.% (Figure 3-7b) and 20.15 wt.% (Figure 3-7c), respectively may be related to the thermal-oxidative decomposition of $Ni_{1-x}Cu_x(OH)_2$.

It could be noted that Figure 3-7d demonstrated that the sample underwent five distinct weight losses corresponding to 44˚C, 82˚C, 182˚C, 283˚C and 896˚C. These observations were similar to that reported in the literature (Kozai *et al.*, 2006).

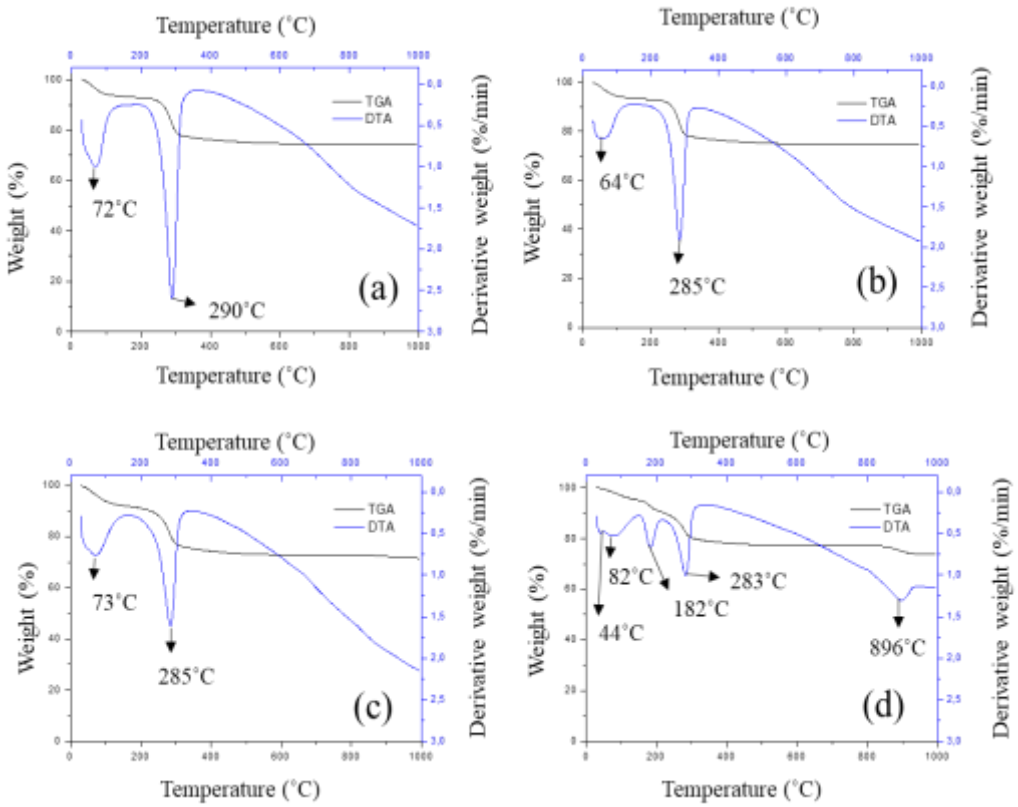

Figure 3-7: TG - DTA) curves of (a) $Ni_{0.95}Cu_{0.05}(OH)_2$, (b) $Ni_{0.9}Cu_{0.1}(OH)_2$ (c) $Ni_{0.75}Cu_{0.25}(OH)_2$, and (d) $Ni_{0.5}Cu_{0.5}(OH)_2$.

The BET surface areas ranged between 130 m^2/g to 119 m^2/g, and the BHJ average pore size adsorption ranged from 7.666 nm to 11.370 nm (Table 3-4). The elemental composition confirmed using ICP and SEM/EDS agreed with the intended compositions of $Ni_{0.95}Cu_{0.05}(OH)_2$, $Ni_{0.9}Cu_{0.1}(OH)_2$, $Ni_{0.75}Cu_{0.25}(OH)_2$ and $Ni_{0.5}Cu_{0.5}(OH)_2$ (Table 3-4).

Table 3-4: BET specific surface area and elemental composition ratio of $Ni_{1-x}Cu_x(OH)_2$.

Sample name	BET Surface area (m^2/g)	Pore size (nm)	Expected Ni^{2+}:Cu^{2+}	ICP-OES Ni^{2+}:Cu^{2+}	SEM-EDS Ni^{2+}:Cu^{2+}
$Ni_{0.95}Cu_{0.05(}OH)_2$	129.688	11.370	0.95: 0.05	0.95: 0.05	0.94: 0.06
$Ni_{0.9}Cu_{0.1}(OH)_2$	130.064	9.125	0.90: 0.10	0.90: 0.10	0.89: 0.11
$Ni_{0.75}Cu_{0.25}(OH)_2$	119.073	7.666	0.75:0.25	0.75:0.25	0.74: 0.26
$Ni_{0.5}Cu_{0.\ 5}(OH)_2$	119.076	13.198	0.50: 0.50	0.52: 0.48	0.47:0.53

Figure 3-8 shows the nitrogen adsorption-desorption isotherm of the synthesized $Ni_{1-x}Cu_x(OH)_2$, which could be classified as type IV isotherm with a distinct hysteresis loop, indicating the presence of mesoporous structures at the relative pressure (P/P°) range between 0.5and 1.0 (Figure 3-8a-d). These

findings were in agreement with the results reported in literature (Coudun *et al.*, 2006; Zheng *et al.*, 2017; Yu *et al.*, 2019).

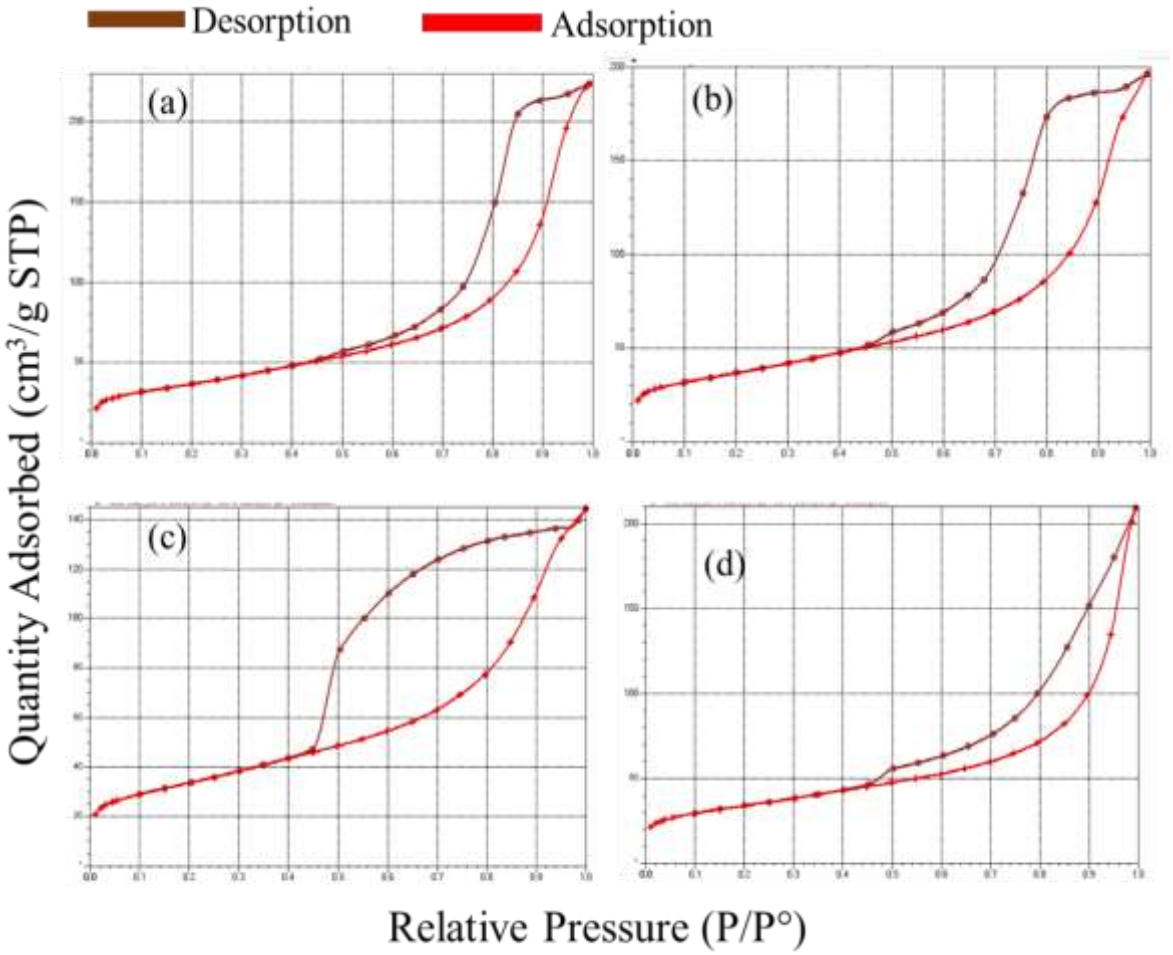

Figure 3-8: Nitrogen adsorption – desorption isotherm of the (a) $Ni_{0.95}Cu_{0.05}(OH)_2$, (b) $Ni_{0.9}Cu_{0.1}(OH)_2$ (c) $Ni_{0.75}Cu_{0.25}(OH)_2$, and (d) $Ni_{0.5}Cu_{0.5}(OH)_2$.

3.4.1.3 Morphological characterization of synthesized $Ni(OH)_2$ and $Ni_{0.75}Cu_{0.25}(OH)_2$

Figure 3-9 demonstrates the TEM images of the charged state and the discharged state of both synthesized $Ni(OH)_2$ and $Ni_{0.75}Cu_{0.25}(OH)_2$ after 20 cycles, compared to their pure materials before hot pressing and after hot pressing. Morphological changes of the synthesized $Ni(OH)_2$ were observed after hot pressing compared to pure powdered form before hot pressing (Figure 3-9a,b). Although structural changes of the charge states on the synthesized $Ni(OH)_2$ (Figure 3-9c) was observed, it could be noted that the discharged states (Figure 3-9d) were similar to the observed morphology after hot pressing (Figure 3-9b). This could be an indication of the good reversibility of the active materials. A similar trend was observed for the $Ni_{0.75}Cu_{0.25}(OH)_2$ active material (Figure 3-9e-f).

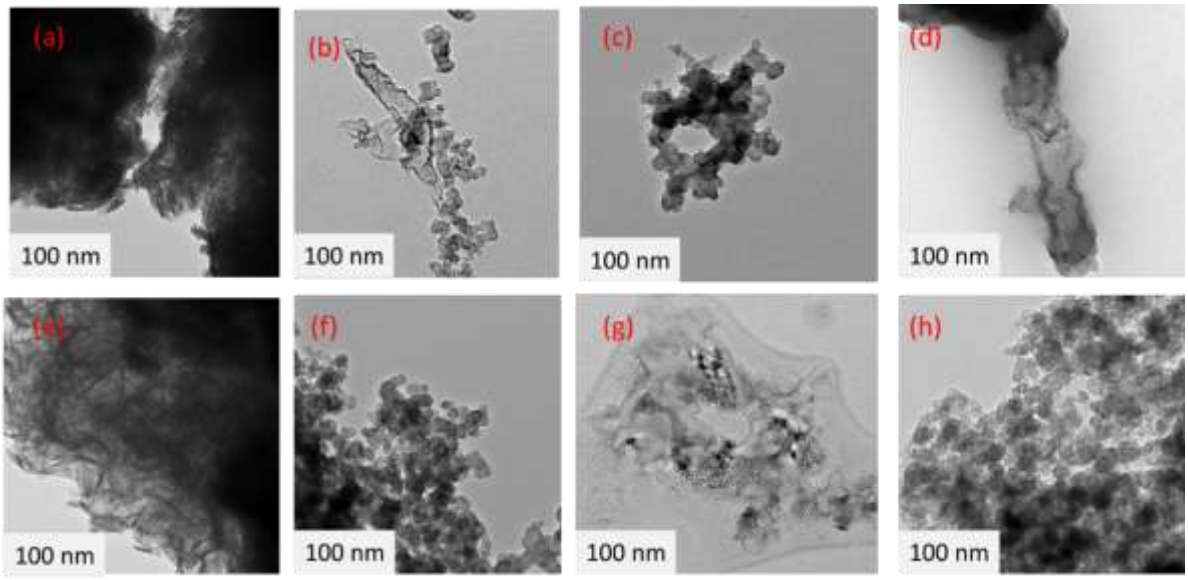

Figure 3-9: TEM images of (a) Pure $Ni(OH)_2$ before hot pressing, (b) 85% $Ni(OH)_2$ with 5% carbon black and 10% coathylene after hot pressing (c) Charge state of 85% $Ni(OH)_2$ with 5% carbon black and 10% coathylene after the 20 cycles charge-discharge (d) Discharge state of 85% $Ni(OH)_2$ with 5% carbon black and 10% coathylene after the 20 cycles charge-discharge, (e) Pure $Ni_{0.75}Cu_{0.25}(OH)_2$ before hot pressing, (f) 85% $Ni_{0.75}Cu_{0.25}(OH)_2$ with 5% carbon black and 10% coathylene after hot pressing (g) Charge state of 85% $Ni_{0.75}Cu_{0.25}(OH)_2$ with 5% carbon black and 10% coathylene after the 20 cycles charge-discharge (h) Discharge state of $Ni_{0.75}Cu_{0.25}(OH)_2$ with 5% carbon black and 10% coathylene after the 20 cycles charge-discharge.

3.4.2 Influence of Cu^{2+} on electrochemical performance of the electrode

3.4.2.1 Cyclic voltammetry of the synthesized $Ni(OH)_2$ and $Ni_{0.75}Cu_{0.25}(OH)_2$

Figure 3-10a shows the cyclic voltammograms (CVs) of the synthesized $Ni(OH)_2$ with and without carbon black, compared to the commercial $Ni(OH)_2$. There is no difference observed between the synthesized $Ni(OH)_2$ and the commercial $Ni(OH)_2$; the results demonstrated broad oxidation and potential reduction peaks for all the CVs presented. The broad peaks may indicate the capacitive nature of the material where capacitive current overlaps with Faradiac current or a result of a diffusion-limited process.

It can be noted that $Ni_{0.75}Cu_{0.25}(OH)_2$ (Figure 3-10b) also showed the broad oxidation-reduction potential peaks; thus, the incorporation of copper and the addition of carbon black did not affect the electrochemical redox reactions of the $Ni(OH)_2$. However, from Figure 8c, it can be noted that the oxidation of copper occurs at negative potentials and that the addition of carbon black promotes the oxidation of copper. At -0.4 V, a small anodic peak is observed corresponding to the formation of the $Cu(OH)_2$ species, while at -0.14 V, the $Cu(OH)_2$ species are oxidized to form Cu_2O (Giri and Sarkar, 2016).

Although both oxidation and reduction peaks (Figure 3-10a-b) were broader, their appearance in the approximately same potential window indicates good reversibility of the active materials. These findings are in agreement with the TEM images, which showed good reversibility as noted in the similar structural appearance of the hot-pressed electrode ((Figure 3-9b,f) and discharged electrode (Figure 3-9d,h).

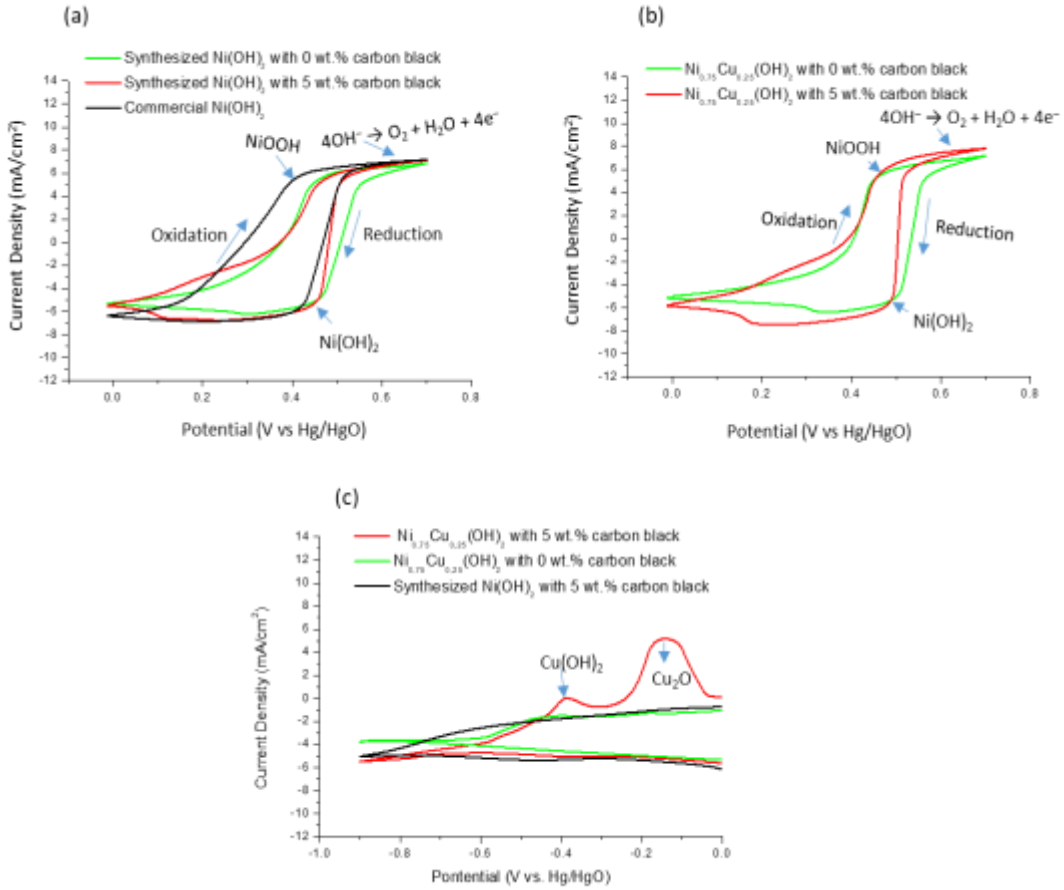

Figure 3-10: Cyclic voltammograms curves of (a) Synthesized $Ni(OH)_2$ compared to commercial $Ni(OH)_2$, (b) $Ni_{0.75}Cu_{0.25}(OH)_2$ and (c) synthesized $Ni(OH)_2$ and $Ni_{0.75}Cu_{0.25}(OH)_2$ scanned at a negative potential at a scanning rate of 5 mVs^{-1}.

3.4.2.2 Optimization of Cu^{2+} substitution to $Ni(OH)_2$

The electrodes were prepared using the synthesized $Ni_{1-x}Cu_x(OH)_2$ (where x is 5wt.%, 10wt.%, 25wt.%, 50wt.%) and the specific discharged capacities were calculated from the chrono charge-discharge galvanostatic (CCDG) curves using Equation 3-5. The plots of the calculated specific discharge capacities over 20 cycles are presented in Figure 3-11.

Equation 3-5: Specific discharge capacity formula

$$Specific\ discharge\ capacity\ = \frac{Applied\ current\ (mA) x\ Discharge\ time\ (h)}{Loading\ mass\ (g)\ of\ the\ active\ material}$$

It can be seen in Figure 3-11 that there was no reduction in specific discharge capacities observed over the 20 cycles for 5%wt., 10%wt., and 25%wt copper substitution. The specific discharge capacity for the substitution of 50wt.% copper weight percentage decreased slightly after 12 cycles.

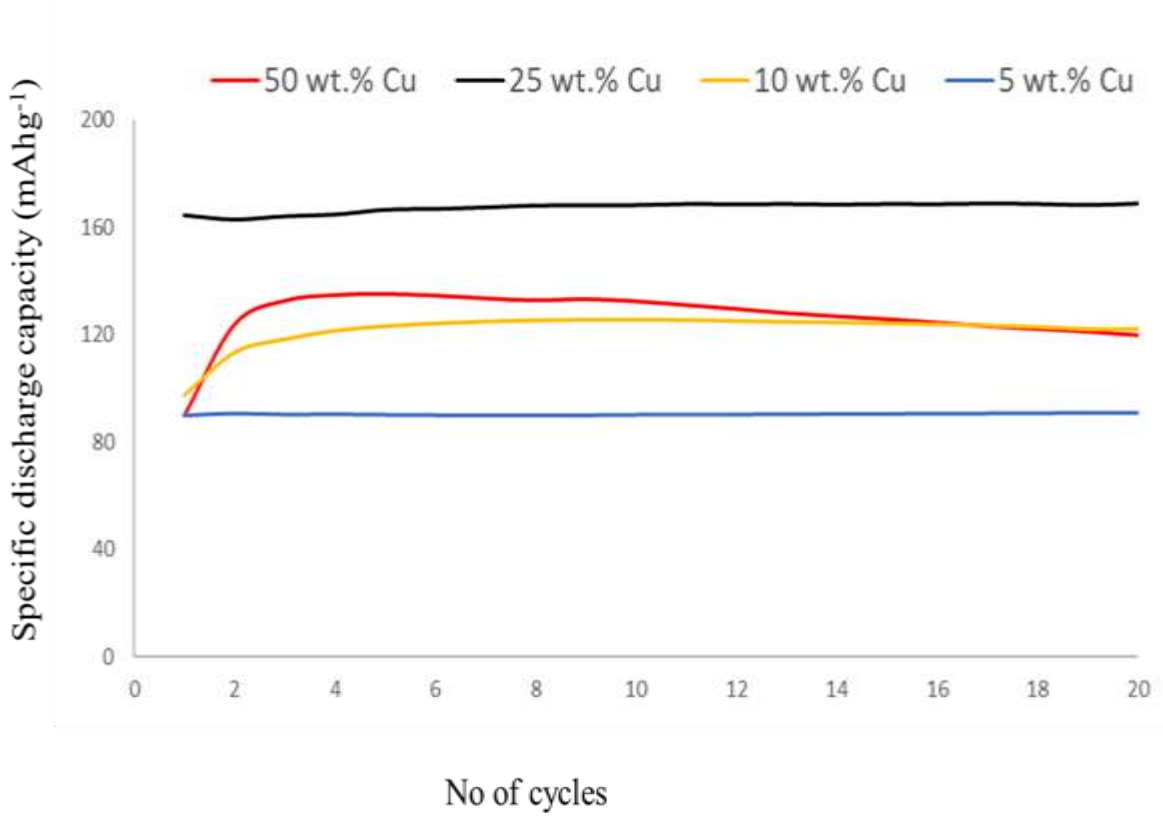

Figure 3-11: Specific discharge capacity; assessing the effect of copper as a potential modifier to $Ni(OH)_2$ after the 20th cycles.

Table 3-5 presents the calculated specific discharge capacities of 5%wt., 10%wt., 25%wt., and 50wt.% copper substitution for $Ni(OH)_2$ at 20^{th} cycles. As shown in Table 3-5, the discharge capacity of 169 mAh/g at 20 cycles was obtained when 25wt% Cu^{2+} was partially substituted for $Ni(OH)_2$ and appeared to exhibit the optimal composition.

Table 3-5: Specific discharge capacity; assessing the effect of copper as a potential modifier to $Ni(OH)_2$ after the 20th cycles.

5wt.% Cu^{2+}	**10wt.% Cu^{2+}**	**25wt.% Cu^{2+}**	**50 wt.% Cu^{2+}**
91mAh/g	122 mAh/g	169 mAh/g	120 mAh/g

3.4.2.3 Stability testing of the synthesized $Ni(OH)_2$ and $Ni_{0.75}Cu_{0.25}(OH)_2$

Figure 3-12 presents the specific discharge capacities of the synthesized $Ni(OH)_2$ and $Ni_{0.75}Cu_{0.25}(OH)_2$ active materials after 80 cycles, and Table 3-6, depicts their calculated specific discharge capacities

over 80 cycles. The results are compared with the commercial $Ni(OH)_2$ electrode. The electrode of the synthesized $Ni(OH)_2$ without the addition of carbon black showed a reduction of only 18% decrease after the 80th cycle (Figure 3-12a) when compared to the electrode with the addition of 5wt.% carbon black, which demonstrated a 66 % decrease in discharge capacity after 80 cycles (Figure 3-12b).

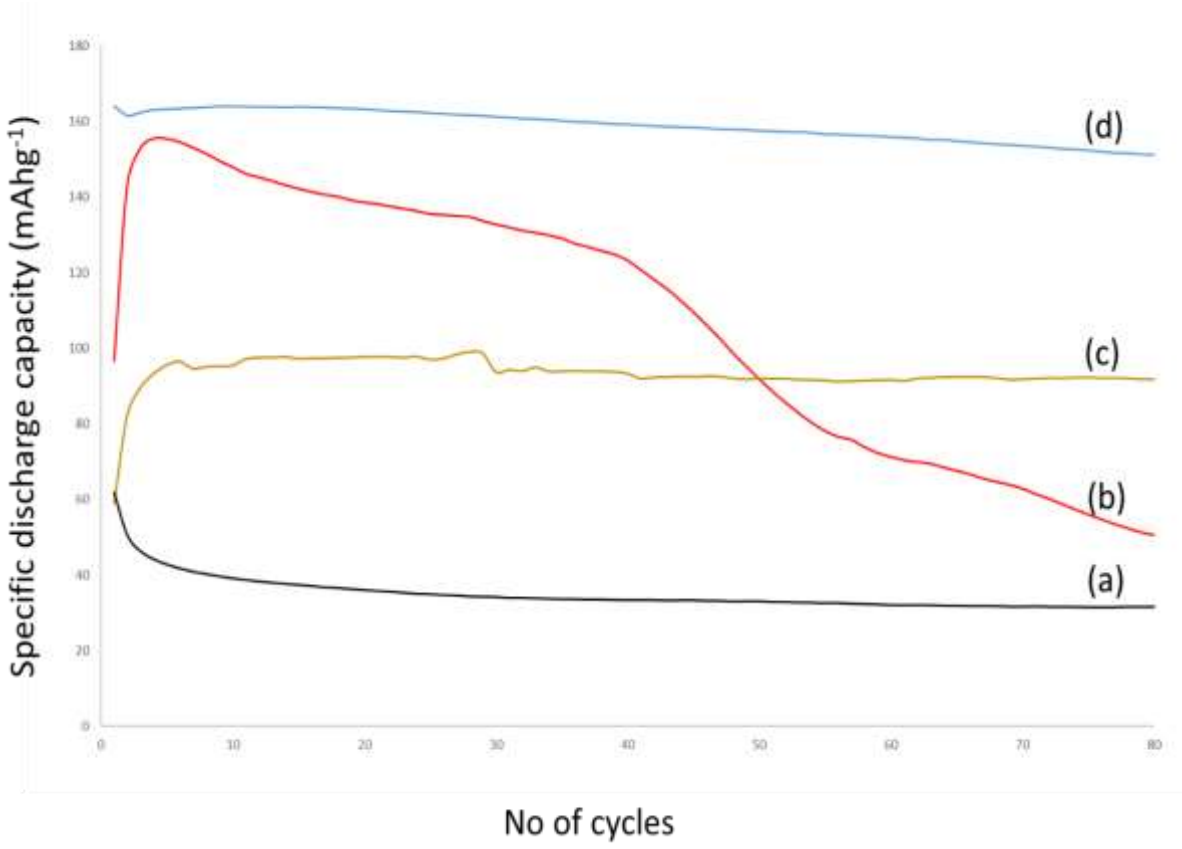

Figure 3-12: Specific discharge capacities of (a) synthesized $Ni(OH)_2$ with 0 wt.% carbon black, (b) synthesized $Ni(OH)_2$ with 5 wt.% carbon black, (c) $Ni_{0.75}Cu_{0.25}(OH)_2$ with 5 wt.% carbon black and (d) commercial $Ni(OH)_2$ over 80 cycles.

Both the commercial $Ni(OH)_2$ electrode (Figure 3-12c) and $Ni_{0.75}Cu_{0.25}(OH)_2$ electrode (Figure 3-12d) showed no reduction after 80 cycles. However, the $Ni_{0.75}Cu_{0.25}(OH)_2$ electrode (Figure 3-12d) demonstrated a drastically improved capacity (39% higher than of the commercial $Ni(OH)_2$ electrode) and stability with a specific discharge capacity of 151mAh/g after 80 cycles. It can also be said that copper stabilized the synthesized $Ni(OH)_2$, resulting in a specific discharge capacity of 151 mAh/g after the 80th cycle as compared to 51 mAh/g and 92 mAh/g (Table 3-6) for the unmodified $Ni(OH)_2$ and the commercial $Ni(OH)_2$, respectively.

Table 3-6 : Specific discharge capacities (mAh/g) of synthesized $Ni(OH)_2$ with 0 wt.% carbon black, synthesized $Ni(OH)_2$ with 5 wt.% carbon black, $Ni_{0.75}Cu_{0.25}(OH)_2$ with 5 wt.% carbon black and commercial $Ni(OH)_2$ after various cycle numbers.

Sample name	10th	20th	30th	40th	50th	60th	70th	80th
Synthesized $Ni(OH)_2$ with 0 wt.% carbon black	39	36	34	33	33	32	32	32
Synthesized $Ni(OH)_2$ with 5 wt.% carbon black	148	139	133	123	92	71	63	51
$Ni_{0.75}Cu_{0.25}(OH)_2$ with 5 wt.% carbon black	164	163	161	159	152	151	151	151
Commercial $Ni(OH)_2$	96	98	94	93	92	92	92	92

Table 3-7 illustrates the specific charge and discharge capacities of the synthesized $Ni(OH)_2$ and $Ni_{0.75}Cu_{0.25}(OH)_2$ active materials and their coulombic efficiencies measured at different currents (10 mA, 25mA, 50mA, and 75mA). A coulombic efficiency of 76% was achieved when a current of 10mA was applied as compared to when currents of 25mA, 50mA and 75mA were used, where a coulombic efficiency of 25%, 14% and 10% were obtained, respectively. These results show that the synthesized $Ni(OH)_2$ may operate better at lower currents. The $Ni_{0.75}Cu_{0.25}(OH)_2$ can be applied in both low current and higher current applications. This is evident by higher coulombic efficiencies of 86% at 10mA and 72% at 25mA, and 55% at 50mA

Table 3-7: Specific charge and discharge capacities in mAh/g at 10mA, 25mA, 50mA, and 75mA and their coulombic efficiencies in %.

	$Ni(OH)_2$ + 5wt.% carbon black			$Ni_{0.75}Cu_{0.25}(OH)_2$ + 5wt.% carbon black		
Current Applied	Specific Charge Capacity	Specific Discharge Capacity	Coulombic efficiencies	Specific Charge Capacity	Specific Discharge Capacity	Coulombic efficiencies
10	205	156	76	209	179	86
25	205	51	25	209	151	72
50	205	28	14	209	116	55
75	205	20	10	209	22	11

3.4.3 Effect of carbon black with different weight percentages (0wt.%, 5wt.%, 10wt.%, and 20wt.%) on the electrochemical performance of the electrode.

Different weight percentages of carbon black (i.e., 0wt.% 5wt.%, 10wt.%, and 20wt.%) were assessed, and the attained results were compared with 0wt.% of carbon black (active material without a carbon

black). The electrodes were prepared using the synthesized $Ni(OH)_2$ and $Ni_{0.95}Cu_{0.05}(OH)_2$, and the specific discharged capacities were calculated from the CCDG curves using Equation 3-5. The prepared electrodes were cycled 20 times at 25mA, and the plotted graphs are shown in Figure 3-13 and Figure 3-14. The calculated specific discharge capacities at 20th cycles are presented in Table 3-8.

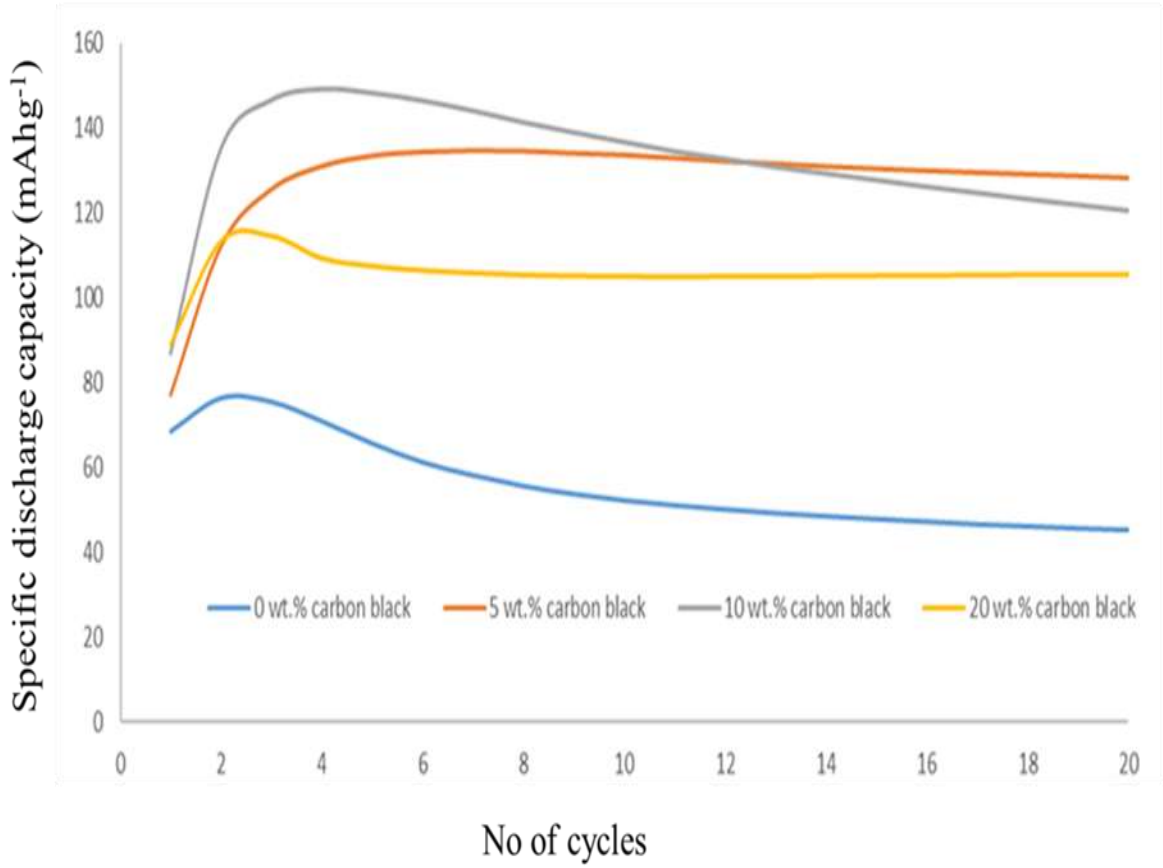

Figure 3-13: Specific discharge capacity; assessing the effect of carbon black to the synthesized $Ni(OH)_2$

As shown in Figure 3-13 and Table 3-8, the discharge capacity of 45mAh/g resulting in a coulombic efficiency of only 30% was obtained for $Ni(OH)_2$ after 20 cycles when carbon black was not added. Mixing 5wt.% carbon black into the electrochemically active material leads to an increase of capacity and coulombic efficiency to 128mAh/g and 87%, respectively. The specific discharge capacity and coulombic efficiencies decreases as more carbon black was added. The addition of 10wt.% and 20wt.% carbon black resulted in a coulombic efficiency of 59% and 51%, respectively. The decrease in capacities may be the result of the electrode becoming too bulky, which hinders the electron transfer between active material particles and the active $Ni(OH)_2$ sites.

Table 3-8: Specific discharge capacity; assessing the effect of carbon black to the synthesized $Ni(OH)_2$ and $Ni_{0.95}Cu_{0.05}(OH)_2$ after the 20th cycles.

Sample name	0 wt.% carbon black	5 wt.% carbon black	10 wt.% carbon black	20 wt.% carbon black
Synthesized $Ni(OH)_2$	45mAh/g	128 mAh/g	121 mAh/g	105 mAh/g
Synthesized $Ni_{0.95}Cu_{0.05}(OH)_2$	18 mAh/g	91 mAh/g	89 mAh/g	73 mAh/g

The same trend was observed for $Ni_{0.95}Cu_{0.05}(OH)_2$ (Table 3-8 and Figure 3-14). Therefore, based on the obtained results, it was therefore concluded that 5wt.% carbon black (85% active material and 10% binder) could be the optimum percentage needed to improve the utilization of active material in this current research.

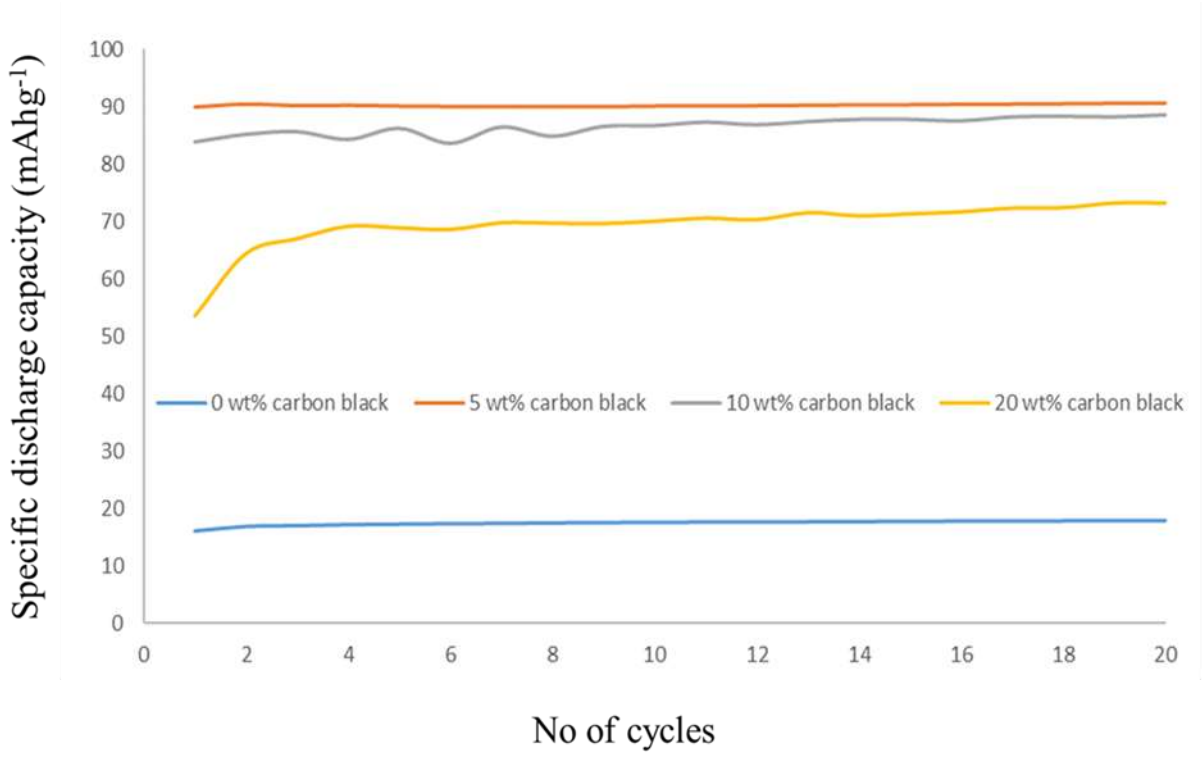

Figure 3-14: Specific discharge capacity; assessing the effect of carbon black to the synthesized $NiCu(OH)_2$

3.5 Conclusion

In this work β-$Ni(OH)_2$ and β-$Ni_{1-x}Cu_x(OH)_2$ active materials were successfully prepared by co-precipitation method followed by hydrothermal treatment. The effect of carbon black was evaluated, and the CCDG results demonstrated an improved utilization of the active material when 5 wt.% of carbon black was added to the electrode composition. The specific discharge capacity (after 20 cycle

activation) was increased by 74% compared to 0 wt.% carbon black added to the positive nickel electrode. However, a drastic decrease in specific discharge capacity was observed after an additional 60 cycles. The specific discharge capacity of the synthesized $Ni(OH)_2$ with 5 wt.% carbon black electrode decreased by 66%, while the synthesized $Ni(OH)_2$ with 0 wt.% carbon black decreased by only 18% after the 80 cycles. The addition of 25 wt.% Cu^{2+} to the $Ni(OH)_2$ material resulted in improved stability and a specific discharge capacity of 151 mAh/g compared to 51 mAh/g of unmodified $Ni(OH)_2$. Unmodified $Ni(OH)_2$ has a coulombic efficiency of 25 % compared to 76% for the modified $Ni(OH)_2$ after 80 cycles when a current of 25 mA was applied. Therefore, the Cu^{2+} modified $Ni(OH)_2$ active material may be acknowledged as a promising material for NiFe battery positive electrode applications.

3.6 Acknowledgements

The authors would like to acknowledge the financial and strategic support from the Department of Science and Innovation of South Africa; Eskom Research, Testing and Development (R,T&D) Department of South Africa; and the National Research Foundation of South Africa (Grant Number: 121413).

3.7 References

Abas, N., Kalair, A. and Khan, N. (2015). Review of fossil fuels and future energy technologies. Futures 69: 31-49.

Abbas, S. A., Iqbal, M. I., Kim, S. H., Khan, H. A. and Jung, K. D. (2019). Facile synthesis of alfa-nickel hydroxide by an ultrasound-assisted method and its application in energy storage devices. Applied Surface Science 474: 218-226.

Abdalla, A. H., Oseghale, C. I., Posada, J. O. G. and Hall, P. J. (2016). Rechargeable nickel-iron batteries for large-scale energy storage. Institution of Engineering and Technology Renewable Power Generation 10(10): 1529-1534.

Adekunle, A. S., Oyekunle, J. A., Oluwafem, O., Joshua, A. O., Makinde, A. O., Ogunfowokan, A. O., Eleruja, M. A. and Ebenso, E. E. (2014). Comparative catalytic properties of $Ni(OH)_2$ and NiO nanoparticles towards the degradation of nitrite (NO_2^-) and nitric oxide (NO). International Journal of Electrochemical Science 9: 3008 - 3021.

Alhebshi, N. A. and Alshareef, H. N. (2015). Ternary Ni-Cu-OH and Ni-Co-OH electrodes for electrochemical energy storage. Materials for Renewable and Sustainable Energy 4(4): 1-9.

Begum, S. N., Muralidharan, V. and Basha, C. A. (2009). The influences of some additives on electrochemical behaviour of nickel electrodes. International Journal of Hydrogen Energy 34(3): 1548-1555.

Chen, W., Jin, Y., Zhao, J., Liu, N. and Cui, Y. (2018). Nickel-hydrogen batteries for large-scale energy storage. Proceedings of the National Academy of Sciences 115(46): 11694-11699.

Coudun, C., Grillon, F. and Hochepied, J. F. (2006). Surfactant effects on pH-controlled synthesis of nickel hydroxides. Colloids and Surfaces A: Physicochemical and Engineering Aspects 280(1-3): 23-31.

Du, H., Wang, Y., Yuan, H. and Jiao, L. (2016). Facile synthesis and high capacitive performance of 3D hierarchical $Ni(OH)_2$ microspheres. Journal of Electrochimica Acta 196: 84-91.

Giri, S. D. and Sarkar, A. (2016). Electrochemical study of bulk and monolayer copper in alkaline solution. Journal of the Electrochemical Society 163(3): H252-H259.

Gonçalves, J. M., Alves, K. M., Gonzalez-Huila, M. F., Duarte, A., Martins, P. R. and Araki, K. (2018). Unexpected Stabilization of α-$Ni(OH)_2$ Nanoparticles in GO Nanocomposites. Journal of Nanomaterials 2018: 13.

Hall, D. S., Lockwood, D. J., Bock, C. and MacDougall, B. R. (2015). Nickel hydroxides and related materials: a review of their structures, synthesis and properties. Proceedings of the Royal Society A: Mathematical, Physical and Engineering Sciences 471(2174): 20140792.

Jin, Z., Li, P., Jin, Y. and Xiao, D. (2018). Superficial-defect engineered nickel/iron oxide nanocrystals enable high-efficient flexible fiber battery. Energy Storage Materials 13: 160-167.

Kim, K. H., Mikami, M., Abe, Y., Kawamura, M. and Kiba, T. (2018). Structural and electrochemical properties of nanolayer-stacking structured copper-doped nickel hydroxide. International Journal of Electrochemical Science 13: 7655-7662.

Kovalenko, V., Kotok, V., Sykchin, A., Mudryi, I., Ananchenko, B., Burkov, A., Sololvov, V., Deabate, S., Mehdi, A. and Bantignies, J.-L. (2017). Nickel hydroxide obtained by high-temperature two-step synthesis as an effective material for supercapacitor applications. Journal of Solid State Electrochemistry 21(3): 683-691.

Kozai, N., Mitamura, H., Fukuyama, H., Esaka, F. and Komarneni, S. (2006). Synthesis and characterization of nickel–copper hydroxide acetate, $NiCu(OH)_{3.1}(OCOCH_3)_{0.9}.0.9H_2O$. Microporous and Mesoporous Materials 89(1-3): 123-131.

Kumar, A. N., Harish, S. and Joseph, J. (2014). New route for synthesis of electrocatalytic $Ni(OH)_2$ modified electrodes—electrooxidation of borohydride as probe reaction. Bulletin of Materials Science 37(3): 635-641.

Kumar, N. and Panda, H. (2015). Facile synthesis of amorphous Co/Ni hydroxide hierarchical films and the study of their morphology and electrochemical properties. Royal Society of Chemistry Advances 5(33): 25676-25683.

Lassoued, A., Lassoued, M. S., Karolak, F., García-Granda, S., Dkhil, B., Ammar, S. and Gadri, A. (2017). Synthesis, structural, optical, morphological and magnetic characterization of copper substituted nickel ferrite ($Cu_xNi_{1-x}Fe_2O_4$) through co-precipitation method. Journal of Materials Science: Materials in Electronics 28(24): 18480-18488.

Liu, L., Hou, Y., Gao, Y., Yang, N., Liu, J. and Wang, X. (2019). Co doped α-$Ni(OH)_2$ multiple-dimensional structure electrode material. Journal of Electrochimica Acta 295: 340-346.

Motlagh, M. K., Youzbashi, A. and Sabaghzadeh, L. (2011). Synthesis and characterization of nickel hydroxide/oxide nanoparticles by the complexation-precipitation method. International Journal of Physical Sciences 6(6): 1471-1476.

Nejat, P., Jomehzadeh, F., Taheri, M. M., Gohari, M. and Majid, M. Z. A. (2015). A global review of energy consumption, CO_2 emissions and policy in the residential sector (with an overview of the top ten CO_2 emitting countries). Renewable and Sustainable Energy Reviews 43: 843-862.

Oseghale, C., Abdalla, A., Posada, J. and Hall, P. (2016). A new synthesis route for sustainable gold copper utilization in direct formic acid fuel cells. International Journal of Hydrogen Energy 41(37): 16394-16401.

Perera, F. (2017). Pollution from fossil-fuel combustion is the leading environmental threat to global pediatric health and equity: Solutions exist. Environmental Research and Public Health 15(1): 16.

Posada, J. O. G. and Hall, P. J. (2016). Towards the development of safe and commercially viable nickel-iron batteries: improvements to coulombic efficiency at high iron sulphide electrode formulations. Applied Electrochemistry 46(4): 451-458.

Riahi, K., Van Vuuren, D. P., Kriegler, E., Edmonds, J., O'neill, B. C., Fujimori, S., Bauer, N., Calvin, K., Dellink, R. and Fricko, O. (2017). The shared socioeconomic pathways and their energy, land use, and greenhouse gas emissions implications: an overview. Global Environmental Change 42: 153-168.

Sarrias-Mena, R., Fernández-Ramírez, L. M., García-Vázquez, C. A. and Jurado, F. (2014). Improving grid integration of wind turbines by using secondary batteries. Renewable and Sustainable Energy Reviews 34: 194-207.

Shanaj, B. and John, X. (2016). Effect of calcination time on structural, optical and antimicrobial properties of nickel oxide nanoparticles. Journal of Theoretical Computer Science 3(2).

Su, Y.-Z., Xiao, K., Li, N., Liu, Z.-Q. and Qiao, S.-Z. (2014). Amorphous $Ni(OH)_2$ @ three-dimensional Ni core–shell nanostructures for high capacitance pseudocapacitors and asymmetric supercapacitors. Journal of Materials Chemistry A 2(34): 13845-13853.

Wang, H., Liang, Y., Gong, M., Li, Y., Chang, W., Mefford, T., Zhou, J., Wang, J., Regier, T. and Wei, F. (2012). An ultrafast nickel–iron battery from strongly coupled inorganic nanoparticle/nanocarbon hybrid materials. Journal of Nature Communications 3: 917.

Warren, P. (2014). A review of demand-side management policy in the UK. Renewable and Sustainable Energy Reviews 29: 941-951.

Wiston, B. R. and Ashok, M. (2019). Electrochemical performance of hydrothermally synthesized flower-like α-nickel hydroxide. Vacuum 160: 12-17.

Xu, W., Lan, R., Du, D., Humphreys, J., Walker, M., Wu, Z., Wang, H. and Tao, S. (2017). Directly growing hierarchical nickel-copper hydroxide nanowires on carbon fibre cloth for efficient electrooxidation of ammonia. Applied Catalysis B: Environmental 218: 470-479.

Young, K.-H., Wang, L., Yan, S., Liao, X., Meng, T., Shen, H. and Mays, W. (2017). Fabrications of high-capacity alpha-$Ni(OH)_2$. Batteries 3(1): 6.

Young, K., Wang, L., Mays, W., Reichman, B., Chao-Ian, H., Wong, D. and Nei, J. (2018). Nickel hydroxide positive electrode for alkaline rechargeable battery, Google Patents.

Yu, J., Pan, S., Zhang, Y., Liu, Q. and Li, B. (2019). Facile synthesis of monodispersed α-$Ni(OH)_2$ microspheres assembled by ultrathin nanosheets and its performance for oxygen evolution reduction. Frontiers in Materials 6: 124.

Zhai, Z., Liu, Q., Zhu, Y., Cao, J. and Shi, S. (2019). Synthesis of $Ni(OH)_2$/graphene composite with enhanced electrochemical property by stirring solvothermal method. Journal of Alloys and Compounds 775: 1316-1323.

Zheng, Y., Zhu, B., Chen, H., You, W., Jiang, C. and Yu, J. (2017). Hierarchical flower-like nickel (II) oxide microspheres with high adsorption capacity of Congo red in water. Journal of Colloid and Interface Science 504: 688-696.

CHAPTER 4

4 Electrochemical Studies of the Nickel-Based Hydroxide Electrode for the Oxygen Evolution Reaction and Coulombic Efficiency of the Electrode.

THIS CHAPTER HAS BEEN PUBLISHED:

Zide, D., Felix, C., Oosthuysen, T. and Bladergroen, B.J., 2020. Electrochemical studies of the nickel-based hydroxide electrode for the oxygen evolution reaction and coulombic efficiency of the electrode. Electroanalysis, 32(12), pp.2703-2712.

4.1 Abstract

Nickel hydroxide, $Ni(OH)_2$ electrode material has been used as a positive electrode in commercial alkaline secondary batteries for more than 100 years. This is because $Ni(OH)_2$ has a good high-rate discharge ability performance, wide operation and storage temperature range and relatively low cost. However, the $Ni(OH)_2$ positive electrode exhibits poor performance, which results from (i) competitive reactions of the oxidation of the active material and the evolution of oxygen. (ii) The reduced charge acceptance of $Ni(OH)_2$ positive electrode is suspected to be related to a relatively long distance between $Ni(OH)_2$ particles and the nearest portion of the substrate. In this study, electrodes are prepared using β-$Ni(OH)_2$ powder as the active electrode material, hot-pressed onto a nickel mesh current collector. The Ni^{2+} in the compound β-$Ni(OH)_2$ material is partially substituted with $Co^{2+,}$ and Al^{3+} metals and the performance of as-prepared materials are optimized and examined. XRD, FTIR, TG-DTA, SEM/EDS, and ICP confirms the formation of the expected compositions. The samples with 5 wt.% Co^{2+}, and 10 wt.% Al^{3+} metals are found to be the optimal compositions with promising electrochemical activities. The modification of $Ni(OH)_2$ by the partial substitution of Co^{2+} and Al^{3+} metals for Ni^{2+} shows some effect on the redox peaks of $Ni(OH)_2$ and the oxygen evolution reaction (OER). E.g., the onset for oxidation of the active material is significantly improved with partial substitution of Ni^{2+} by Co^{2+} metal. On the other hand, partial substitution of Ni^{2+} with Al^{3+} metal moves the onset of electrode oxidation to a higher potential. In addition, the partial substitution of 10 wt.% Al^{3+} metal improves both discharge capacity (from 128 mAh/g to 170 mAh/g) and the coulombic efficiency (from 87% to 93%) of the β-$Ni(OH)_2$ electrode.

Key Words: Oxygen evolution; Coulombic efficiency; β-nickel hydroxide; β-nickel-cobalt hydroxide; α/β/-nickel aluminium hydroxide

4.2 Introduction

Nickel hydroxide, $Ni(OH)_2$ electrode material has been used as a positive electrode in commercial alkaline secondary batteries for more than 100 years. This is because $Ni(OH)_2$ has a good high rate discharge ability performance, wide operation and storage temperature range and relatively low cost (Young, Kwo-Hsiung *et al.*, 2017). The $Ni(OH)_2$ material has been widely studied (Falahati *et al.*, 2015; Hall *et al.*, 2015; Holmberg, 2017; Bresser *et al.*, 2018; Young, Kwo *et al.*, 2018), and the most significant advance in the understanding of the overall reaction was reported by Falahati and his co-workers (Falahati *et al.*, 2015). Falahati and co-workers explained the behaviour of the electrochemical redox reactions of $Ni(OH)_2$ during the charge-discharge of an electrode. According to the authors, $Ni(OH)_2$ could exist in a β-form or α-form. The β-form is anhydrous and has a layered brucite, $Co(OH)_2$ structure, while the α-form is hydrated and has intercalated water between brucite like-layers. Oxidation

of β-$Ni(OH)_2$ on charge produces β-NiOOH, which discharge to yield β-$Ni(OH)_2$ and if overcharged, the β-$Ni(OH)_2$ could be converted to γ-NiOOH. The oxidation of α-$Ni(OH)_2$ on charge produces γ-NiOOH, which discharged to form α-$Ni(OH)_2$. In general, α-Ni $(OH)_2$ is unstable and can be transformed to β-Ni $(OH)_2$ in a neutral or KOH aqueous solution. Primarily α-$Ni(OH)_2$ is slowly dissolved in the aqueous solution and then re-nucleated to form β-$Ni(OH)_2$.

β-$Ni(OH)_2$ is often selected as a discharged-state active material in the preparation of nickel electrodes (Gonçalves *et al.*, 2018) because (i) it is stable in strong alkaline electrolyte and has good reversibility when charged to β-NiOOH. (ii) β-NiOOH has a similar structure with a lattice constant of inter-sheet (4.85Å); thus, the volume expansion associated with cycling is less than any other forms. However, the overcharge of β-$Ni(OH)_2$ may result in the formation of γ-NiOOH, which contains Ni^{4+} (Yang, LJ *et al.*, 2007; Hall *et al.*, 2015) with an average oxidation state of nickel in this phase between 3.3−3.7 (Yang, LJ *et al.*, 2007). The conversion of β-$Ni(OH)_2$ to γ-NiOOH is accompanied by a large volumetric change. This may result in loss of contact between the active material and the conductive substrate, thus causing fast capacity fading during charge-discharge cycling. Disadvantages of using β-$Ni(OH)_2$ as the active material for the nickel electrode is the relative low theoretical specific capacity, which is limited to 289 mAh/g according to Equation 4-1 (Yang, LJ *et al.*, 2007; Begum *et al.*, 2009; Huang, Jichun *et al.*, 2013).

Equation 4-1: Redox reaction of $Ni(OH)_2$/NiOOH electrode

$$\beta - Ni(OH)_2 + OH^- \rightleftharpoons \beta - NiOOH + H_2O + e^- \qquad E° = 0.395V \text{ vs } Hg/HgO/KOH$$

This specific capacity corresponds to the exchange of one electron ($1e^-$) per Ni atom and in practice, the specific capacity of β-$Ni(OH)_2$ material is below the said theoretical value (Begum *et al.*, 2009). The practical specific capacity of the positive nickel electrode depends on how well the β-$Ni(OH)_2$ particles are embedded within a conductive electron network allowing electrons to move between particles and the current collector. The limited performance of $Ni(OH)_2$ electrode is also said to be due to competitive reactions of the oxidation of the active material and the evolution of oxygen (Wang, Xianyou *et al.*, 2004; Begum *et al.*, 2009). The reduced charge acceptance of nickel hydroxide positive electrode is suspected to be related to a relatively long distance between nickel hydroxide particles and the nearest portion of the substrate(Begum *et al.*, 2009). Notwithstanding the drawbacks of the oxygen evolution reaction, the oxygen evolution is known to play a key role in developing clean energy conversion and storage technologies, as it generates electrons that can reduce water to hydrogen, carbon dioxide to carbon-containing fuels, and metal ions to metal in recharge of metal–air batteries (Suntivich *et al.*, 2011; Oh *et al.*, 2012; Wang, Haotian *et al.*, 2015; Blasco-Ahicart *et al.*, 2018).

The modification of $Ni(OH)_2$ material with specific additives could increase the potential gap between the oxidation of electrode material and the oxygen evolution reaction (OER). Various studies have

revealed that the incorporation of divalent elements such as magnesium, cobalt, and zinc can improve active material utilization and prevent the formation of γ-NiOOH (Young, Kwo-Hsiung *et al.*, 2017; Liu, Ling *et al.*, 2019). Conversely, the incorporation of divalent elements could lead to structural disorder, which could play a vital role in the electrochemical properties of β-$Ni(OH)_2$. Although the relationship between structural disorder and the measured electrochemical properties is not always clear, a well crystallised β-$Ni(OH)_2$ has lower electrochemical activity than disordered β-$Ni(OH)_2$ materials (Hall *et al.*, 2015).

In the present study, the partial substitution of Co^{2+} and Al^{3+} metals for Ni^{2+} in β-$Ni(OH)_2$ is examined for oxygen evolution, material utilisation, and discharge capacity in $Ni(OH)_2$ positive electrodes nickel-iron battery.

4.3 Material and methods

4.3.1 Materials

Sodium carbonate (99%), sodium hydroxide (98%), nickel nitrate hexahydrate, cobalt nitrate hexahydrate (98%), and aluminium nitrate nanohydrate (98%) were purchased from Sigma-Aldrich (South Africa). Carbon black was purchased from Alfa Aesar (United States), coatheylene was purchased from Axalta (United States), and nickel mesh was purchased from Q-Lite batteries (China).

4.3.2 Synthesis of nickel hydroxide active material

Nickel-based active material was prepared using a modified co-precipitation method and followed by hydrothermal treatment at pH = 14 (Lassoued *et al.*, 2017). For the production of $Ni(OH)_2$, two solutions were prepared; solution 1 (contained NaOH and Na_2CO_3), and solution 2 contained Ni^{2+} as $Ni(NO_3)_2 \cdot 6H_2O$ salt. The two solutions were mixed dropwise under vigorous stirring at room temperature. The slurry was further agitated at room temperature for 30 min and thereafter subjected to hydrothermal treatment at 65°C for 18h. The resulting precipitates were allowed to cool at room temperature, then filtered and washed with Milli-Q water. The precipitated samples were dried at 110°C for 12h. The dried samples were milled and transferred into vials for later application.

For modification of $Ni(OH)_2$; cobalt and aluminium were used as partial substituent for nickel. The above method was adopted and a composition of $Ni_{1-x}M_x(OH)_2$ was prepared, where "x" (5, 10, 25, and 50 wt.%), and "M" (Co, and Al) is the weight percentage and the partially substituted metal, respectively.

4.3.3 Structural and morphological characterization of the materials

The diffraction patterns were collected using a multi-purpose X-ray Diffractometer D8-Advance from BRUKER AXS (Germany). The functional groups present in the materials were identified using a Fourier Transform Infra-Red Spectrum II spectrometer (UATR-FTIR, Llantrisant UK). The thermal analysis was studied using a Perkin-Elmer (8000 instrument) thermal gravimetric analysis coupled with

differential thermal analysis (TGA-DTA). Surface areas were analysed using Brunauer-Emmett-Teller (BET) nitrogen adsorption isotherms and adsorption pore size using Barrett-Joyner-Halenda (BHJ). The crystal structures of the synthesized materials were confirmed using scanning electron microscopy (SEM). The elemental composition was determined using inductively coupled plasma optical emission spectroscopy (ICP-OES) and SEM/EDS.

4.3.4 Fabrication of electrodes

The nickel electrodes were prepared by mixing 85 wt.% active material, 5 wt.% carbon black and 10 wt.% coathylene binder thoroughly. The mixture was poured onto a nickel mesh sheet and hot-pressed at 80˚C at 6MPa using a custom-designed hydraulic press for 5min to assure good electrical contact between the nickel mesh and the active material. Electrode dimensions were kept at 1cm × 1cm for all the samples.

4.3.5 Electrochemical characterization

The as-prepared nickel electrodes were soaked in electrolyte prior to the electrochemical measurements for 2h. Cyclic voltammetry (CV) was used for the identification of redox couples and chrono charge-discharge galvanostatic (CCDG) for capacities of the active materials. Electrochemical characterization was studied using 4M of KOH as an electrolyte in a three-electrode set-up configuration, performed using the Metrohm AutoLab PGSTAT302N. A graphite sheet (3cm x 4cm), and Hg/HgO/KOH were used as a counter, and reference electrode, respectively.

4.4 Results and Discussion

4.4.1 Structural characterization of synthesized Ni-based hydroxide materials

Figure 4-1a-c shows the XRD patterns of the Ni-based hydroxide powders. Figure 4-1a could be indexed to pure β-$Ni(OH)_2$ (JCP-No 00-014-0117). Figure 4-1b was indexed to both β-$Ni(OH)_2$ (JCP-No 00-014-0117) and β-$Co(OH)_2$ (JCP-No-00-030-0443), illustrating that the partial substituted Co^{2+} metal may be incorporated into the lattice of β-$Ni(OH)_2$. β-$Ni(OH)_2$ is isostructural to β-$Co(OH)_2$, and both have a hexagonal lattice structure (JCP-No 00-014-0117; JCP-No-00-030-0443). The Al^{3+} partial substituted $Ni(OH)_2$ could be indexed to β-$Ni(OH)_2$ (JCP-No 00-014-0117), α-$Ni(OH)_2$ (JCP-No 00-038-0715) and pure $Ni_5Al_4O_{11}$ •$18H_2O$ (JCP-No 00-022-0452) demonstrating a mixture of α/β-form (Yang, LJ *et al.*, 2007; Huang, Jichun *et al.*, 2013). Therefore, the formulae of the Ni-based hydroxide materials may be written as β-$Ni(OH)_2$, β-$Ni_{1-x}Co_x(OH)_2$ and α/β-$Ni_{1-x}Al_x(OH)_2$. Where Co_x is 5%wt., and Al_x is 10%wt.

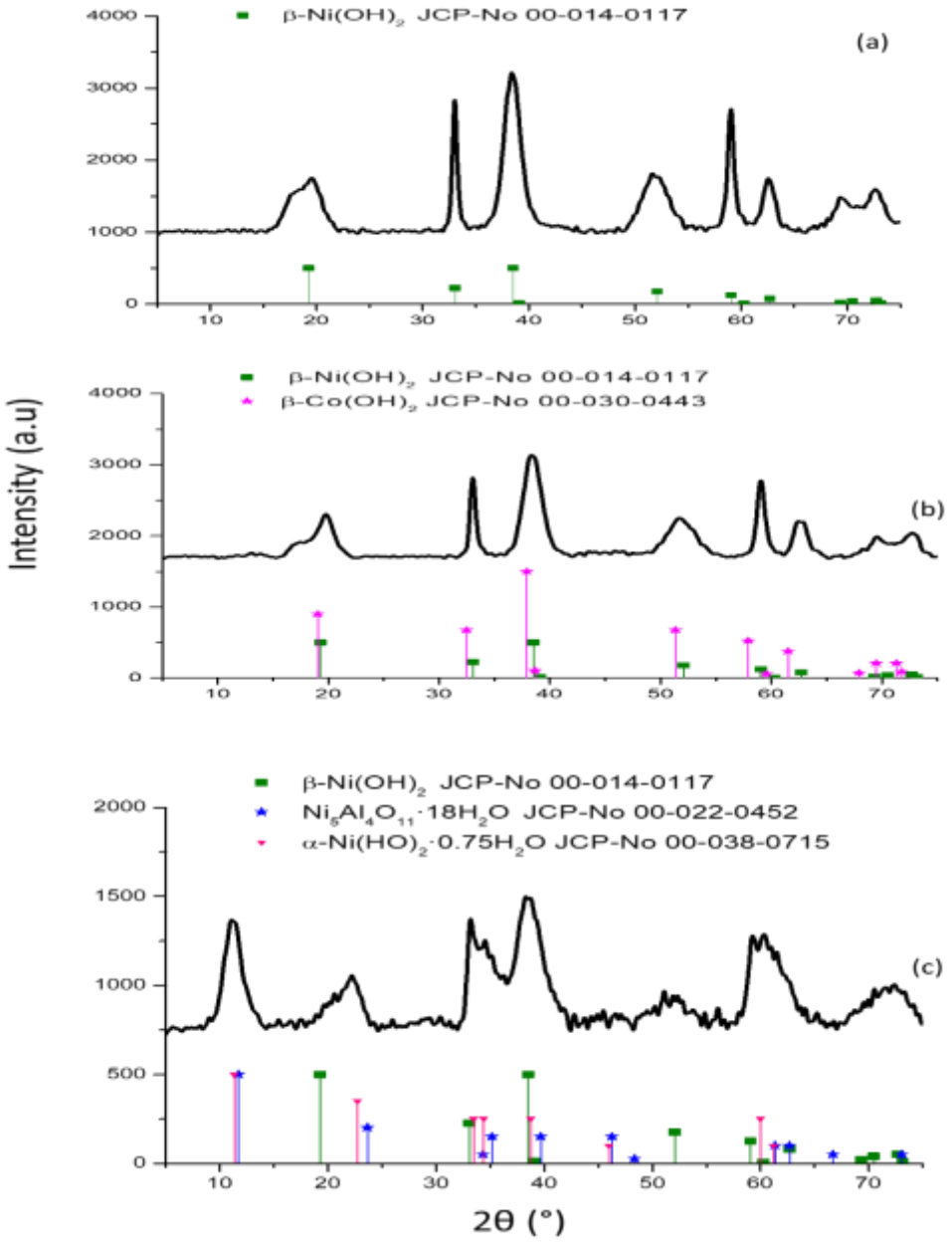

Figure 4-1: Diffractograms of (a) $Ni(OH)_2$, (b) $Ni_{0.95}Co_{0.05}(OH)_2$ and (c) $Ni_{0.9}Al_{0.1}(OH)_2$

The crystallite sizes of the materials were calculated from the two major peaks (001), and (101) using Debye-Scherer's formula (Equation 4-2), and the unit cell parameters "a" and "c" were calculated using the formulae $a = 2d_{110}$, and $c = d_{001}$; where d_{001} and d_{110} are the basal spacing at a Miller index (hkl) of (001) and (110), which were obtained using Bragg's law equation (Equation 4-3), assuming hexagonal stacking (Wiston and Ashok, 2019).

Equation 4-2: Debye-Scherer's equation

$$D = \frac{K\lambda}{\beta Cos\theta})$$

Where D is the crystallite size, K is the Scherer's constant (K = 0.9), β is the full width of half maximum (FWHM), and θ is the maximum diffraction angle (˚).

Equation 4-3: Bragg's law

$$n\lambda = 2d \sin\theta$$

Where n is the order number, λ is the wavelength (1.54098 Å), d is the basal spacing (Å), θ is the maximum diffraction angle (˚).

Table 4-1 summarizes the XRD crystallite sizes (D), the lattice parameter "a", "c", and the interlayer distance (d-spacing) for the respective powders. The crystalline size values are different for each Ni-based material, with the pure $Ni(OH)_2$ powder illustrating the lowest crystalline size, while the cobalt modified sample has the largest. It can also be noted that the parameter "a" decreases gradually in the presence of partial Al^{3+} in the $Ni(OH)_2$ lattice. This is may be due to the difference of metal ionic radii between Al^{3+} and Ni^{2+}. The radius of Al^{3+} ions is 0.54 Å, smaller than the radius of Ni^{2+} (0.69 Å) in the lattice of $Ni(OH)_2$ (Yang, LJ *et al.*, 2007). The c-parameters decreases in the order of β-$Ni(OH)_2$ > β-$Ni_{0.95}Co_{0.05}(OH)_2$ > α/β-$Ni_{0.9}Al_{0.1}(OH)_2$. The value of interlayer distance, d, increases slightly for the sample with partial Co^{2+}. A significant increase is observed in the presence of partial Al3+ compared to both pure $Ni(OH)_2$ and cobalt partially substituted sample. This may be owed to the reason that the more Ni^{2+} ions are partially replaced by Al^{3+} ions, the more positive charge of the $Ni(OH)_2$ layer possess (Yang, LJ *et al.*, 2007). Consequently, more anions, such as NO_3^- and OH^-, are hosted between the layers to compensate for the positive charge, (Hall *et al.*, 2015) maintaining the stability of the structure.

Table 4-1: XRD crystallite sizes, and lattice parameter "a", "c" and "d-spacing" of the nickel-based hydroxide materials

Sample name	**(001) D (nm)**	**(101) D (nm)**	**(001) 2θ (˚)**	**d001 (Å)**	**(110) 2θ (˚)**	**d110 (Å)**	**a (Å)**	**c (Å)**
$Ni(OH)_2$	2.59	3.35	19.21	4.62	59.11	1.56	3.12	4.62
$Ni_{0.95}Co_{0.05}(OH)_2$	8.66	5.78	19.73	4.50	59.10	1.56	3.12	4.50
$Ni_{0.9}Al_{0.1}(OH)_2$	3.79	3.46	21.81	4.07	59.97	1.54	3.08	4.07

Figure 4-2, depicts the FTIR spectra of the synthesized Ni-based hydroxides materials. The findings are in agreement with the obtained XRD results; the presence of the sharp peaks at around 3600 cm^{-1} is the confirmation of $Ni(OH)_2$ formation (Motlagh *et al.*, 2011; Shanaj and John, 2016); and these absorption bands are assigned to O-H stretching vibrations (Begum *et al.*, 2009; Su *et al.*, 2014; Hall *et al.*, 2015; Shanaj and John, 2016). The peaks at around 1600 cm^{-1} are attributed to the bending vibration mode of H_2O molecules. The absorption bands at about 1300 cm^{-1}, 500 cm^{-1} and 400 cm^{-1} are attributed to the existence of interlayer nitrate anions (NO_3^-), Ni-O stretching vibrations, and an in-plane Ni-O-H

bending vibration, respectively (Begum *et al.*, 2009; Su *et al.*, 2014; Hall *et al.*, 2015; Shanaj and John, 2016).

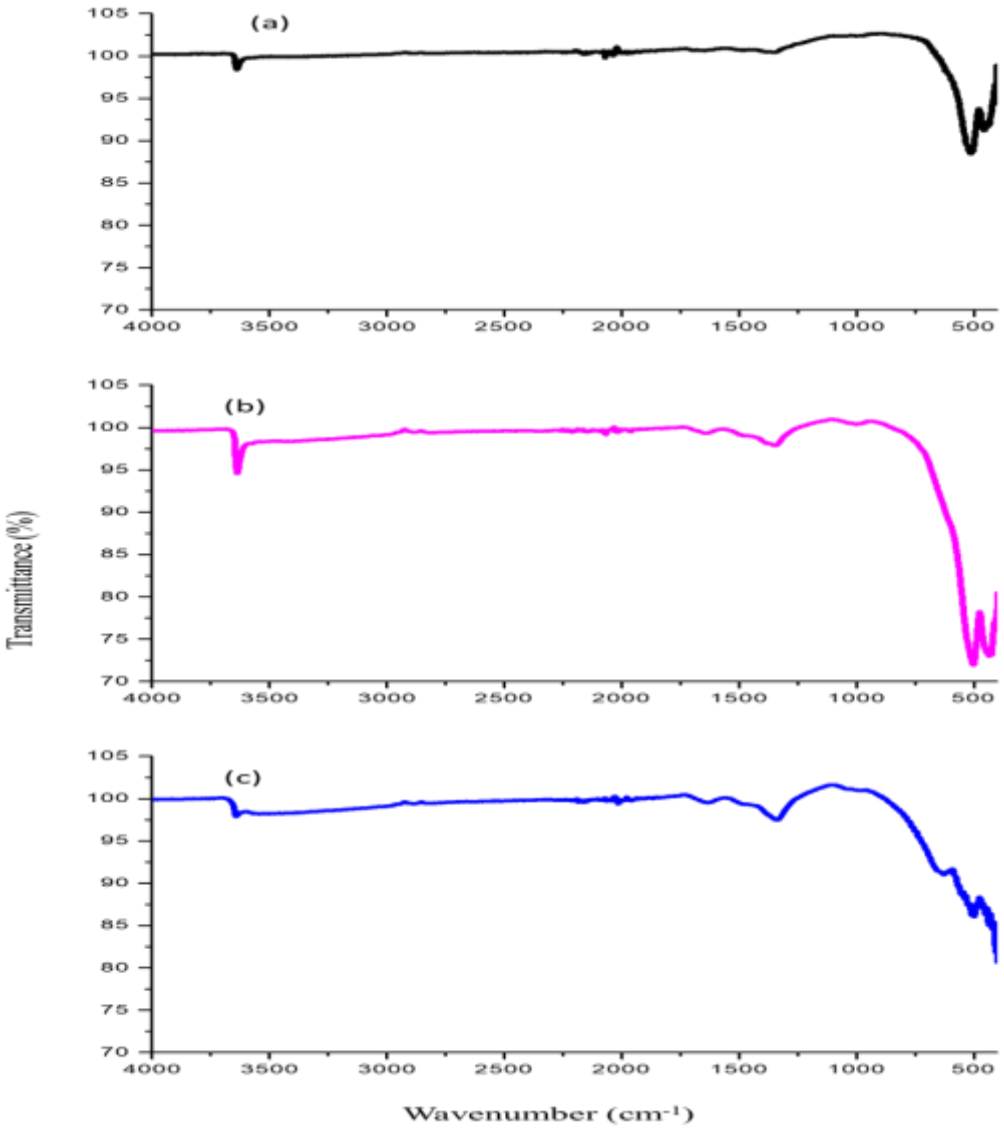

Figure 4-2: FTIR spectra of (a) $Ni(OH)_2$, (b) $Ni_{0.95}Co_{0.05}(OH)_2$, and (c) $Ni_{0.9}Al_{0.1}(OH)_2$

The thermal gravimetric analysis (TGA) and the corresponding insert of the differential thermal analysis (DTA) curves of the nickel-based hydroxide materials are given in Figure 4-3. All the samples demonstrate two distinct weight losses with initial weight losses of 5.20 wt.%, 5.38 wt.%, and 10.78 wt.% corresponding to small endothermic peaks at 73˚C, 75˚C, and 75˚C for $Ni(OH)_2$, $Ni_{0.95}Co_{0.05}(OH)_2$, and $Ni_{0.9}Al_{0.1}(OH)_2$, respectively.

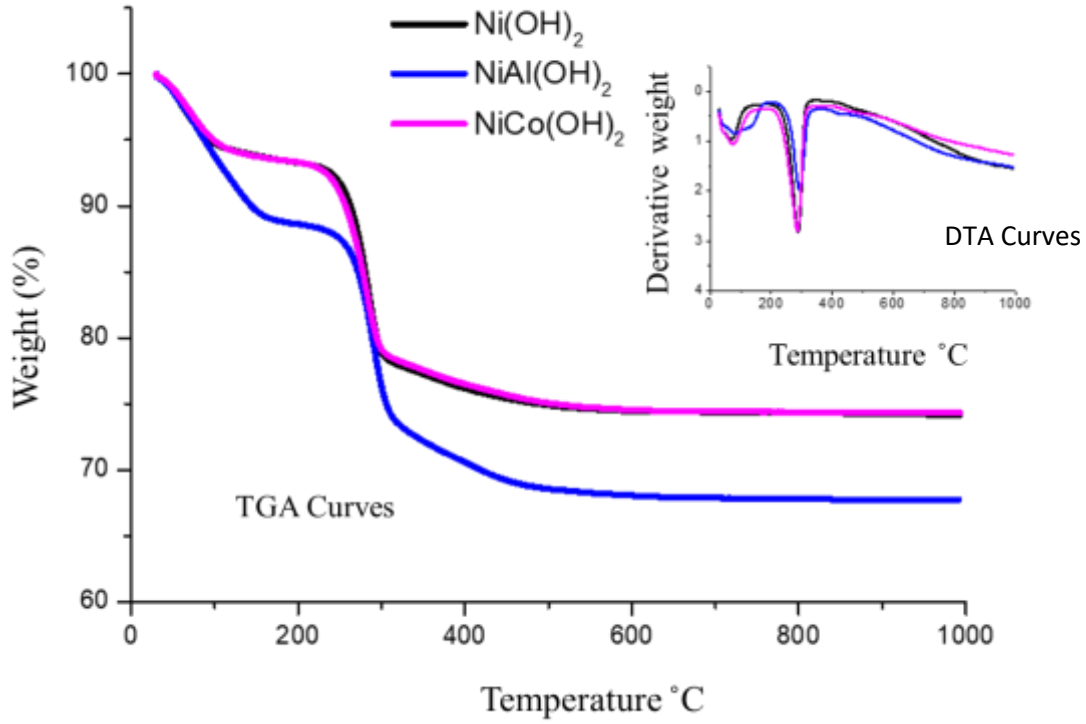

Figure 4-3: TG-DTA curves of $Ni(OH)_2$, $Ni_{0.95}Co_{0.05}(OH)_2$, and $Ni_{0.9}Al_{0.1}(OH)_2$

A second weight losses of 12.26 wt.%, 17.66 wt.%, and 19.503 wt.% corresponding to a sharp endothermic peak at 285˚C, 285˚C, and 295˚C for $Ni(OH)_2$, $Ni_{0.95}Co_{0.05}(OH)_2$, $Ni_{0.9}Al_{0.1}(OH)_2$, respectively.

The small endothermic peaks at a temperature ranged between 62˚C – 75˚C is associated with the removal of surface water in the samples. The sharp endothermic peaks at around 285˚C – 309˚C is due to the decomposition of $Ni(OH)_2$ to NiO (Shanaj and John, 2016; Kovalenko *et al.*, 2017). These results agree with the presented XRD diffractograms and the FTIR spectra, which further confirms the formation of anhydrous β-$Ni(OH)_2$. The dehydration process of $Ni(OH)_2$ may be illustrated as follows (Equation 4-4 to Equation 4-6) (Hall *et al.*, 2015; Shanaj and John, 2016; Kovalenko *et al.*, 2017):

Equation 4-4: Removal of adsorbed water molecules (X_{ad}) in $Ni(OH)_2$

$$Ni(OH)_2.(X_{ad} + Y_{st})H_2O \xrightarrow{50℃-90℃} Ni(OH)_2.Y_{st}H_2O + XH_2O$$

Equation 4-5: Removal of incorporated water molecules (Y_{st}) in $Ni(OH)_2$

$$Ni(OH)_2.Y_{st}H_2O \xrightarrow{90℃-180℃} Ni(OH)_2 + YH_2O$$

Equation 4-6: Structural decomposition of $Ni(OH)_2$

$$Ni(OH)_2 \xrightarrow{180°C-525°C} NiO + H_2O$$

The equations above clearly show that the TGA behaviour of β-$Ni(OH)_2$ materials, which illustrates a surface removal of water ranged at 50˚C and 90˚C, followed by dehydration between 90˚C and 180˚C, and broad features at 180˚C < T < 525˚C from decomposition to NiO (Hall *et al.*, 2015; Shanaj and John, 2016).

The BET surface areas ranged between 86.81 m^2/g to 361.92 m^2/g, and the BHJ average pore size adsorption ranged from 5.36 nm to 8.69 nm (Table 4-2). The elemental composition confirmed using ICP and SEM/EDS agreed with intended compositions of $Ni_{0.9}Al_{0.1}(OH)_2$ and $Ni_{0.95}Co_{0.05}(OH)_2$ (Table 4-2).

Table 4-2: BET specific surface area and elemental composition ratio of $Ni_{1-x}M_x(OH)_2$ (M_X =5 wt.% Co^{2+} and 10wt% Al^{3+})

Sample name	**BET Surface area (m^2/g)**	**Pore size (nm)**	**Expected Ni^{2+}:M^{x+}**	**ICP-OES Ni^{2+}:M^{x+}**	**SEM-EDS Ni^{2+}:M^{x+}**
$Ni(OH)_2$	361.92	6.29	*	*	*
$Ni_{0.95}Co_{0.05}(OH)_2$	125.15	8.69	0.95: 0.05	0.95: 0.05	0.95: 0.05
$Ni_{0.9}Al_{0.1}(OH)_2$	86.81	5.63	0.90: 0.10	0.90: 0.10	0.89: 0.11

Figure 4-4, shows the nitrogen adsorption-desorption isotherm of the synthesized $Ni_{1-x}M_x(OH)_2$, which could be classified as type IV isotherm with H3-type hysteresis loop (Luan *et al.*, 2018), reflecting the presence of mesoporous structure at the relative pressure (P/P°) range between 0.7 and 1.0 (Figure 4-4a), and 0.48 and 1.0 (Figure 4-4b-c). These findings were in agreement with the results reported in the literature (Coudun *et al.*, 2006; Zheng *et al.*, 2017; Luan *et al.*, 2018; Yu *et al.*, 2019).

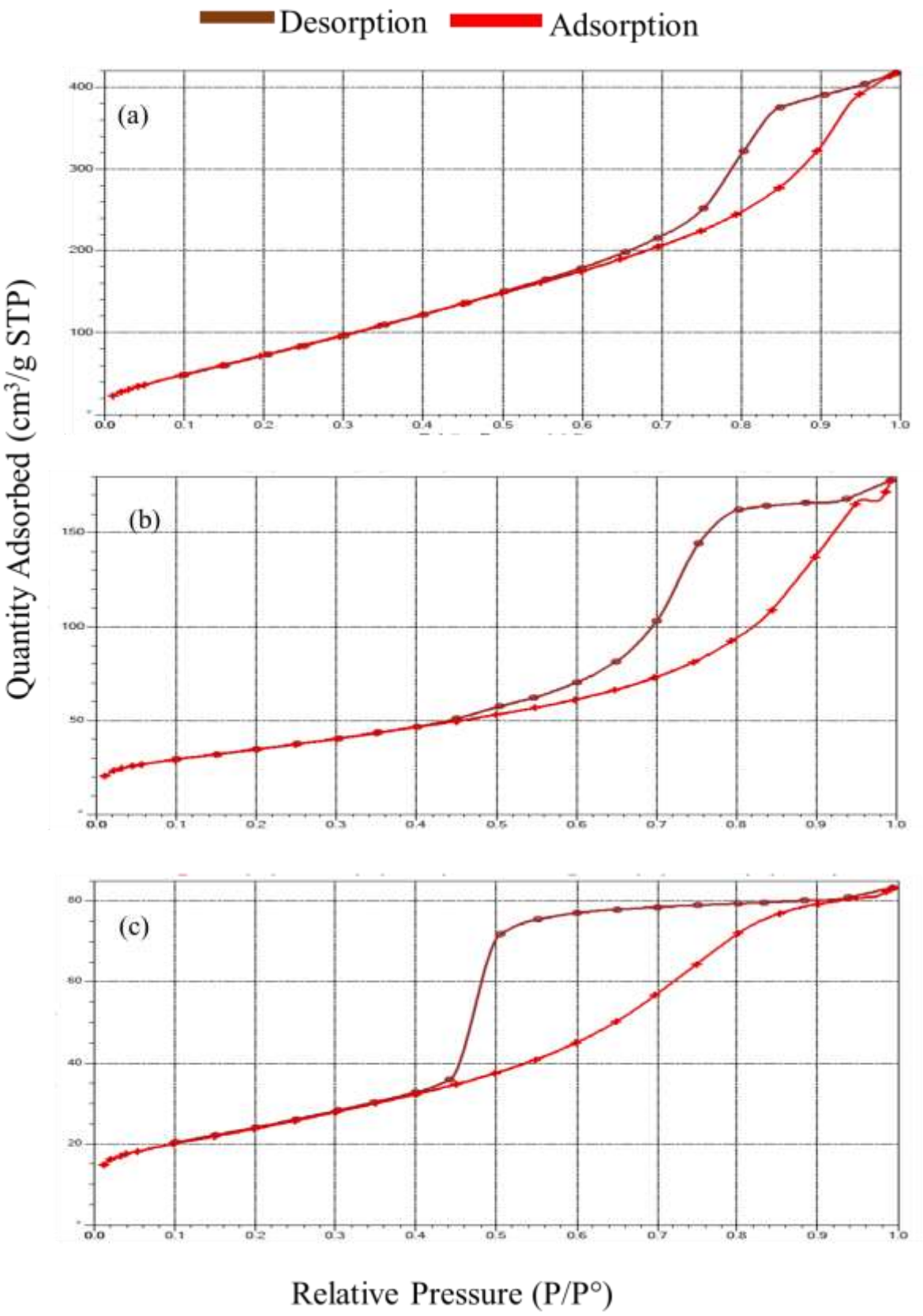

Figure 4-4: Nitrogen adsorption – desorption isotherms of (a) $Ni(OH)_2$, (b) $Ni_{0.95}Co_{0.05}(OH)_2$, and (c) $Ni_{0.9}Al_{0.1}(OH)_2$

Figure 4-5, shows the SEM images of synthesised Ni-based hydroxide powders at a magnification of 25kx. The average Ni-based hydroxide particle sizes at this magnification were found to be between 2.6 nm and 8.7 nm. Similar morphologies for β-$Ni(OH)_2$ and α/β-Al form were reported (Yang, LJ *et al.*, 2007). According to the authors (Yang, LJ *et al.*, 2007), the stacking porous structure is beneficial to the penetration of electrolyte, the diffusion of protons, and the electrochemical activity of electrode.

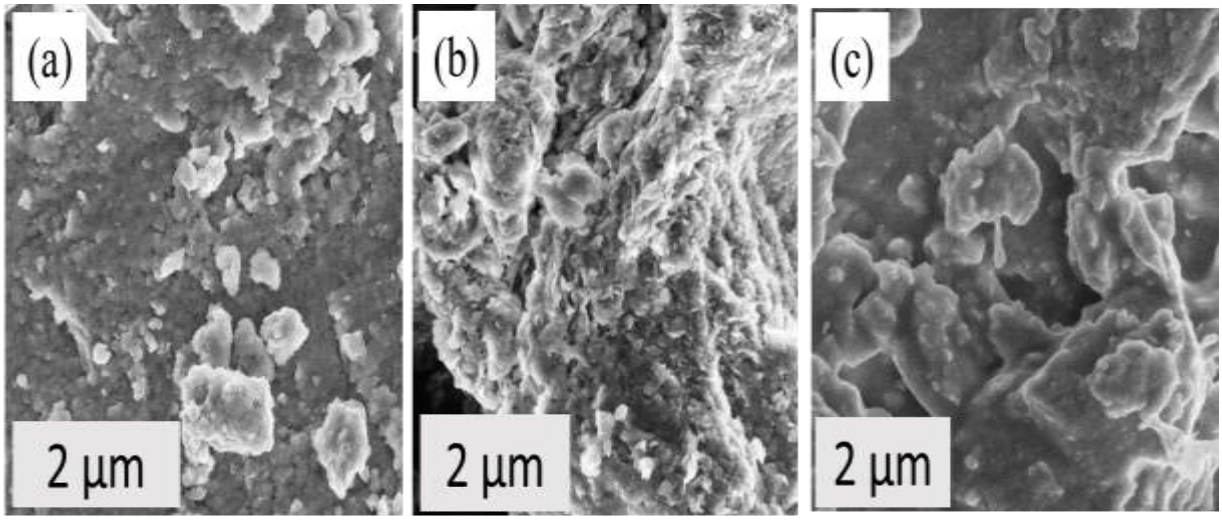

Figure 4-5: SEM images of (a) $Ni(OH)_2$, (b) $Ni_{0.95}Co_{0.05}(OH)_2$, and (b) $Ni_{0.9}Al_{0.1}(OH)_2$

4.4.2 Electrochemical characterization of synthesized $Ni(OH)_2$ based materials

The transformation of Ni(II) oxide to Ni(III) oxide was studied by applying a potential sweep rate of 20 mVs^{-1} at potentials ranging from 0.0 V to 0.7 V (vs Hg/HgO/4M KOH) at room temperature. The obtained voltammograms for the Ni-based hydroxide electrodes are provided in Figure 4-6. An electrode of pure $Ni(OH)_2$ without any additive material (Figure 4-6a) shows broader cathodic and anodic peaks. Similar results were reported in literature (Begum *et al.*, 2009; Wang, Hailiang *et al.*, 2012). This may be an indication that the oxygen evolution reaction (OER) is overlapping with the oxidation potential of NiOOH to $Ni(OH)_2$. The reaction process may be explained according to Equation 4-7 and Equation 4-8 (Carbonio *et al.*, 1982; Zimmerman and Effa, 1984).

Equation 4-7: Charge transfer process involving redox reaction of NiOOH active material in the lattice

$$Ni(OH)_2 \rightleftharpoons NiOOH + H^+ + e^-$$

Equation 4-8: Formation of protons at the electrode/electrolyte interface

$$H^+ + OH^- \rightleftharpoons H_2O$$

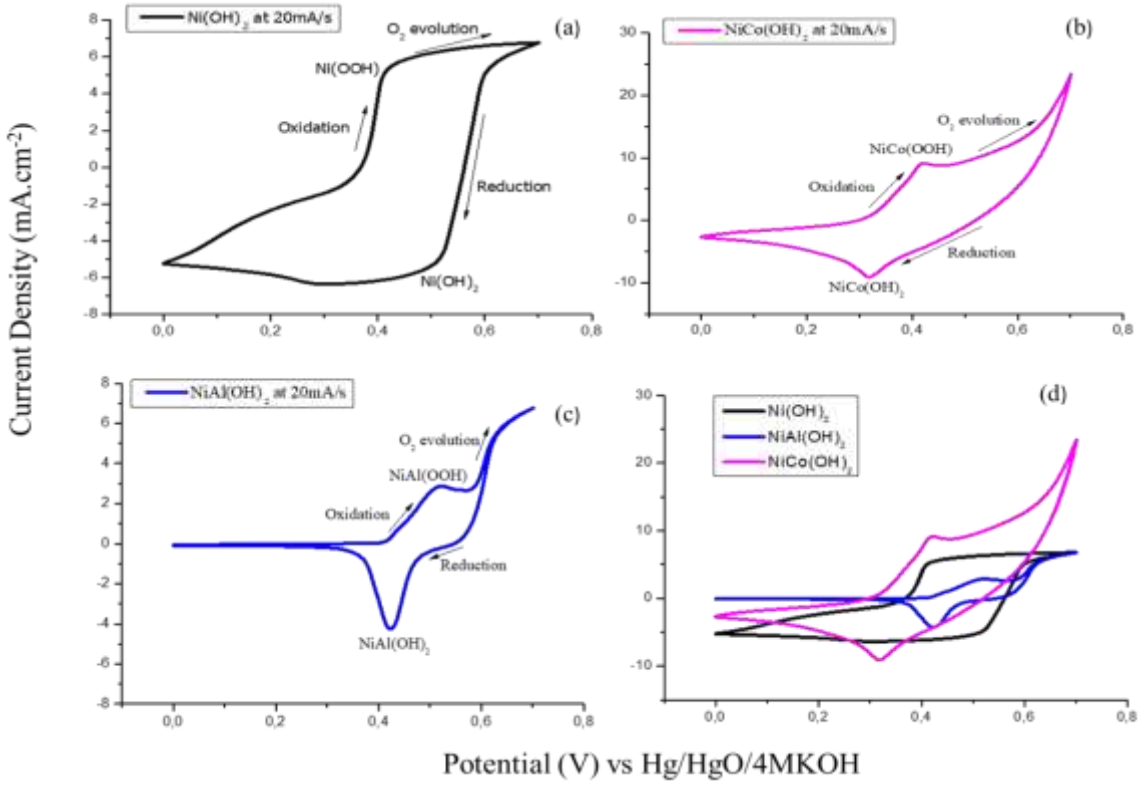

Figure 4-6: Cyclic voltammogram of (a) $Ni(OH)_2$, (b) $Ni_{0.95}Co_{0.05}(OH)_2$ (c) $Ni_{0.9}Al_{0.1}(OH)_2$, (d) Overlapped [(a), (b), and (c)] curves.

As the hydroxide ions arrive in the $Ni(OH)_2$ layer alkaline solution interface, may be facilitated by Equation 4-7 and Equation 4-8. According to Zimmerman and Effa (Zimmerman and Effa, 1984), Equation 4-8 may be rate-limiting and appears to be more consistent with diffusion of OH^- between the bulk electrolyte and the active material surface as the rate-liming step for high rate electrode operation, particularly at reduced concentrations of OH^-.

A sharp cathodic and anodic peaks were obtained in the partial substituted Co^{2+} (Figure 4-6b) and Al^{3+} (Figure 4-6c) $Ni(OH)_2$ electrodes as compared to the broader redox peaks for the pure $Ni(OH)_2$ (Figure 4-6a). It can be noted that the partial substitution of Co^{2+} and Al^{3+} for $Ni(OH)_2$ allowed the separation of anodic/cathodic peaks of the material and oxygen evolution. It can also be noted that the oxygen evolution has shifted to a more negative potential, making it easier to identify the cathodic and anodic peak potentials. On the hypothesis that the reduced charge acceptance of $Ni(OH)_2$ positive electrode is related to a relatively long distance between nickel hydroxide particles and the nearest portion of the substrate (Begum *et al.*, 2009); the potential difference between anodic and cathodic peaks was calculated. The potential difference between anodic and cathodic peaks was used as a measure of the reversibility of electrochemical redox reactions, and the higher the reversibility, the smaller the value of the anodic and cathodic peaks potential difference will be (Yang, LJ *et al.*, 2007). The oxidation and reduction potential peaks of the partial substituted Co^{2+} electrode is located at 0.419V and 0.319V,

respectively. While the oxidation and reduction potential peaks of the partial substituted Al^{3+} electrode shifted to the more positive position at 0.518V and 0.424V. Therefore, the redox peak differences were found to be 0.10V and 0.094V, respectively, illustrating that the partial substituted Al^{3+} electrode is more reversible than the partial substituted Co^{2+} electrode.

The partial substitution of Al^{3+} for Ni^{2+} has been reported (Yang, LJ *et al.*, 2007; Huang, Jichun *et al.*, 2013). The authors reported a formation of a mixed-phase (α/β), and the two anodic peak and cathodic peaks were observed. These peaks were attributed to the conversion of β-$Ni(OH)_2$ to β-NiOOH, and the additional anodic and cathodic peaks were attributed to the conversion between α-$Ni(OH)_2$ to γ-NiOOH. However, in the current report, single anodic/cathodic peaks were observed. This may indicate that the obtained α'-phase corresponds to the hexagonal lattice structure of nickel aluminium oxide hydrate, $Ni_5Al_4O_{11} \cdot 18H_2O$ (JCP-No 00-022-0452). These finds are in good agreement with the results obtained by XRD, FTIR, and TG-DTA above. Therefore, electro oxidation-reduction process (Figure 4-6c) may be assumed to follow the conversion of β-Ni(II) to β-Ni (III) (Equation 4-1), while both pure β-$Ni(OH)_2$ in Figure 4-6a and β-$Ni_{0.95}Co_{0.05}(OH)_2$ (Figure 4-6b) follows Equation 4-7 and Equation 4-8.

On the assumption that the poor capacities of the electrodes are attributable to a low efficiency resulting from competitive reactions of the oxidation of the active material and the evolution of oxygen reaction (OER) (Begum *et al.*, 2009), the Co^{2+} and Al^{3+} were used as dopants materials for β-$Ni(OH)_2$ material. Both the dopants (Co^{2+} and Al^{3+}) were optimised using compositions of 5wt.%, 10wt.%, 25wt.%, and 50wt.%. The electrodes were prepared as mentioned in Section 4.3.4 above. The prepared electrodes were cycled 20 times at 25mA, and the specific discharged capacities were calculated from the chrono charge-discharge galvanostatic (CCDG) curves using Equation 4-9.

Equation 4-9: Specific discharge capacity formula

$$\text{Specific discharge capacity} = \frac{\text{Applied current (mA)x Discharge time (h)}}{\text{Loading mass (g) of the active material}}$$

The obtained electrochemical performance of the materials is presented in Figure 4-7. As demonstrated in Figure 4-7a and Figure 4-7b, respectively, the material with 5wt.% Co^{2+} and 10wt.% Al^{3+} showed optimal percentages with promising electrochemical properties over 20 cycles. The charge state and discharge state at the 20th cycles are shown in Figure 4-7c-d. Both curves illustrate two flat charges (Figure 4-7c) and two flat discharge (Figure 4-7d) plateau for both β-$Ni(OH)_2$ and β-$Ni_{0.95}Co_{0.05}OH_2$ electrodes indicating that two redox systems are involved in electrochemical reactions. The two discharged plateaus are observed at 0.360V and 0.266V, and 0.344V and 0.225V for both the pure β-$Ni(OH)_2$ and β-$Ni_{0.95}Co_{0.05}(OH)_2$, respectively. The first plateaus on both pure β-$Ni(OH)_2$ and β-$Ni_{0.95}Co_{0.05}(OH)_2$ curves may be an indication of Equation 4-7, while the second plateaus may be an

indication of Equation 4-8 formation (Carbonio *et al.*, 1982; Zimmerman and Effa, 1984). The α/ β-$Ni_{0.9}Al_{0.01}(OH)_2$ electrode demonstrated one discharge plateau at 0.259V, which could be an indication of Equation 4-1 formation (Carbonio *et al.*, 1982). These findings are in good agreement with the CV results reported above, which could be explained by assuming the multistage reduction process presented in Equation 4-7 and Equation 4-8.

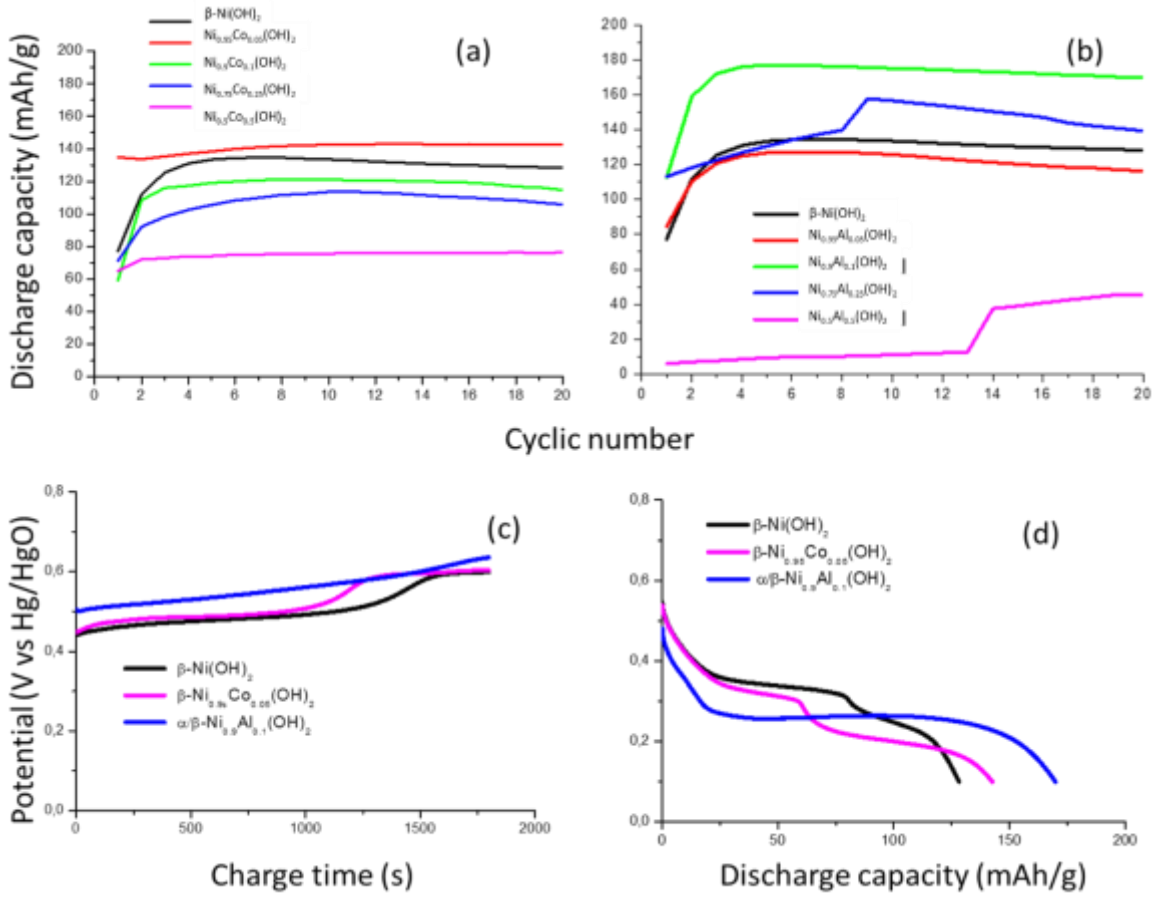

Figure 4-7: Optimization discharge capacities of (a) partial Co^{2+} substituent, (b) partial Al^{3+} substituent, and $Ni(OH)_2$, $Ni_{0.95}Co_{0.05}(OH)_2$, $Ni_{0.9}Al_{0.1}(OH)_2$ (c) charge potential at 20 cycle, (d) Discharge curve at 20 cycle

As presented in Figure 4-7d, the first discharge plateaus were about 0.360V and 0.344V for $Ni(OH)_2$ and $Ni_{0.95}Co_{0.05}OH_2$ electrodes, respectively and were much higher than that of the Al substituted $Ni(OH)_2$ electrode (0.277V). According to Huang and co-workers (Yang, LJ *et al.*, 2007), this could be attributed to the unique two phases (α/β) structure providing fast ion and electron transfer, and good electrochemical activity (Huang, Jichun *et al.*, 2013), which might be favourable to the proton diffusion during charge−discharge processes. Furthermore, the partial substitution of Al^{3+} enhances the discharge output of the $Ni(OH)_2$ electrode with a discharge capacity of 170 mAh/g and coulombic efficiency of

93%. It also promotes complete oxidation of $Ni(OH)_2$ electrode, and these results were in agreement with the cyclic voltammetry reported above. The discharge capacities for pure β-$Ni(OH)_2$ and β-$Ni_{0.95}Co_{0.05}(OH)_2$ were 128 mAh/g and 142 mAh/g with a coulombic efficiency of 87% and 80%, respectively

4.5 Conclusion

β-$Ni(OH)_2$, β-$Ni_{0.95}Co_{0.05}(OH)_2$, and α/ β-$Ni_{0.9}Al_{0.01}(OH)_2$ were synthesised by co-precipitation followed by hydrothermal treatment. The crystal structure, functional groups present in the materials, thermal analysis, surface areas and pore sizes, elemental compositions were confirmed using XRD, FTIR, TG-DTA, BET and BHJ, and SEM/EDS and ICP-OES, respectively. XRD, FTIR, TG-DTA confirmed the formation of β-phase of pure $Ni(OH)_2$, the β-phase of the partial substituted Co^{2+} for Ni^{2+} in $Ni(OH)_2$ material, and the formation of mixed α/β-phase for the partial substituted Al^{3+} for Ni^{2+} in $Ni(OH)_2$ material. The BET surface areas ranged between 86.81 m^2/g to 361.92 m^2/g, and the BHJ average pore size adsorption ranged from 5.36 nm to 8.69 nm. Both ICP-OES and SEM-EDS further confirm the formation of the intended compositions of $Ni_{0.9}Al_{0.1}(OH)_2$ and $Ni_{0.95}Co_{0.05}(OH)_2$. The sample with partial Al^{3+} exhibited the maximum discharge capacity of 170 mAh/g, corresponding to a coulombic efficiency of 93%. Aluminium has a significantly lower cost than nickel; therefore, gaining capacity by partial substitution of Ni^{2+} for the less expensive Al^{3+} may be a cost reduction for $Ni(OH)_2$ NiFe battery. While pure $Ni(OH)_2$ and the electrode with partial Co^{2+} substituted $Ni(OH)_2$ showed discharge capacities of 128mAh/g and 143 mAh/g corresponding to coulombic efficiencies of 87% and 80%, respectively. The relationship between structural and electrochemical properties of the material is not well understood. However, according to Huang *et al.,* 2013 (Huang, Jichun *et al.*, 2013) the physical properties of $Ni(OH)_2$, such as specific surface area and chemical compositions, are strongly influencing the performance of the positive $Ni(OH)_2$ electrodes. In this study, it is observed that the lower the surface area, the better the specific discharge capacity. E.g., The discharge capacities increases in the order of pure β-$Ni(OH)_2$ (128 mAh/g) > β-$Ni_{0.95}Co_{0.05}(OH)_2$ (142 mAh/g) > α/β-$Ni_{0.9}Al_{0.1}(OH)_2$ (170 mAh/g), while the specific BET surface area was decreasing in order of β-$Ni(OH)_2$ (361.92 m^2/g) > β-$Ni_{0.95}Co_{0.05}(OH)_2$ (125.15 m^2/g) > α/β- $Ni_{0.9}Al_{0.1}(OH)_2$ (86.81 m^2/g). These results are contrary to what is commonly observed. Usually, a higher surface area gives better performance. However, the authors of the current manuscript do acknowledge that the surface area accessible for gas molecules does not necessarily represent the electrochemically active surface area. The future work will focus on more comprehensive cycling stability of the electrodes over more cycles.

4.6 Acknowledgements

The authors would like to acknowledge the financial and strategic support from the Department of Science and Innovation of South Africa, Eskom Research, Testing and Development (R, T&D) Department of South Africa, and the National Research Foundation of South Africa (Grant Number: 121413).

4.7 References

Begum, S. N., Muralidharan, V. and Basha, C. A. (2009). The influences of some additives on electrochemical behaviour of nickel electrodes. International Journal of Hydrogen Energy 34(3): 1548-1555.

Blasco-Ahicart, M., Soriano-López, J., Carbó, J. J., Poblet, J. M. and Galan-Mascaros, J. R. (2018). Polyoxometalate electrocatalysts based on earth-abundant metals for efficient water oxidation in acidic media. Nature Chemistry 10(1): 24.

Bresser, D., Buchholz, D., Moretti, A., Varzi, A. and Passerini, S. (2018). Alternative binders for sustainable electrochemical energy storage–the transition to aqueous electrode processing and bio-derived polymers. Energy and Environmental Science 11(11): 3096-3127.

Carbonio, R., Macagno, V., Giordano, M., Vilche, J. and Arvia, A. (1982). A transition in the kinetics of the $Ni(OH)_2$/NiOOH electrode reaction. Journal of the Electrochemical Society 129(5): 983-991.

Coudun, C., Grillon, F. and Hochepied, J. F. (2006). Surfactant effects on pH-controlled synthesis of nickel hydroxides. Colloids and Surfaces A: Physicochemical and Engineering Aspects 280(1-3): 23-31.

Falahati, H., Kim, E. and Barz, D. P. (2015). Fabrication and characterization of thin film nickel hydroxide electrodes for micropower applications. American Chemical Society: Applied Materials and Interfaces 7(23): 12797-12808.

Gonçalves, J. M., Alves, K. M., Gonzalez-Huila, M. F., Duarte, A., Martins, P. R. and Araki, K. (2018). Unexpected Stabilization of α-$Ni(OH)_2$ Nanoparticles in GO Nanocomposites. Journal of Nanomaterials 2018: 13.

Hall, D. S., Lockwood, D. J., Bock, C. and MacDougall, B. R. (2015). Nickel hydroxides and related materials: a review of their structures, synthesis and properties. Proceedings of the Royal Society A: Mathematical, Physical and Engineering Sciences 471(2174): 20140792.

Holmberg, F. (2017). Recycling of nickel metal hydride (NiMH) batteries. Chalmers University of Technology.

Huang, J., Cao, D., Lei, T., Yang, S., Zhou, X., Xu, P. and Wang, G. (2013). Structural and electrochemical performance of Al-substituted β-$Ni(OH)_2$ nanosheets electrodes for nickel metal hydride battery. Journal of Electrochimica Acta 111: 713-719.

Kovalenko, V., Kotok, V., Sykchin, A., Mudryi, I., Ananchenko, B., Burkov, A., Sololvov, V., Deabate, S., Mehdi, A. and Bantignies, J.-L. (2017). Nickel hydroxide obtained by high-temperature two-step synthesis as an effective material for supercapacitor applications. Journal of Solid State Electrochemistry 21(3): 683-691.

Lassoued, A., Lassoued, M. S., Karolak, F., García-Granda, S., Dkhil, B., Ammar, S. and Gadri, A. (2017). Synthesis, structural, optical, morphological and magnetic characterization of copper substituted nickel ferrite ($Cu_xNi_{1-x}Fe_2O_4$) through co-precipitation method. Journal of Materials Science: Materials in Electronics 28(24): 18480-18488.

Liu, L., Hou, Y., Gao, Y., Yang, N., Liu, J. and Wang, X. (2019). Co doped α-$Ni(OH)_2$ multiple-dimensional structure electrode material. Journal of Electrochimica Acta 295: 340-346.

Luan, C., Liu, G., Liu, Y., Yu, L., Wang, Y., Xiao, Y., Qiao, H., Dai, X. and Zhang, X. (2018). Structure effects of 2D materials on α-Nickel hydroxide for oxygen evolution reaction. American Chemical Society: Nano 12(4): 3875-3885.

Motlagh, M. K., Youzbashi, A. and Sabaghzadeh, L. (2011). Synthesis and characterization of nickel hydroxide/oxide nanoparticles by the complexation-precipitation method. International Journal of Physical Sciences 6(6): 1471-1476.

Oh, S. H., Black, R., Pomerantseva, E., Lee, J.-H. and Nazar, L. F. (2012). Synthesis of a metallic mesoporous pyrochlore as a catalyst for lithium-O_2 batteries. Nature Chemistry 4(12): 1004-1010.

Shanaj, B. and John, X. (2016). Effect of calcination time on structural, optical and antimicrobial properties of nickel oxide nanoparticles. Journal of Theoretical Computer Science 3(2).

Su, Y.-Z., Xiao, K., Li, N., Liu, Z.-Q. and Qiao, S.-Z. (2014). Amorphous $Ni(OH)_2$ @ three-dimensional Ni core–shell nanostructures for high capacitance pseudocapacitors and asymmetric supercapacitors. Journal of Materials Chemistry A 2(34): 13845-13853.

Suntivich, J., May, K. J., Gasteiger, H. A., Goodenough, J. B. and Shao-Horn, Y. (2011). A perovskite oxide optimized for oxygen evolution catalysis from molecular orbital principles. Science 334(6061): 1383-1385.

Wang, H., Lee, H.-W., Deng, Y., Lu, Z., Hsu, P.-C., Liu, Y., Lin, D. and Cui, Y. (2015). Bifunctional non-noble metal oxide nanoparticle electrocatalysts through lithium-induced conversion for overall water splitting. Journal of Nature Communications 6(1): 1-8.

Wang, H., Liang, Y., Gong, M., Li, Y., Chang, W., Mefford, T., Zhou, J., Wang, J., Regier, T. and Wei, F. (2012). An ultrafast nickel–iron battery from strongly coupled inorganic nanoparticle/nanocarbon hybrid materials. Journal of Nature Communications 3: 917.

Wang, X., Luo, H., Yang, H., Sebastian, P. and Gamboa, S. (2004). Oxygen catalytic evolution reaction on nickel hydroxide electrode modified by electroless cobalt coating. International Journal of Hydrogen Energy 29(9): 967-972.

Wiston, B. R. and Ashok, M. (2019). Electrochemical performance of hydrothermally synthesized flower-like α-nickel hydroxide. Vacuum 160: 12-17.

Yang, L., Gao, X., Wu, Q., Zhu, H. and Pan, G. (2007). Phase distribution and electrochemical properties of Al-substituted nickel hydroxides. The Journal of Physical Chemistry C 111(12): 4614-4619.

Young, K.-H., Wang, L., Yan, S., Liao, X., Meng, T., Shen, H. and Mays, W. (2017). Fabrications of high-capacity alpha-Ni$(OH)_2$. Batteries 3(1): 6.

Young, K., Wang, L., Mays, W., Reichman, B., Chao-Ian, H., Wong, D. and Nei, J. (2018). Nickel hydroxide positive electrode for alkaline rechargeable battery, Google Patents.

Yu, J., Pan, S., Zhang, Y., Liu, Q. and Li, B. (2019). Facile synthesis of monodispersed α-Ni$(OH)_2$ microspheres assembled by ultrathin nanosheets and its performance for oxygen evolution reduction. Frontiers in Materials 6: 124.

Zheng, Y., Zhu, B., Chen, H., You, W., Jiang, C. and Yu, J. (2017). Hierarchical flower-like nickel (II) oxide microspheres with high adsorption capacity of Congo red in water. Journal of Colloid and Interface Science 504: 688-696.

Zimmerman, A. and Effa, P. (1984). Discharge kinetics of the nickel electrode. Journal of the Electrochemical Society 131(4): 709-713.

CHAPTER 5

5 Synthesis, Structural Characterization, and Electrochemical Properties of the Mg and Mn Doped-Ni$(OH)_2$ for Use as Active Cathode Materials in Ni-Fe Batteries.

THIS CHAPTER HAS BEEN PUBLISHED:

Zide, D., Felix, C., Oosthuysen, T. and Bladergroen, B.J., 2021. Synthesis, structural characterization, and electrochemical properties of the Mg and Mn doped-Ni $(OH)_2$ for use as active cathode materials in Ni-Fe batteries. *Journal of Electroanalytical Chemistry*, p.115418.

5.1 Abstract

$Ni(OH)_2$ is one of the most interesting electrode substances for high-performance nickel-iron batteries owing to its low cost, high specific capacitance, and environmental compatibility. However, the $Ni(OH)_2$ cathode electrode exhibits poor performance due to (i) competitive reactions such as the oxidation of the active material and oxygen evolution. (ii) the reduced charge acceptance of the $Ni(OH)_2$ positive electrode is related to a relatively long distance between the $Ni(OH)_2$ particles and the nearest portion of the substrate. In this study, β-$Ni(OH)_2$ is used as a starting material. Then, the Ni^{2+} in the compound β-$Ni(OH)_2$ material is partially substituted with Mg^{2+} and Mn^{2+}, separately, and the performance of the as-prepared materials was optimized and examined. XRD, FTIR, TG-DTA, SEM/EDS, and ICP-OES confirmed the formation of the expected compositions. The $Ni_{0.95}Mg_{0.05}(OH)_2$ and $Ni_{0.9}Mn_{0.1}(OH)_2$ based-samples were optimal compositions with promising electrochemical activities. The partial substitution of Mg^{2+} allowed separation of anodic/cathodic peaks and oxygen evolution. For example, the anodic and cathodic peaks are easier to identify because their potential shifted to more negative potentials. When using three-electrode configurations, the un-doped $Ni(OH)_2$ electrode discharge capacity showed a reduction of 76 % after the 100^{th} cycle. In contrast, the $Ni_{0.95}Mg_{0.05}(OH)_2$ and $Ni_{0.9}Mn_{0.1}(OH)_2$ electrode demonstrated a reduction of only 15% and 12% in discharge capacities after 100^{th} cycles, respectively. When using a two-electrode configuration, the obtained discharge capacities were 40 mAh/g for the un-doped $Ni(OH)_2$ electrode, 120 mAh/g for the $Ni_{0.95}Mg_{0.05}(OH)_2$ electrode, and 159 mAh/g for the $Ni_{0.9}Mn_{0.1}(OH)_2$ electrode with an electrode cycle life of 43.49 %, 88.24 %, 88.54 %, respectively.

Key Words: β-nickel hydroxide; β-nickel magnesium hydroxide; nickel manganese hydroxide; NiFe battery; positive nickel electrode

5.2 Introduction

$Ni(OH)_2$ is an interesting electrode substance for high-performance NiFe batteries due to its low cost, high specific capacitance, and environmental compatibility (Yin *et al.*, 2019). Structurally, the α- and β-phases are typical polymorphic forms of layered $Ni(OH)_2$ (Lee, Jeong Woo *et al.*, 2011). α-$Ni(OH)_2$ is the metastable phase and displays a higher theoretical capacitance than β-$Ni(OH)_2$. However, α-$Ni(OH)_2$ tends to convert to β-$Ni(OH)_2$ in alkaline solution or when subjected to charge-discharge cycles (Lee, Jeong Woo *et al.*, 2011). Due to instability of the α-$Ni(OH)_2$ in alkaline solution or when subjected to charge-discharge processes, β-$Ni(OH)_2$ is the most preferred active material over α-$Ni(OH)_2$ in the preparation of nickel-electrodes (Hall *et al.*, 2015; Posada and Hall, 2016; Zide *et al.*, 2020b, a). The β-$Ni(OH)_2$ is stable in strong alkaline electrolytes and has good reversibility when charged to β-NiOOH. Moreover, the β-NiOOH has a similar structure with a lattice constant of inter-sheet equal to 4.85Å; thus, the volume expansion associated with cycling is less than any other forms. However the overcharge of β-$Ni(OH)_2$ may result in the formation of γ-NiOOH which contains Ni^{4+} (Yang, LJ *et al.*, 2007; Hall *et al.*, 2015) with an average oxidation state of nickel in this phase of 3.3 −

3.7 (Yang, LJ *et al.*, 2007). A large volumetric change accompanies the conversion of β-Ni(OH)2 to γ-NiOOH, resulting in loss of contact between the active material and the conductive substrate causing fast capacity fading during charge-discharge cycling (Hall *et al.*, 2015).

The practical, specific capacity of the $Ni(OH)_2$ electrode depends on how well the $Ni(OH)_2$ particles are embedded within a conductive electron network allowing electrons to move between particles and the current collector (Begum *et al.*, 2009). The limited performance of the $Ni(OH)_2$ electrode is correspondingly suspected to be due to oxidation of the active material and the evolution of oxygen appearing in the same potential window (Wang, Xianyou *et al.*, 2004; Begum *et al.*, 2009). The reduced charge acceptance of $Ni(OH)_2$ positive electrode is suspected to be related to a relatively long distance between $Ni(OH)_2$ particles and the nearest portion of the substrate(Begum *et al.*, 2009).

Different modifiers and additives are used to enhance the performance of nickel-based electrodes. Various studies have revealed that the incorporation of divalent elements such as magnesium, cobalt, (Co) (Zhang, Yong *et al.*, 2020c; Zhang, Yong *et al.*, 2021), molybdenum (Mo) (Zhang, Yong *et al.*, 2015; Zhang, Yong *et al.*, 2018; Zhang, Yong *et al.*, 2020a; Zhang, Yong *et al.*, 2020b; Zhang, Yong *et al.*, 2020c), and zinc (Zn) can improve active material utilization and prevent the formation of γ-NiOOH (Young, Kwo-Hsiung *et al.*, 2017; Liu, Ling *et al.*, 2019; Yin *et al.*, 2019). Yuan *et al.* (Yuan *et al.*, 2016) report the electrochemical properties of a prepared porous pompon-like Mg-incorporated α-$Ni(OH)_2$ using a facile chemical co-precipitation method. The downside of α-$Ni(OH)_2$ it tends to convert to β-$Ni(OH)_2$ in an alkaline solution or when subjected to charge-discharge cycles (Lee, Jeong Woo *et al.*, 2011).

In the present study, the partial substitutions of Mn^{2+} and Mg^{2+} for Ni^{2+} in the β-$Ni(OH)_2$ active material were examined as potential additives to suppress the oxygen evolution side reaction, improve material utilization and discharge capacities of a positive electrode for the nickel-iron (Ni-Fe) battery. Mg^{2+} and Mn^{2+} are chosen as additives due to their low cost, safety, and excellent stability.

5.3 Material and methods

5.3.1 Materials

Sodium carbonate (99%), sodium hydroxide (98%), nickel nitrate hexahydrate, manganese sulfate monohydrate (99.9%), and magnesium nitrate hexahydrate (99%) were purchased from Sigma-Aldrich (South Africa). Carbon black, Super P Conductive (CAS number: 1333-86-4) was purchased from Alfa Aesar (United States). Coathylene binder was purchased from Axalta (United States). Nickel mesh was purchased from Q-Lite batteries (China). The $FeCu_{0.25}$ electrode was based on the in-house $FeCu_{0.25}$ material previously prepared, as reported (Tawonezvi *et al.*, 2020).

5.3.2 Synthesis of un-doped $Ni(OH)_2$, $Ni_{1-x}Mnx(OH)_2$ and $Ni1-xMgx(OH)_2$ active material

The compositions of nickel-manganese ($Ni_{1-x}Mn_x(OH)_2$) and nickel-magnesium ($Ni_{1-x}Mg_x(OH)_2$) based active hydroxide materials were prepared using a co-precipitation method followed by hydrothermal treatment at pH = 14 (Zide *et al.*, 2020b). Ni^{2+} was partially substituted with Mn^{2+} as $Ni_{1-x}Mn_x(OH)_2$ and with Mg^{2+} as $Ni_{1-x}Mg_x(OH)_2$. Where "x" is the molar composition of Mn^{2+} and Mg^{2+} i.e., 0.05; 0.1; 0.25; and 0.5. The different feeding mole ratios of Ni^{2+} and Mn^{2+} is expressed as $Ni_{0.95}Mn_{0.05}(OH)_2$, $Ni_{0.9}Mn_{0.1}(OH)_2$, $Ni_{0.75}Mn_{0.25}(OH)_2$, and $Ni_{0.5}Mn_{0.5}(OH)_2$ for the partially substituted manganese; and $Ni_{0.95}Mg_{0.05}(OH)_2$, $Ni_{0.9}Mg_{0.1}(OH)_2$, $Ni_{0.75}Mg_{0.25}(OH)_2$, and $Ni_{0.5}Mg_{0.5}(OH)_2$, for the partially substituted magnesium. The typical process flow diagram for the synthesis of the active materials is shown in Figure 5-1. The un-dope $Ni(OH)_2$ was prepared as described in our early published article (Zide *et al.*, 2020a, b).

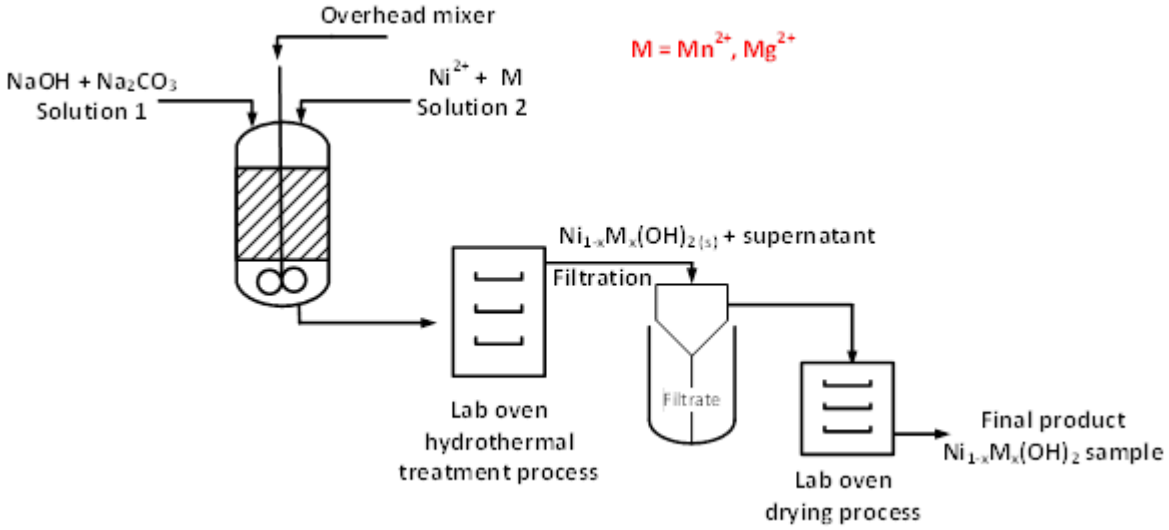

Figure 5-1: Process flow diagram of the active production.

Briefly, two solutions were prepared where solution 1 contained NaOH and Na_2CO_3, and solution 2 had Ni^{2+} as $Ni(NO_3)_2{\cdot}6H_2O$ salt, and Mn^{2+} as $MnSO_4{\cdot}H_2O$ salt for the Ni-Mn composite hydroxides preparation. The two solutions were mixed dropwise under vigorous stirring at room temperature. The slurry was further agitated at room temperature for 30 min and thereafter subjected to hydrothermal treatment at 65 °C for 18 h. The resulting precipitates were cooled at room temperature then filtered and washed with Milli-Q water. The precipitated samples were dried at 110 °C for 12 h. The exact procedure was used to prepare the Ni-Mg composite hydroxides, and the $Mg(NO_3)_2{\cdot}6H_2O$ salt was used to prepare solution 2 as a source of Mg^{2+}.

5.3.3 Structural and morphological characterization of the materials

The diffraction patterns were collected using a multi-purpose X-ray Diffractometer D8-Advance from BRUKER AXS (Germany). Bragg's law (Equation 5-1) was used to calculate the cell parameters of the

materials where n is the order number, λ is the wavelength (1.54098 Å), d is the basal spacing (Å) and θ is the maximum diffraction angle (˚).

Equation 5-1: Bragg's law

$$n\lambda = 2d \sin\theta$$

The functional groups present in the materials were identified using a Fourier Transform Infra-Red Spectrum II spectrometer (UATR-FTIR, Llantrisant UK). The thermal analysis was studied using a Perkin-Elmer (8000 instrument) thermal gravimetric analysis coupled with differential thermal analysis (TGA-DTA). Surface areas were analyzed using Brunauer-Emmett-Teller (BET) nitrogen adsorption isotherms and adsorption pore size using Barrett-Joyner-Halenda (BHJ). The morphologies of the synthesized materials were confirmed using scanning electron microscopy (SEM). The elemental compositions were determined using inductively coupled plasma equipped with optical emission spectroscopy (ICP-OES). To further confirm the elemental composition, SEM equipped with energy dispersive spectroscopy (SEM/EDS) was used.

5.3.4 Fabrication of electrodes

The nickel electrodes were prepared for specific capacities analysis by mixing 85 wt.% active material, 5 wt.% carbon black, and 10 wt.% cocaethylene binder thoroughly. The mixture was transferred onto a pre-cut nickel mesh and hot-pressed at 80˚C at 61 kg/cm^2 (~6 MPa). A custom-designed hydraulic press with integrated heated press plates (HyJack, Cape Town) was used to hot pressed the desired electrode for 5 min to ensure good electrical contact between the nickel mesh and the active material. Electrode dimensions were kept at 1cm × 1cm for all the samples.

The nickel electrodes were also prepared for cyclic voltammetry (CV) analysis using a pine rotating disc electrode (RDE) with a 0.196 cm^2 working area. The electrode was cleaned and polished using 0.05 µm deagglomerated alumina paste (Buehler) before and after each use. It was then ultrasonicated in ultrapure water for 15 min. The electrode was dried for 15 min at 2,500 rotations per minute (rpm) at ambient conditions. The catalyst ink was prepared by combining 13 mg active material with 50 µL (5 wt. %) Nafion® solution (Alfa Aesar) and 1,950 µL ultrapure water. The mixture was ultrasonicated for 20 min. A micropipette was used to drop 30 µL of the catalyst ink onto the RDE. The working electrode was covered and dried overnight at ambient conditions. A catalyst loading of 1 mg per cm^2 was obtained.

5.3.5 Electrochemical characterization

The electrochemical properties of the un-doped $Ni(OH)_2$, $Ni_{1-x}Mg_x(OH)_2$, and $Ni_{1-x}Mn_x(OH)_2$ materials were first tested using a three-electrode configuration. A three-electrode system consisting of the as-prepared un-doped $Ni(OH)_2$, $Ni_{1-x}Mg_x(OH)_2$, and $Ni_{1-x}Mn_x(OH)_2$ materials were used as the working

electrodes, a graphite sheet (3cm x 4cm) as the counter electrode, Hg/HgO/4M KOH as the reference electrode and a KOH solution (4M) as the electrolyte. All tests were carried out at room temperature. Cyclic voltammetry (CV) was used to identify redox couples' active materials. The chrono-charge discharge galvanostatic (CCDG) was used for the capacities and cycling stability of the functional materials. Electrochemical characterization was performed using the Metrohm Auto Lab PGSTAT302N. The specific discharge capacities were calculated using Equation 5-2

Equation 5-2: Specific discharge capacity formula

$$\text{Specific discharge capacity} = \frac{\text{Applied current (mA)x Discharge time (h)}}{\text{Loading mass (g) of the active material}}$$

$Ni(OH)_2$and the best performing doped electrodes were further cycled on a NEWARE BTS-400 battery-tester using a two-electrode system to evaluate the material's performance further. A two-electrode system consisting of the as-prepared un-doped $Ni(OH)_2$, $Ni_{0.95}Mg_{0.05}(OH)_2$ and $Ni_{0.9}Mn_{0.1}(OH)_2$ materials were used as the cathode electrodes, an inhouse $FeCu_{0.25}$ electrode previously prepared as reported (Tawonezvi *et al.,* 2020) was used as the anode and a 6M KOH/1M LiOH solution as the electrolyte. All tests were carried out at room temperature. The anode was used as an excess in a ratio of 5:1 ($FeCu_{0.25}$ anode: nickel-based cathode). The cycling stability and discharge rate capability were performed. Current-limiting charge-discharge of 150mA/g - 100mA/g and a voltage window of 1.75V - 0.7V was used.

The addition of lithium to the electrolyte is vital but not fully understood. According to literature reports (Subbaraman *et al.,* 2011; Hill and Choi, 2012; Kenney *et al.*, 2013; Ding *et al.*, 2015; Han *et al.,* 2019), lithium hydroxide improves cell capacity, cyclic stability and facilitates nickel electrode kinetics. It also inflates the working plateau on charge and delays oxygen evolution. The electrolyte remains essentially invariant and plays no part in the overall reaction of the Ni-Fe battery during charge-discharge. However, the individual electrode reactions do involve an intimate reaction with the electrolyte (Tsais and Chan, 2013).

5.4 Results and Discussion

5.4.1 Structural characterization of the un-doped $Ni(OH)_2$, $Ni_{1-x}Mn_x(OH)_2$ and $Ni_{1-x}Mg_x(OH)_2$ active material

Figure 5-2 shows the diffractograms of the $Ni_{1-x}Mg_x(OH)_2$ powders compared with the un-doped $Ni(OH)_2$ material. Figure 5-2 also provides the standard peaks of β-phase $Ni(OH)_2$ (JCPDS No. 00-014-0117) and β-$Mg(OH)_2$ (JCPDS No. 01-075-1527). Both the un-doped $Ni(OH)_2$ (Figure 5-2a) and $Ni_{1-x}Mg_x(OH)_2$ (Figure 5-2b-e) materials were indexed to β-$Ni(OH)_2$ (JCPSD No 00-014-0117) and β-

$Mg(OH)_2$ (JCPSD No-01-075-1527). This may be because the β-$Ni(OH)_2$ is isostructural to the brucites β-$Mg(OH)_2$ structure, and both have a hexagonal lattice structure (Hall *et al.*, 2015).

Overlapping peaks were noticed for the $Ni_{1-x}Mg_x(OH)_2$ (Figure 5-2b-e) materials; this may be illustrating that the partial substituted Mg^{2+} may be incorporated into the lattice of β-$Ni(OH)_2$, resulting in a slight shift of the peak position (Hall *et al.*, 2015; Miao *et al.*, 2015; Yin *et al.*, 2019) as perceived at the diffraction angle at around 19.8°. Yin et al. (Yin *et al.*, 2019) reported the peak shift at the diffraction angle at approximately 19.8° due to water molecules and anions in the interlayer space or magnesium doping.

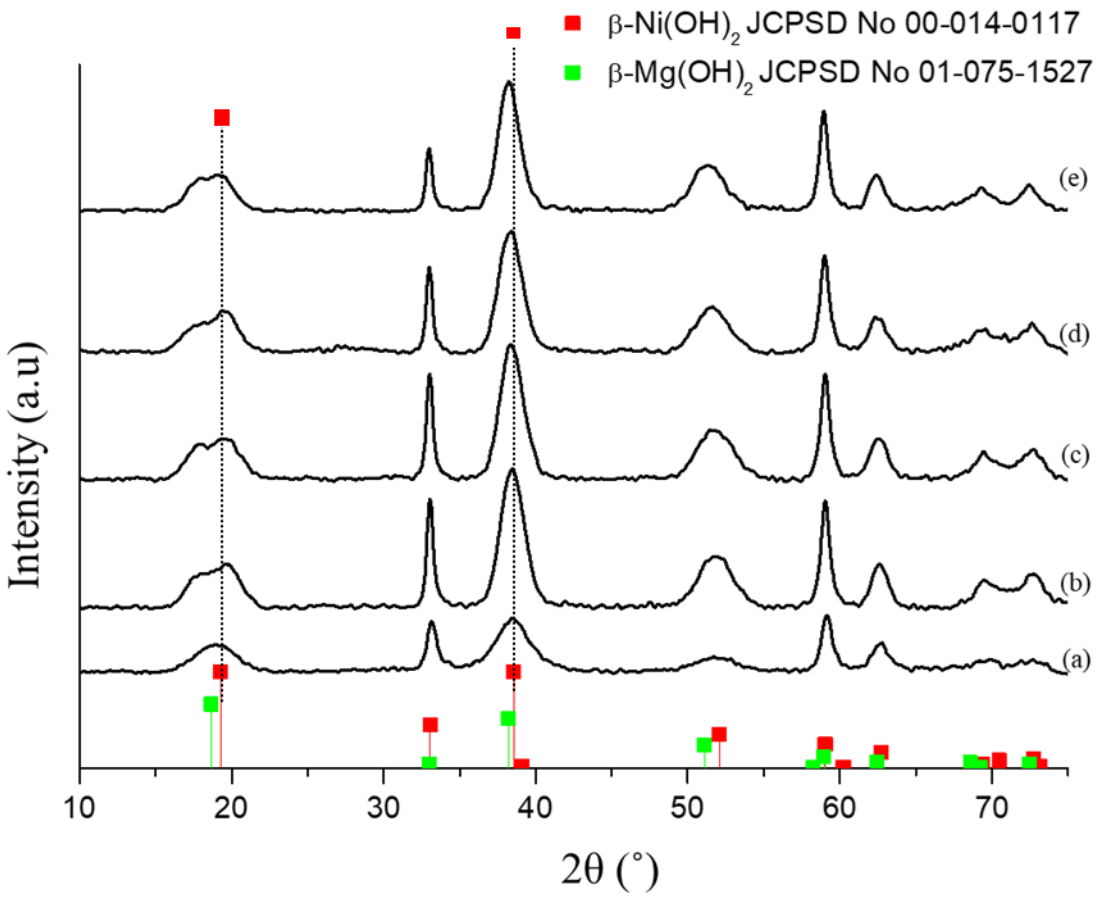

Figure 5-2: Diffractograms of (a) un-doped $Ni(OH)_2$, (b) $Ni_{0.95}Mg_{0.05}(OH)_2$, (c) $Ni_{0.9}Mg_{0.1}(OH)_2$, (d) $Ni_{0.75}Mg_{0.25}(OH)_2$ and (e) $Ni_{0.5}Mg_{0.5}(OH)_2$

The standard peaks of β-phase $Ni(OH)_2$ (JCPDS No. 00-014-0117), α-phase $Ni(OH)_2$ (JCPDS No. 00-038-7215) and $Mn(OH)_2$ (JCPDS No. 01-073-1604) along with the XRD spectra of the $Ni_{1-x}Mn_x(OH)_2$ materials compared with un-doped $Ni(OH)_2$ are presented in Figure 5-3.

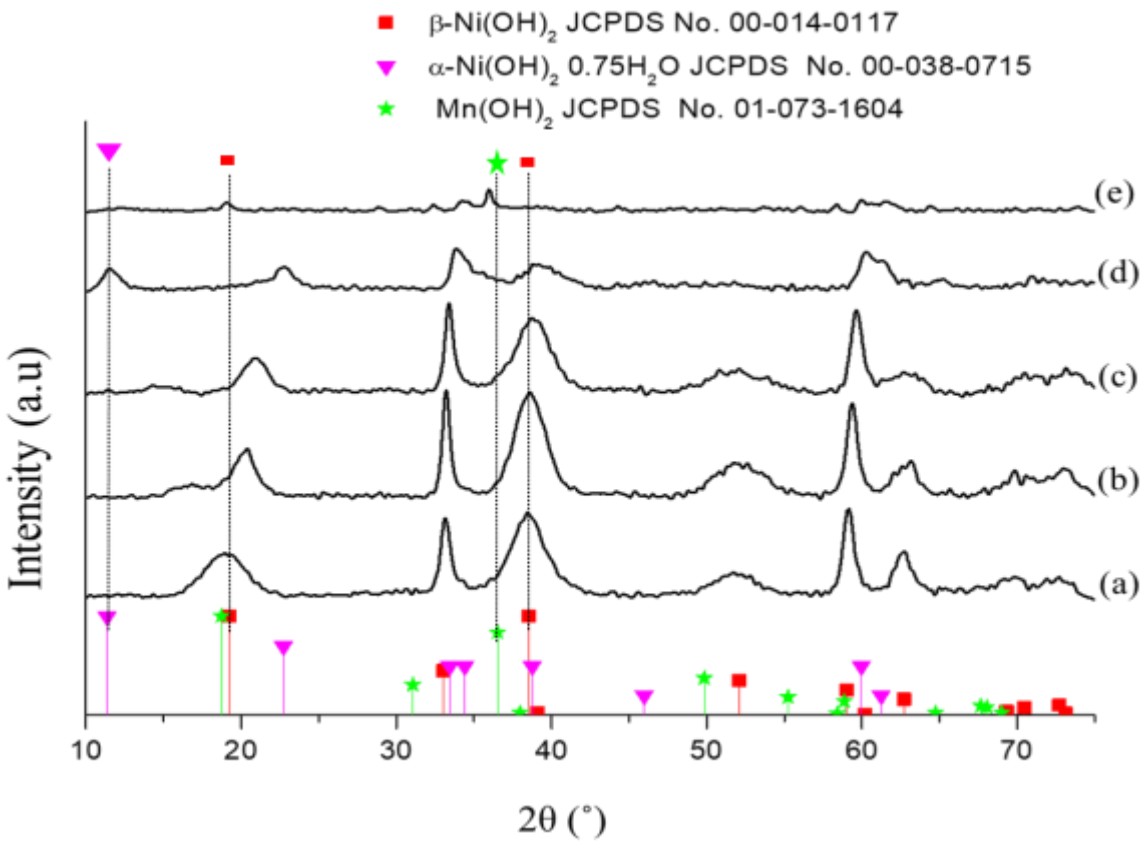

Figure 5-3: Diffractograms of (a) $Ni(OH)_2$, (b) $Ni_{0.95}Mn_{0.05}(OH)_2$, (c) $Ni_{0.9}Mn_{0.1}(OH)_2$, (d) $Ni_{0.75}Mn_{0.25}(OH)_2$ and (e) $Ni_{0.5}Mn_{0.5}(OH)_2$

Interestingly, from the obtained spectra, the partial substitution of Mn^{2+} for Ni^{2+} was the main factor that affected the phase formation of the prepared composite materials. The XRD pattern for the un-doped β-$Ni(OH)_2$ in Figure 5-3a reveals a clear presence of the β-$Ni(OH)_2$ phase (JCPDS No. 00-014-0117) with all main peaks present and no sign of any α-$Ni(OH)_2$ phase.

The partial substitution of Mn^{2+} for Ni^{2+} at relatively small molar ratios appears to cause a shift of the peaks at the diffraction angle around 19.8° and 38° to a higher diffraction angle $Ni_{1-x}Mn_x(OH)_2$ composite materials (Figure 5-3b-c). This may be owing to water molecules, anions or Mn^{2+} doping in the interlayer space or an indication of the presence of a mixed-phase, in this case, it may be a mixture of β-phase $Ni(OH)_2$ (JCPDS No. 00-014-0117) and α-phase $Ni(OH)_2$ (JCPDS No. 00-038-7215).

When the molar ratio of Mn^{2+} was increased (Figure 5-3d), the formation of α-phase $Ni(OH)_2$ based material (JCPDS No. 00-038-7215) gained preference over the β-phase $Ni(OH)_2$ (JCPDS No. 00-014-0117). Further increase of the molar ratio of Mn^{2+} (Figure 5-3e) resulted in a more amorphous structure, which may be due to impurities in the sample or the non-uniform composition of the product. For example, while the diffraction peak at around 19.8° shows the presence of a β-$Ni(OH)_2$ (JCPDS No. 00-014-0117). The evident absence of a β-$Ni(OH)_2$ (JCPDS No. 00-014-0117) at a diffraction peak at

about 38° confirms that the product sample may not be purely a β-$Ni(OH)_2$ (JCPDS No. 00-014-0117). This diffraction peak at about 38° is a close fit for $Mn(OH)_2$ (JCPDS No. 01-073-1604). A typical α-phase of partially substituted manganese for nickel-based oxide/hydroxide is commonly reported in the literature (Chen, Hao *et al.*, 2014; Guo *et al.*, 2016; Liu, Hao *et al.*, 2020).

Table 3-2 summarizes the XRD lattice parameters a, c, and the interlayer distance (d-spacing) for the respective powders. The unit cell parameters a and c were calculated using the formulae $a = 2d_{110}$, and $c = d_{001}$; where d_{001} and d_{110} are the basal spacing at a miller index (hkl) of (001) and (110). The basal spacing/ the interlayer distance, "d," was obtained using Bragg's law equation (Equation 5-1), assuming hexagonal stacking (Wiston and Ashok, 2019).

Table 5-1: XRD lattice parameter a, c and d-spacing of the $Ni(OH)_2$, $Ni_{1-x}Mg_x(OH)_2$ and $Ni_{1-x}Mn_x(OH)_2$ materials

Sample name	**(001) 2θ (˚)**	**d001 (Å)**	**(110) 2θ (˚)**	**d110 (Å)**	**a (Å)**	**c (Å)**
$Ni(OH)_2$	19.21	4.62	59.11	1.56	3.12	4.62
$Ni_{0.95}Mg_{0.05}(OH)_2$	19.37	4.58	59.11	1.56	3.12	4.58
$Ni_{0.9}Mg_{0.1}(OH)_2$	19.37	4.58	59.02	1.56	3.12	4.58
$Ni_{0.75}Mg_{0.25}(OH)_2$	19.37	4.58	58.99	1.56	3.12	4.58
$Ni_{0.5}Mg_{0.5}(OH)_2$	19.37	4.58	59.11	1.56	3.12	4.58
$Ni_{0.95}Mn_{0.05}(OH)_2$	20.46	4.34	59.46	1.55	3.11	4.34
$Ni_{0.9}Mn_{0.1}(OH)_2$	20.74	4.28	59.77	1.55	3.11	4.28
$Ni_{0.75}Mn_{0.25}(OH)_2$	22.73	3.91	60.39	1.53	3.06	3.91
$Ni_{0.5}Mn_{0.5}(OH)_2$	19.12	4.64	60.01	1.54	3.08	4.64

The a-parameter was not affected by the partial substitution of Mg^{2+} compared to a slight decrease observed in the partially substituted Mn^{2+} composites when equated to an un-doped $Ni(OH)_2$. The lattice c-parameter was 4.62 Å for the un-doped $Ni(OH)_2$. A slight reduction was observed for all the $Ni_{1-x}Mg_x(OH)_2$ compositions, resulting in a constant value of 4.58 Å (Figure 5-2b-e). Contrary to $Ni_{1-x}Mn_x(OH)_2$ compositions, the obtained lattice parameter "c" was 4.34 Å, 4.28 Å, 3.91 Å, and 4.64 Å for $Ni_{0.95}Mn_{0.05}(OH)_2$, $Ni_{0.9}Mn_{0.1}(OH)_2$, $Ni_{0.75}Mn_{0.25}(OH)_2$, and $Ni_{0.5}Mn_{0.5}(OH)_2$, respectively. The intersheet distance, d, is equal to the lattice parameter, c ($c = d_{001}$) by definition (Hall *et al.*, 2015). Furthermore, the c-parameter is more significant (larger or smaller) if the interlayer space contains anionic impurities (Hall *et al.*, 2015). In this study, the value of interlayer distance, d, decreases slightly for the composition with partial Mg^{2+} (Figure 5-2b-e) and Mn^{2+} (Figure 5-3b-d). A significant increase was observed in the partially substituted Mn^{2+} composition (Figure 5-3e) compared to un-doped

$Ni(OH)_2$ presented in Figure 5-3a, which may be owed to the presence of remained anions, such as NO_3^- during the synthesis of the material (Hall *et al.*, 2015).

Figure 5-4 and Figure 5-5 show the FTIR spectra of $Ni_{1-x}Mg_x(OH_2$ and $Ni_{1-x}Mn_x(OH_2$ compared with un-doped $Ni(OH)_2$, respectively. The findings are in agreement with the obtained XRD results; the presence of the peaks at around 3600 cm^{-1} (Figure 5-4a-e) and (Figure 5-5a-c) is the confirmation of $Ni(OH)_2$ formation (Motlagh *et al.*, 2011; Shanaj and John, 2016), and these absorption bands are assigned to O-H stretching vibrations (Begum *et al.*, 2009; Su *et al.*, 2014; Hall *et al.*, 2015; Shanaj and John, 2016). It could be noted that the O-H stretching vibrations (Figure 5-5d-e) disappeared, which could be owing to a difference in structure, as also confirmed in the XRD spectra (Figure 5-3d-e). The peaks at around 1600 cm^{-1} are attributed to the bending vibration mode of H_2O molecules. The absorption bands at about 1300 cm^{-1}, 500 cm^{-1}, and 400 cm^{-1} are ascribed to the existence of interlayer nitrate anions (NO_3), Ni-O stretching vibrations, and an in-plane Ni-O-H bending vibration, respectively (Begum *et al.*, 2009; Su *et al.*, 2014; Hall *et al.*, 2015; Shanaj and John, 2016).

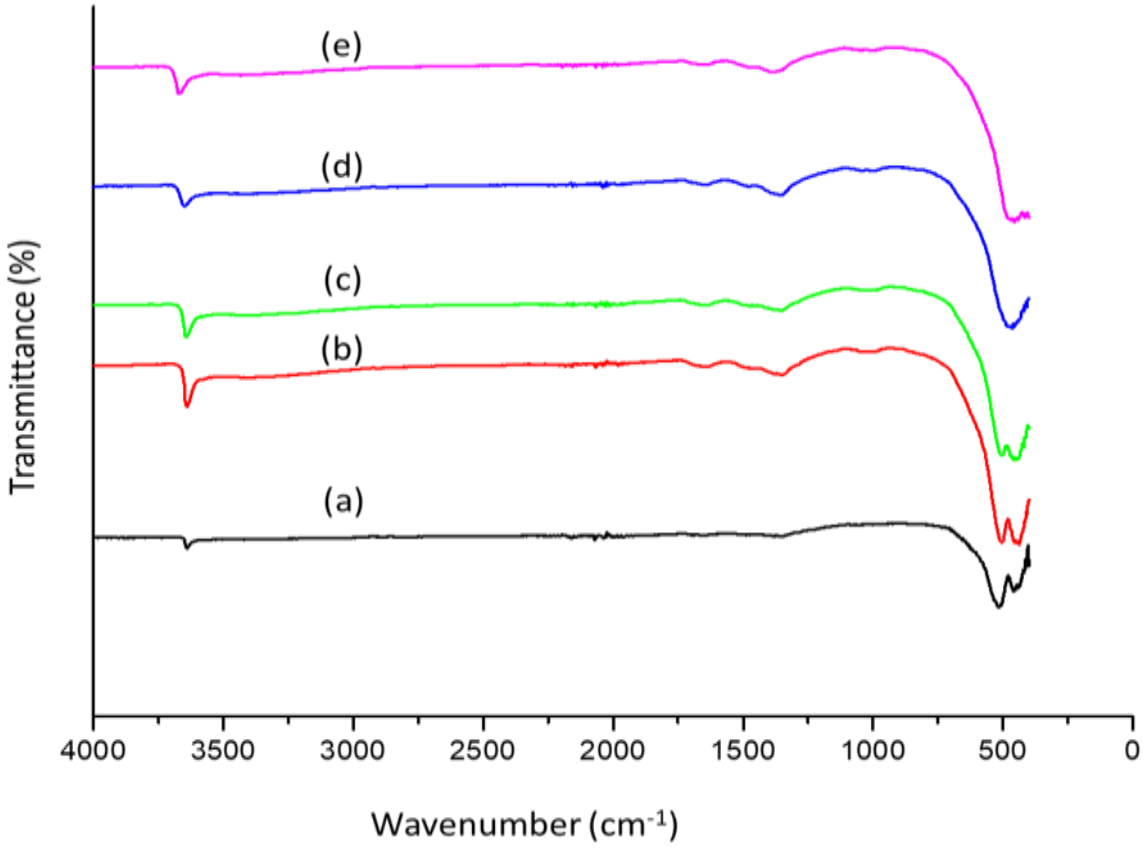

Figure 5-4: FTIR spectra of (a) $Ni(OH)_2$, (b) $Ni_{0.95}Mg_{0.05}(OH)_2$, (c) $Ni_{0.9}Mg_{0.1}(OH)_2$, (d) $Ni_{0.75}Mg_{0.25}(OH)_2$ and (e) $Ni_{0.5}Mg_{0.5}(OH)_2$

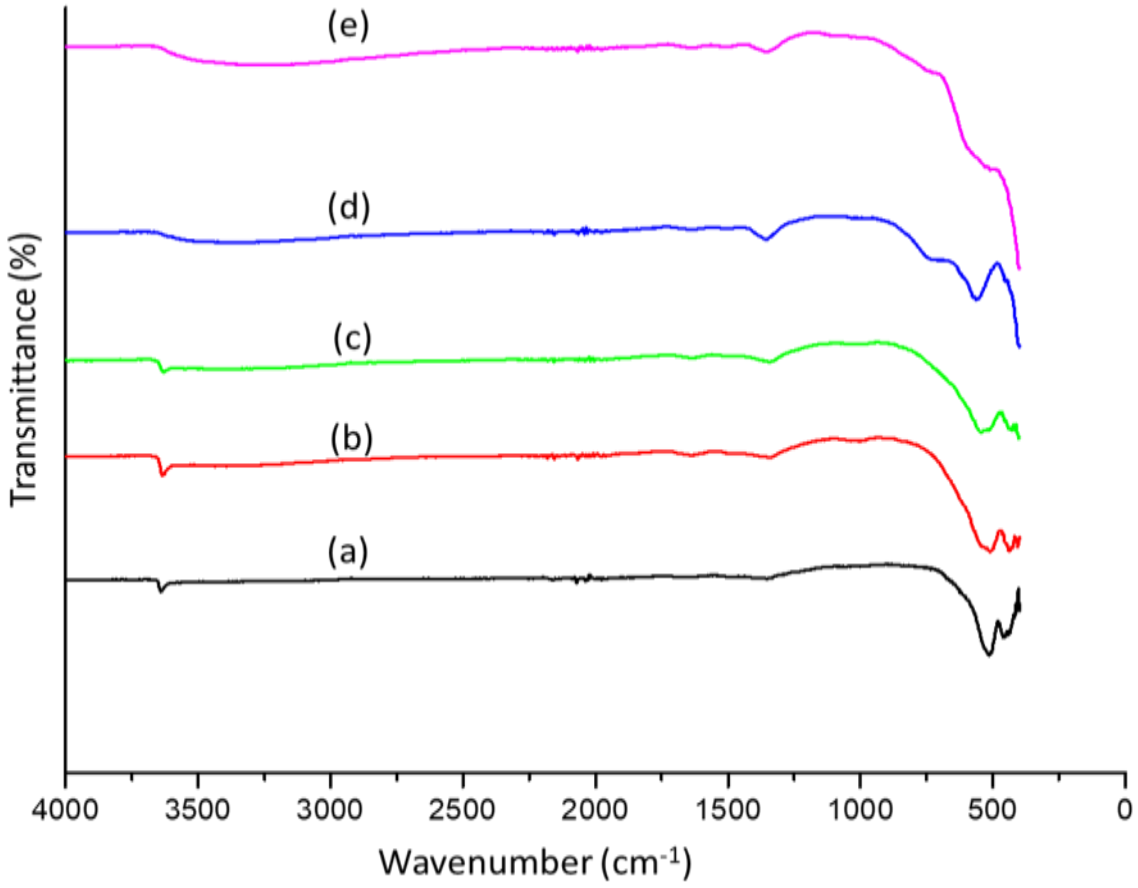

Figure 5-5: FTIR spectra of (a) $Ni(OH)_2$, (b) $Ni_{0.95}Mn_{0.05}(OH)_2$, (c) $Ni_{0.9}Mn_{0.1}(OH)_2$, (d) $Ni_{0.75}Mn_{0.25}(OH)_2$ and (e) $Ni_{0.5}Mn_{0.5}(OH)_2$

The thermal gravimetric analysis (TGA) and the corresponding inset of the differential thermal analysis (DTA) curves of $Ni_{1-x}Mg_x(OH)_2$ and $Ni_{1-x}Mn_x(OH)_2$ compared with un-doped $Ni(OH)_2$ are presented in Figure 5-6a,b respectively. All the $Ni_{1-x}Mg_x(OH)_2$ materials (Figure 5-6a) demonstrate two distinct weight losses similar to the un-doped $Ni(OH)_2$ sample. The calculated initial weight losses were 5.19 wt.% (73˚C), 4.89 wt.% (61˚C), 4.56 wt.% (61˚C), 6.78 wt.% (65˚C), and 5.87 wt.% (61˚C) for the un-doped $Ni(OH)_2$, $Ni_{0.95}Mg_{0.05}(OH)_2$, $Ni_{0.9}Mg_{0.1}(OH)_2$, $Ni_{0.75}Mg_{0.25}(OH)_2$, and $Ni_{0.5}Mg_{0.5}(OH)_2$, respectively (Table 5-2). A second weight loss of 14.24 wt.% (285˚C), 14.35 wt.% (291˚C), 14.05 wt.% (298˚C), 14.87 wt.% (291˚C), and 17.26 wt.% (317˚C) for the un-doped $Ni(OH)_2$, $Ni_{0.95}Mg_{0.05}(OH)_2$, $Ni_{0.9}Mg_{0.1}(OH)_2$, $Ni_{0.75}Mg_{0.25}(OH)_2$, and $Ni_{0.5}Mg_{0.5}(OH)_2$, respectively (Table 5-2). The small endothermic peaks at a temperature ranged between 61˚C – 75˚C are associated with the removal of surface water in the samples. The sharp endothermic peaks at around 285˚C – 317˚C are due to the $Ni(OH)_2$ decomposition to NiO (Shanaj and John, 2016; Kovalenko *et al.*, 2017).

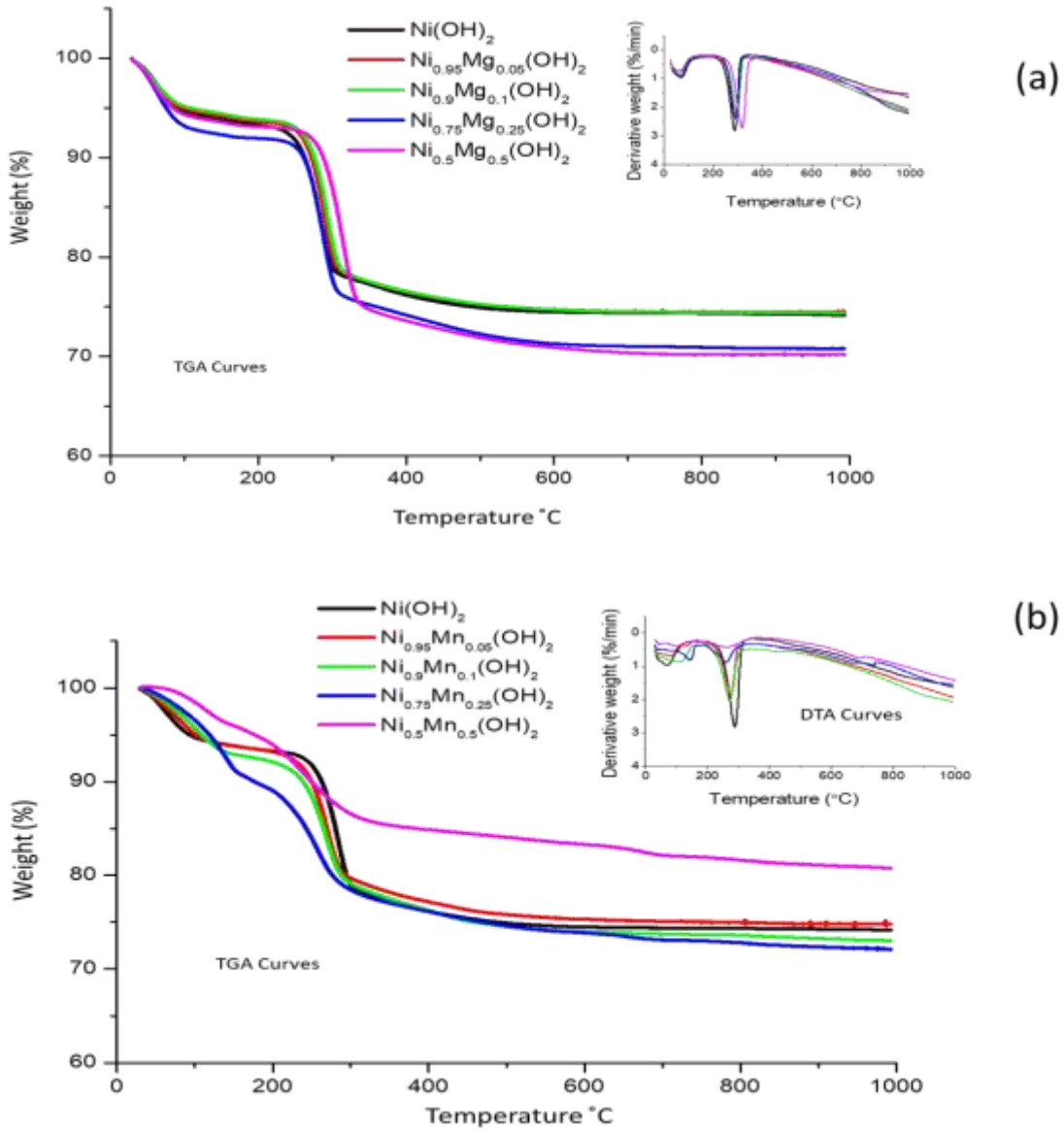

Figure 5-6: TGA-DTA curves of (a) $Ni_{1-x}Mg_x(OH)_2$ compared to the un-doped $Ni(OH)_2$, (b) $Ni_{1-x}Mn_x(OH)_2$ compared to the un-doped $Ni(OH)_2$

These results agree with the presented XRD diffractograms (Figure 5-2) and the FTIR spectra (Figure 5-4), which further confirms the formation of anhydrous β-$Ni(OH)_2$. The dehydration process of $Ni(OH)_2$ may be demonstrated as follows (Equation 5-3 to Equation 5-5) (Hall *et al.*, 2015; Shanaj and John, 2016; Kovalenko *et al.*, 2017).

Equation 5-3: Removal of adsorbed water molecules in $Ni(OH)_2$

$$Ni(OH)_2.(X_{ad} + Y_{st})H_2O \xrightarrow{50℃-90℃} Ni(OH)_2.Y_{st}H_2O + XH_2O$$

Equation 5-4: Removal of incorporated water molecules in $Ni(OH)_2$

$$Ni(OH)_2.Y_{st}H_2O \xrightarrow{90℃-180℃} Ni(OH)_2 + YH_2O$$

Equation 5-5: Structural decomposition of $Ni(OH)_2$

$$Ni(OH)_2 \xrightarrow{180℃-525℃} NiO + H_2O$$

The TG-DTA curves for the $Ni_{1-x}Mg_x(OH)_2$ and β-$Ni(OH)_2$ materials illustrated the removal of adsorbed water molecules from $Ni(OH)_2$ at temperatures between 61˚C and 73˚C (Equation 5-3), followed by $Ni(OH)_2$ decomposition to NiO as represented by Equation 5-5 (Hall *et al.*, 2015; Shanaj and John, 2016). As established by the observed two distinct weight losses (Figure 5-6a), Equation 5-4 did not play any role. This may be because the removal of incorporated water molecules from $Ni(OH)_2$ (Equation 5-4) usually is observed on the structure of α-$Ni(OH)_2$ formation(Hall *et al.*, 2015).

Similar decompositions were obtained for the $Ni_{1-x}Mn_x(OH)_2$ (Figure 5-6b). All the Mn^{2+} partial substituted $Ni(OH)_2$ samples demonstrate two distinct weight losses, and the calculated weight losses corresponding to their respective endothermic peaks are presented in Table 5-2.

Table 5-2: TG-DTA analysis of the un-doped $Ni(OH)_2$, $Ni_{1-x}Mg_x(OH)_2$ and $Ni_{1-x}Mn_x(OH)_2$ materials

	Removal of adsorbed (61.24 °C - 87.53 °C) and incorporated (123.27 °C - 144.66 °C) water molecules in the $Ni(OH)_2$ based composites		**Decomposition of $Ni(OH)_2$ based-composites to NiO based-composites**	
Sample name	**DTA: temp. (°C)**	**TGA: weight loss (%)**	**DTA: temp. (°C)**	**TGA: weight loss (%)**
$Ni(OH)_2$	73	5.19	285	14.24
$Ni_{0.95}Mg_{0.05}(OH)_2$	61.2	4.89	291.1	14.35
$Ni_{0.9}Mg_{0.1}(OH)_2$	61.2	4.56	298. 5	14.05
$Ni_{0.75}Mg_{0.25}(OH)_2$	65.8	6.78	291.1	14.87
$Ni_{0.5}Mg_{0.5}(OH)_2$	61.2	5.84	317.6	17.26
$Ni_{0.95}Mn_{0.05}(OH)_2$	70.2	5.63	274.8	12.41
$Ni_{0.9}Mn_{0.1}(OH)_2$	87.5	6.57	269.7	11.99
$Ni_{0.75}Mn_{0.25}(OH)_2$	144.7	9.25	262.0	10.61
$Ni_{0.5}Mn_{0.5}(OH)_2$	123.3	5.62	251.8	6.86

The nitrogen adsorption-desorption isotherms of the of $Ni_{1-x}Mg_x(OH)_2$ and $Ni_{1-x}Mn_x(OH)_2$ materials compared with un-doped $Ni(OH)_2$ are presented in Figure 5-7a,b, respectively.

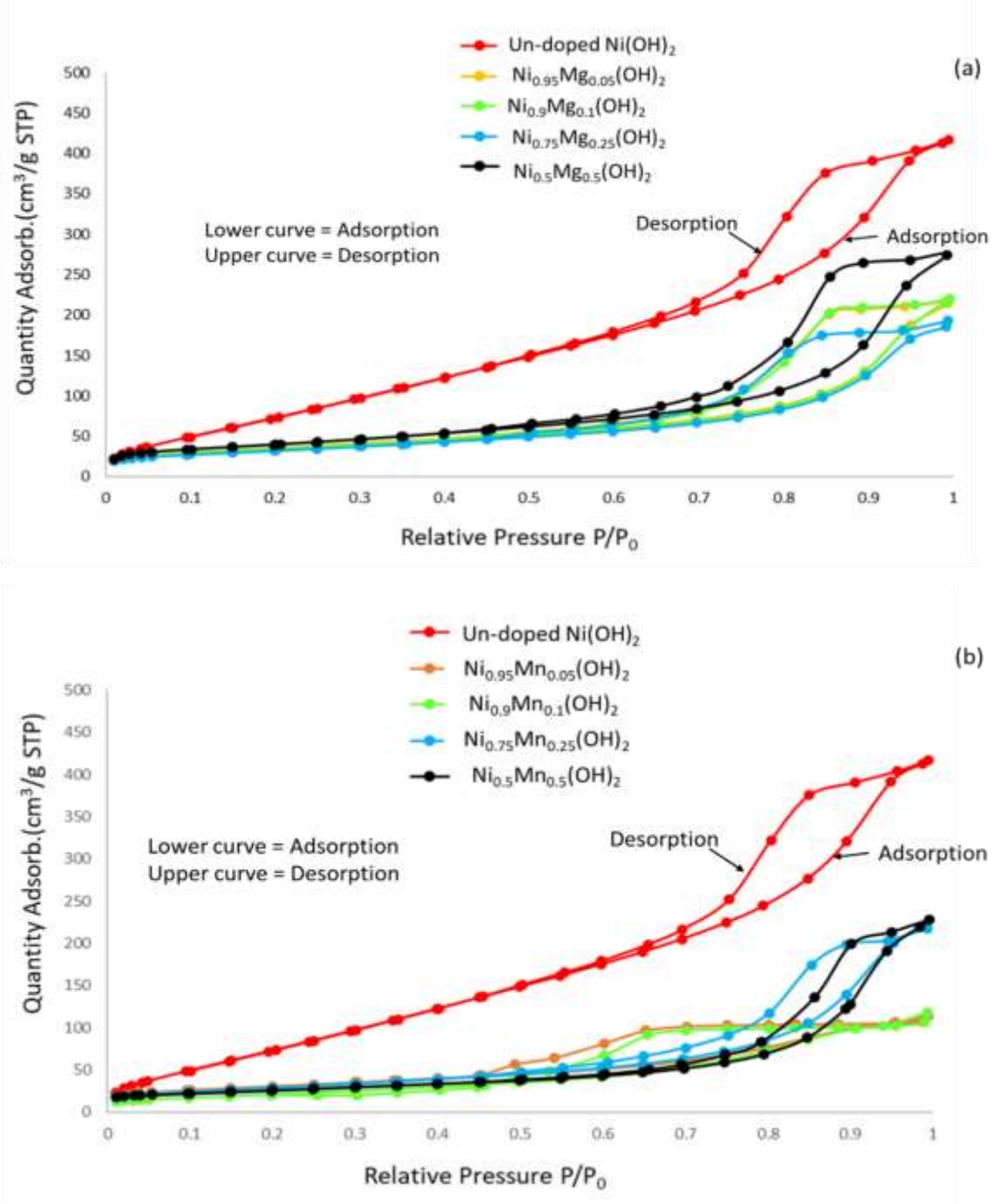

Figure 5-7: Nitrogen adsorption-desorption isotherm of (a) $Ni_{1-x}Mg_x(OH)_2$ compared to un-doped $Ni(OH)_2$, (b) $Ni_{1-x}Mn_x(OH)_2$ compared to un-doped $Ni(OH)_2$

The $Ni_{1-x}Mg_x(OH)_2$ compared with un-doped $Ni(OH)_2$ (Figure 5-7a) may be classified as type IV isotherm with H3-type hysteresis loop at the relative pressure (P/P°) ranges between 0.7 and 1.0, reflecting the presence of mesoporous structure (Luan *et al.*, 2018). These findings were in agreement

with the results reported in the literature (Coudun *et al.*, 2006; Zheng *et al.*, 2017; Luan *et al.*, 2018; Yu *et al.*, 2019).

The nitrogen adsorption-desorption isotherms of the $Ni_{1-x}Mn_x(OH)_2$ compared with un-doped $Ni(OH)_2$ are presented in Figure 5-7b, also reflecting the presence of mesoporous structure at the relative pressure (P/P°) range between 0.6 and 1.0. The N_2 adsorption-desorption isotherms of the materials may also be classified as type IV isotherm with H3-type hysteresis loop. Similar isotherms of the Ni/Mn composite were reported in the literature (Xia *et al.*, 2015; Liu, Hao *et al.*, 2020).

As presented in Table 5-3, the BET surface areas ranged between 115.90 m^2/g to 142.06 m^2/g and from 80.67 m^2/g to 109.08 m^2/g for Mg^{2+}, and Mn^{2+} partially substituted $Ni(OH)_2$, respectively. Their BHJ average pore size adsorption ranged from 10.22 nm to 11.42 nm and 6.85 nm to 14.64 nm, respectively. The BET surface area of the unmodified $Ni(OH)_2$ is 361.92 m^2/g, and the BHJ average pore size is 6.29 nm. This shows that the partial substitution of the Ni^{2+} with either Mg^{2+} or Mn^{2+} decreases the BET surface area of the $Ni(OH)_2$. The confirmed elemental compositions using ICP/OES and SEM/EDS (Table 3) agreed with the intended compositions of the partially substituted materials.

Table 5-3: BET surface areas and elemental compositions of the un-doped $Ni(OH)_2$, $Ni_{1-x}Mg_x(OH)_2$, and $Ni_{1-x}Mn_x(OH)_2$ materials

Sample name	**BET Surface area (m^2/g)**	**Pore size (nm)**	**Expected Ni^{2+}:M^{x+}**	**ICP-OES Ni^{2+}:M^{x+}**	**SEM-EDS Ni^{2+}:M^{x+}**
$Ni(OH)_2$	361.92	6.29	*	*	*
$Ni_{0.95}Mg_{0.05}(OH)_2$	126.07	10.66	0.95: 0.05	0.95: 0.05	0.95: 0.05
$Ni_{0.9}Mg_{0.1}(OH)_2$	124.07	11.22	0.90: 0.10	0.90: 0.10	0.90: 0.10
$Ni_{0.75}Mg_{0.25}(OH)_2$	115.90	10.22	0.75: 0.25	0.75: 0.25	0.74: 0.26
$Ni_{0.5}Mg_{0.5}(OH)_2$	142.06	11.42	0.50: 0.50	0.50: 0.50	0.51: 0.49
$Ni_{0.95}Mn_{0.05}(OH)_2$	109.08	6.85	0.95: 0.05	0.95: 0.05	0.95: 0.05
$Ni_{0.9}Mn_{0.1}(OH)_2$	80.67	7.76	0.90: 0.10	0.90: 0.10	0.91: 0.09
$Ni_{0.75}Mn_{0.25}(OH)_2$	102.91	11.74	0.75: 0.25	0.76: 0.24	0.77: 0.23
$Ni_{0.5}Mn_{0.5}(OH)_2$	91.26	14.64	0.50: 0.50	0.55: 0.45	0.52: 0.48

The SEM images of the $Ni_{1-x}Mg_x(OH)_2$ and $Ni_{1-x}Mn_x(OH)_2$ materials and the un-doped $Ni(OH)_2$ are presented in Figure 5-8. The morphologies of as-prepared Ni-based hydroxide materials were formed as an accumulation of aggregates particles. However, the observed crystallinities were not clear, which

may be due to the aggregation of the particles. For future studies, transmission electron microscopy (TEM) will be used to access the structural morphology of these materials.

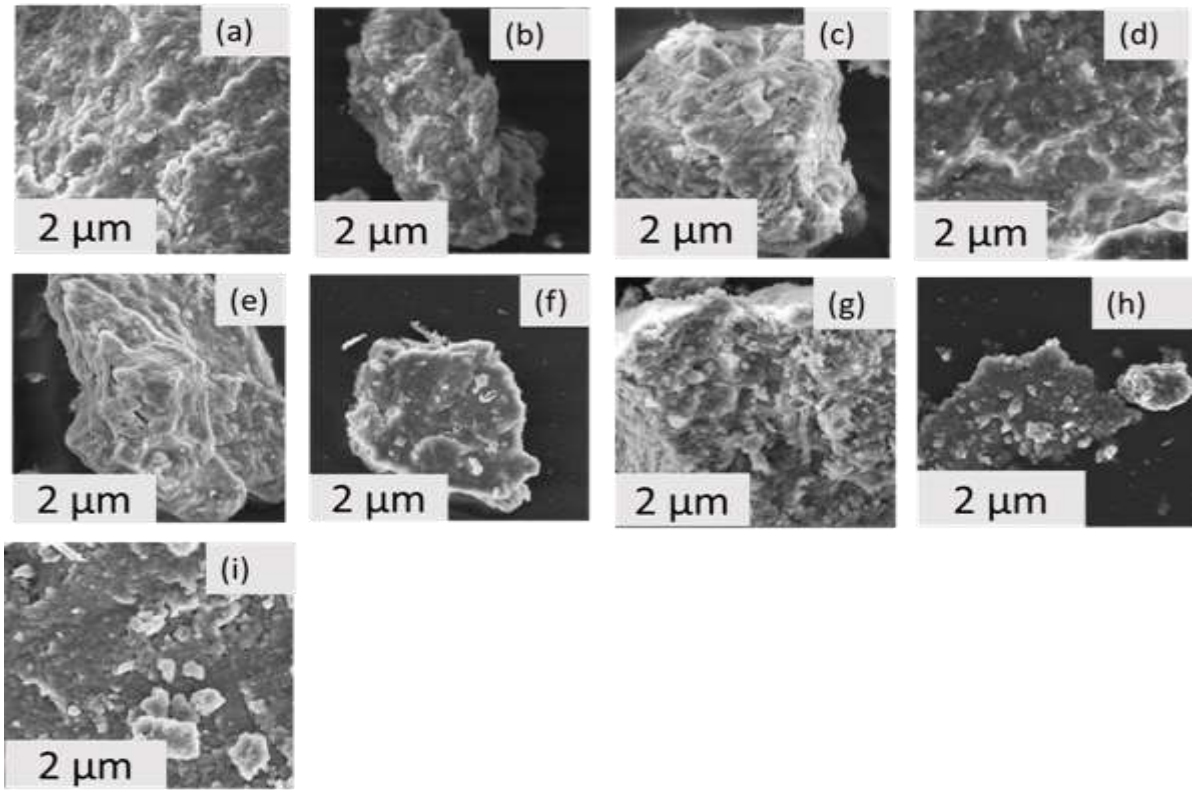

Figure 5-8: SEM images of (a) $Ni_{0.95}Mg_{0.05}(OH)_2$, (b) $Ni_{0.9}Mg_{0.1}(OH)_2$, (c) $Ni_{0.75}Mg_{0.25}(OH)_2$, (d) $Ni_{0.5}Mg_{0.5}(OH)_2$, (e) $Ni_{0.95}Mn_{0.05}(OH)_2$, (f) $Ni_{0.9}Mn_{0.1}(OH)_2$, (g) $Ni_{0.75}Mn_{0.25}(OH)_2$, (h) $Ni_{0.5}Mn_{0.5}(OH)_2$, and (i) un-doped $Ni(OH)_2$

5.4.2 Electrochemical properties of the un-doped $Ni(OH)_2$, $Ni_{1-x}Mg_x(OH)_2$, and $Ni_{1-x}Mn_x(OH)_2$ materials

5.4.2.1 Performance evaluation of the un-doped $Ni(OH)_2$, $Ni_{1-x}Mg_x(OH_2$ and $Ni_{1-x}Mn_x(OH_2$ using a three-electrode test

The electrochemical properties of the un-doped $Ni(OH)_2$, $Ni_{1-x}Mg_x(OH)_2$, and $Ni_{1-x}Mn_x(OH)_2$ active materials were first investigated in a three-electrode configuration. The chrono-charge discharge galvanostatic (CCDG) curves of as-prepared composites are presented in Figure 5-9. The electrodes were cycled 20 times at 250 mA/g.

The discharge capacities were calculated using Equation 5-2; as presented in Figure 5-9a and Figure 5-9b, respectively, the materials $Ni_{0.95}Mg_{0.05}(OH)_2$ and $Ni_{0.9}Mn_{0.1}(OH)_2$ showed optimal compositions with promising electrochemical properties over the 20^{th} cycles. The charge state and discharge state at the 20^{th} cycles are shown in Figure 5-9c-d.

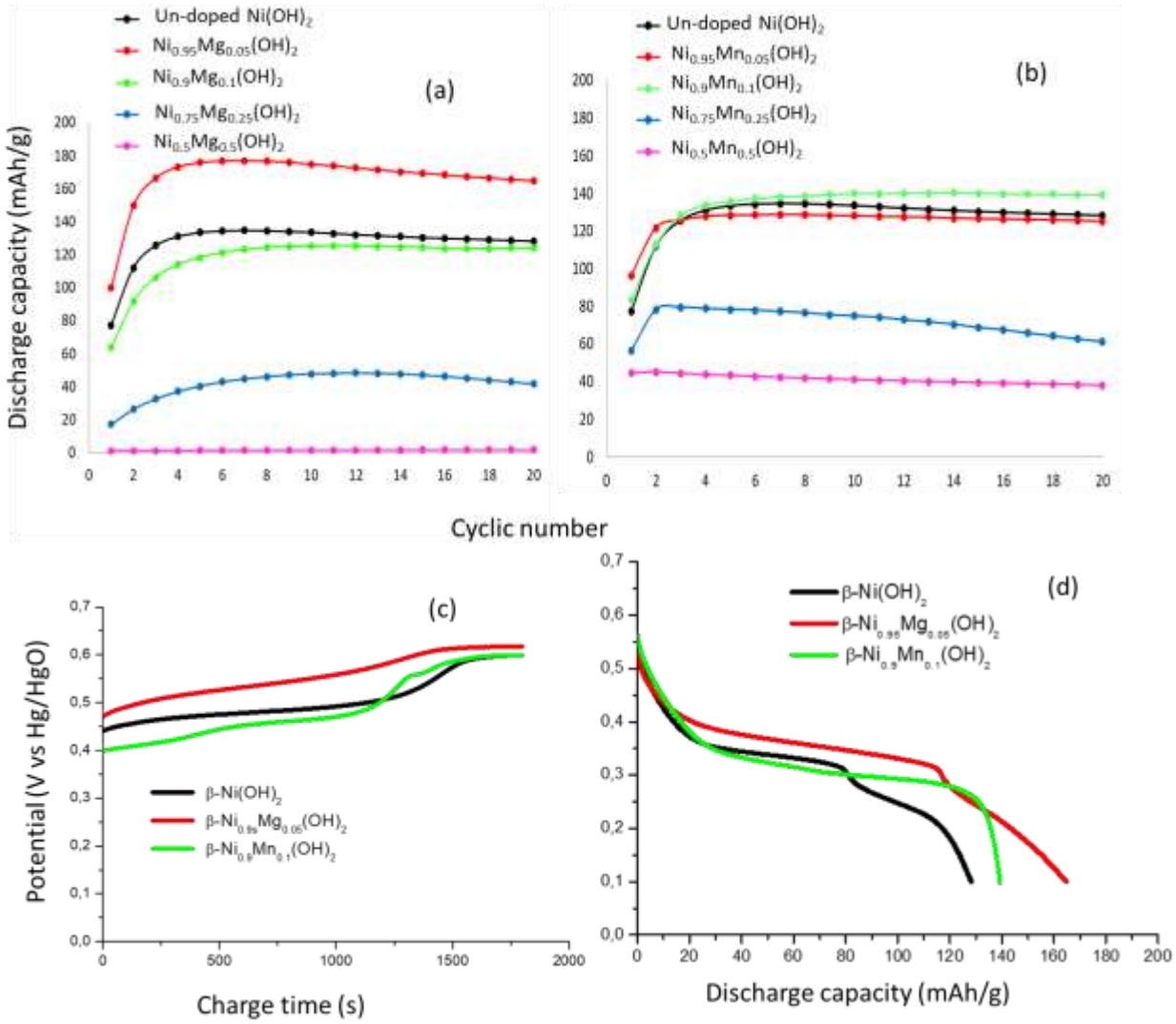

Figure 5-9: CCDG discharge capacities curves of (a) $Ni_{1-x}Mg_x(OH)_2$ compositions, (b) $Ni_{1-x}Mn_x(OH)_2$ compositions, and the (c) charge curve (d) discharge curve at the 20th cycle of the un-doped $Ni(OH)_2$, $Ni_{0.95}Mg_{0.05}(OH)_2$ and $Ni_{0.9}Mn_{0.1}(OH)_2$

Both curves illustrate a single flat-charge (Figure 5-9c) and single flat-discharge (Figure 5-9d) plateau for both $Ni_{0.95}Mg_{0.05}(OH)_2$ and $Ni_{0.9}Mn_{0.1}(OH)_2$ electrode indicating that a single redox couple may be involved in electrochemical reactions. Two flat-discharge (Figure 5-9d) plateaus for the un-doped $Ni(OH)_2$ electrode were observed, indicating that a two redox couple may be involved in the electrochemical reactions. These findings may be the confirmation of the proposed chemical redox reactions (Equation 5-9 and Equation 5-10) for the un-doped $Ni(OH)_2$ and Equation 5-9 for both 5 wt.% Mg^{2+} and 10 wt.% Mn^{2+}doped $Ni(OH)_2$ electrodes.

Figure 5-10 presents the specific discharge capacities of the un-doped $Ni(OH)_2$, $Ni_{0.95}Mg_{0.05}(OH)_2$, and $Ni_{0.9}Mn_{0.1}(OH)_2$ electrodes over 100 cycles.

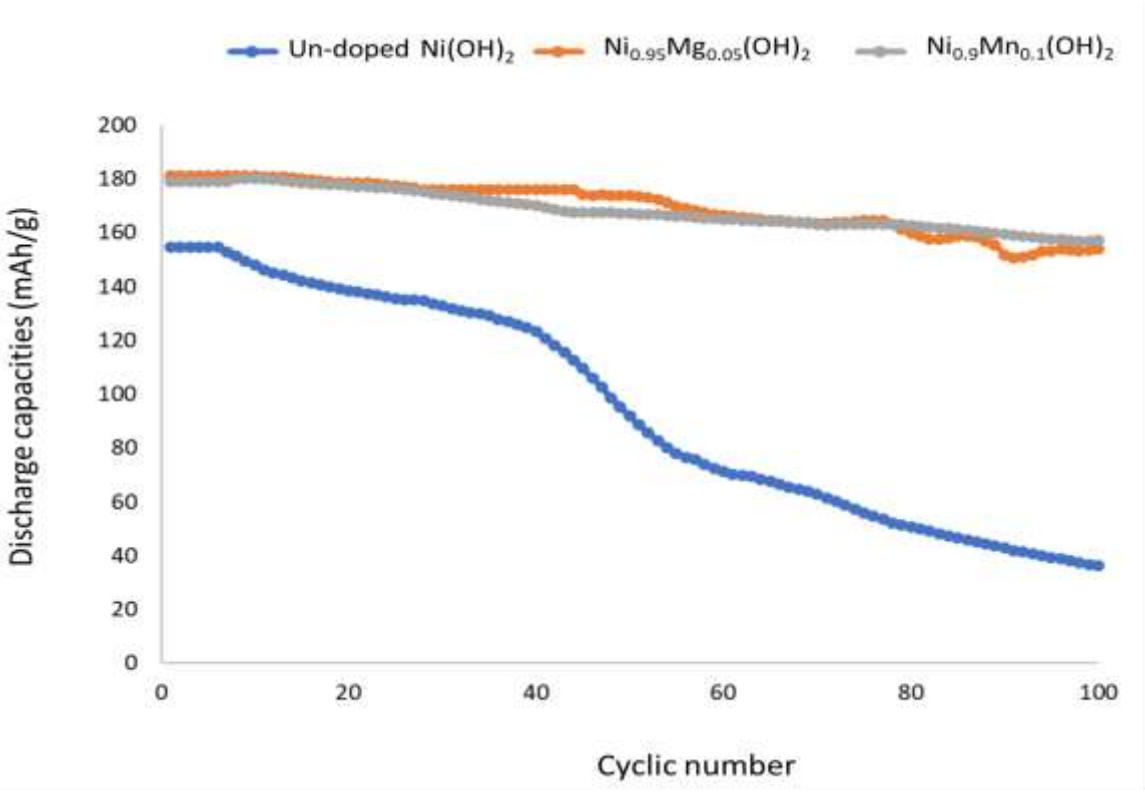

Figure 5-10: CCDG discharge capacities curves over 100 cycles for un-doped $Ni(OH)_2$, $Ni_{0.95}Mg_{0.05}(OH)_2$, and $Ni_{0.9}Mn_{0.1}(OH)_2$ using the three-electrode test

The un-doped $Ni(OH)_2$ electrode showed a 76% reduction in discharge capacity at the 100th cycle when compared to the $Ni_{0.95}Mg_{0.05}(OH)_2$ and $Ni_{0.9}Mn_{0.1}(OH)_2$ electrodes, which demonstrated a 15% and 12% decrease in discharge capacity at the 100th cycle, respectively. Both$Ni_{0.95}Mg_{0.05}(OH)_2$ and $Ni_{0.9}Mn_{0.1}(OH)_2$ electrodes demonstrated drastically improved discharge capacities of 85% and 88% higher than of the un-doped $Ni(OH)_2$ electrode at the 100th cycle, respectively. The specific discharge capacities of the un-doped $Ni(OH)_2$, $Ni_{0.95}Mg_{0.05}(OH)_2$, and $Ni_{0.9}Mn_{0.1}(OH)_2$ electrode were 36 mAh/g, 154 mAh/g, and 157 mAh/g at the 100th cycle, respectively, which equates to coulombic efficiencies of 18%, 75%, and 77%, respectively.

5.4.2.2 Performance evaluation of the un-doped $Ni(OH)_2$, $Ni_{0.95}Mg_{0.05}(OH)_2$, and $Ni_{0.9}Mn_{0.1}(OH)_2$ based-electrodes using two-electrode test

The discharge capacity curves of the un-doped $Ni(OH)_2$, $Ni_{0.95}Mg_{0.05}(OH)_2$, and $Ni_{0.9}Mn_{0.1}(OH)_2$ electrodes measured over the 100th cycles using two-electrode configurations are shown in Figure 5-11. An-house $FeCu_{0.25}$ electrode (Tawonezvi *et al.*, 2020) was used as the anode, current-limiting charge-discharge of 150 mA/g and 100 mA/g was used within a voltage window of 1.75 V -0.7 V. As presented in Figure 5-11, the partial substitution of both 5% Mg^{2+} and 10% Mn^{2+} for Ni^{2+} improves the utilization of $Ni(OH)_2$. The obtained discharge capacities were 40 mAh/g for the un-doped $Ni(OH)_2$ electrode, 120

mAh/g for the $Ni_{0.95}Mg_{0.05}(OH)_2$ electrode, and 159 mAh/g for the $Ni_{0.9}Mn_{0.1}(OH)_2$ electrode at the 100th cycle. The electrode cycle life was 43.49%, 88.24%, 88.54% for the un-doped $Ni(OH)_2$, $Ni_{0.95}Mg_{0.05}(OH)_2$, and $Ni_{0.9}Mn_{0.1}(OH)_2$, respectively. It may also be noted that the stability of the un-doped $Ni(OH)_2$ electrode was improved.

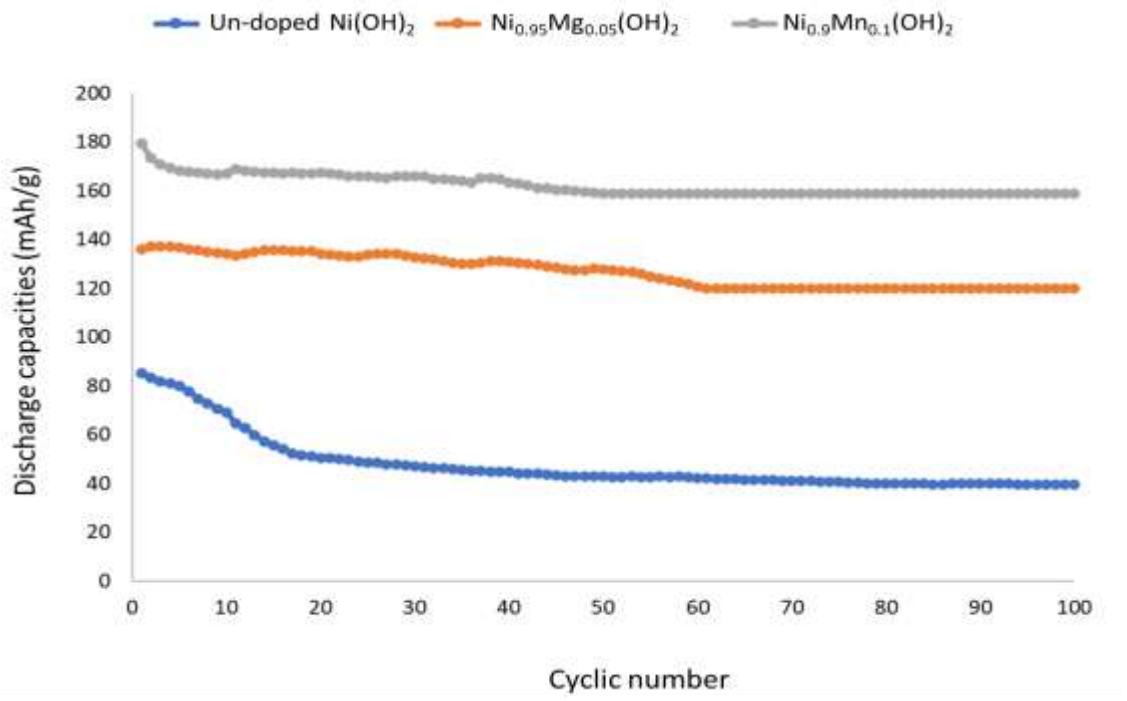

Figure 5-11: Specific discharge capacity curves over 100 cycles for un-doped $Ni(OH)_2$, $Ni_{0.95}Mg_{0.05}(OH)_2$, and $Ni_{0.9}Mn_{0.1}(OH)_2$ using a two-electrode test

In addition, the time-voltage-current charge-discharge curves of the materials at the 100th cycle is shown in Figure 5-12. It has been reported that the overall reaction of the NiFe battery electrode results in the transfer of oxygen from one electrode to the other (Wang, Hailiang *et al.*, 2012; Tsais and Chan, 2013). Although the exact details of the reaction may be complex and include many species of transitory existence, the plateaus observed in Figure 5-12 may be the representation of Equation 5-6 and Equation 5-7, resulting in the overall reaction presented in Equation 5-8 (Tsais and Chan, 2013).

Equation 5-6: First plateau of charge-discharge reaction of NiFe battery electrode

$$Fe + 2NiOOH + 2H_2O \underset{\text{Charge}}{\overset{\text{Discharge}}{\rightleftharpoons}} 2Ni(OH)_2 + Fe(OH)_2 \ldots\ldots\ldots\ldots\ldots\ldots\ldots\ldots\ldots \text{First plateau}$$

Equation 5-7: Second plateau of charge-discharge reaction of NiFe battery electrode

$$3Fe(OH)_2 + 2NiOOH \underset{\text{Charge}}{\overset{\text{Discharge}}{\rightleftharpoons}} 2Ni(OH)_2 + Fe_3O_4 + 2H_2O \ldots\ldots\ldots\ldots\ldots\ldots\ldots \text{Second plateau}$$

Equation 5-8: Overall charge-discharge reaction of NiFe battery electrode

$$3Fe + 8NiOOH + 4H_2O \underset{\text{Charge}}{\overset{\text{Discharge}}{\rightleftharpoons}} 8Ni(OH)_2 + Fe_3O_4 \ldots\ldots\ldots\ldots\ldots\ldots\ldots\ldots\ldots \text{Overall reaction}$$

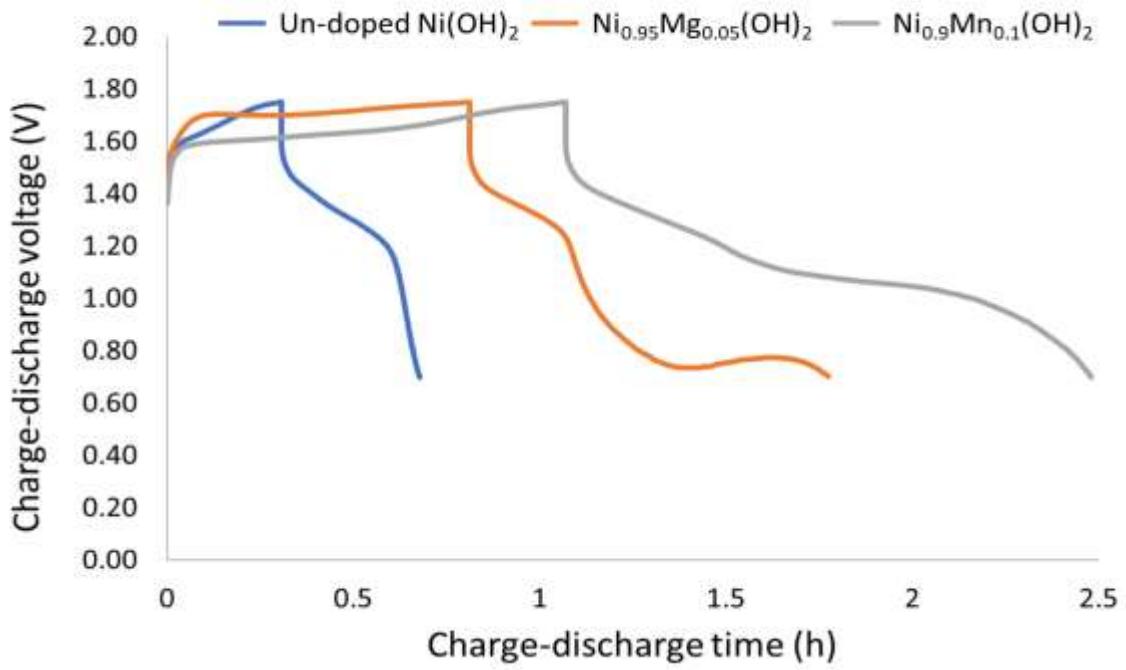

Figure 5-12: Time-voltage charge-discharge curves of $Ni(OH)_2$, $Ni_{0.95}Mg_{0.05}(OH)_2$, and $Ni_{0.9}Mn_{0.1}(OH)_2$ at the 100th cycle

5.4.2.3 Effect of Mg^{2+} and Mn^{2+} on the potential sweep of $Ni(OH)_2$ electrode using three-electrode test

Figure 5-13 presents the cyclic voltammograms of un-doped $Ni(OH)_2$, $Ni_{0.95}Mg_{0.05}(OH)_2$, and $Ni_{0.9}Mn_{0.1}(OH)_2$. Cyclic voltammograms were obtained at room temperature, a potential sweep rate of 20 mVs^{-1}, and a potential window of 0.0 V to 0.7 V (vs Hg/HgO/ 4M KOH).

The oxidation peaks and the corresponding reduction peaks appeared at around 0.591 V and 0.339 V for the un-doped $Ni(OH)_2$, 0.569 V and 0.366 V for the $Ni_{0.95}Mg_{0.05}(OH)_2$ attributing to the Ni (II)/Ni (III) redox reactions were observed. The reduction peak at 0.278 V was obtained for the $Ni_{0.9}Mn_{0.1}(OH)_2$, and the "oxidation peak" could not be defined. The ΔE (the potential difference between the cathodic and anodic peak) of un-doped $Ni(OH)_2$ (Figure 5-13a) was found to be 0.252 V, which is greater than the Mg^{2+} partial substituted $Ni(OH)_2$ electrodes (ΔE = 0.203 V) presented in Figure 5-13b, indicating poor reversibility compared to the Mg^{2+}doped material (Yang, LJ *et al.*, 2007).

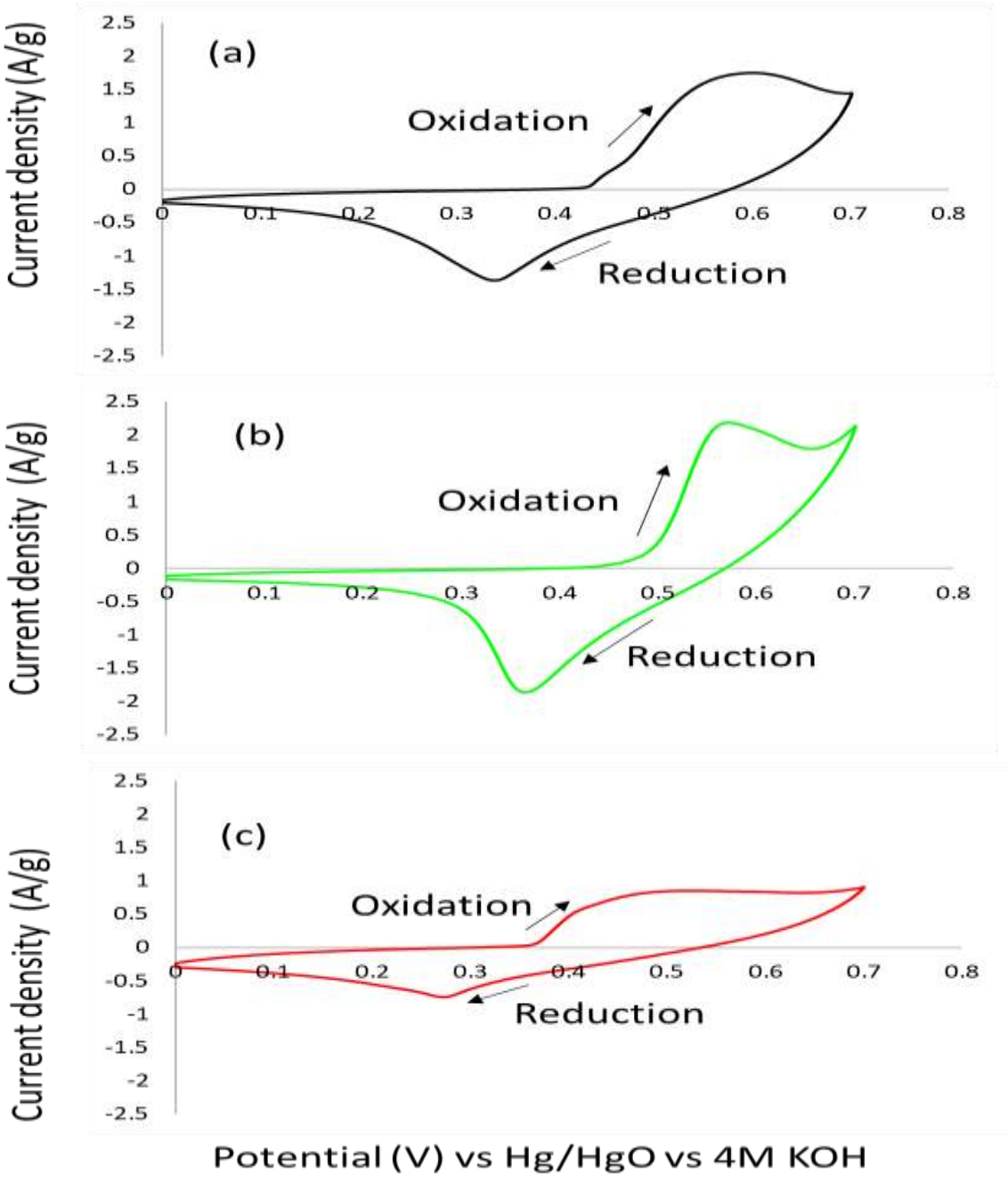

Figure 5-13: Cyclic voltammograms of (a) $Ni(OH)_2$, (b) $Ni_{0.95}Mg_{0.05}(OH)_2$ (c) $Ni_{0.9}Mn_{0.1}(OH)_2$

The observed broader redox peaks for the un-doped $Ni(OH)_2$ (Figure 5-13a) and $Ni_{0.9}Mn_{0.1}(OH)_2$ (Figure 5-13c) may be an indication that the oxygen evolution reaction (OER) is overlapping with the oxidation potential of NiOOH to $Ni(OH)_2$. Typical broader redox peaks of $NiOOH/Ni(OH)_2$ were reported in the literature (Begum *et al.*, 2009; Wang, Hailiang *et al.*, 2012). The redox mechanism of the observed un-doped $Ni(OH)_2$ and $Ni_{0.9}Mn_{0.1}(OH)_2$ may be expressed by Equation 5-9 and Equation 5-10. According to Zimmerman and Effa (Zimmerman and Effa, 1984), Equation 5-10, it may be rate-limiting and appears to be more consistent with diffusion of OH^- between the bulk electrolyte and the

active material surface as the rate-liming step for high rate electrode operation, particularly at reduced concentrations of OH^-.

Equation 5-9: Charge transfer process involving reduction of NiOOH active material in the lattice

$$Ni(OH)_2 \rightleftharpoons NiOOH + H^+ + e^-$$

Equation 5-10: Formation of protons at the electrode/electrolyte interface

$$H^+ + OH^- \rightleftharpoons H_2O$$

The partial substitution of Mg^{2+} ($Ni_{0.95}Mg_{0.05}(OH)_2$) for Ni^{2+} (Figure 5-13b) allowed the separation of anodic/cathodic peaks and oxygen evolution. For example, the anodic and cathodic peaks are easier to identify because their potential shifted to more negative potentials. This could be due to faster electrode kinetics as indicated by the smaller ΔE (the potential difference between the cathodic and anodic peak). The redox mechanism of the $Ni_{0.95}Mg_{0.05}(OH)_2$ may be attributed to Equation 5-9.

5.5 Conclusion

Un-doped $Ni(OH)_2$, nickel-manganese ($Ni_{1-x}Mn_x(OH)_2$), and nickel-magnesium ($Ni_{1-x}Mg_x(OH)_2$) composite hydroxide active material were prepared using a co-precipitation method followed by hydrothermal treatment. Physical characterizations were performed using XRD, FTIR, TG-DTA, BET, BHJ, SEM/EDS, and ICP-OES. XRD, FTIR, TG-DTA confirmed the formation of the β-phase of the un-doped $Ni(OH)_2$ and the β-phase of the partially substituted Mg^{2+} for Ni^{2+} in $Ni(OH)_2$ material.

Interestingly, from the obtained spectra, the partial substitution of Mn^{2+} for Ni^{2+} was the main factor that affected the phase formation of the prepared composite materials. The BET surface areas ranged from 115.90 m^2/g to 142.06 m^2/g and from 80.67 m^2/g to 109.08 m^2/g for the Mg^{2+}, and Mn^{2+} partially substituted $Ni(OH)_2$, respectively compared to a larger BET surface area (361.92 m^2/g) of the unmodified $Ni(OH)_2$. The confirmed elemental composition using ICP/OES and SEM/EDS was in agreement with the intended compositions of the partially substituted Mg^{2+} and Mn^{2+} $Ni(OH)_2$ materials.

Although the relationship between structural and electrochemical properties of the material is not well understood (Falahati *et al.*, 2015); according to Huang et al. (Huang, Jichun *et al.*, 2013), the physical properties of $Ni(OH)_2$, such as specific surface area and chemical compositions, are strongly influencing the performance of the positive $Ni(OH)_2$ electrodes. In this study, the $Ni_{0.95}Mg_{0.05}(OH)_2$ composition demonstrated a slightly higher BET surface area compared to $Ni_{0.9}Mg_{0.1}(OH)_2$, $Ni_{0.75}Mg_{0.25}(OH)_2$, $Ni_{0.5}Mg_{0.5}(OH)_2$ compositions. Also, $Ni_{0.9}Mn_{0.1}(OH)_2$ has a lower BET surface area as compared to $Ni_{0.95}Mn_{0.05}(OH)_2$, $Ni_{0.75}Mn_{0.25}(OH)_2$, and $Ni_{0.5}Mn_{0.5}(OH)_2$ compositions.

Additionally, according to the demonstrated XRD diffractograms, both $Ni_{0.95}Mg_{0.05}(OH)_2$ (Figure 5-2b) and $Ni_{0.9}Mn_{0.1}(OH)_2$ (Figure 5-3c) compositions could be indexed to the β-form of $Ni(OH)_2$. According

to the literature (Hall *et al.*, 2015; Posada and Hall, 2016; Zide *et al.*, 2020b, a), the β-$Ni(OH)_2$ is stable in strong alkaline electrolyte and has good reversibility when charged to β-NiOOH. Moreover, the β-NiOOH has a similar structure with a lattice constant of inter-sheet (4.85Å) thus the volume expansion associated with cycling is less than any other forms.

Moreover, in this study, the CV analysis showed that the partial substitution of Mg^{2+} for Ni^{2+} improves the reversibility of the $Ni(OH)_2$ based electrode, the separation of anodic/cathodic peaks, and the oxygen evolution. The $Ni_{0.95}Mg_{0.05}(OH)_2$ electrode and $Ni_{0.9}Mn_{0.1}(OH)_2$ electrode demonstrated an improved specific discharge capacities performance compared to the un-doped $Ni(OH)_2$. The specific discharge capacities were 36 mAh/g, 154 mAh/g, and 157 mAh/g at the 100^{th} cycles for the un-doped $Ni(OH)_2$, $Ni_{0.95}Mg_{0.05}(OH)_2$, and $Ni_{0.9}Mn_{0.1}(OH)_2$ electrode, respectively. The un-doped $Ni(OH)_2$ based electrode had a 76 % reduction in specific discharge capacity after the 100^{th} cycle when compared to the electrodes of the $Ni_{0.95}Mg_{0.05}(OH)_2$ and $Ni_{0.9}Mn_{0.1}(OH)_2$, which demonstrated a reduction in specific discharge capacities of only 15% and 12% after 100^{th} cycles, respectively.

When two-electrode configuration was used, the obtained discharge capacities were 40 mAh/g for un-doped $Ni(OH)_2$ electrode, 120 mAh/g for $Ni_{0.95}Mg_{0.05}(OH)_2$ electrode, and 159 mAh/g for $Ni_{0.9}Mn_{0.1}(OH)_2$ electrode with an electrode cycle life of 43.49 %, 88.24 %, 88.54 %, respectively.

5.6 CRediT (Contributor Roles Taxonomy) author statement

Dorcas Zide: Conceptualization, Methodology, Software, Validation, Formal analysis, Investigation, Resources, Writing - Original Draft, Writing - Review & Editing, Supervision, Project administration. **Cecil Felix:** Writing - Review & Editing**. Tobie Oosthuysen:** Writing - Review & Editing, Supervision**; Bernard Jan Bladergroen**: Conceptualization, Software, Resources, Writing - Review & Editing, Supervision, Funding acquisition

5.7 Acknowledgements

The authors would like to acknowledge the financial and strategic support from the Department of Science and Innovation of South Africa; Eskom Holdings SOC Ltd Reg no 2002/015527/30 (Eskom Research, Testing, and Development Business Unit); and the National Research Foundation of South Africa (Grant Number: 121413).

5.8 Data Availability Statement

The data that support the findings of this study are available from the corresponding author upon reasonable request.

5.9 References

Begum, S. N., Muralidharan, V. and Basha, C. A. (2009). The influences of some additives on electrochemical behaviour of nickel electrodes. International Journal of Hydrogen Energy 34(3): 1548-1555.

Chen, H., Zhou, S. and Wu, L. (2014). Porous nickel hydroxide–manganese dioxide-reduced graphene oxide ternary hybrid spheres as excellent supercapacitor electrode materials. American Chemical Society: Applied Materials and Interfaces 6(11): 8621-8630.

Coudun, C., Grillon, F. and Hochepied, J. F. (2006). Surfactant effects on pH-controlled synthesis of nickel hydroxides. Colloids and Surfaces A: Physicochemical and Engineering Aspects 280(1-3): 23-31.

Ding, C., Zhou, X., Shi, J., Yan, P., Wang, Z., Liu, G. and Li, C. (2015). Abnormal effects of cations (Li^+, Na^+, and K^+) on photoelectrochemical and electrocatalytic water splitting. The Journal of Physical Chemistry B 119(8): 3560-3566.

Falahati, H., Kim, E. and Barz, D. P. (2015). Fabrication and characterization of thin film nickel hydroxide electrodes for micropower applications. American Chemical Society: Applied Materials and Interfaces 7(23): 12797-12808.

Guo, X. L., Liu, X. Y., Hao, X. D., Zhu, S. J., Dong, F., Wen, Z. Q. and Zhang, Y. X. (2016). Nickel-manganese layered double hydroxide nanosheets supported on nickel foam for high-performance supercapacitor electrode materials. Journal of Electrochimica Acta 194: 179-186.

Hall, D. S., Lockwood, D. J., Bock, C. and MacDougall, B. R. (2015). Nickel hydroxides and related materials: a review of their structures, synthesis and properties. Proceedings of the Royal Society A: Mathematical, Physical and Engineering Sciences 471(2174): 20140792.

Han, T., Shi, Y., Yu, Z., Shin, B. and Lanza, M. (2019). Potassium hydroxide mixed with lithium hydroxide: An advanced electrolyte for oxygen evolution reaction. Solar Rrl 3(10): 1900195.

Hill, J. C. and Choi, K. S. (2012). Effect of electrolytes on the selectivity and stability of n-type WO_3 photoelectrodes for use in solar water oxidation. The Journal of Physical Chemistry C 116(14): 7612-7620.

Huang, J., Cao, D., Lei, T., Yang, S., Zhou, X., Xu, P. and Wang, G. (2013). Structural and electrochemical performance of Al-substituted β-$Ni(OH)_2$ nanosheets electrodes for nickel metal hydride battery. Journal of Electrochimica Acta 111: 713-719.

Kenney, M. J., Gong, M., Li, Y., Wu, J. Z., Feng, J., Lanza, M. and Dai, H. (2013). High-performance silicon photoanodes passivated with ultrathin nickel films for water oxidation. Science 342(6160): 836-840.

Kovalenko, V., Kotok, V., Sykchin, A., Mudryi, I., Ananchenko, B., Burkov, A., Sololvov, V., Deabate, S., Mehdi, A. and Bantignies, J.-L. (2017). Nickel hydroxide obtained by high-temperature two-step synthesis as an effective material for supercapacitor applications. Journal of Solid State Electrochemistry 21(3): 683-691.

Lee, J. W., Ko, J. M. and Kim, J.-D. (2011). Hierarchical microspheres based on α-Ni $(OH)_2$ nanosheets intercalated with different anions: synthesis, anion exchange, and effect of intercalated anions on electrochemical capacitance. The Journal of Physical Chemistry C 115(39): 19445-19454.

Liu, H., Liang, Z., Liu, S., Zhang, L., Xia, H. and Xie, W. (2020). Nickel manganese hydroxides with thin-layer nanosheets and multivalences for high-performance supercapacitor. Results in Physics 16: 102831.

Liu, L., Hou, Y., Gao, Y., Yang, N., Liu, J. and Wang, X. (2019). Co doped α-$Ni(OH)_2$ multiple-dimensional structure electrode material. Journal of Electrochimica Acta 295: 340-346.

Luan, C., Liu, G., Liu, Y., Yu, L., Wang, Y., Xiao, Y., Qiao, H., Dai, X. and Zhang, X. (2018). Structure effects of 2D materials on α-Nickel hydroxide for oxygen evolution reaction. American Chemical Society: Nano 12(4): 3875-3885.

Miao, C., Zhu, Y., Zhao, T., Jian, X. and Li, W. (2015). Synthesis and electrochemical performance of mixed phase α/β nickel hydroxide by codoping with Ca^{2+} and PO_4^{3-}. Ionics 21(12): 3201-3208.

Motlagh, M. K., Youzbashi, A. and Sabaghzadeh, L. (2011). Synthesis and characterization of nickel hydroxide/oxide nanoparticles by the complexation-precipitation method. International Journal of Physical Sciences 6(6): 1471-1476.

Posada, J. O. G. and Hall, P. J. (2016). Towards the development of safe and commercially viable nickel-iron batteries: improvements to coulombic efficiency at high iron sulphide electrode formulations. Applied Electrochemistry 46(4): 451-458.

Shanaj, B. and John, X. (2016). Effect of calcination time on structural, optical and antimicrobial properties of nickel oxide nanoparticles. Journal of Theoretical Computer Science 3(2).

Su, Y.-Z., Xiao, K., Li, N., Liu, Z.-Q. and Qiao, S.-Z. (2014). Amorphous $Ni(OH)_2$ @ three-dimensional Ni core–shell nanostructures for high capacitance pseudocapacitors and asymmetric supercapacitors. Journal of Materials Chemistry A 2(34): 13845-13853.

Subbaraman, R., Tripkovic, D., Strmcnik, D., Chang, K.-C., Uchimura, M., Paulikas, A. P., Stamenkovic, V. and Markovic, N. M. (2011). Enhancing hydrogen evolution activity in water splitting by tailoring Li^+-$Ni(OH)_2$ - Pt interfaces. Science 334(6060): 1256-1260.

Tawonezvi, T., Bladergroen, B. J. and John, J. (2020). Development of $FeCu_x$/FeS/Graphite composite electrode materials for iron-based Alkaline batteries. Internatinal Journal of Electrochemical Science 15: 12428 – 12446.

Tsais, P.-J. and Chan, L. (2013). Nickel-based batteries: Materials and chemistry. Electricity Transmission, Distribution and Storage Systems, Elsevier: 309-397.

Wang, H., Liang, Y., Gong, M., Li, Y., Chang, W., Mefford, T., Zhou, J., Wang, J., Regier, T. and Wei, F. (2012). An ultrafast nickel–iron battery from strongly coupled inorganic nanoparticle/nanocarbon hybrid materials. Journal of Nature Communications 3: 917.

Wang, X., Luo, H., Yang, H., Sebastian, P. and Gamboa, S. (2004). Oxygen catalytic evolution reaction on nickel hydroxide electrode modified by electroless cobalt coating. International Journal of Hydrogen Energy 29(9): 967-972.

Wiston, B. R. and Ashok, M. (2019). Electrochemical performance of hydrothermally synthesized flower-like α-nickel hydroxide. Vacuum 160: 12-17.

Xia, Q. X., San Hui, K., Hui, K. N., Kim, S. D., Lim, J. H., Choi, S. Y., Zhang, L. J., Mane, R. S., Yun, J. M. and Kim, K. H. (2015). Facile synthesis of manganese carbonate quantum dots/$Ni(HCO_3)_2$–$MnCO_3$ composites as advanced cathode materials for high energy density asymmetric supercapacitors. Journal of Materials Chemistry A 3(44): 22102-22117.

Yang, L., Gao, X., Wu, Q., Zhu, H. and Pan, G. (2007). Phase distribution and electrochemical properties of Al-substituted nickel hydroxides. The Journal of Physical Chemistry C 111(12): 4614-4619.

Yin, J., Zhou, G., Gao, X., Chen, J., Zhang, L., Xu, J., Zhao, P. and Gao, F. (2019). α-and β-Phase Ni-Mg hydroxide for high performance hybrid supercapacitors. Nanomaterials 9(12): 1686.

Young, K.-H., Wang, L., Yan, S., Liao, X., Meng, T., Shen, H. and Mays, W. (2017). Fabrications of high-capacity alpha-$Ni(OH)_2$. Batteries 3(1): 6.

Yu, J., Pan, S., Zhang, Y., Liu, Q. and Li, B. (2019). Facile synthesis of monodispersed α-$Ni(OH)_2$ microspheres assembled by ultrathin nanosheets and its performance for oxygen evolution reduction. Frontiers in Materials 6: 124.

Yuan, S., Wang, X., Lu, C. and Chen, C.-M. (2016). The fine control of porous pompon-like Mg-incorporated α-$Ni(OH)_2$ for enhanced supercapacities. Functional Materials Letters 9(05): 1650057.

Zhang, Y., Chang, C.-R., Jia, X.-D., Cao, Y., Yan, J., Luo, H.-W., Gao, H.-L., Ru, Y., Mei, H.-X. and Zhang, A.-Q. (2020a). Influence of metallic oxide on the morphology and enhanced supercapacitive performance of $NiMoO_4$ electrode material. Inorganic Chemistry Communications 112: 107697.

Zhang, Y., Chang, C.-R., Jia, X.-D., Huo, Q.-Y., Gao, H.-L., Yan, J., Zhang, A.-Q., Ru, Y., Mei, H.-X. and Gao, K.-Z. (2020b). Morphology-dependent $NiMoO_4$/carbon composites for high performance supercapacitors. Inorganic Chemistry Communications 111: 107631.

Zhang, Y., Gao, H.-L., Jia, X.-D., Wang, S.-W., Yan, J., Luo, H.-W., Gao, K.-Z., Fang, H., Zhang, A.-Q. and Wang, L.-Z. (2018). $NiMoO_4$ nanorods supported on nickel foam for high-performance supercapacitor electrode materials. Journal of Renewable and Sustainable Energy 10(5): 054101.

Zhang, Y., Mei, H.-X., Cao, Y., Yan, X.-H., Yan, J., Gao, H.-L., Luo, H.-W., Wang, S.-W., Jia, X.-D. and Kachalova, L. (2021). Recent advances and challenges of electrode materials for flexible supercapacitors. Coordination Chemistry Reviews 438: 213910.

Zhang, Y., Mei, H.-X., Yang, J., Wang, S.-W., Gao, H.-L., Jia, X.-D., Yan, J., Cao, Y., Luo, H.-W. and Gao, K.-Z. (2020c). New $NiMoO_4$/$CoMoO_4$ composite electrodes for enhanced performance supercapacitors. Ionics 26(7): 3579-3590.

Zhang, Y., Yao, Q. Q., Gao, H. L., Zhang, L. S., Wang, L. Z., Zhang, A. Q., Song, Y. H. and Wang, L. X. (2015). Synthesis and electrochemical performance of MnO_2/BC composite as active materials for supercapacitors. Journal of Analytical and Applied Pyrolysis 111: 233-237.

Zheng, Y., Zhu, B., Chen, H., You, W., Jiang, C. and Yu, J. (2017). Hierarchical flower-like nickel (II) oxide microspheres with high adsorption capacity of Congo red in water. Journal of Colloid and Interface Science 504: 688-696.

Zide, D., Felix, C., Oosthuysen, T. and Bladergroen, B. J. (2020a). Electrochemical studies of the nickel-based hydroxide electrode for the oxygen evolution reaction and coulombic efficiency of the electrode. Electroanalysis 32(12): 2703-2712.

Zide, D., Felix, C., Oosthuysen, T. and Bladergroen, B. J. (2020b). The influence of copper and carbon black on electrochemical behavior of nickel positive electrode. Journal of Electroanalytical Chemistry 878: 114539.

Zimmerman, A. and Effa, P. (1984). Discharge kinetics of the nickel electrode. Journal of the Electrochemical Society 131(4): 709-713.

CHAPTER 6

6 Towards the development of a novel bipolar-based battery in aqueous electrolyte: Evaluation of the electrochemical properties of NiCu based hydroxide electrodes fabricated on Ni–mesh and graphite composite current collectors

THIS CHAPTER HAS BEEN PUBLISHED:

Zide, D., Felix, C., Oosthuysen, T., Burfeind, J., Grevé, A. and Bladergroen, B.J., 2022. Towards the development of a novel bipolar-based battery in aqueous electrolyte: Evaluation of the electrochemical properties of NiCu based hydroxide electrodes fabricated on Ni–mesh and graphite composite current collectors. *Journal of Energy Storage*, 45, p.103719.

6.1 Abstract

The use of bipolar electrodes in rechargeable batteries can improve specific power, simplify cell design, and reduce manufacturing costs. However, bipolar-based batteries still suffer from many drawbacks. Therefore, developing high-performance active materials and developing improvement strategies encompassing the entire cell's design is essential. The current collector significantly impacts the viability of mass production; however, it is the most neglected feature of electrochemical energy storage devices. The current collector serves a dual purpose; it allows the movement of electrons among active electrode material and provides mechanical support. It can also act as transportation of current to terminals of the battery. This study constructed a novel bipolar battery cell utilizing graphite as a current collector, and its discharge capacities for Ni-Fe battery applications were evaluated. Monopolar NiFe cells, one using a graphite substrate current collector and the other using a Ni-mesh current collector, were used for comparison. The monopolar-based electrode coated onto a graphite substrate demonstrated a 29% (199 mAh/g) higher discharge capacity than the Ni-mesh-based electrode (142mAh/g) after the 100th cycle. In contrast, the bipolar-based NiFe battery cell resulted in a discharge capacity of 158 mAh/g after the 100th cycle, corresponding to a coulombic efficiency of 72%.

Key Words: Bipolar NiFe battery; monopolar electrode; graphite substrate; Ni-mesh substrate; current collector; β-nickel copper hydroxide cathode; Iron-copper anode.

6.2 Introduction

The assembling of bipolar batteries' knowledge originates at the initiation of electrochemical science from the voltaic pile battery (Bruce, 1997). The initial Pb-acid-based bipolar battery that utilized a pile of hallow-shaped electrodes dived by glass balls was patented by Tribelhorn in 1897 (Bruce, 1997). A maximum power density of 35 kW/kg was obtained by Kapitza in 1923 when he immersed a Pb plate in an electrolyte solution made of H_2SO_4 to contract a bipolar Pb-acid battery (Bruce, 1997; Liu, Tiefeng *et al.*, 2020). However, due to short-circuiting bipolar Pb-acid that employed liquid electrolytes went in vain. Since then, bipolar electrode designs have been introduced into the design of various battery chemistry technologies such as nickel-metal hydrides (Chang *et al.*, 2016), Li-ion batteries and post-Li ion batteries, Li-S batteries (Kim, Se-Hee *et al.*, 2019), and Na-ion batteries (Alamgir and Abraham, 1995; Peled *et al.*, 1995; Liu, Tiefeng *et al.*, 2019; Liu, Tiefeng *et al.*, 2020). Some researchers incorporate the bipolar plate design into alkaline batteries of Al and Zn metals as active electrode materials for high-power operation (Müller *et al.*, 1995; Rota *et al.*, 1995; Ullah *et al.*, 2011). Golodnitsky and co-workers donated to the essential understanding and archetypal design utilizing the Li/CPE/FeS_2 batteries (Livshits *et al.*, 2001).

Currently, research scientists are investigating the technological drawbacks that hinder the advances of the bipolar construction (Gambe *et al.*, 2015; Janek and Zeier, 2016; Jung *et al.*, 2019; Liu, Tiefeng *et*

al., 2020), which include (i) possible inner short-circuiting among cell units caused by the electrolyte, (ii) the possible bipolar plates decomposition vulnerability and (iii) complex cell stacking production progressions. Thus, developing high-performance active materials and developing strategies encompassing the entire cell's design is essential. The current collector is a commonly ignored constituent of electrochemical-based energy storage devices, which significantly impacts the viability of upscaling. The current collector serves a dual purpose; it allows the movement of electrons among active electrode material and provides mechanical support. It can also act as transportation of current to terminals of the battery. The current collector should have a relatively low-cost, high electrical conductivity, high mechanical strength, and good (electro) chemical stability in the electrolyte under various operating potentials to be suitable for profitable high-powered aqueous devices. Additionally, thin and lightweight current collectors are essential for the typical capacity and weight (Ng *et al.*, 2009; Zhou *et al.*, 2012; Yan, Jun *et al.*, 2014; Gheytani *et al.*, 2016; Yamada *et al.*, 2016). It is, however, challenging to design or select current collectors that simultaneously satisfy all or most of these critical requirements.

Carbon-based current collectors are firm over a broader scope of electrolytes and have many advantages over metals as current collectors (Zuo *et al.*, 2017). The carbon current collector/electrode interface typically has lower contact resistance because of the passivating oxide film (Wu *et al.*, 2009). Due to large kinetic overpotentials, carbon can suppress hydrogen and oxygen evolution, improving electrochemical stability over a wider potential window in aqueous electrolytes (Lukatskaya *et al.*, 2017). Therefore, various carbon materials have been studied as current collectors. Although the use of carbon fibre, carbon nanotube papers, and mats have been explored as current collectors, these current collectors are porous, fragile, and not suitable for practical applications (Yan, Jun *et al.*, 2014; Liu, Tiefeng *et al.*, 2020). Various researchers have studied expanded graphite foils and have shown that it is ideal as current collectors for aqueous electrochemical energy storage (Whitacre *et al.*, 2012; Dyatkin *et al.*, 2013; Ziv *et al.*, 2013; Blomquist *et al.*, 2017).

In monopolar design, current collectors, also called monopolar plates, act as negative (anode) or positive (cathode) electrodes (Shen and Halpert, 1993; Karami *et al.*, 2003; Gambe *et al.*, 2015; Yoshima *et al.*, 2016; Jung *et al.*, 2019). These monopolar configurations are typically composed of a number of cells linked in a series by external wire, resulting in reduced gravimetric or volumetric energy density of a battery unit. Nevertheless, this increases the cost of material and intricacy of the battery. The advantages of a typical monopolar configuration include easy construction of unit cells in the presents of liquid-based electrolytes. The limitations are high power and high voltage applications owing to the external electrical connections causing increased resistance due to long electron pathways (Jung *et al.*, 2019). For example, on discharge, the electrons that move from the anode of one cell travels through the in-

plane of the monopolar plate towards a negative terminal. Then, it moves via the outer wire towards the positive terminal of the next cell. Lastly, from the in-plain of the monopolar plate to enter the cathode.

The downsides of monopolar-based batteries encourage the development and evaluation of the bipolar-based electrode for Ni-Fe application. Contrary to monopolar design, external wiring is evaded in bipolar design, where the bipolar plate connects several cells in series. The exclusion of external wiring does not only gives an operative manner to mount and join the cells, but it also diminishes the electrical resistance, volume, weight, and cost of a typical bipolar-based battery (Jung *et al.*, 2019; Kim, Se-Hee *et al.*, 2019). Moreover, in a bipolar battery, anode and cathode materials are placed on opposite sides of a conductive substrate, which allows the through-plane movements of electrons to the next cell. The through-plane movement of electrons provides a quicker electrical pathway and a minimized power loss owing to the Ohmic drop in the circuit. Additionally, eradicating external circuit constituents like terminals, straps, and poles can reduce the volume of the battery (Lukatskaya *et al.*, 2017; Jung *et al.*, 2019).

This study prepared and evaluated a novel bipolar battery cell using a $Ni_{0.75}Cu_{0.25}(OH)_2$ cathode and a $FeCu_{0.25}$ anode with graphite composite as the current collector for Ni-Fe battery devices. Though the compactness of a bipolar battery configuration offers interesting advantages, it also poses some challenges. Charging and discharging parameters are applied over the entire stack without individual cell control and balancing, typically performed by a battery management system. This limitation requires robust electrode chemistry that is not sensitive to undercharge and overcharge conditions, rendering Li-ion battery chemistries less suitable in bipolar battery configuration. Ni-Fe batteries show some renewed interest in renewable energy applications due to their potentially long life, robust and durable qualities (Abdalla *et al.*, 2016; Posada and Hall, 2016; Chen, Wei *et al.*, 2018). However, the Ni-Fe battery suffers from drawbacks such as low efficiency (50% - 60%) and low specific energy. Ni-Fe batteries are typically confined to stationary applications due to its heavy and bulky design; however, with the bipolar design and the use of a thermoplastic graphite composite bipolar plate, weight and size reductions may be achieved, extending the possible applications of Ni-Fe batteries.

In an attempt to mitigate the aforementioned downsides of Ni-Fe batteries, in our previous studies, the active materials for both the anode (Tawonezvi *et al.*, 2020) and cathode (Zide *et al.*, 2020a, b, 2021) were optimized. A summary of our findings are as follows: Among different metal dopants (Mn^{2+} (Zide *et al.*, 2021), Mg^{2+} (Zide *et al.*, 2021), Co^{2+} (Zide *et al.*, 2020a), Al^{3+} (Zide *et al.*, 2020a) and Cu^{2+} (Zide *et al.*, 2020b) at different ratios (0.95:0.05; 0.9:0.1; 0.75:0.25 and 0.5:0.5) of Ni: metal dopants (Mn^{2+}, Mg^{2+}, Co^{2+}, Al^{3+} and Cu^{2+}) 0.75:0.25 Ni:Cu was found to be the optimal ratio and the best composition in terms of electrochemical performance as reported in our publications (Zide *et al.*, 2020a, b, 2021). In one of our in-house studies (Tawonezvi *et al.*, 2020), Fe electrode material was synthesized and evaluated for its electrochemical performance. The study utilized a combination of both Cu and FeS

additives plus graphite particles. Briefly, FeS/C substituted Fe-Cu composite material was synthesized as anode material to be utilized in Fe-based alkaline batteries. The rationale behind this was that Cu should circumvent Fe particle agglomeration during cycling, graphite should formulate a good conductive network, subsequently improving the reversibility of the active material, and FeS should impede the parasitic hydrogen evolution reaction and the passivation process. The FeCu0.25/15%FeS/5%C electrode exhibited stable performances marked by high specific capacity coupled with negligible capacity decay and high efficiency.

In this work, we attempted to further improve the performance and practicality of the Ni-Fe battery by using a bipolar configuration. In this study, the polypropylene graphite sheets were developed and supplied by Fraunhofer UMSICHT, Germany. By using a heated multi-roll rolling mill and a compound of graphite, carbon black, and a thermoplastic elastomer, Fraunhofer UMSICHT has successfully manufactured a conductive and highly flexible bipolar plate in a continuous one-stage process (Kopietz *et al.*, 2018). When the roll size or welding of several sheets was used, the polypropylene graphite sheets could be manufactured in any size up to several square meters and current thicknesses down to 0.4 mm (Kopietz *et al.*, 2018). The manufactured polypropylene graphite sheets are gas-tight, chemical resistant, mechanically stable, and allow for a subsequent reshaping. The specification of as-prepared polypropylene graphite sheets by Fraunhofer UMSICHT (Kopietz *et al.*, 2018) are summarized in Table 4.

Table 4: Bipolar plate specifications (Sourced (Kopietz *et al.*, 2018))

Norm	Elastic modulus	Tensile strength	Filling grade	In-plane conductivity	Through-plane conductivity
DIN EN ISO 527-3	1100 N/mm²	7.4 N/mm²	80% Graphite 20% PP	250 S/m - 500 S/m (Depending on the carbon content, particle size, and morphology)	In-plane conductivity exceeds the through-plane conductivity consistently by a factor of 10 to 100

DIN EN ISO 527-3 tensile tests have shown an elastic modulus of 1100 N/mm² as well as a tensile strength of 7.4 N/mm² at a strain of 1.6% and filling grade of 80% graphite and carbon black (Kopietz *et al.*, 2018). Depending on the carbon content, particle size, and morphology, the in-plane conductivity of the polypropylene graphite sheets ranges from 250 S/m up to 5000 S/m and exceeds the through-plane conductivity consistently by a factor ranging from 10 to 100 (Kopietz *et al.*, 2018).

Currently, the authors could not find any literature reporting on a bipolar Ni-Fe battery. The results of this study are presented systematically. First, the electrochemical discharge capacities of two battery cells consisting of monopolar electrodes prepared with graphite composite film and Ni-mesh substrates

as the current collectors, respectively, are evaluated and compared. In addition, a bipolar-based battery cell consisting of a bipolar electrode prepared with a graphite substrate as the current collector is assessed as a novel bipolar Ni-Fe battery. Advantages of using a standard bipolar-based electrode include but are not limited to improved specific power, simplify cell mechanisms, and reduce engineering costs aimed at secondary batteries.

6.3 Material and methods

6.3.1 Materials

The $Ni_{0.75}Cu_{0.25}(OH)_2$ material was synthesized using analytical grade materials, the in-house $FeCu_{0.25}$ was used as the anode electrode material (Tawonezvi *et al.*, 2020). Ni-mesh was obtained from Q-Lite Batteries in China, and the modified graphite substrate was obtained from Fraunhofer Umsicht (Germany). Lithium monohydrate and potassium hydroxide were purchased from KIMIX (South Africa).

6.3.2 Synthesis of $Ni_{0.75}Cu_{0.25}(OH)_2$

The $Ni_{0.75}Cu_{0.25}(OH)_2$ material was prepared as explained by Zide and co-workers (Zide *et al.*, 2020b). Briefly, a solution composed of NaOH and Na_2CO_3, and the second solution contained Ni^{2+} as $Ni(NO_3)_2 \cdot 6H_2O$ salt and Cu^{2+} as $Cu(NO_3)_2 \cdot 3H_2O$ salt were prepared. These solutions were titrated dropwise while continuously stirred at room temperature. The resulting slurry was aged further for 30 min, then hydrothermally treated at 65^{o}C for 18h, cooled at room temperature, then sieved and splashed with Milli Q water. The final residues were then dried at 110^{o}C for 12h.

6.3.3 Electrode Preparation

The $Ni_{0.75}Cu_{0.25}(OH)_2$ electrodes were fabricated by thoroughly mixing 85 wt.% active material, 10 wt.% Coathylene binder and 5 wt.% carbon black. The schematic diagram for the electrode production is shown in Figure 6-1.

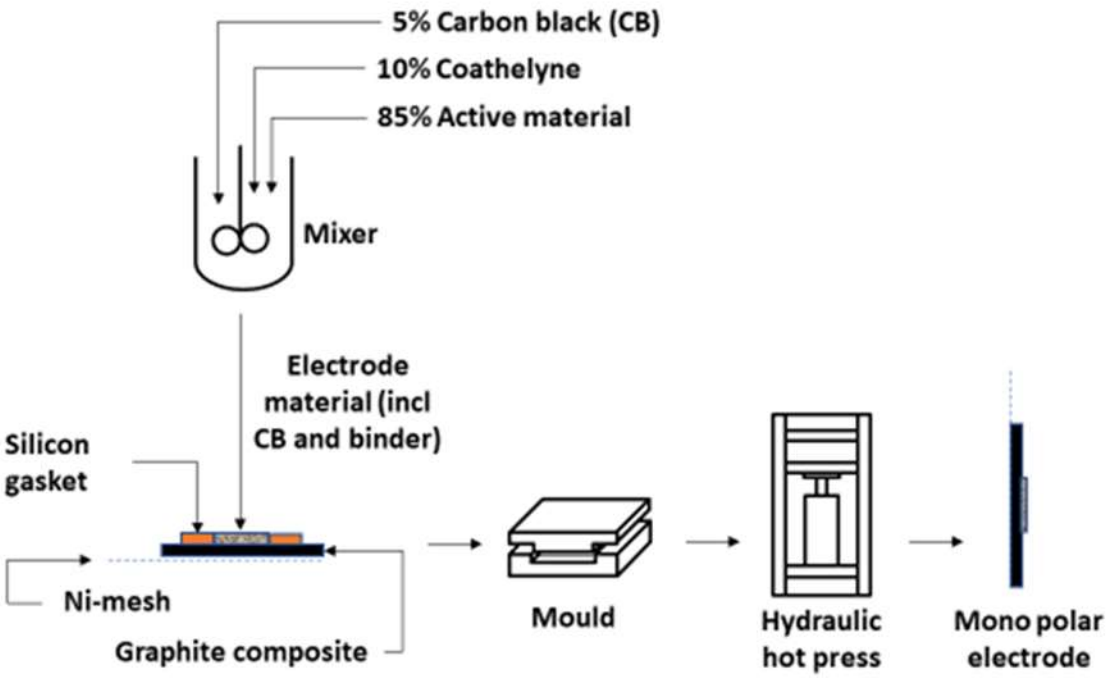

Figure 6-1: Schematic illustration of the construction process flow of the Ni-based electrode production

Briefly, the composite materials were hot-pressed onto a substrate (nickel mesh and graphite) using a custom-built hydraulic press with integrated hot plates (HyJack, Cape Town). The pressure of the hydraulic system was set at 6 MPa, which corresponds to 61.18 kgf/cm^2. The pressing process was started after the pressure plates reached 80˚C. The compaction pressure on the sample was maintained for 5 min to ensure good electrical contact between the substrate and active material.

6.3.4 Galvanostatic capacity measurements

Galvanostatic capacity measurements were conducted in a two-electrode setup consisting of the in-house $FeCu_{0.25}$ anode and $Ni_{0.75}Cu_{0.25}(OH)_2$ cathode electrodes in a 6M KOH/1M LiOH electrolyte. The monopolar electrodes using Ni-mesh and graphite composite substrates were evaluated first for their discharge capacities. Subsequently, a bipolar cell consisted of a bipolar graphite composite electrode coupled with two Ni-mesh monopolar electrodes.

6.4 Results and Discussion

6.4.1 Structural characterization of $Ni_{0.75}Cu_{0.25}(OH)_2$

Figure 6-2 provides the structural characterization of $Ni_{0.75}Cu_{0.25}(OH)_2$ (Figure 6-2a) compared to the unmodified $Ni(OH)_2$ (Figure 6-2b). The diffraction patterns were obtained using a multi-purpose X-ray Diffractometer D8-Advance from BRUKER AXS (Germany).

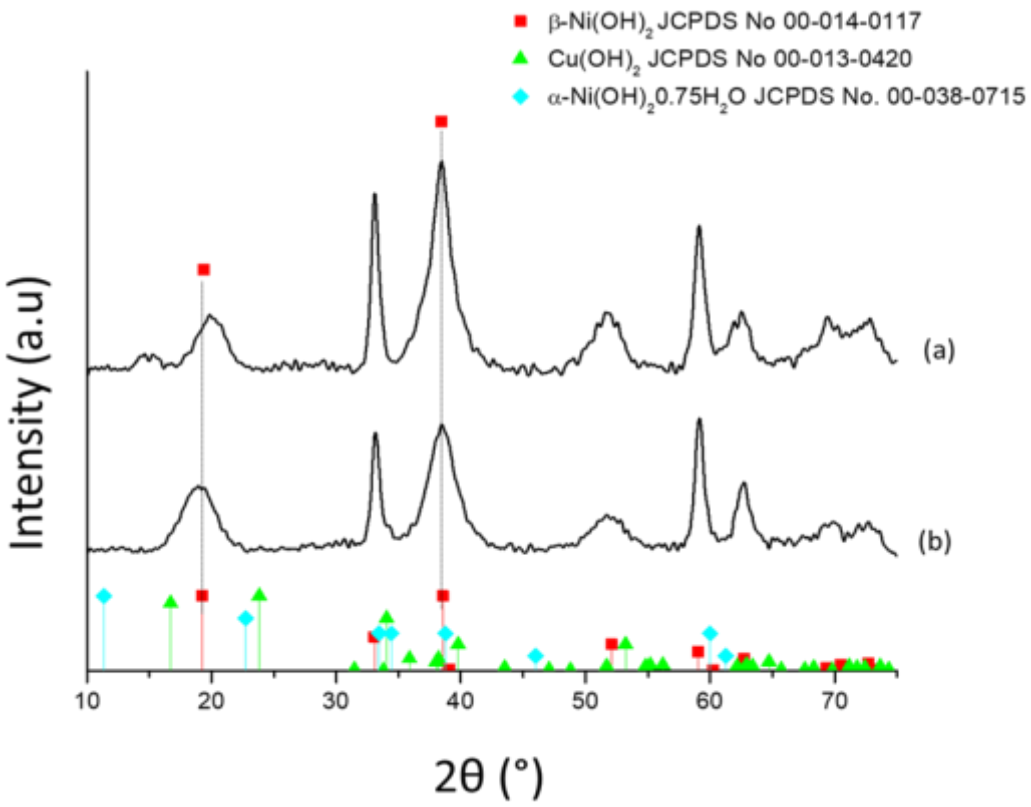

Figure 6-2: Diffractogram of (a) $Ni_{0.75}Cu_{0.25}(OH)_2$ and (b) unmodified $Ni(OH)_2$

Diffraction angles of 20.024°, 32.964°, 38.43°, 51.769°, and 59.106° were observed for the $Ni_{0.75}Cu_{0.25}(OH)_2$. While the diffraction pattern shows a close fit of the Joint Committee on Powder Diffraction Standards (JCPDS) of β-$Ni(OH)_2$ (JCPDS No 00–014-0117), there is no evidence for the presence of crystalline $Cu(OH)_2$ (JCPDS No 00–013-0420). A clear shift to the right is observed for the diffraction angle at about 20°. The shift to the left at this diffraction angle (~20°) may be explained by the fact that the Cu^{2+} has an ionic radius of 0.73 Å [11] which is slightly higher than Ni^{2+} (0.72 Å). In addition, the elemental composition from ICP (0.75:0.25) and SEM/EDS (0.74: 0.26) were in agreement with the intended composition of $Ni_{0.75}Cu_{0.25}(OH)_2$.

6.4.2 Electrochemical characterization of $Ni_{0.75}Cu_{0.25}(OH)_2$

6.4.2.1 Comparison of NiFe battery cells consisting of monopolar electrodes prepared with graphite composite and Ni-mesh substrates as current collectors

Figure 6-3 shows the charge-discharge curves of the battery cells prepared with the two monopolar electrode types after the 100th cycle. Two plateaus are observed, which may be represented by the reactions in Equation 5-6 and Equation 6-2 (Hariprakash *et al.*, 2005; Wang, Hailiang *et al.*, 2012; Tsais and Chan, 2013).

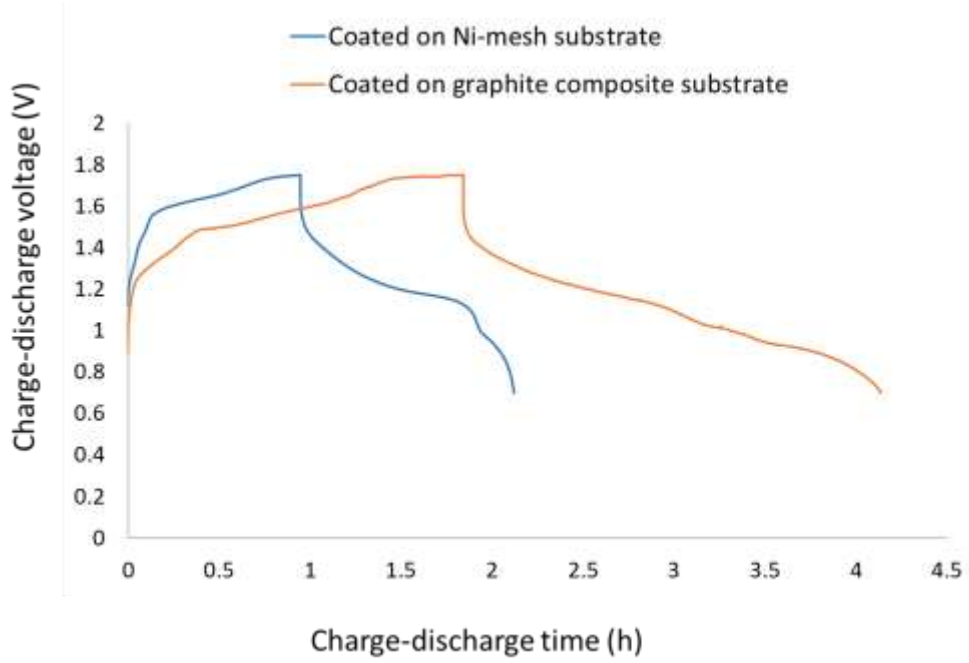

Figure 6-3: Evaluation of the NiFe battery cells with monopolar- electrodes: time-voltage-current charge-discharge curves of $Ni_{0.75}Cu_{0.25}(OH)_2$ at the 100th cycle

The reaction in Equation 5-6 is typically formed during the discharge of a NiFe battery cell with a negative limited configuration (Hariprakash *et al.*, 2005; Wang, Hailiang *et al.*, 2012; Tsais and Chan, 2013). The discharge reaction (Equation 5-6) can further proceed in a second step (Equation 6-2) at a potential lower than the first step (Equation 5-6) (Hariprakash *et al.*, 2005).

Equation 6-1: First plateau of charge-discharge reaction of NiFe battery electrode

$$Fe + 2NiOOH + 2H_2O \underset{\text{Charge}}{\overset{\text{Discharge}}{\rightleftharpoons}} 2Ni(OH)_2 + Fe(OH)_2 \qquad \text{First plateu (Ecell} = 1.37\text{V)}$$

Equation 6-2: Second plateau of charge-discharge reaction of NiFe battery electrode

$$3Fe(OH)_2 + 2NiOOH \underset{\text{Charge}}{\overset{\text{Discharge}}{\rightleftharpoons}} 2Ni(OH)_2 + Fe_3O_4 + 2H_2O \qquad \text{Second plateau (Ecell} = 1.05\text{V)}$$

During charge-discharge, the electrolyte remains fundamentally invariant and plays no part in the NiFe battery's overall reaction (Equation 3) although, the individual electrode reactions involve an intimate reaction with the electrolyte (Tsais and Chan, 2013).

Equation 6-3: Overall charge-discharge reaction of NiFe battery electrode

$$3Fe + 8NiOOH + 4H_2O \underset{\text{Charge}}{\overset{\text{Discharge}}{\rightleftharpoons}} 8Ni(OH)_2 + Fe_3O_4 \qquad \text{Overall reaction}$$

As shown in Figure 6-4, constant discharge capacities were observed over the 100 cycles with no noticeable drop in discharge capacities.

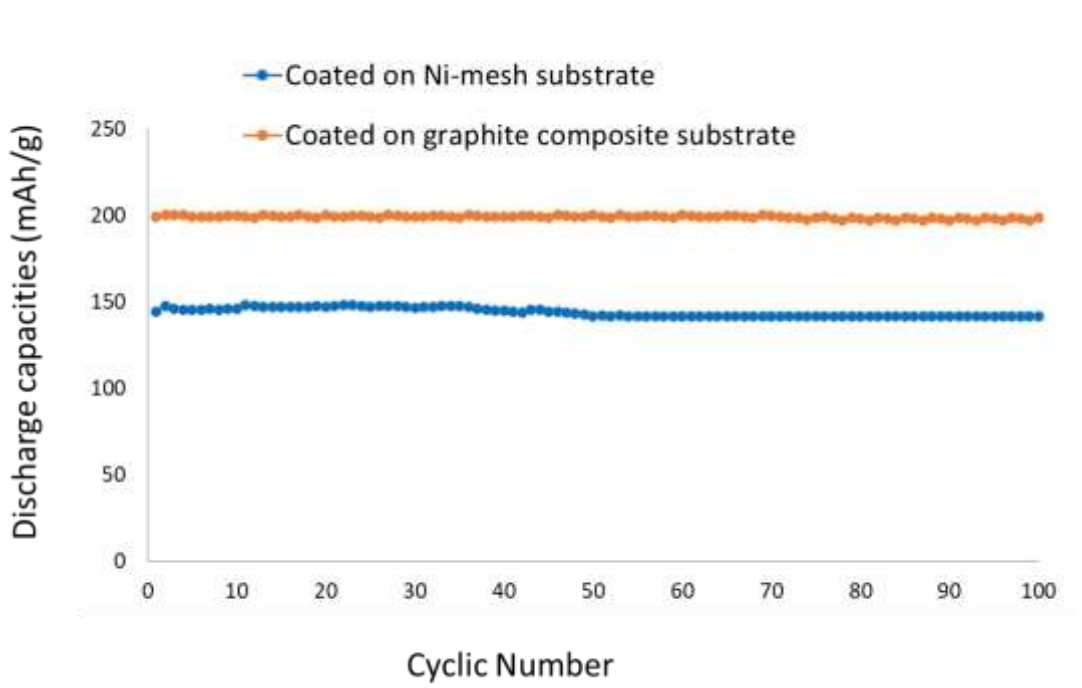

Figure 6-4: Evaluation of the NiFe battery cells with monopolar- electrodes: specific discharge capacity curves over 100 cycles for $Ni_{0.75}Cu_{0.25}(OH)_2$.

The electrodes demonstrated a discharge capacity of 144 mAh/g and 199 mAh/g after the 100^{th} cycles, corresponding to a coloumbic efficiency of 87% and 84% for monopolar electrodes with Ni-mesh and graphite substrates, respectively.

Graphite is more chemically stable compared to metals during potential cycling. Metals are known to corrode, which may lead to morphology changes that can increase interfacial contact resistance between the active material and the substrate. Additionally, metals are known to form surface oxides that lead to increased interfacial contact resistance between the active material and the substrate (Yeetsorn *et al.*, 2011; Zhong *et al.*, 2020; Fatima *et al.*, 2021). It appears that such side reactions may have contributed to the lower performances of the Ni-mesh substrate-based electrodes; however, additional experiments are required to evaluate such a claim. Thermoplastic composite bipolar plates have the advantage over metallic plates of being more resistant to chemical attack, flexible and lightweight (Yeetsorn *et al.*, 2011; Zhong *et al.*, 2020; Fatima *et al.*, 2021); however, in this study, the chemical stability is probably the main factor in improving the graphite-based cell's performance.

Table 6-5 summarises the test parameters and the discharge capacities obtained for the battery cells consisting of the two monopolar electrodes types after various charge-discharge cycles. The discharge

capacities (over 1st cycle, 10th cycle, 50th cycle and 100th cycle) provided in Table 6-5 are the obtained specific discharge capacities after the activation step (30 cycles). As evident in Table 6-5, the electrode fabricated on Ni-mesh showed a lower discharge capacity after the 100th cycle compared to the electrode fabricated on graphite substrate as the current collector.

Table 6-5: Electrochemical test specifications for the NiFe battery cells with the two monopolar electrode types.

Electrochemical test specifications	**A**				**B**			
Cathode and anode substrate	2 cm x 2 cm Ni-mesh sheet				2 cm x 2 cm graphite composite (80% Graphite, 20% Poly propylene, Fraunhofer Umsicht			
Cathode active mass loading (limited)	0.2 g $Ni_{0.75}Cu_{0.25}(OH)_2$				0.2g $Ni_{0.75}Cu_{0.25}(OH)_2$			
Anode active mass loading	0.9 g $FeCu_{0.25}$				0.9 g $FeCu_{0.25}$			
Electrolyte	6M KOH/1M LiOH				6M KOH/1M LiOH			
The charge cut off voltage (V)	1.75 V				1.75 V			
Discharge cut off voltage (V)	0.7 V				0.7 V			
Specific CC charge and discharge current	100 mA/g				100 mA/g			
Numbers of cycles	1	10	50	100	1	10	50	100
Electrode capacity (mAh)	28.8	29.6	28.3	28.3	39.9	39.9	40.0	39.7
Specific capacity (mAh/g)	144	146	142	142	199	200	200	199
Coulombic efficiency				87%				84%

6.4.3 Bipolar-based NiFe battery cell with bipolar electrode prepared with graphite substrate as the current collector

In order to develop the bipolar-based Ni-Fe battery cell, a bipolar electrode was prepared by depositing the anode material ($FeCu_{0.25}$) on one side of the graphite substrate and the cathode material (85% $Ni_{0.75}Cu_{0.25}(OH)_2$, 10% Coathylene binder and 5% carbon black) on the other side. The bipolar-based NiFe battery cell was evaluated using a two-chamber cell (Figure 6-5).

The configuration used demonstrates the design that an up-scaled bipolar Ni-Fe battery would follow. The thermoplastic graphite composite material has a much lower weight and better corrosion resistance than the Ni-mesh. Therefore, it will be utilized as the bipolar plate, which is a constituent of every cell of the bipolar battery. This will be a key factor in reducing the overall stack complexity, weight, and size of the Ni-Fe battery. The electronic conductivity of a Ni-Mesh is almost 20 times higher than the electronic conductivity of the graphite bipolar plate. In a bipolar electrode, the current only flows in the through-plane direction over a distance of 50 microns. In the endplate, the current needs to flow in the

in-plane direction towards the external terminals. The ohmic resistance observed in an endplate is therefore far greater than for a central bipolar electrode.

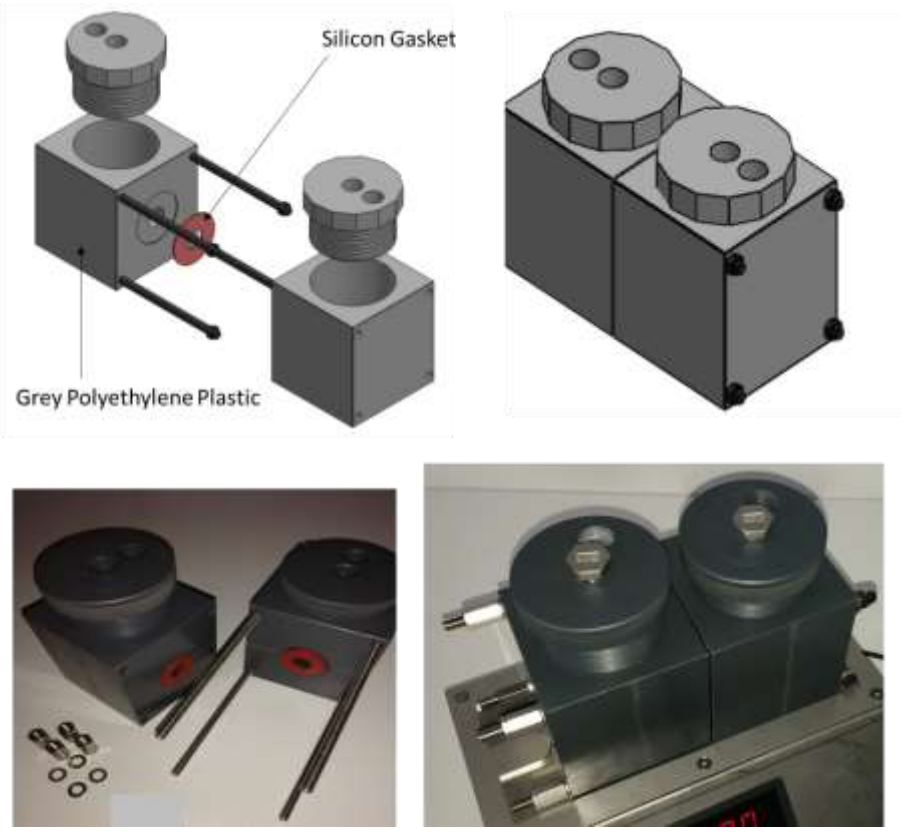

Figure 6-5: Drawings and pictures of the two-chamber test cell.

The bipolar electrode (Figure 6-6) was placed at the chamber's centre (Figure 6-5), and the anodic and cathodic monopolar current collectors were positioned inside each chamber, as demonstrated in Figure 6-7.

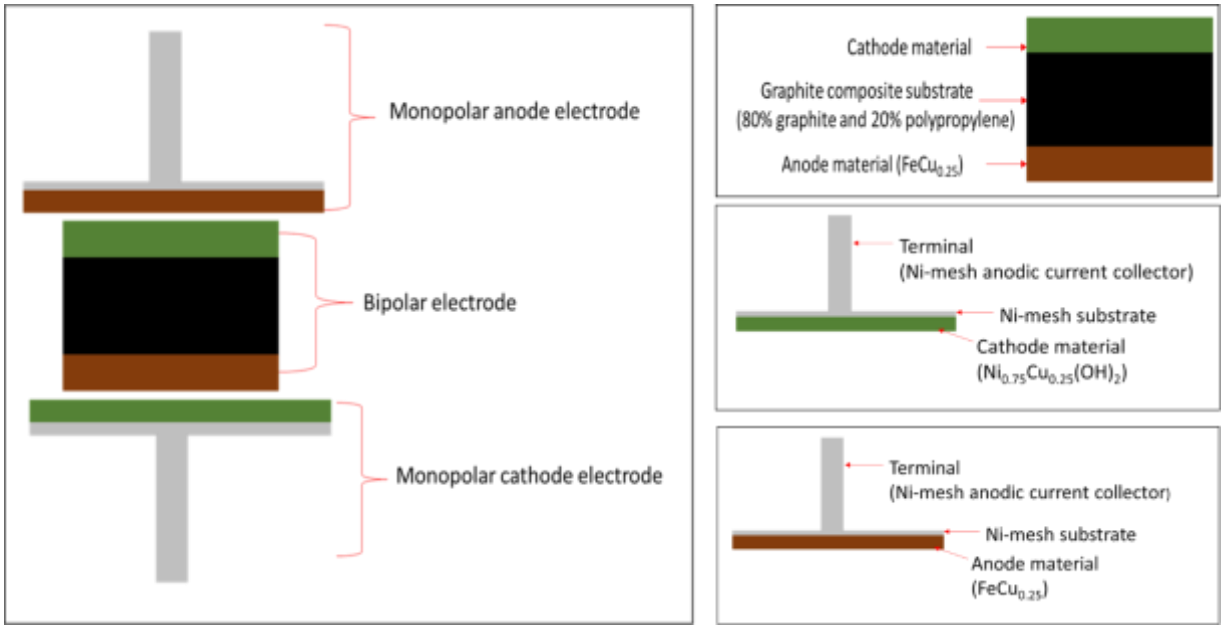

Figure 6-6: Schematic representation of the construct of the bipolar based NiFe Cell.

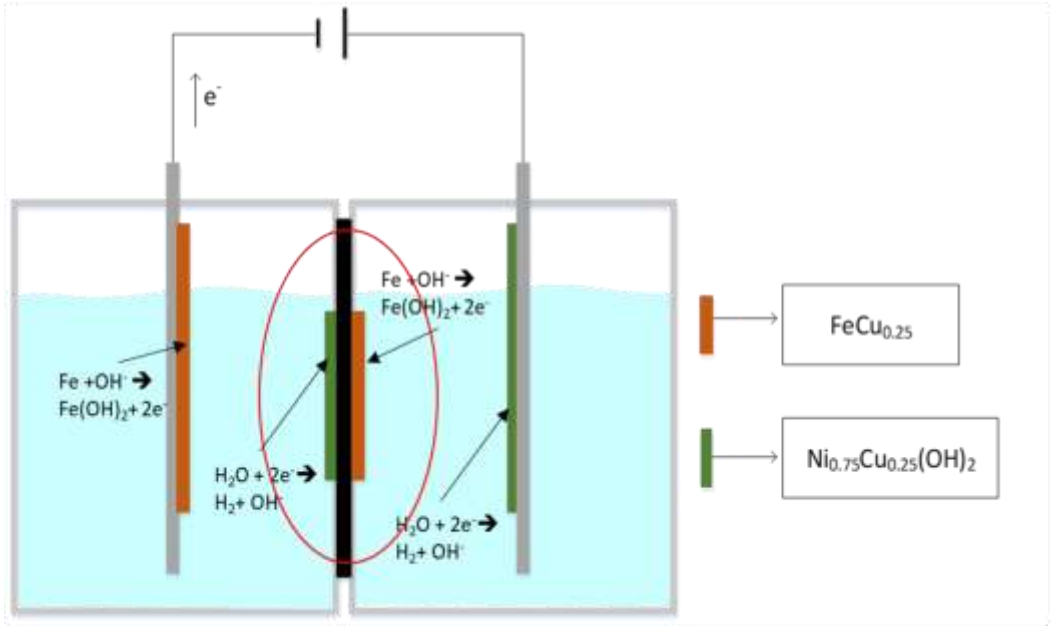

Figure 6-7: Schematic diagram of a typical bipolar galvanostatic cell

The charge-discharge cut-off voltage-limiting was kept at 3.5 V - 0.7 V, and the cut-off current-limiting was set at 500 mA/g for both electrodes. The time-voltage charge-discharge curves of the bipolar based Ni-Fe cell at the 1st ,10th , 50th, and 100th cycle is shown in Figure 6-8. The presence of two plateaus may denote the reactions in Equation 5-6 and Equation 6-2 (Hariprakash *et al.*, 2005; Wang, Hailiang *et al.*, 2012; Tsais and Chan, 2013).

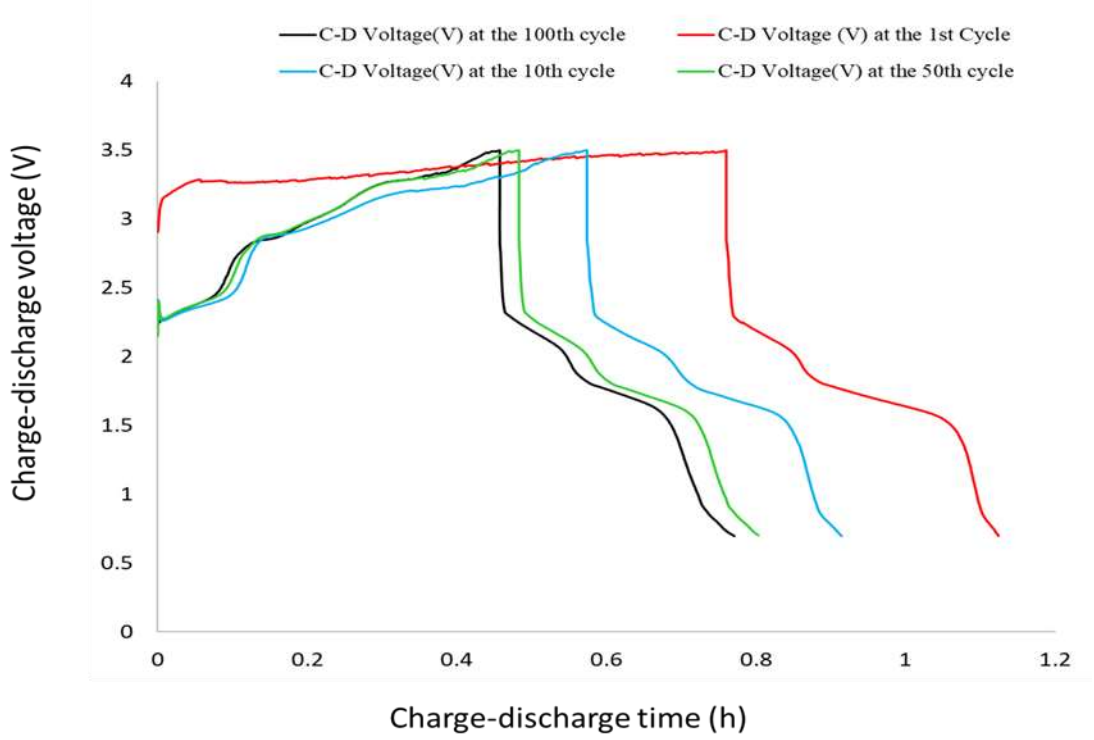

Figure 6-8: Evaluation of the bipolar-based NiFe battery cell: time-voltage charge-discharge curves at the 1st, 10th, 50th, and the 100th cycle.

It is noteworthy that the activation process is a fundamental step in secondary alkaline battery technology. The electrode exhibited superlative cycling stability as it retained 88% (158 $mAhg^{-1}$) of the initial discharge capacity (180 $mAhg^{-1}$). This is attributed to the ability of Cu to lower the particle surface energy through its highly conductive network embedded in the electrode (Huang, Lanxiang *et al.*, 2018; Tawonezvi *et al.*, 2020). There were no noticeable changes in terms of plateau voltages observed between the 1^{st}, 10^{th}, $50^{th,}$ and the 100^{th} cycle charge-discharge profiles. However, the long-distance observed between the cycle charge-discharge profiles could be due to the differences in coulombic efficiencies, which are 51% (180 $mAhg^{-1}$), 63% (169 $mAhg^{-1}$), 70% (156 $mAhg^{-1}$), and 72% (158 $mAhg^{-1}$) for the 1^{st}, 10^{th}, 50^{th} and the 100^{th} cycle charge-discharge profiles. Therefore, 49% of the energy stored during the 1^{st} charge cycle was wasted as only 51% was released on the 1^{st} discharge cycle.

Figure 6-9 shows the specific discharge capacity curves of the bipolar-based Ni-Fe cell after 100 cycles. Discharge capacities were observed over 100 cycles with no noticeable drop in discharge capacity after the 20^{th} cycle (activation). The electrode demonstrated a discharge capacity of 158 mAh/g after the 100^{th} cycle, corresponding to a coloumbic efficiency of 72% and 87% cell capacity remaining.

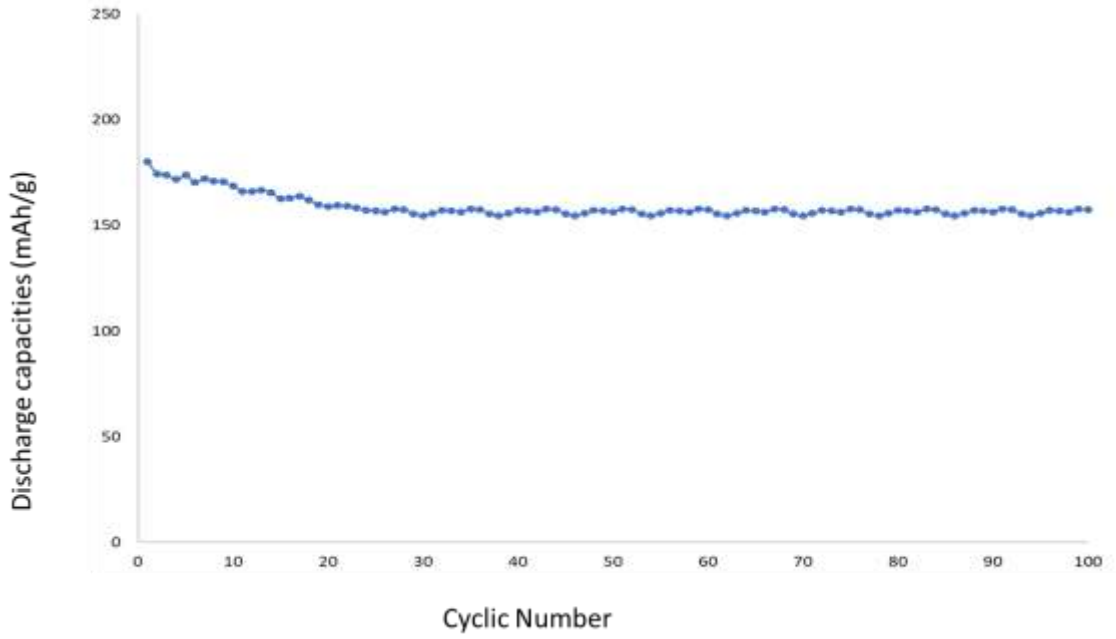

Figure 6-9: Evaluation of the bipolar-based NiFe battery cell: specific discharge capacity curve over 100 cycles.

A summary of the test parameters and the discharge capacities obtained for the bipolar-based Ni-Fe electrode is shown in Table 6-6. The discharge capacities over the 1st, 10th, 50th, and 100th cycles presented in Table 6-6 were attained after the activation step (30 cycles).

Table 6-6: Electrochemical test specifications for the bipolar-based NiFe cell.

Electrochemical test specifications	**Bipolar cell**			
Monopolar cathode / anode substrate	5 cm x 5 cm Ni-mesh sheet			
Cathode active mass loading on a monopolar electrode	1.0 g $Ni_{0.75}Cu_{0.25}(OH)_2$			
Anode active mass loading on a monopolar electrode	2.5 g $FeCu_{0.25}$			
Bipolar substrate	10mm diameter graphite composite (80% Graphite, 20% Poly propylene, Fraunhofer Umsicht)			
The active area of the bipolar substrate	0.8cm^2			
Cathode active mass loading on a bipolar electrode	0.04 g $Ni_{0.75}Cu_{0.25}(OH)_2$			
Anode active mass loading on a bipolar electrode	0.08 g $Fe_{0.75}Cu_{0.25}$			
Electrolyte	6M KOH/1M LiOH			
The charge cut off voltage (over 2 cells effectively)	3.5 V			
Discharge cut off voltage (over 2 cells effectively)	0.7 V			
Specific CC charge and discharge current (mA/g)	500			
Numbers of cycles	1	10	50	100
Electrode capacity (mAh)	7.2	6.7	6.3	6.3
Specific capacity (mAh/g)	180	169	156	158
Coulombic efficiency	-	-	-	72%

6.5 Conclusion

In order to move to even thinner bipolar plates and prevent unacceptable mechanical strain in the electrodes, the technological challenges related to the production of reproducible bipolar electrodes need to be improved. A thermoplastic graphite composite bipolar plate consisting of graphite and polypropylene was developed and utilized in this study, which aids with the mechanical properties of the bipolar plate by increasing the flexibility and reducing the required thickness cell (Yeetsorn *et al.*, 2011; Zhong *et al.*, 2018; Zhong *et al.*, 2020; Fatima *et al.*, 2021).

A novel bipolar design for the Ni-Fe battery was successfully prepared, and the preliminary results for cell discharge capacities are presented. Three NiFe battery cell types were prepared and gauged for their charge-discharge capacities. The first two cell types consisted of monopolar electrodes. One cell used the graphite composite as the current collector, and the other cell used the Ni-mesh substrates as the current collector. The third cell type consisted of a bipolar electrode prepared with a graphite substrate as the current collector coupled to two monopolar electrodes composed with Ni-mesh substrates as current collectors.

The two cells with monopolar electrodes demonstrated discharge capacities of 144 mAh/g and 199 mAh/g after the 100^{th} cycles, corresponding to coloumbic efficiencies of 87% and 84% for the monopolar-based electrodes fabricated on Ni-mesh and graphite substrate, respectively. The bipolar-based NiFe battery two-cell demonstrated a discharge capacity of 158 mAh/g after the 100^{th} cycle, corresponding to a coloumbic efficiency of 72%. Physical characterization such as scanning electron microscopy (SEM) and additional electrochemical characterizations such as electrochemical impedance spectroscopy and conductivity measurements of the electrodes are needed to understand the reasons for the improved discharged capacity observed when the graphite composite was used as compared to the Ni-mesh used as the current collector. The discharge capacities for bipolar NiFe cells were notably lower than the monopolar electrode using the graphite composite as the current collector. Thus, these characterizations will form part of future research to enable improvements to the bipolar NiFe battery design.

6.6 Data availability statement

Upon a reasonable request, the data that support the finding of this study may be obtainable from the corresponding author.

6.7 Contributor Roles Taxonomy (CRediT) author declaration

Dorcas Zide: Conceptualization, methodology, software, data validation, formal analysis, investigation, resources, writing of the original draft, review and editing of the final draft, supervision and project administration. **Cecil Felix:** review and editing of the final draft. **Tobie Oosthuysen:** review and editing of the final draft. **Jens Burfeid:** review and editing of the final draft. **Anna Grevé**: review

and editing of the final draft. **Bernard Jan Bladergroen:** Conceptualization, software, resources, review and editing of the final draft, and supervision.

6.8 Declaration of Competing Interest

The authors declare that they have no known competing personal relationships or financial interests that may appear to influence the work reported in this study.

6.9 Acknowledgements

The South African authors acknowledge the financial and strategic support from the Department of Science and Innovation of South Africa; Eskom Holdings SOC Ltd Reg no 2002/015527/30 (Eskom Research, Testing, and Development Business Unit); the National Research Foundation of South Africa (Grant Numbers: 121413,130409), in Germany the authors acknowledge the BMBF founding organization within the CLIENT II initiative. The project is granted under the following number: FKZ 01LZ1715A-B.

6.10 References

Abdalla, A. H., Oseghale, C. I., Posada, J. O. G. and Hall, P. J. (2016). Rechargeable nickel-iron batteries for large-scale energy storage. Institution of Engineering and Technology Renewable Power Generation 10(10): 1529-1534.

Alamgir, M. and Abraham, K. (1995). Room temperature rechargeable polymer electrolyte batteries. Power Sources 54(1): 40-45.

Blomquist, N., Wells, T., Andres, B., Bäckström, J., Forsberg, S. and Olin, H. (2017). Metal-free supercapacitor with aqueous electrolyte and low-cost carbon materials. Scientific Reports 7(1): 1-7.

Bruce, P. G. (1997). Promising electrochemical systems for rechargeable batteries. Journal of Electroanalytical Chemistry 421(1-2): 222-223.

Chang, S., Young, K.-h., Nei, J. and Fierro, C. (2016). Reviews on the US Patents regarding nickel/metal hydride batteries. Batteries 2(2): 10.

Chen, W., Jin, Y., Zhao, J., Liu, N. and Cui, Y. (2018). Nickel-hydrogen batteries for large-scale energy storage. Proceedings of the National Academy of Sciences 115(46): 11694-11699.

Dyatkin, B., Presser, V., Heon, M., Lukatskaya, M. R., Beidaghi, M. and Gogotsi, Y. (2013). Development of a green supercapacitor composed entirely of environmentally friendly materials. ChemSusChem 6(12): 2269-2280.

Fatima, H., Zhong, Y., Wu, H. and Shao, Z. (2021). Recent advances in functional oxides for high energy density sodium-ion batteries. Materials Reports: Energy: 100022.

Gambe, Y., Sun, Y. and Honma, I. (2015). Development of bipolar all-solid-state lithium battery based on quasi-solid-state electrolyte containing tetraglyme-LiTFSA equimolar complex. Scientific Reports 5(1): 1-4.

Gheytani, S., Liang, Y., Jing, Y., Xu, J. Q. and Yao, Y. (2016). Chromate conversion coated aluminium as a light-weight and corrosion-resistant current collector for aqueous lithium-ion batteries. Journal of Materials Chemistry A 4(2): 395-399.

Hariprakash, B., Martha, S., Hegde, M. and Shukla, A. (2005). A sealed, starved-electrolyte nickel–iron battery. Applied Electrochemistry 35(1): 27-32.

Huang, L., Yang, J., Liu, P., Zhu, D. and Chen, Y. (2018). Copper/Iron Composite Anode prepared by in situ co-precipitation with Excellent High-rate and Low-temperature Performance for Rechargeable Nickel-Iron Battery. International Journal of Electrochemical Science 13: 7045-7056.

Janek, J. and Zeier, W. G. (2016). A solid future for battery development. Nature Energy 1(9): 1-4.

Jung, K. N., Shin, H. S., Park, M. S. and Lee, J. W. (2019). Solid-state lithium batteries: bipolar design, fabrication, and electrochemistry. ChemElectroChem 6(15): 3842-3859.

Karami, H., Mousavi, M. F. and Shamsipur, M. (2003). A novel dry bipolar rechargeable battery based on polyaniline. Power Sources 124(1): 303-308.

Kim, S. H., Kim, J. H., Cho, S. J. and Lee, S. Y. (2019). All-solid-state printed bipolar Li-S batteries. Advanced Energy Materials 9(40): 1901841.

Kopietz, L., Girschik, J., Schwerdt, P., Burfeind, J., Grevé, A. and Doetsch, C. (2018). Highly flexible bipolar plates for redox-flow-batteries. International Conference on Carbon Materials and Technology. Fraunhofer Institute for Environmental, Safety, and Energy Technology Umsicht.

Liu, T., Yuan, Y., Tao, X., Lin, Z. and Lu, J. (2020). Bipolar electrodes for next-generation rechargeable batteries. Advanced Science 7(17): 2001207.

Liu, T., Zhang, Y., Chen, C., Lin, Z., Zhang, S. and Lu, J. (2019). Sustainability-inspired cell design for a fully recyclable sodium ion battery. Journal of Nature Communications 10(1): 1-7.

Livshits, V., Blum, A., Strauss, E., Ardel, G., Golodnitsky, D. and Peled, E. (2001). Development of a bipolar Li/composite polymer electrolyte/pyrite battery for electric vehicles. Power Sources 97: 782-785.

Lukatskaya, M. R., Kota, S., Lin, Z., Zhao, M.-Q., Shpigel, N., Levi, M. D., Halim, J., Taberna, P.-L., Barsoum, M. W. and Simon, P. (2017). Ultra-high-rate pseudocapacitive energy storage in two-dimensional transition metal carbides. Nature Energy 2(8): 1-6.

Müller, S., Holzer, F., Haas, O., Schlatter, C. and Comninellis, C. (1995). Development of rechargeable monopolar and bipolar zinc/air batteries. CHIMIA International Journal for Chemistry 49(1-2): 27-32.

Ng, K. C., Zhang, S., Peng, C. and Chen, G. Z. (2009). Individual and bipolarly stacked asymmetrical aqueous supercapacitors of CNTs/SnO_2 and CNTs/MnO_2 nanocomposites. Journal of the Electrochemical Society 156(11): A846.

Peled, E., Golodnitsky, D., Ardel, G., Lang, J. and Lavi, Y. (1995). Development and characterization of bipolar lithium composite polymer electrolyte (CPE)-FeS_2 battery for applications in electric vehicles. Power Sources 54(2): 496-500.

Posada, J. O. G. and Hall, P. J. (2016). Towards the development of safe and commercially viable nickel-iron batteries: improvements to coulombic efficiency at high iron sulphide electrode formulations. Applied Electrochemistry 46(4): 451-458.

Rota, M., Comninellis, C., Moller, S., Holzer, F. and Haas, O. (1995). Bipolar Al/O_2 battery with planar electrodes in alkaline and acidic electrolytes. Applied Electrochemistry 25(2): 114-121.

Shen, D. H. and Halpert, G. (1993). Design concepts of high power bipolar rechargeable lithium battery. Power Sources 43(1-3): 327-338.

Tawonezvi, T., Bladergroen, B. J. and John, J. (2020). Development of $FeCu_x$/FeS/Graphite composite electrode materials for iron-based Alkaline batteries. Internatinal Journal of Electrochemical Science 15: 12428 – 12446.

Tsais, P.-J. and Chan, L. (2013). Nickel-based batteries: Materials and chemistry. Electricity Transmission, Distribution and Storage Systems, Elsevier: 309-397.

Ullah, S., Amin Badshah, F. A., Raza, R., Altaf, A. A. and Hussain, R. (2011). Electrodeposited zinc electrodes for high current Zn/AgO bipolar batteries.

Wang, H., Liang, Y., Gong, M., Li, Y., Chang, W., Mefford, T., Zhou, J., Wang, J., Regier, T. and Wei, F. (2012). An ultrafast nickel–iron battery from strongly coupled inorganic nanoparticle/nanocarbon hybrid materials. Journal of Nature Communications 3: 917.

Whitacre, J., Wiley, T., Shanbhag, S., Wenzhuo, Y., Mohamed, A., Chun, S., Weber, E., Blackwood, D., Lynch-Bell, E. and Gulakowski, J. (2012). An aqueous electrolyte, sodium ion functional, large format energy storage device for stationary applications. Power Sources 213: 255-264.

Wu, H.-C., Lin, Y.-P., Lee, E., Lin, W.-T., Hu, J.-K., Chen, H.-C. and Wu, N.-L. (2009). High-performance carbon-based supercapacitors using Al current-collector with conformal carbon coating. Materials Chemistry and Physics 117(1): 294-300.

Yamada, Y., Usui, K., Sodeyama, K., Ko, S., Tateyama, Y. and Yamada, A. (2016). Hydrate-melt electrolytes for high-energy-density aqueous batteries. Nature Energy 1(10): 1-9.

Yan, J., Wang, Q., Wei, T. and Fan, Z. (2014). Recent advances in design and fabrication of electrochemical supercapacitors with high energy densities. Advanced Energy Materials 4(4): 1300816.

Yeetsorn, R., Fowler, M. W. and Tzoganakis, C. (2011). A review of thermoplastic composites for bipolar plate materials in PEM fuel cells. Nanocomposites with unique properties and applications in medicine and industry: 317-344.

Yoshima, K., Harada, Y. and Takami, N. (2016). Thin hybrid electrolyte based on garnet-type lithium-ion conductor $Li7La_3Zr_2O_{12}$ for 12V-class bipolar batteries. Power Sources 302: 283-290.

Zhong, Y., Xu, X., Liu, Y., Wang, W. and Shao, Z. (2018). Recent progress in metal–organic frameworks for lithium–sulfur batteries. Polyhedron 155: 464-484.

Zhong, Y., Xu, X., Veder, J.-P. and Shao, Z. (2020). Self-recovery chemistry and cobalt-catalyzed electrochemical deposition of cathode for boosting performance of aqueous zinc-ion batteries. Iscience 23(3): 100943.

Zhou, X., Peng, C. and Chen, G. Z. (2012). 20 V stack of aqueous supercapacitors with carbon (−), titanium bipolar plates and CNT-polypyrrole composite (+). AIChE Journal 58(3): 974-983.

Zide, D., Felix, C., Oosthuysen, T. and Bladergroen, B. J. (2020a). Electrochemical studies of the nickel-based hydroxide electrode for the oxygen evolution reaction and coulombic efficiency of the electrode. Electroanalysis 32(12): 2703-2712.

Zide, D., Felix, C., Oosthuysen, T. and Bladergroen, B. J. (2020b). The influence of copper and carbon black on electrochemical behavior of nickel positive electrode. Journal of Electroanalytical Chemistry 878: 114539.

Zide, D., Felix, C., Oosthuysen, T. and Bladergroen, B. J. (2021). Synthesis, structural characterization, and electrochemical properties of the Mg and Mn doped-Ni (OH) 2 for use as active cathode materials in NiFe batteries. Journal of Electroanalytical Chemistry 895: 115418.

Ziv, B., Haik, O., Zinigrad, E., Levi, M. D., Aurbach, D. and Halalay, I. C. (2013). Investigation of graphite foil as current collector for positive electrodes of Li-ion batteries. Journal of the Electrochemical Society 160(4): A581.

Zuo, W., Li, R., Zhou, C., Li, Y., Xia, J. and Liu, J. (2017). Battery-supercapacitor hybrid devices: recent progress and future prospects. Advanced Science 4(7): 1600539.

CHAPTER 7

7 General Discussion and Conclusion

Ni-Fe batteries are experiencing a rebirth for renewable energy applications due to their incredibly long life and robust and durable qualities (Abdalla *et al.*, 2016; Posada and Hall, 2016; Chen, Wei *et al.*, 2018).

I. However, the Ni-Fe battery suffers from severe drawbacks, induced mainly by the nickel-electrode, impels low efficiency (50% - 60%) and low specific energy.
II. Furthermore, the nickel-electrode exhibits poor performance, which results from the competitive reaction between the oxidation of the active material and the evolution of oxygen (Wang, Xianyou *et al.*, 2004; Begum *et al.*, 2009).
III. In addition, the reduced charge acceptance of nickel-electrode is suspected to be related to a relatively long distance between $Ni(OH)_2$ particles and the nearest portion of the substrate(Begum *et al.*, 2009).
IV. The practical capacity of nickel-electrode is said to depend on how well the $Ni(OH)_2$ particles are embedded within a conductive electron network allowing electrons to move between particles and the current collector (Begum *et al.*, 2009).

These current limitations of the nickel-electrode (I – IV) generated the opportunity and potential of the present study. Accordingly, this study focused on improving the performance of the nickel-electrode, which could contribute to an overall cost reduction of the Ni-Fe battery. This was achieved by modifying the $Ni(OH)_2$ cathode active material with cost-effective divalent and trivalent elements. The fundamental interest was to develop a composite nickel-electrode suitable for a bipolar-based Ni-Fe battery in response to the global demand for a cost-effective energy storage system.

During the proposal stage of this study, the following five objectives were proposed and have been achieved. There has been no additions or subtractions from the proposed objectives.

VI. Synthesization of $Ni(OH)_2$ active material using the modified existing chemical precipitation method followed by hydrothermal treatment.
VII. To chemically modified the $Ni(OH)_2$ using the selected divalent and trivalent modifiers (Cu, Co, Mg, Mn, and Al) following the existing modified method (I).
VIII. To physically characterized the synthesized $Ni(OH)_2$-based materials (I) and (II) using XRD, FTIR, ICP/OES, and SEM/EDS.
IX. To screen the synthesized materials (I) and (II) by assessing their electrochemical properties.
X. To evaluate the best synthesized $Ni(OH)_2$-based material (IV) towards developing a bi-polar Ni-electrode for a bipolar Ni-Fe battery.

The experimental results achieved in this thesis are presented in CHAPTER 3 to CHAPTER 6. All the results chapters are offered in an article form according to the journal's specific writing style. CHAPTER 3 (Zide *et al.*, 2020b), CHAPTER 4 (Zide *et al.*, 2020a), CHAPTER 5 (Zide *et al.*, 2021), respectively, generally responding to objectives (I) to (IV) and CHAPTER 6 responds to objective (V).

CHAPTER 3 reports on the synthesis of $Ni(OH)_2$ using the co-precipitation method followed by hydrothermal treatment. The chapter first addresses the effect of stirring, ageing and hydrothermal treatment step during synthesis. Secondly, it assessed the impact of carbon black as a conductive network for $Ni(OH)_2$ active material. Lastly, the influence of copper as addictive material for $Ni(OH)_2$ active material was optimised and evaluated. The morphologies of the material were assessed using XRD, FTIR, TG-DTA, and BET. ICP and SEM/EDS and were used to confirm the elemental composition of the materials. Lastly, the electrochemical performance of the materials was performed using a three-electrode test in a Metrohm Autolab Potentiostat/Galvanostat Instrument. Based on the morphological and structural characterization demonstrated by XRD, FTIR and TG-DTA, it was concluded that the hydrothermal treatment step was vital for this study to produce the expected $Ni(OH)_2$-based materials. The addition 5 wt.% of carbon black powder improves the utilization of the active material; however, it leads to a decrease in the stability of the electrode. The partial substitution of Cu^{2+} for β-$Ni(OH)_2$ significantly improves the coulombic efficiency of the β-$Ni(OH)_2$ active material. It also increases the specific discharge capacity and enhances the stability of the electrode, for example, the addition of 25 wt.% Cu^{2+} to the $Ni(OH)_2$ material resulted in improved stability and a specific discharge capacity of 151 mAh/g compared to 51 mAh/g of un-modified $Ni(OH)_2$. Un-modified $Ni(OH)_2$ has a coulombic efficiency of 25 % compared to 76% for the modified $Ni(OH)_2$ after 80 cycles when a current of 25 mA was applied. It was then suggested that the Cu^{2+} modified $Ni(OH)_2$ active material may be acknowledged as a promising material for Ni-Fe battery positive electrode applications.

CHAPTER 4 reports on the influence of cobalt and aluminium as additives materials for $Ni(OH)_2$ active material. $Ni_{1-x}Co_x(OH)_2$ and $Ni_{1-x}Al_x(OH)_2$ were optimised and evaluated. The morphologies of the material were assessed using XRD, FTIR, TG-DTA, and BET. ICP and SEM/EDS and were used to confirm the elemental composition of the materials. Lastly, the electrochemical performance of the materials was performed using a three-electrode test in a Metrohm Autolab Potentiostat/Galvanostat Instrument. As presented in CHAPTER 4, the onset for oxidation of the active material is significantly improved with partial substitution of Ni^{2+} by Co^{2+} metal. On the other hand, partial substitution of Ni^{2+} with Al^{3+} metal moves the onset of electrode oxidation to a higher potential. In addition, the partial substitution of 10 wt.% Al^{3+} metal improves both discharge capacity (from 128 mAh/g to 170mAh/g) and the coulombic efficiency (from 87% to 93%) of the β-$Ni(OH)_2$ electrode. Aluminium has a significantly lower cost than nickel; therefore, gaining capacity by partial substitution of Ni^{2+} for the less expensive Al^{3+} may be a cost reduction for $Ni(OH)_2$ Ni-Fe battery. It must also be noted that only

the structural and morphological composition $Ni_{0.95}Co_{0.05}(OH)_2$ and $Ni_{0.9}Al_{0.01}(OH)_2$ were presented in CHAPTER 4 because they were the only composition found to be the optimal composition with promising electrochemical activities. However, a complete comparison of the morphological and structural characterizations of $Ni_{1-x}Co_x(OH)_2$ and $Ni_{1-x}Al_x(OH)_2$ can be accessible in Appendix A 1 to Appendix A 5 and Appendix B 1 to Appendix B 5, respectively.

CHAPTER 5 reports on the influence of magnesium and manganese as additives materials for $Ni(OH)_2$ active material. $Ni_{1-x}Mg_x(OH)_2$ and $Ni_{1-x}Mn_x(OH)_2$ were optimised and evaluated. The morphologies of the material were assessed using XRD, FTIR, TG-DTA, and BET. ICP and SEM/EDS and were used to confirm the elemental composition of the materials. The electrochemical performance of the materials was performed using a three-electrode test in a Metrohm Autolab Potentiostat/Galvanostat Instrument. The composition of $Ni_{1-x}Mg_x(OH)_2$ and $Ni_{1-x}Mn_x(OH)_2$ that gave the best electrochemical performance was further accessed using a two-electrode configuration system.

The partially substituted Mg^{2+} for Ni^{2+} in $Ni(OH)_2$ material led to the formation of β-phase of the $Ni(OH)_2$ based material (CHAPTER 5). In contrast, the partial substitution of Mn^{2+} for Ni^{2+} was the main factor that affected the phase formation of the prepared composite materials. Moreover, the CV analysis showed that the partial substitution of Mg^{2+} for Ni^{2+} improves the reversibility of the $Ni(OH)_2$ based electrode, the separation of anodic/cathodic peaks, and the oxygen evolution. The $Ni_{0.95}Mg_{0.05}(OH)_2$ electrode and $Ni_{0.9}Mn_{0.1}(OH)_2$ electrode demonstrated an improved specific discharge capacities performance compared to the un-doped $Ni(OH)_2$. When using three-electrode configurations, the un-modified $Ni(OH)_2$ electrode discharge capacity showed a reduction of 76 % after the 100^{th} cycle. In contrast, the $Ni_{0.95}Mg_{0.05}(OH)_2$ and $Ni_{0.9}Mn_{0.1}(OH)_2$ electrodes demonstrated a reduction of only 15% and 12% in discharge capacities after 100^{th} cycles, respectively. When using a two-electrode configuration, the obtained discharge capacities were 40 mAh/g for the un-modified $Ni(OH)_2$ electrode, 120 mAh/g for the $Ni_{0.95}Mg_{0.05}(OH)_2$ electrode, and 159 mAh/g for the $Ni_{0.9}Mn_{0.1}(OH)_2$ electrode with an electrode cycle life of 43.49 %, 88.24 %, 88.54 %, respectively.

CHAPTER 6 reports on a novel bipolar battery cell prepared using $Ni_{0.75}Cu_{0.25}(OH)_2$ as the active cathode material and evaluated for Ni-Fe battery applications. The results of this Chapter are presented systematically. First, the electrochemical discharge capacities of two battery cells consisting of monopolar electrodes prepared with graphite composite film with Ni-mesh substrates as the current collectors, respectively, are evaluated and compared. In addition, a bipolar-based battery cell consisting of a bipolar electrode prepared with a graphite substrate as the current collector is assessed as a novel bipolar Ni-Fe battery. The two cells with monopolar electrodes demonstrated discharge capacities of 144 mAh/g and 199 mAh/g after the 100^{th} cycles, corresponding to coloumbic efficiencies of 87% and 84% for the monopolar-based electrodes fabricated on Ni-mesh and graphite substrate, respectively.

The bipolar-based Ni-Fe battery two-cell demonstrated a discharge capacity of 158 mAh/g after the 100th cycle, corresponding to a coloumbic efficiency of 72%.

Furthermore, a cost evaluation (Appendix C) of the typical battery plant for a bipolar based Ni-Fe was estimated. The bipolar design reduces the production cost by 33% (from R12/Wh to R8/Wh).

7.1 The novelty of the thesis

In this study, a novel bipolar battery cell is prepared using $Ni_{0.75}Cu_{0.25}(OH)_2$ as the active cathode material and evaluated for Ni-Fe battery applications (see CHAPTER 6). There is currently no literature reporting on a bipolar Ni-Fe battery. The bipolar-based battery cell prepared in this study was made of a bipolar electrode prepared with a graphite substrate as the current collector is assessed as a novel bipolar Ni-Fe battery. The graphite composite sheets are chemical resistant, mechanically stable, and allows subsequent formatting and reshaping.

In addition, the improved coulombic efficiency of $Ni(OH)_2$ material to 87% compared to 50 - 60% coulombic efficiency commonly reported in the literature on a typical monopolar based Ni-Fe battery.

Contrary to the α-$Ni(OH)_2$ commonly reported in the literature (Yuan *et al.*, 2016), the material composition ($Ni_{0.75}Cu_{0.25}(OH)_2$ (see CHAPTER 3), $Ni_{0.95}Co_{0.05}(OH)_2$ (see CHAPTER 4), $Ni_{0.95}Mg_{0.05}(OH)_2$ (see CHAPTER 5), and $Ni_{0.9}Mn_{0.1}(OH)_2$ (see CHAPTER 5) prepared in this study could be indexed to the β-form of $Ni(OH)_2$. The β-$Ni(OH)_2$ is stable in strong alkaline electrolytes with good reversibility when charged to β-NiOOH (Hall *et al.*, 2015; Posada and Hall, 2016; Zide *et al.*, 2020b, a). Furthermore, the β-NiOOH has a similar structure with a lattice constant of inter-sheet (4.85Å); thus, the volume expansion associated with cycling is less than any other form. The downside of α-$Ni(OH)_2$ it tends to convert to β-$Ni(OH)_2$ in an alkaline solution or when subjected to charge-discharge cycles (Lee, Jeong Woo *et al.*, 2011).

7.2 Recommendations

In this study, for the screening of various materials ($Ni(OH)_2$, $Ni_{1-x}Cu_x(OH)_2$, $Ni_{1-x}Co_x(OH)_2$, $Ni_{1-x}Al_x(OH)_2$, $Ni_{1-x}Mg_x(OH)_2$, and $Ni_{1-x}Mn_x(OH)_2$), the 100-cycle limit was considered sufficient to provide a stability trend. However, to establish the long-term stability of the electrode, 100 cycles may be regarded as insufficient. It is therefore recommended to conduct a cycling performance of at least 1000 cycles for future studies. In addition, electrochemical impedance spectroscopy (EIS) may play a vital role to understand the reaction mechanism; however, EIS analysis was not within the scope of this current study. For future studies, it is recommended that EIS supplemented with equivalent circuit fitting be performed.

In order to achieve a practical bipolar electrode, further optimisation for electrode production is recommended. It is also recommended to increase the mass loading of the active material to at least 1g per square centimetre.

7.3 References

Abdalla, A. H., Oseghale, C. I., Posada, J. O. G. and Hall, P. J. (2016). Rechargeable nickel-iron batteries for large-scale energy storage. Institution of Engineering and Technology Renewable Power Generation 10(10): 1529-1534.

Begum, S. N., Muralidharan, V. and Basha, C. A. (2009). The influences of some additives on electrochemical behaviour of nickel electrodes. International Journal of Hydrogen Energy 34(3): 1548-1555.

Chen, W., Jin, Y., Zhao, J., Liu, N. and Cui, Y. (2018). Nickel-hydrogen batteries for large-scale energy storage. Proceedings of the National Academy of Sciences 115(46): 11694-11699.

Hall, D. S., Lockwood, D. J., Bock, C. and MacDougall, B. R. (2015). Nickel hydroxides and related materials: a review of their structures, synthesis and properties. Proceedings of the Royal Society A: Mathematical, Physical and Engineering Sciences 471(2174): 20140792.

Lee, J. W., Ko, J. M. and Kim, J.-D. (2011). Hierarchical microspheres based on α-Ni $(OH)_2$ nanosheets intercalated with different anions: synthesis, anion exchange, and effect of intercalated anions on electrochemical capacitance. The Journal of Physical Chemistry C 115(39): 19445-19454.

Posada, J. O. G. and Hall, P. J. (2016). Towards the development of safe and commercially viable nickel-iron batteries: improvements to coulombic efficiency at high iron sulphide electrode formulations. Applied Electrochemistry 46(4): 451-458.

Wang, X., Luo, H., Yang, H., Sebastian, P. and Gamboa, S. (2004). Oxygen catalytic evolution reaction on nickel hydroxide electrode modified by electroless cobalt coating. International Journal of Hydrogen Energy 29(9): 967-972.

Yuan, S., Wang, X., Lu, C. and Chen, C.-M. (2016). The fine control of porous pompon-like Mg-incorporated α-$Ni(OH)_2$ for enhanced supercapacities. Functional Materials Letters 9(05): 1650057.

Zide, D., Felix, C., Oosthuysen, T. and Bladergroen, B. J. (2020a). Electrochemical studies of the nickel-based hydroxide electrode for the oxygen evolution reaction and coulombic efficiency of the electrode. Electroanalysis 32(12): 2703-2712.

Zide, D., Felix, C., Oosthuysen, T. and Bladergroen, B. J. (2020b). The influence of copper and carbon black on electrochemical behavior of nickel positive electrode. Journal of Electroanalytical Chemistry 878: 114539.

Zide, D., Felix, C., Oosthuysen, T. and Bladergroen, B. J. (2021). Synthesis, structural characterization, and electrochemical properties of the Mg and Mn doped-Ni (OH) 2 for use as active cathode materials in NiFe batteries. Journal of Electroanalytical Chemistry 895: 115418.

APPENDIX A: Physical characterizations of Co-doped $Ni(OH)_2$

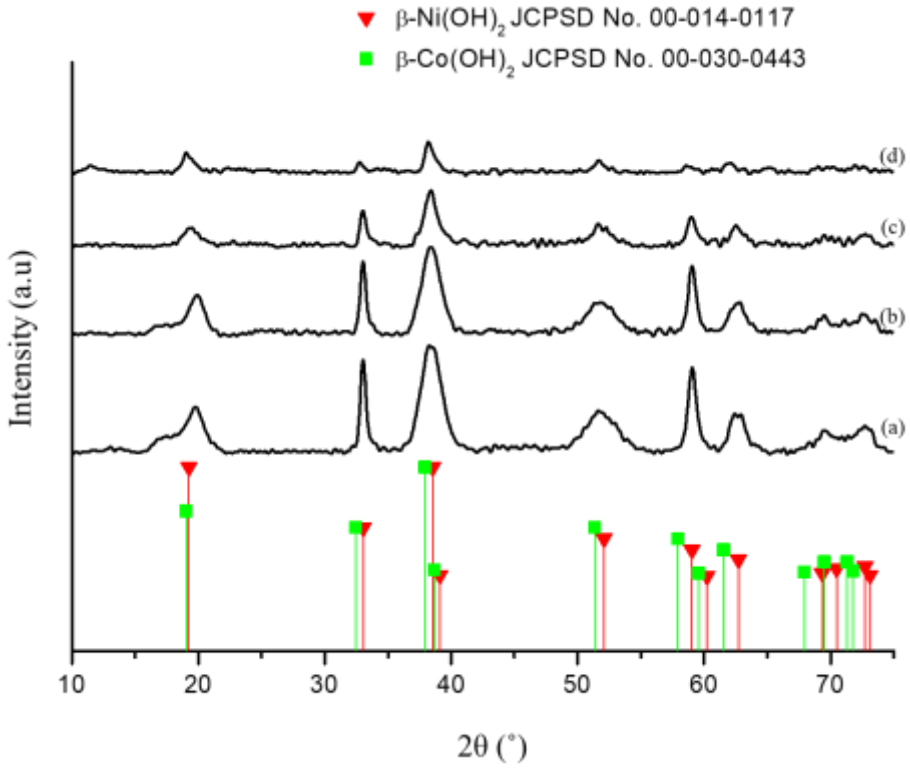

Appendix A 1: Diffractograms of (a) $Ni_{0.95}Co_{0.05}(OH)_2$, (b) $Ni_{0.9}Co_{0.1}(OH)_2$ (c) $Ni_{0.75}Co_{0.25}(OH)_2$, and (d) $Ni_{0.5}Co_{0.5}(OH)_2$.

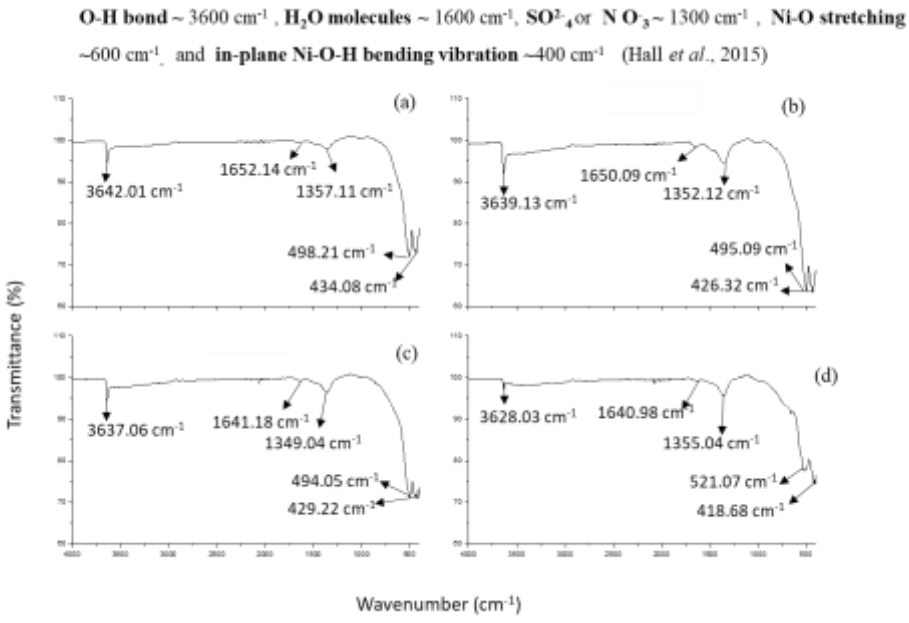

Appendix A 2: FTIR of (a) $Ni_{0.95}Co_{0.05}(OH)_2$, (b) $Ni_{0.9}Co_{0.1}(OH)_2$ (c) $Ni_{0.75}Co_{0.25}(OH)_2$, and (d) $Ni_{0.5}Co_{0.5}(OH)_2$.

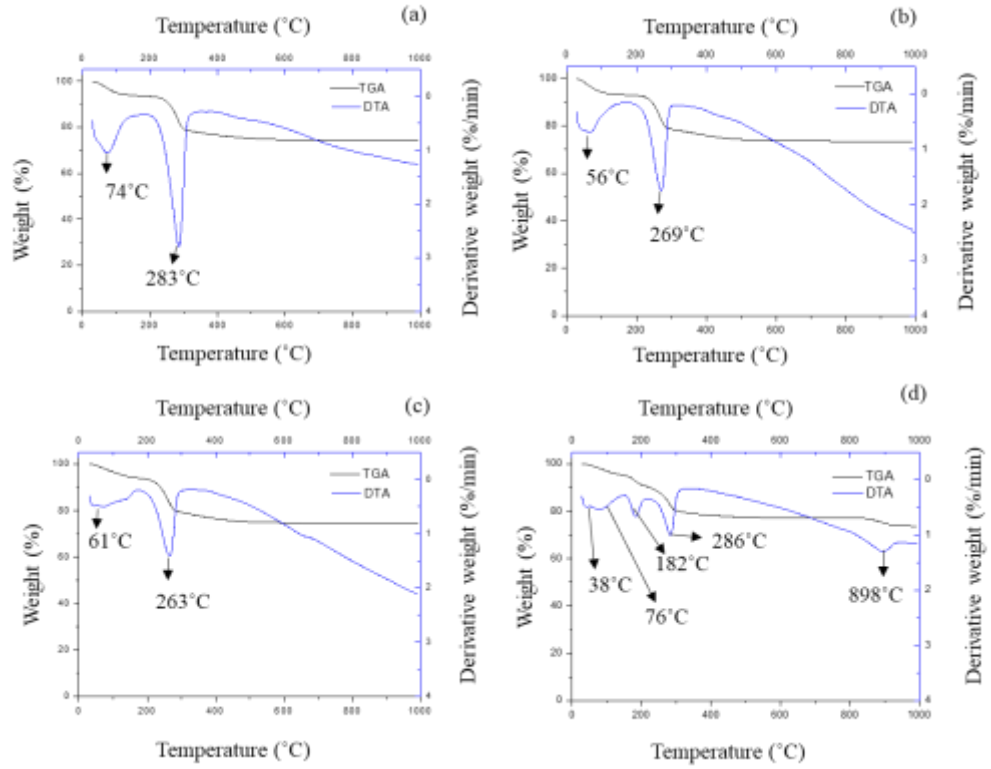

Appendix A 3: TG-DTA curves of (a) $Ni_{0.95}Co_{0.05}(OH)_2$, (b) $Ni_{0.9}Co_{0.1}(OH)_2$ (c) $Ni_{0.75}Co_{0.25}(OH)_2$, and (d) $Ni_{0.5}Co_{0.5}(OH)_2$.

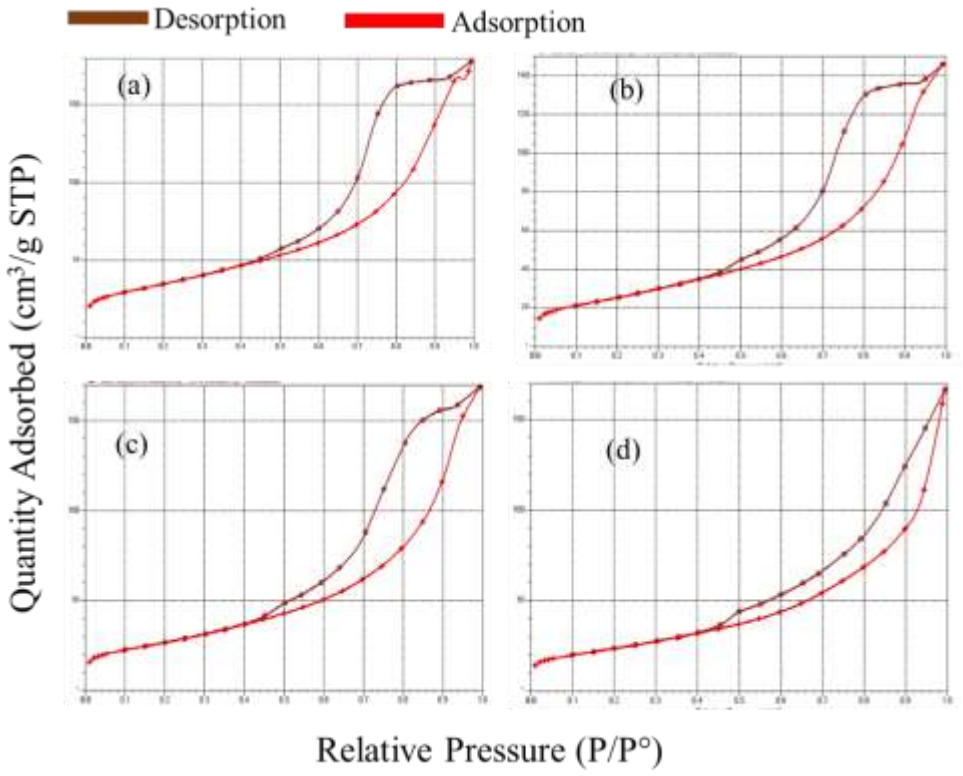

Appendix A 4: N_2-adsorption-disorption isotherms of (a) $Ni_{0.95}Co_{0.05}(OH)_2$, (b) $Ni_{0.9}Co_{0.1}(OH)_2$ (c) $Ni_{0.75}Co_{0.25}(OH)_2$, and (d) $Ni_{0.5}Co_{0.5}(OH)_2$.

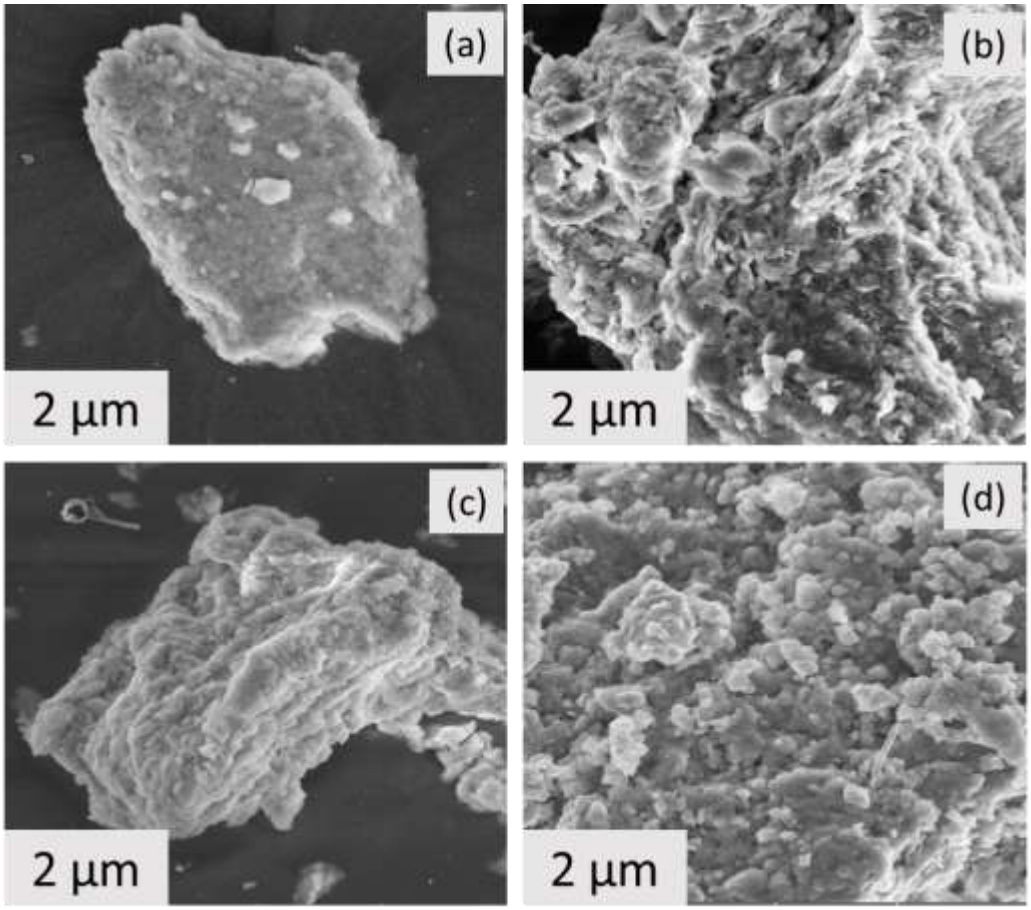

Appendix A 5: SEM images of (a) $Ni_{0.95}Co_{0.05}(OH)_2$, (b) $Ni_{0.9}Co_{0.1}(OH)_2$ (c) $Ni_{0.75}Co_{0.25}(OH)_2$, and (d) $Ni_{0.5}Co_{0.5}(OH)_2$.

APPENDIX B: Physical characterizations of Al doped $Ni(OH)_2$

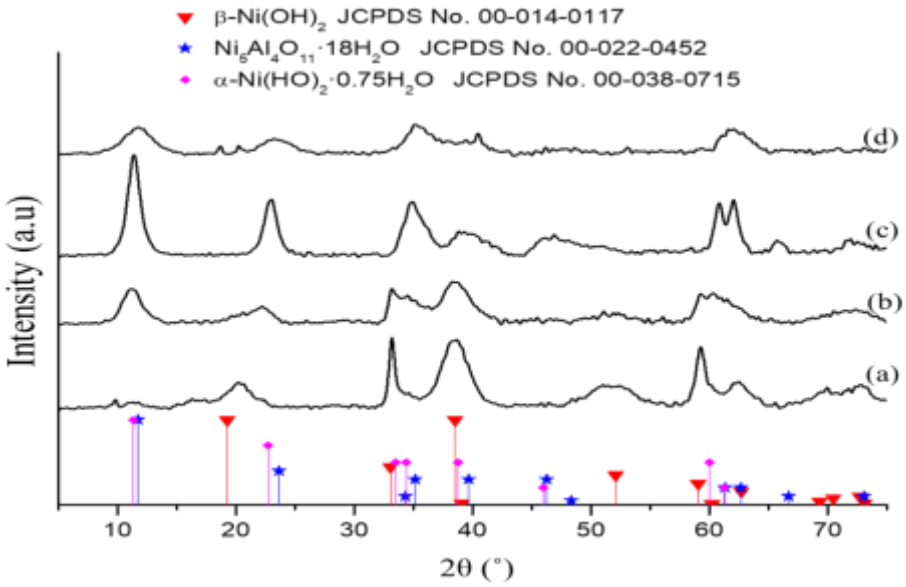

Appendix B 1: Diffractograms of (a) $Ni_{0.95}Al_{0.05}(OH)_2$, (b) $Ni_{0.9}Al_{0.1}(OH)_2$ (c) $Ni_{0.75}Al_{0.25}(OH)_2$, and (d) $Ni_{0.5}Al_{0.5}(OH)_2$.

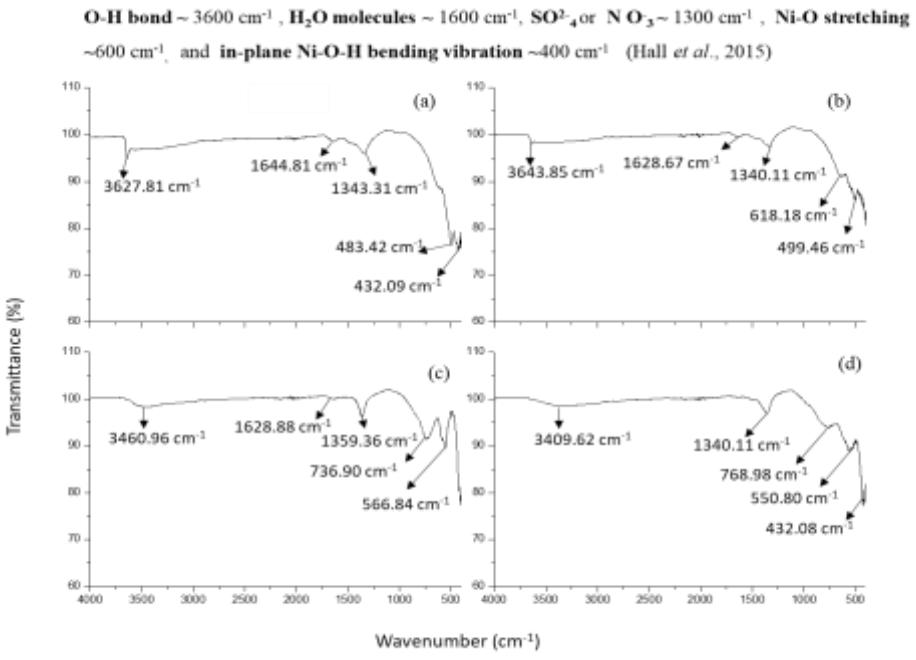

Appendix B 2: FTIR of (a) $Ni_{0.95}Al_{0.05}(OH)_2$, (b) $Ni_{0.9}Al_{0.1}(OH)_2$ (c) $Ni_{0.75}Al_{0.25}(OH)_2$, and (d) $Ni_{0.5}Al_{0.5}(OH)_2$.

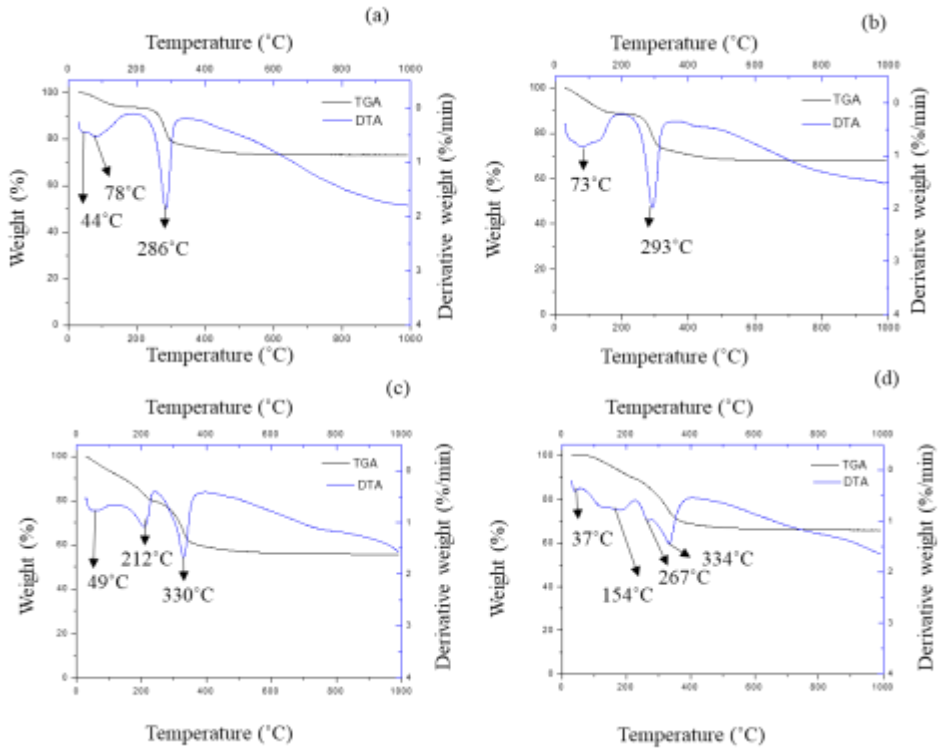

Appendix B 3: TG-DTA curves of (a) $Ni_{0.95}Al_{0.05}(OH)_2$, (b) $Ni_{0.9}Al_{0.1}(OH)_2$ (c) $Ni_{0.75}Al_{0.25}(OH)_2$, and (d) $Ni_{0.5}Al_{0.5}(OH)_2$.

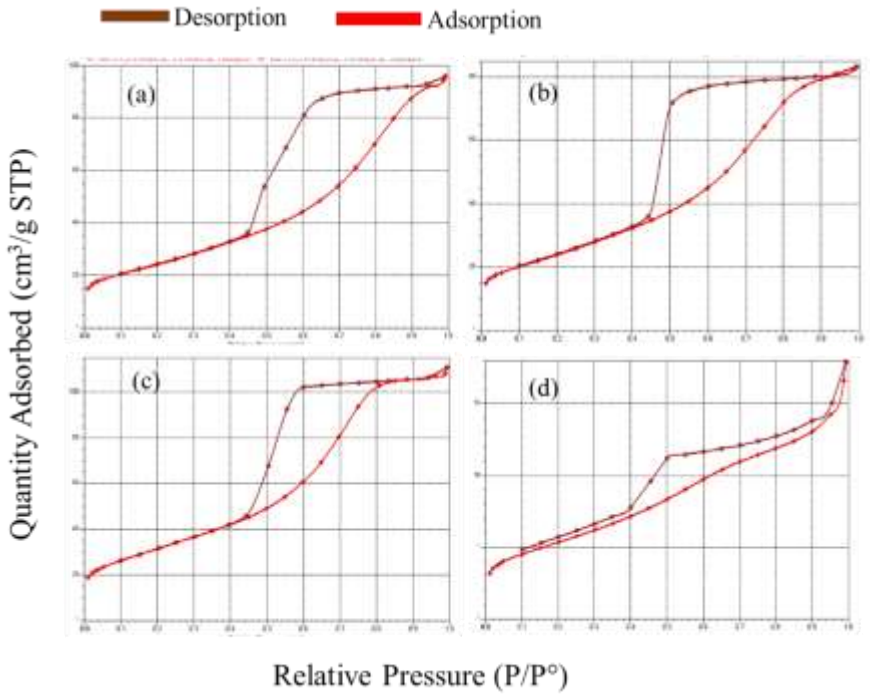

Appendix B 4: N_2 adsorption-desorption isotherm of (a) $Ni_{0.95}Al_{0.05}(OH)_2$, (b) $Ni_{0.9}Al_{0.1}(OH)_2$ (c) $Ni_{0.75}Al_{0.25}(OH)_2$, and (d) $Ni_{0.5}Al_{0.5}(OH)_2$.

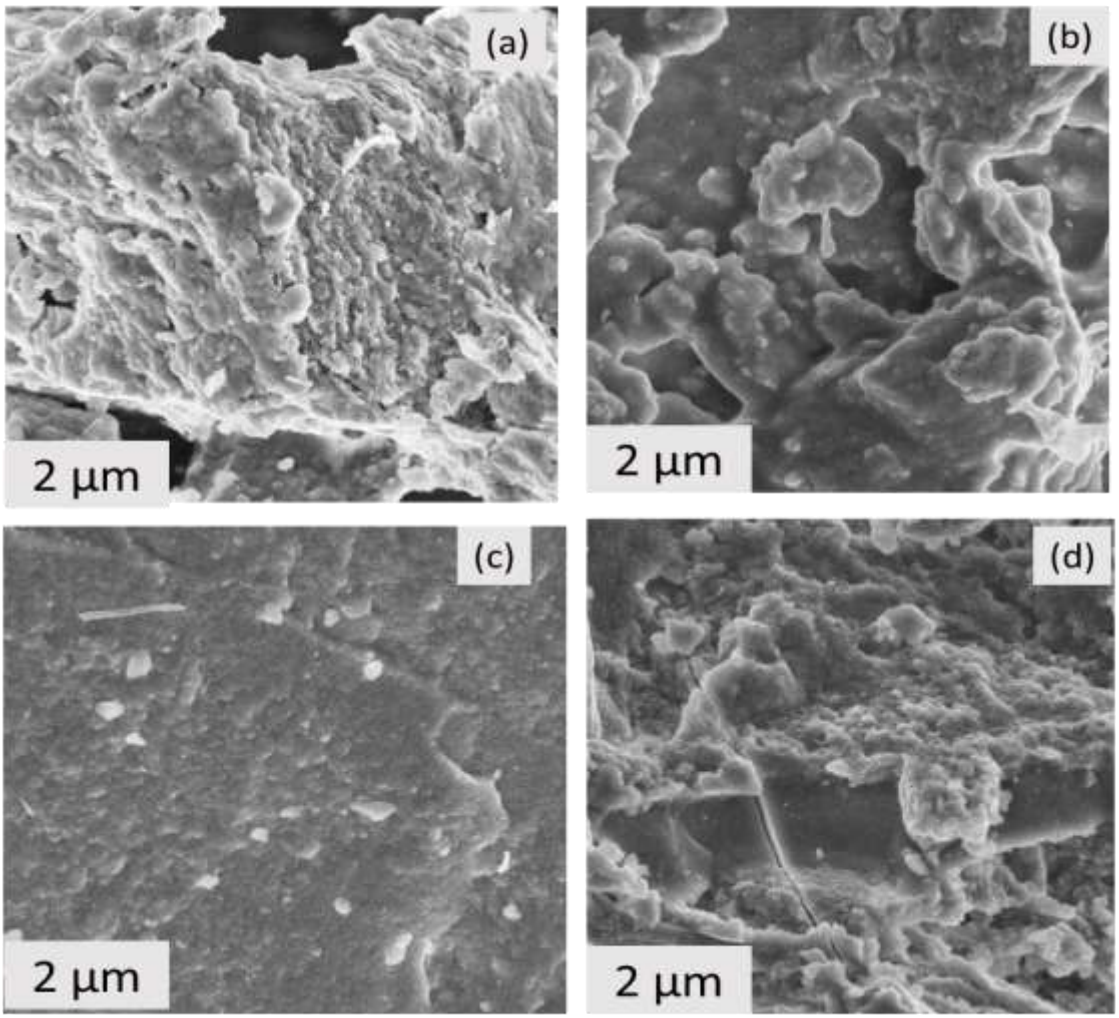

Appendix B 5: SEM images of (a) $Ni_{0.95}Al_{0.05}(OH)_2$, (b) $Ni_{0.9}Al_{0.1}(OH)_2$ (c) $Ni_{0.75}Al_{0.25}(OH)_2$, and (d) $Ni_{0.5}Al_{0.5}(OH)_2$.

APPENDIX C-1: Cost Evaluation

Cost Evaluation

Since the study aimed to develop a composite nickel-electrode suitable for a bipolar-based nickel-iron battery in response to the global demand for a cost-effective energy storage system, it was important to assess the cost involved in the bipolar Ni-Fe battery constructed using electrode formulation $Ni_{0.75}Cu_{0.25}(OH)_2$ as cathode material, and $FeCu_{0.25}$ as anode material was investigated. The calculations embodied included the cost of raw materials, utilities, labour costs, the cost of Ni-Fe batteries per watthour (Wh) and cash flow statement for a plant with a capacity of 2600 batteries/year.

All the calculations and estimation provided in this Appendix for cost evaluation were sourced from a published Master's thesis of my colleague Tawonezvi (Tawonezvi, 2019) who produced the $FeCu_{0.25}$ anode materials contributing towards developing a bipolar based Ni-Fe battery in our lab. Calculations in this study were updated were needed. The estimates of the Material and Energy Balance needed to produce a typical bipolar Ni-Fe battery can also be accessed from Tawonezvi (Tawonezvi, 2019), they are excluded in this study.

Energy Production Cost of a Plant Capacity of 2600 Batteries/Year

The production cost of a plant capacity of 2600 Ni-Fe batteries/year was determined. The calculations included the cost of raw materials, energy consumption (by the oven, hydraulic press and oven), operating labour and the cost of Ni-Fe batteries per kilowatt-hour during the battery production process. Appendix C 1 depicts the cost of raw materials utilised to construct a 25 Wh typical NiFe battery.

Appendix C 1: Raw materials cost estimation of a single bipolar Ni-Fe battery

Raw materials	Amount [Kg]	Cost [R/Kg]	Actual Cost [R]
NaOH	0.0200	16	0.32
Fe	0.0514	62	3.19
Bi_2S_3	0.0046	75	0.34
$CuN_2O_6.3H_20$	0.0800	25	2.00
CB	0.0092	10	0.09
Coathelyne	0.0152	22	0.33
Minor Components	0.1150	50	5.75
KOH	0.0080	390	3.12
LiOH	0.0006	310	0.19
DI H_2O	4.3250	1.25	5.41
$N_2NiO_6.6H_20$	0.1350	36	4.86

$CuSO_4$	0.0680	50	3.40
Na_2CO_3	0.0200	50	1.00
Total Mass [Kg]	4.8520	**Total Cost [R]**	30.00

The mass of the bipolar Ni-Fe battery was 563 g (determined by my colleague in our lab (Tawonezvi, 2019)), 10 batteries could be produced per batch or day) which was the rate of production of Ni-Fe batteries in this study. In addition, all the calculations involved in this section (cost of production of Ni-Fe batteries) were determined using formulas and procedures reported by Apostolakou *et al.* (Apostolakou *et al.*, 2009). Thus, the calculated cost of production of 10 Ni-Fe batteries per year or 5.36 kg per day (where 12 months are equivalent to 260 working days) was investigated in this section. This implied that 2600 batteries/year was the plant capacity of the Ni-Fe batteries production.

It was relevant to determine how much money was spent per year using 10 Ni-Fe batteries/day production rate. Thus, the cost estimation was carried out as shown next. The cost estimation was initiated by determining the fixed capital investment at the plant capacity of 2600 batteries/year. Fixed capital investment is a vital parameter in computing the production cost, as it estimates the cost of acquisition and maintenance of major long-term equipment utilised in the bipolar Ni-Fe battery production process. Appendix C 2 presents the sum of installed equipment cost (SIEC), total installed equipment cost (TIEC) and fixed capital investment (FCI).

Appendix C 2: Cost of major equipment utilised in the production of Ni-Fe batteries (2600 batteries/year)

Equipment and Size	**Price [R]**	**Supplier**
Hydraulic Press (Pressing Plate 30cm X 30 cm)	76 000	Hyjack, Cape Town
Vacuum Oven (400L)	24 000	Labotec
Battery Management System (50 Channels)	44 000	NEWARE
Mould (9 cm x 6 cm)	500	WAKE Engineering
Overheard Mixer (40cm)	16 000	Labotec
Sum of installed equipment	160 500	
Total installed equipment cost	192 600	
Fixed Capital Investment	385 200	

The calculations were carried out as follows:

$$\text{TIEC} = 1.2 \times \text{SIEC} = 1.2 \times 160\,500 = \text{R}192\,600$$

$$\text{FCI} = 2 \times \text{SIEC} = 2 \times 192\,600 = \text{R}385\,200$$

The fixed capital investment of R385 200 was used to determine the production cost of Ni-Fe batteries. The cost of raw materials/cells was estimated in Appendix C 1. The cost of raw materials per year was calculated as R258 596 (R99.46/battery × 2600 batteries). Then, the cost of utilities was estimated as shown below:

In the present study, the cost of utilities consisted of the cost of electricity. The energy consumed during the electrode production process was estimated from the equipment's specifications (mixer, hydraulic press, BMS and vacuum dryer). The mixer consumed 0.2 kW, it was used for 1 hour, and the rate of power was 0.2 kWh per day. The BMS consumed 10kW, it was used for 10 hours, and the rate of power was 100 kWh per day. The oven consumed 0.705 kW, it was used for 24 hours, and the rate of power was 16.9 kWh per day. The hydraulic press consumed 0.526 kW, it was used for 4 hours, and the rate of power was 2.1 kWh per day. The rate of electricity in South Africa is 89.13c per kWh (R0.89) (Tawonezvi, 2019). Appendix C 3 presents the estimation cost of utilities per year.

Appendix C 3: Estimation cost of the plant utilities per year (plant with capacity 2600 batteries/year)

Equipment & Size	**KWh/day**	**KWh/Year**	**Rand/Year**
Hydraulic Press	2.1	546	485
Vacuum Dryer	16.9	4 400	3 916
Overheard Mixer	0.2	52	47
Battery Management System	100	26 000	23 140
		Total	27 588

Thereafter, the operating labour cost was estimated. Two operators were running the battery production process. During this process, the operator was working for 5 hours per day which was equivalent to 1300 hours per year. Each operator was earning R43.05 per hour which was the PayScale for a production operator in South Africa (Tawonezvi, 2019). Thus, Appendix C 4 shows the operating labour cost.

Appendix C 4: Operating labour cost for 1300 hours per year using a plant capacity for Ni-Fe batteries at a rate of 2600 batteries/year

Cost Item	**R/hr**	**R/Year**
Operator 1	43.05	55 900
Operator 2	43.05	55 900
	Total cost	111 800

Appendix C 4 showed that a production operator working on the manufacturing of Ni-Fe batteries received R55 926 per year. Since two operators were working at the pilot plant; therefore, R 111 852 was the operating labour cost. Thus, the total production cost of Ni-Fe batteries was estimated in the next section (Appendix C 5).

Appendix C 5: Manufacturing cost estimation for production of Ni-Fe batteries (2600 batteries/year)

Cost Item	**Calculations**	**Rand (ZA)**	**%**
1. Raw Materials	From Material Balance	258 596	41.0
2. Miscellaneous Material	1% of FCI	3 852	0.6
3. Utilities	From Energy Balance	27 588	4.4
(A) Variable Costs	*(1) +(2) +(3)*	290 036	46.0
4. Maintenance	10% of FCI	38 520	6.1
5. Operation labour	Manning Estimates	111 800	17.7
6. Lab Costs	20% of (5)	22 360	3.5
7. Supervision	20% of (5)	22 360	3.5
8. Plant Overheads	50% of (5)	55 900	8.9
9. Capital Charges	15% of FCI	57 780	9.2
10. Insurance, Local Taxes and Royalties	4% of FCI	15 408	2.4
(B)Fixed Costs	*(4) +(5) +(6) +(10)*	324 128	51.4
Direct Production Costs	(A)+(B)	614 164	97.4
(C) General Overheads + R&D	*5% of FCI of the direct production cost*	19 260	3.1
Annual Production Cost	Subtotal (A)+(B)+ (C)	633 424	
Energy Production cost	[R/Wh]	8	

Appendix C 5 indicated that R 8 was the cost estimated for a kilowatt-hour in a Ni-Fe system. In addition, R633 424 annual production cost and fixed costs of R324 128 were reported in Appendix C 5. This indicated that a significant amount of money was spent on raw materials and equipment. The production cost of a bipolar Ni-Fe battery was computed to 8R/Wh, which is an enormous decrease from the 12R/Wh reported for prismatic Ni-Fe batteries by Iron Edison Co. (2019). The levelized cost of energy of a bipolar Ni-Fe battery is expected to be drastically low (enormous decrease from the production cost) due to the long cycle life and low to no maintenance requirements. The Ni-Fe battery production was performed at lab-scale, the production capacity of Ni-Fe batteries per day estimated during the material balance was 10 batteries; this rate of production was projected to a capacity of 2600 batteries/year. The cost of production was inordinate because the process was performed on a small scale. The factors that influenced the process to be costly at a small scale were the operating labour

cost, raw materials cost and utility cost, which constituted the energy (per year) consumed by a mixer, hydraulic press, BMS and vacuum dryer. These factors do not depend much on the production rate and are often constant no matter the size of the plant. When a bigger plant is modelled, the cost of purchasing the equipment (per unit of capacity) remains steady concurrently with a decrease in the price of raw materials per kg. Thus, it is relevant to scale up the production capacity to reduce the cost of battery production. Based on the production cost of Ni-Fe batteries obtained at the plant capacity of 2600 batteries/year, a scale-up is recommended up to a plant capacity of 26000 batteries/year.

Cash Flow of a Plant Capacity of 2600 Batteries/Year

Appendix C 6 illustrates the cumulative cash flow diagram of a plant with capacity 2600 batteries/year.

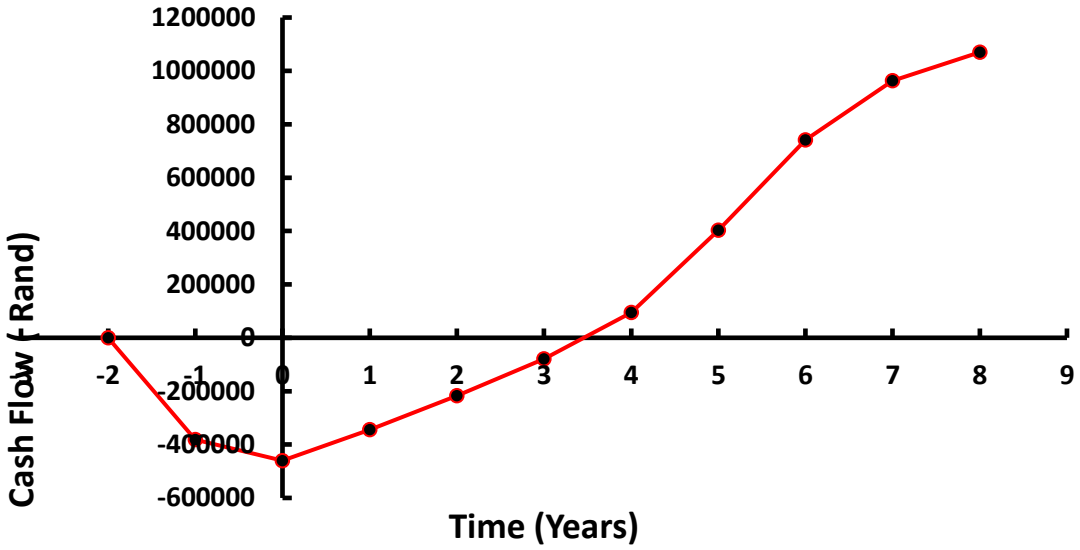

Appendix C 6: Cash flow of a plant with capacity 2600 batteries/year

$$\text{Total NPW of project} = \sum_{n=1}^{n=t} \frac{NFW}{(1+r)^n} = \text{R350 294}$$

List of assumptions

- The process is run at steady-state conditions
- The plant operates 260 days a year
- The sales increase by 10% in the first 2 years after the project has been running for a year, by 30 and 40% in the 3rd and 4th year, 10 % in the 5th year, and drop by 5% in the last 2 years of the project

- The operating expenses increased by 10% in the first 2 years after the project has been running for a year, 30% in the 3rd and 4th year and by 5% until the end of the project life
- The salvage value of the project is negligible
- The cost associated with land is negligible

Different methods are used to analyse the profitability of projects and processes. From the given data, the amount that needs to be invested in building the plant and starting it up is R460 200. The revenue is attained from sales of 25 Wh Ni-Fe batteries at R300 /battery unit. The trend of both the sales and operating costs throughout the project life was predicted based on sound judgement keeping in mind that in the early years of the project, both operating costs and sales increase and towards the end of the project, operating costs continue to increase due to wear and tear of equipment while sales decrease since project completion will be looming.

The payback profitability analysis shows that it takes 3.5 years (Appendix C 6) from the inaugural year of the project to recover the money invested and break even. Profit is only made for the last 4.5 years of the project. Payback analysis does not take the time value of money into an account. A better method for profitability analysis is the net present value (NPV) which represents the present value of money of future cash flows. For the company's required interest rate of return of 15%, the NPV is found to be R350 293. A negative NPV indicates that the anticipated expenditure costs in the present rand surpass the projected earnings generated by a project or investment, also in the present rand. In general, a negative NPV means that the project will subtract value from the plant's present value; it has to be rejected. A positive NPV indicates that the projected earnings generated by a project or investment in present rand exceed the anticipated costs, also in present rand. In general, a positive NPV is profitable. In order to make the project more profitable, it is suggested that the company drops its required IRR. Calculations done for an assumed IRR of 10%, for example, yields an NPV of R525 606. A lower rate of return means recovering money at a lower rate but the probability of making a profit is higher. The cash flow statement with values and methodology utilised in computing NPV and payback period is embodied in Appendix D 1.

Appendix C-2: References

Apostolakou, A., Kookos, I., Marazioti, C. and Angelopoulos, K. (2009). Techno-economic analysis of a biodiesel production process from vegetable oils. Fuel Processing Technology 90(7-8): 1023-1031.

Tawonezvi, T. (2019). Development of a composite iron-matrix electrode for nickel-iron battery energy storage systems, Cape Peninsula University of Technology.

Appendix D: Cash Flow Statement

Appendix D 1: Cash flow statement (in Rands)

		Total operating costs	634 424			**IRR**	15%				
		Total Operating cost	633 424			**Taxation Rate**	30%				
Year	-2	-1	0	1	2	3	4	5	6	7	8
Fixed Capital Investment		382 200									
Working Capital			-78 000								
Total Capital Investment		-382 200									
Profit - Loss Statement											
Revenue				780 000.0	858 000.0	943 800.0	1 226 940.0	1 717 716.0	1 889 487.6	1 795 013.2	1 705 262.6
Cash Operating Expenses				633 424.0	696 623.4	766 285.7	996 171.5	1 295 022.9	1 424 525.2	1 495 751.5	1 570 539.0
Depreciation				47 775.0	47 775.0	47 775.0	47 775.0	47 775.0	47 775.0	47 775.0	47 775.0
Total Operating Expenses				681 069.0	744 398.4	814 060.7	1043 946.5	1 342 797.9	1 472 300.2	1 543 526.5	1 618 314.0
Operating Income				146 706.0	161 376.6	177 514.3	230 768.5	422 693.1	464 962.4	299 261.8	134 723.5
Net Income Before Taxes				98 931.0	113 601.6	129 739.3	182 993.5	374 918.1	417 187.4	251 486.8	86 948.5
Federal Income Taxes				29 679.3	34 080.5	38 921.8	54 898.1	112 475.4	125 156.2	75 446.0	26 084.6
Net Income After Taxes				69 251.7	79 521.1	90 817.5	128 095.5	262 442.7	292 031.2	176 040.7	60 864.0
After Tax Cash Flow			-460 200	117 026.7	127 296.1	138 592.5	175 870.5	310 217.7	339 806.2	223 815.7	108 639.0
Capital Recovery											
Cumulative Cash Flow	0	-382 200	-460 200	-343 173.3	-215 877.2	-772 84.7	98 585.8	408 803.4	748 609.6	972 425.4	1 081 064.3
PV			-460 200	101 762.3	96 254.2	91 126.8	100 554.5	154 233.0	146 907.6	84 140.6	35 514.3
NPV			350 293.3								

References / Bibliography

Abas, N., Kalair, A. and Khan, N. (2015). Review of fossil fuels and future energy technologies. Futures 69: 31-49.

Abbas, S. A., Iqbal, M. I., Kim, S. H., Khan, H. A. and Jung, K. D. (2019). Facile synthesis of alfa-nickel hydroxide by an ultrasound-assisted method and its application in energy storage devices. Applied Surface Science 474: 218-226.

Abdalla, A. H., Oseghale, C. I., Posada, J. O. G. and Hall, P. J. (2016). Rechargeable nickel-iron batteries for large-scale energy storage. Institution of Engineering and Technology Renewable Power Generation 10(10): 1529-1534.

Adekunle, A. S., Oyekunle, J. A., Oluwafem, O., Joshua, A. O., Makinde, A. O., Ogunfowokan, A. O., Eleruja, M. A. and Ebenso, E. E. (2014). Comparative catalytic properties of $Ni(OH)_2$ and NiO nanoparticles towards the degradation of nitrite (NO_2^-) and nitric oxide (NO). International Journal of Electrochemical Science 9: 3008 - 3021.

Alamgir, M. and Abraham, K. (1995). Room temperature rechargeable polymer electrolyte batteries. Power Sources 54(1): 40-45.

Alhebshi, N. A. and Alshareef, H. N. (2015). Ternary Ni-Cu-OH and Ni-Co-OH electrodes for electrochemical energy storage. Materials for Renewable and Sustainable Energy 4(4): 1-9.

Apostolakou, A., Kookos, I., Marazioti, C. and Angelopoulos, K. (2009). Techno-economic analysis of a biodiesel production process from vegetable oils. Fuel Processing Technology 90(7-8): 1023-1031.

Badwal, S. P., Giddey, S. S., Munnings, C., Bhatt, A. I. and Hollenkamp, A. F. (2014). Emerging electrochemical energy conversion and storage technologies. Frontiers in Chemistry 2: 79.

Bantignies, J. L., Deabate, S., Righi, A., Rols, S., Hermet, P., Sauvajol, J. L. and Henn, F. (2008). New insight into the vibrational behavior of nickel hydroxide and oxyhydroxide using inelastic neutron scattering, far/mid-infrared and Raman spectroscopies. The Journal of Physical Chemistry 112(6): 2193-2201.

Bard, A. J., Faulkner, L. R., Leddy, J. and Zoski, C. G. (1980). Electrochemical methods: fundamentals and applications: Wiley New York.

Barton, J., Gammon, R. and Rahil, A. (2020). Characterisation of a nickel-iron battolyser, an integrated battery and electrolyser. Frontiers in Energy Research 8: 509052.

Begum, S. N., Muralidharan, V. and Basha, C. A. (2009). The influences of some additives on electrochemical behaviour of nickel electrodes. International Journal of Hydrogen Energy 34(3): 1548-1555.

Bernard, P. and Lippert, M. (2015). Nickel-cadmium and nickel-metal hydride battery energy storage. Electrochemical Energy storage for Renewable Sources and Grid Balancing, Elsevier: 223-251.

Blasco-Ahicart, M., Soriano-López, J., Carbó, J. J., Poblet, J. M. and Galan-Mascaros, J. R. (2018). Polyoxometalate electrocatalysts based on earth-abundant metals for efficient water oxidation in acidic media. Nature Chemistry 10(1): 24.

Blomquist, N., Wells, T., Andres, B., Bäckström, J., Forsberg, S. and Olin, H. (2017). Metal-free supercapacitor with aqueous electrolyte and low-cost carbon materials. Scientific Reports 7(1): 1-7.

Bode, H., Dehmelt, K. and Witte, J. (1966). Theory of the nickel hydroxide electrode-I about the nickel (II)-hydroxidhydrat. Journal of Electrochimica Acta 11: 1079-1087.

Bresser, D., Buchholz, D., Moretti, A., Varzi, A. and Passerini, S. (2018). Alternative binders for sustainable electrochemical energy storage–the transition to aqueous electrode processing and bio-derived polymers. Energy and Environmental Science 11(11): 3096-3127.

Breytenbach, K. (2015). How renewable energy has empowered South Africa. South African International Renewable Energy Conference (SAIREC).

Bruce, P. G. (1997). Promising electrochemical systems for rechargeable batteries. Journal of Electroanalytical Chemistry 421(1-2): 222-223.

Cai, M. (2011). Rock mechanics: achievements and ambitions: CRC Press.

Carbonio, R., Macagno, V., Giordano, M., Vilche, J. and Arvia, A. (1982). A transition in the kinetics of the $Ni(OH)_2$/NiOOH electrode reaction. Journal of the Electrochemical Society 129(5): 983-991.

Casas-Cabanas, M., Radin, M. D., Kim, J., Grey, C. P., Van der Ven, A. and Palacín, M. R. (2018). The nickel battery positive electrode revisited: stability and structure of the β-NiOOH phase. Journal of Materials Chemistry A 6(39): 19256-19265.

Chakkaravarthy, C., Periasamy, P., Jegannathan, S. and Vasu, K. (1991). The nickel/iron battery. Power Sources 35(1): 21-35.

Chang, S., Young, K.-h., Nei, J. and Fierro, C. (2016). Reviews on the US Patents regarding nickel/metal hydride batteries. Batteries 2(2): 10.

Che, M. and Védrine, J. C. (2012). Characterization of solid materials and heterogeneous catalysts: From structure to surface reactivity: John Wiley & Sons.

Chen, H., Zhou, S. and Wu, L. (2014). Porous nickel hydroxide–manganese dioxide-reduced graphene oxide ternary hybrid spheres as excellent supercapacitor electrode materials. American Chemical Society: Applied Materials and Interfaces 6(11): 8621-8630.

Chen, W., Jin, Y., Zhao, J., Liu, N. and Cui, Y. (2018). Nickel-hydrogen batteries for large-scale energy storage. Proceedings of the National Academy of Sciences 115(46): 11694-11699.

Ching, S., Dudek, R. and Tabet, E. (1994). Cyclic voltammetry with ultramicroelectrodes. Chemical Education 71(7): 602.

Coudun, C., Grillon, F. and Hochepied, J. F. (2006). Surfactant effects on pH-controlled synthesis of nickel hydroxides. Colloids and Surfaces A: Physicochemical and Engineering Aspects 280(1-3): 23-31.

Crittenden, B. and Thomas, W. J. (1998). Adsorption technology and design: Elsevier.

Daniel, C. and Besenhard, J. O. (2012). Handbook of battery materials: John Wiley & Sons.

Delmas, C., Faure, C. and Borthomieu, Y. (1992). The effect of cobalt on the chemical and electrochemical behaviour of the nickel hydroxide electrode. Materials Science and Engineering: B 13(2): 89-96.

Dennstedt, W. and Löser, W. (1971). Zur kenntnis der nickelhydroxid-elektrode—III. Thermogravimetrische untersuchungen an Nickel (II)-hydroxiden. Journal of Electrochimica Acta 16(3): 429-435.

Dhaka, K. and Toroker, M. C. (2019). Revealing the conducting character of the β-NiOOH catalyst through defect chemistry. The Journal of Physical Chemistry C 123(31): 18895-18904.

Ding, C., Zhou, X., Shi, J., Yan, P., Wang, Z., Liu, G. and Li, C. (2015). Abnormal effects of cations (Li^+, Na^+, and K^+) on photoelectrochemical and electrocatalytic water splitting. The Journal of Physical Chemistry B 119(8): 3560-3566.

Dougherty, B. J., Tanzella, F. L. and Weaver, R. D. (1995). Some nickel-iron, and nickel-metal hydride, cell cycling results. Proceedings of the Tenth Annual Battery Conference on Applications and Advances, IEEE.

Du, H., Wang, Y., Yuan, H. and Jiao, L. (2016). Facile synthesis and high capacitive performance of 3D hierarchical $Ni(OH)_2$ microspheres. Journal of Electrochimica Acta 196: 84-91.

Dubal, D., Lee, S. and Kim, W. (2012). Sponge-like β-$Ni(OH)_2$ nanoparticles: synthesis, characterization and electrochemical properties. Journal of Materials Science 47(8): 3817-3821.

Dyatkin, B., Presser, V., Heon, M., Lukatskaya, M. R., Beidaghi, M. and Gogotsi, Y. (2013). Development of a green supercapacitor composed entirely of environmentally friendly materials. ChemSusChem 6(12): 2269-2280.

El Kharbachi, A., Zavorotynska, O., Latroche, M., Cuevas, F., Yartys, V. and Fichtner, M. (2020). Exploits, advances and challenges benefiting beyond Li-ion battery technologies. Journal of Alloys and Compounds 817: 153261.

Elgrishi, N., Rountree, K. J., McCarthy, B. D., Rountree, E. S., Eisenhart, T. T. and Dempsey, J. L. (2018). A practical beginner's guide to cyclic voltammetry. Journal of chemical education 95(2): 197-206.

Ellabban, O., Abu-Rub, H. and Blaabjerg, F. (2014). Renewable energy resources: Current status, future prospects and their enabling technology. Renewable and Sustainable Energy Reviews 39: 748-764.

Falahati, H., Kim, E. and Barz, D. P. (2015). Fabrication and characterization of thin film nickel hydroxide electrodes for micropower applications. American Chemical Society: Applied Materials and Interfaces 7(23): 12797-12808.

Fatima, H., Zhong, Y., Wu, H. and Shao, Z. (2021). Recent advances in functional oxides for high energy density sodium-ion batteries. Materials Reports: Energy: 100022.

Galushkin, N., Yazvinskaya, N. and Galushkin, D. (2013). Ni-Cd batteries as hydrogen storage units of high-capacity. ECS Electrochemistry Letters 2(1): A1-A2.

Gambe, Y., Sun, Y. and Honma, I. (2015). Development of bipolar all-solid-state lithium battery based on quasi-solid-state electrolyte containing tetraglyme-LiTFSA equimolar complex. Scientific Reports 5(1): 1-4.

Garcia-Martinez, J. and Li, K. (2015). Mesoporous zeolites: preparation, characterization and applications: Wiley-VCH.

Gheytani, S., Liang, Y., Jing, Y., Xu, J. Q. and Yao, Y. (2016). Chromate conversion coated aluminium as a light-weight and corrosion-resistant current collector for aqueous lithium-ion batteries. Journal of Materials Chemistry A 4(2): 395-399.

Giri, S. D. and Sarkar, A. (2016). Electrochemical study of bulk and monolayer copper in alkaline solution. Journal of the Electrochemical Society 163(3): H252-H259.

Gonçalves, J. M., Alves, K. M., Gonzalez-Huila, M. F., Duarte, A., Martins, P. R. and Araki, K. (2018). Unexpected Stabilization of α-$Ni(OH)_2$ Nanoparticles in GO Nanocomposites. Journal of Nanomaterials 2018: 13.

Guerlou-Demourgues, L., Denage, C. and Delmas, C. (1994). New manganese-substituted nickel hydroxides: Part 1. Crystal chemistry and physical characterization. Power Sources 52(2): 269-274.

Guinier, A. (1994). X-ray diffraction in crystals, imperfect crystals, and amorphous bodies: Courier Corporation.

Guney, M. S. and Tepe, Y. (2017). Classification and assessment of energy storage systems. Renewable and Sustainable Energy Reviews 75: 1187-1197.

Guo, X. L., Liu, X. Y., Hao, X. D., Zhu, S. J., Dong, F., Wen, Z. Q. and Zhang, Y. X. (2016). Nickel-manganese layered double hydroxide nanosheets supported on nickel foam for high-performance supercapacitor electrode materials. Journal of Electrochimica Acta 194: 179-186.

Hadian, S. and Madani, K. (2015). A system of systems approach to energy sustainability assessment: Are all renewables really green? Ecological Indicators 52: 194-206.

Hall, D. S., Lockwood, D. J., Bock, C. and MacDougall, B. R. (2015). Nickel hydroxides and related materials: a review of their structures, synthesis and properties. Proceedings of the Royal Society A: Mathematical, Physical and Engineering Sciences 471(2174): 20140792.

Hall, D. S., Lockwood, D. J., Poirier, S., Bock, C. and MacDougall, B. R. (2012). Raman and infrared spectroscopy of α and β phases of thin nickel hydroxide films electrochemically formed on nickel. The Journal of Physical Chemistry A 116(25): 6771-6784.

Hall, D. S., Lockwood, D. J., Poirier, S., Bock, C. and MacDougall, B. R. (2014). Applications of in situ Raman spectroscopy for identifying nickel hydroxide materials and surface layers during chemical aging. American Chemical Society: Applied Materials and Interfaces 6(5): 3141-3149.

Han, T., Shi, Y., Yu, Z., Shin, B. and Lanza, M. (2019). Potassium hydroxide mixed with lithium hydroxide: An advanced electrolyte for oxygen evolution reaction. Solar Rrl 3(10): 1900195.

Hannan, M., Hoque, M., Mohamed, A. and Ayob, A. (2017). Review of energy storage systems for electric vehicle applications: Issues and challenges. Renewable and Sustainable Energy Reviews 69: 771-789.

Hao, F., Han, F., Liang, Y., Wang, C. and Yao, Y. (2018). Architectural design and fabrication approaches for solid-state batteries. MRS Bulletin 43(10): 775-781.

Hariprakash, B., Martha, S., Hegde, M. and Shukla, A. (2005). A sealed, starved-electrolyte nickel–iron battery. Applied Electrochemistry 35(1): 27-32.

Henao, J. and Martinez-Gomez, L. (2017). on rare-earth perovskite-type negative electrodes in nickel-hydride (Ni/H) secondary batteries. Materials for Renewable and Sustainable Energy 6(2): 7.

Hiemenz, P. C. and Rajagopalan, R. (2016). Principles of colloid and surface chemistry, revised and expanded: CRC Press.

Hill, J. C. and Choi, K. S. (2012). Effect of electrolytes on the selectivity and stability of n-type WO_3 photoelectrodes for use in solar water oxidation. The Journal of Physical Chemistry C 116(14): 7612-7620.

Holmberg, F. (2017). Recycling of nickel metal hydride (NiMH) batteries. Chalmers University of Technology.

Hu, P., Wang, T., Zhao, J., Zhang, C., Ma, J., Du, H., Wang, X. and Cui, G. (2015). Ultrafast alkaline Ni/Zn battery based on Ni-foam-supported Ni_3S_2 nanosheets. American Chemical Society: Applied Materials & Interfaces 7(48): 26396-26399.

Huang, J., Cao, D., Lei, T., Yang, S., Zhou, X., Xu, P. and Wang, G. (2013). Structural and electrochemical performance of Al-substituted β-$Ni(OH)_2$ nanosheets electrodes for nickel metal hydride battery. Journal of Electrochimica Acta 111: 713-719.

Huang, K., Li, J. and Xu, Z. (2011). Enhancement of the recycling of waste Ni-Cd and Ni-MH batteries by mechanical treatment. Journal of Waste Management 31(6): 1292-1299.

Huang, L., Yang, J., Liu, P., Zhu, D. and Chen, Y. (2018). Copper/Iron Composite Anode prepared by in situ co-precipitation with Excellent High-rate and Low-temperature Performance for Rechargeable Nickel-Iron Battery. International Journal of Electrochemical Science 13: 7045-7056.

IPCC (2014). Summary for policymakers. IIn: Climate Change 2014: Mitigation of Climate Change. Contribution of Working Group III to the Fifth Assessment Report of the Intergovernmental Panel on Climate Change [Edenhofer, O., R. Pichs-Madruga, Y. Sokona, E. Farahani, S. Kadner, K. Seyboth, A. Adler, I. Baum, S. Brunner, P. Eickemeier, B. Kriemann, J. Savolainen, S. Schlömer, C. von Stechow, T. Zwickel and J.C. Minx (eds.)]. International Institute for Applied Systems Analysis (IIASA), Cambridge University Press, Cambridge, United Kingdom and New York, NY, USA.

Jackovitz, J. F. and Bayles, G. A. (2002). Iron electrode batteries. Handbook of batteries.

Janek, J. and Zeier, W. G. (2016). A solid future for battery development. Nature Energy 1(9): 1-4.

Jensen, W. B. (2013). The Edison nickel-iron alkaline storage cell: notes from the Oesper collections, No. 21, July/August 2013. Oesper Collections in the History of Chemistry.

Jiang, H., Zhao, T., Li, C. and Ma, J. (2011). Hierarchical self-assembly of ultrathin nickel hydroxide nanoflakes for high-performance supercapacitors. Journal of Materials Chemistry 21(11): 3818-3823.

Jin, Z., Li, P., Jin, Y. and Xiao, D. (2018). Superficial-defect engineered nickel/iron oxide nanocrystals enable high-efficient flexible fiber battery. Energy Storage Materials 13: 160-167.

Jung, K. N., Shin, H. S., Park, M. S. and Lee, J. W. (2019). Solid-state lithium batteries: bipolar design, fabrication, and electrochemistry. ChemElectroChem 6(15): 3842-3859.

Kao, C. Y., Tsai, Y. R. and Chou, K. S. (2011). Synthesis and characterization of the iron/copper composite as an electrode material for the rechargeable alkaline battery. Power Sources 196(13): 5746-5750.

Karami, H., Mousavi, M. F. and Shamsipur, M. (2003). A novel dry bipolar rechargeable battery based on polyaniline. Power Sources 124(1): 303-308.

Kenney, M. J., Gong, M., Li, Y., Wu, J. Z., Feng, J., Lanza, M. and Dai, H. (2013). High-performance silicon photoanodes passivated with ultrathin nickel films for water oxidation. Science 342(6160): 836-840.

Kim, K. H., Mikami, M., Abe, Y., Kawamura, M. and Kiba, T. (2018). Structural and electrochemical properties of nanolayer-stacking structured copper-doped nickel hydroxide. International Journal of Electrochemical Science 13: 7655-7662.

Kim, S. H., Kim, J. H., Cho, S. J. and Lee, S. Y. (2019). All-solid-state printed bipolar Li-S batteries. Advanced Energy Materials 9(40): 1901841.

KOBER, F. P. (1967). On the structure of electrochemically active hydrated nickel-oxide electrodes. Power Sources, Elsevier: 257-268.

Kong, D., Wang, Y., Huang, S., Zhang, B., Lim, Y. V., Sim, G. J., Valdivia y Alvarado, P., Ge, Q. and Yang, H. Y. (2020). 3D printed compressible quasi-solid-state nickel-iron battery. American Chemical Society Nano 14(8): 9675-9686.

Kopietz, L., Girschik, J., Schwerdt, P., Burfeind, J., Grevé, A. and Doetsch, C. (2018). Highly flexible bipolar plates for redox-flow-batteries. International Conference on Carbon Materials and Technology. Fraunhofer Institute for Environmental, Safety, and Energy Technology Umsicht.

Kovalenko, V., Kotok, V., Sykchin, A., Mudryi, I., Ananchenko, B., Burkov, A., Sololvov, V., Deabate, S., Mehdi, A. and Bantignies, J.-L. (2017). Nickel hydroxide obtained by high-temperature two-step synthesis as an effective material for supercapacitor applications. Journal of Solid State Electrochemistry 21(3): 683-691.

Kozai, N., Mitamura, H., Fukuyama, H., Esaka, F. and Komarneni, S. (2006). Synthesis and characterization of nickel–copper hydroxide acetate, $NiCu(OH)_{3.1}(OCOCH_3)_{0.9}.0.9H_2O$. Microporous and Mesoporous Materials 89(1-3): 123-131.

Kumar, A. N., Harish, S. and Joseph, J. (2014). New route for synthesis of electrocatalytic $Ni(OH)_2$ modified electrodes—electrooxidation of borohydride as probe reaction. Bulletin of Materials Science 37(3): 635-641.

Kumar, N. and Panda, H. (2015). Facile synthesis of amorphous Co/Ni hydroxide hierarchical films and the study of their morphology and electrochemical properties. Royal Society of Chemistry Advances 5(33): 25676-25683.

Lassoued, A., Lassoued, M. S., Karolak, F., García-Granda, S., Dkhil, B., Ammar, S. and Gadri, A. (2017). Synthesis, structural, optical, morphological and magnetic characterization of copper substituted nickel ferrite ($Cu_xNi_{1-x}Fe_2O_4$) through co-precipitation method. Journal of Materials Science: Materials in Electronics 28(24): 18480-18488.

Lee, J. W., Ko, J. M. and Kim, J.-D. (2011). Hierarchical microspheres based on α-Ni $(OH)_2$ nanosheets intercalated with different anions: synthesis, anion exchange, and effect of intercalated anions on electrochemical capacitance. The Journal of Physical Chemistry C 115(39): 19445-19454.

Lee, S. H., Yi, C. W. and Kim, K. (2011). Characteristics and electrochemical performance of the TiO_2-coated ZnO anode for Ni-Zn secondary batteries. The Journal of Physical Chemistry C 115(5): 2572-2577.

Lei, D., Lee, D. C., Magasinski, A., Zhao, E., Steingart, D. and Yushin, G. (2016). Performance enhancement and side reactions in rechargeable nickel–iron batteries with nanostructured electrodes. American Chemical Society: Applied Materials & Interfaces 8(3): 2088-2096.

Li, Z., Han, J., Fan, L., Wang, M., Tao, S. and Guo, R. (2015). The anion exchange strategy towards mesoporous α-Ni(OH)$_2$ nanowires with multinanocavities for high-performance supercapacitors. Chemical Communications 51(15): 3053-3056.

Liang, Y., Schwab, M. G., Zhi, L., Mugnaioli, E., Kolb, U., Feng, X. and Müllen, K. (2010). Direct access to metal or metal oxide nanocrystals integrated with one-dimensional nanoporous carbons for electrochemical energy storage. Journal of the American Chemical Society 132(42): 15030-15037.

Liberatore, R., Lanchi, M., Giaconia, A. and Tarquini, P. (2012). Energy and economic assessment of an industrial plant for the hydrogen production by water-splitting through the sulfur-iodine thermochemical cycle powered by concentrated solar energy. International Journal of Hydrogen Energy 37(12): 9550-9565.

Linden, D. (1995). Handbook of batteries. Fuel and Energy Abstracts.

Linden, D. and Linden, D. (1984). Handbook of batteries and fuel cells: McGraw-Hill New York et al.

Liu, H., Liang, Z., Liu, S., Zhang, L., Xia, H. and Xie, W. (2020). Nickel manganese hydroxides with thin-layer nanosheets and multivalences for high-performance supercapacitor. Results in Physics 16: 102831.

Liu, J., Guan, C., Zhou, C., Fan, Z., Ke, Q., Zhang, G., Liu, C. and Wang, J. (2016). A flexible quasi-solid-state nickel–zinc battery with high energy and power densities based on 3D electrode design. Advanced Materials 28(39): 8732-8739.

Liu, K., Li, K., Peng, Q. and Zhang, C. (2019). A brief review on key technologies in the battery management system of electric vehicles. Frontiers of Mechanical Engineering 14(1): 47-64.

Liu, L., Hou, Y., Gao, Y., Yang, N., Liu, J. and Wang, X. (2019). Co doped α-Ni(OH)$_2$ multiple-dimensional structure electrode material. Journal of Electrochimica Acta 295: 340-346.

Liu, T., Yuan, Y., Tao, X., Lin, Z. and Lu, J. (2020). Bipolar electrodes for next-generation rechargeable batteries. Advanced Science 7(17): 2001207.

Liu, T., Zhang, Y., Chen, C., Lin, Z., Zhang, S. and Lu, J. (2019). Sustainability-inspired cell design for a fully recyclable sodium ion battery. Journal of Nature Communications 10(1): 1-7.

Livshits, V., Blum, A., Strauss, E., Ardel, G., Golodnitsky, D. and Peled, E. (2001). Development of a bipolar Li/composite polymer electrolyte/pyrite battery for electric vehicles. Power Sources 97: 782-785.

Lowell, S., Shields, J. E., Thomas, M. A. and Thommes, M. (2012). Characterization of porous solids and powders: surface area, pore size and density: Springer Science and Business Media.

Lu, X. and Zhao, C. (2015). Electrodeposition of hierarchically structured three-dimensional nickel–iron electrodes for efficient oxygen evolution at high current densities. Journal of Nature Communications 6(1): 1-7.

Luan, C., Liu, G., Liu, Y., Yu, L., Wang, Y., Xiao, Y., Qiao, H., Dai, X. and Zhang, X. (2018). Structure effects of 2D materials on α-Nickel hydroxide for oxygen evolution reaction. American Chemical Society: Nano 12(4): 3875-3885.

Lukatskaya, M. R., Kota, S., Lin, Z., Zhao, M.-Q., Shpigel, N., Levi, M. D., Halim, J., Taberna, P.-L., Barsoum, M. W. and Simon, P. (2017). Ultra-high-rate pseudocapacitive energy storage in two-dimensional transition metal carbides. Nature Energy 2(8): 1-6.

Lyons, M. E. and Brandon, M. P. (2008). The oxygen evolution reaction on passive oxide covered transition metal electrodes in aqueous alkaline solution. Part 1-nickel. International Journal of Electrochemical Science 3(12): 1386-1424.

Ma, X., Li, Y., Wen, Z., Gao, F., Liang, C. and Che, R. (2015). Ultrathin β-$Ni(OH)_2$ nanoplates vertically grown on nickel-coated carbon nanotubes as high-performance pseudocapacitor electrode materials. American Chemical Society: Applied Materials and Interfaces 7(1): 974-979.

Madou, M. J. and McKubre, M. C. (1983). Impedance measurements and photoeffects on Ni electrodes. Journal of The Electrochemical Society 130(5): 1056.

Martins, P. R., Ferreira, L. M. C., Araki, K. and Angnes, L. (2014). Influence of cobalt content on nanostructured alpha-phase-nickel hydroxide modified electrodes for electrocatalytic oxidation of isoniazid. Sensors and Actuators B: Chemical 192: 601-606.

McEwen, R. (1971). Crystallographic studies on nickel hydroxide and the higher nickel oxides. The Journal of Physical Chemistry 75(12): 1782-1789.

Miao, C., Zhu, Y., Zhao, T., Jian, X. and Li, W. (2015). Synthesis and electrochemical performance of mixed phase α/β nickel hydroxide by codoping with Ca^{2+} and PO_4^{3-}. Ionics 21(12): 3201-3208.

Mirabella, F. M. (1992). Internal reflection spectroscopy: Theory and applications: CRC Press.

Motlagh, M. K., Youzbashi, A. and Sabaghzadeh, L. (2011). Synthesis and characterization of nickel hydroxide/oxide nanoparticles by the complexation-precipitation method. International Journal of Physical Sciences 6(6): 1471-1476.

Motori, A., Sandrolini, F. and Davolio, G. (1994). Electrical properties of nickel hydroxide for alkaline cell systems. Power Sources 48(3): 361-370.

Müller, S., Holzer, F., Haas, O., Schlatter, C. and Comninellis, C. (1995). Development of rechargeable monopolar and bipolar zinc/air batteries. CHIMIA International Journal for Chemistry 49(1-2): 27-32.

Nadeem, F., Hussain, S. S., Tiwari, P. K., Goswami, A. K. and Ustun, T. S. (2018). Comparative review of energy storage systems, their roles, and impacts on future power systems. Institute of Electrical and Electronics Engineers (IEEE) Access 7: 4555-4585.

Nasrollahzadeh, M., Atarod, M., Sajjadi, M., Sajadi, S. M. and Issaabadi, Z. (2019). Plant-mediated green synthesis of nanostructures: mechanisms, characterization, and applications. Interface Science and Technology, Elsevier. 28: 199-322.

Nejat, P., Jomehzadeh, F., Taheri, M. M., Gohari, M. and Majid, M. Z. A. (2015). A global review of energy consumption, CO_2 emissions and policy in the residential sector (with an overview of the top ten CO_2 emitting countries). Renewable and Sustainable Energy Reviews 43: 843-862.

Ng, K. C., Zhang, S., Peng, C. and Chen, G. Z. (2009). Individual and bipolarly stacked asymmetrical aqueous supercapacitors of CNTs/SnO_2 and CNTs/MnO_2 nanocomposites. Journal of the Electrochemical Society 156(11): A846.

Novakovskii, A., Grushkina, S. and Kozlova, R. (1973). Influence of electrical conductivity of the active material on the behavior of the iron plate in an alkaline storage cell. J. Appl. Chem. USSR (Engl. Transl.);(United States) 46(9).

Oh, S. H., Black, R., Pomerantseva, E., Lee, J.-H. and Nazar, L. F. (2012). Synthesis of a metallic mesoporous pyrochlore as a catalyst for lithium-O_2 batteries. Nature Chemistry 4(12): 1004-1010.

Oliva, P., Leonardi, J., Laurent, J., Delmas, C., Braconnier, J., Figlarz, M., Fievet, F. and Guibert, A. d. (1982). Review of the structure and the electrochemistry of nickel hydroxides and oxy-hydroxides. Power Sources 8: 229-255.

Omar, N., Firouz, Y., Monem, M., Samba, A., Gualous, H., Coosemans, T., Van den Bossche, P. and Van Mierlo, J. (2014). Analysis of nickel-based battery technologies for hybrid and electric vehicles.

Oseghale, C., Abdalla, A., Posada, J. and Hall, P. (2016). A new synthesis route for sustainable gold copper utilization in direct formic acid fuel cells. International Journal of Hydrogen Energy 41(37): 16394-16401.

Oshitani, M., Sasaki, Y. and Takashima, K. (1984). Development of a nickel electrode having stable performance at various charge and discharge rates over a wide temperature range. Power Sources 12(3-4): 219-231.

Owusu, P. A. and Asumadu-Sarkodie, S. (2016). A review of renewable energy sources, sustainability issues and climate change mitigation. Cogent Engineering 3(1): 1167990.

Panos, E., Densing, M. and Volkart, K. (2016). Access to electricity in the World Energy Council's global energy scenarios: An outlook for developing regions until 2030. Energy Strategy Reviews 9: 28-49.

Park, J.-K. (2012). Principles and applications of lithium secondary batteries: John Wiley & Sons.

Peled, E., Golodnitsky, D., Ardel, G., Lang, J. and Lavi, Y. (1995). Development and characterization of bipolar lithium composite polymer electrolyte (CPE)-FeS_2 battery for applications in electric vehicles. Power Sources 54(2): 496-500.

Perera, F. (2017). Pollution from fossil-fuel combustion is the leading environmental threat to global pediatric health and equity: Solutions exist. Environmental Research and Public Health 15(1): 16.

Phillippi, C. and Mazdiyasni, K. (1971). Infrared and raman spectra of zirconia polymorphs. Journal of the American Ceramic Society 54(5): 254-258.

Piłatowicz, G., Marongiu, A., Drillkens, J., Sinhuber, P. and Sauer, D. U. (2015). A critical overview of definitions and determination techniques of the internal resistance using lithium-ion, lead-acid, nickel metal-hydride batteries and electrochemical double-layer capacitors as examples. Power Sources 296: 365-376.

Placke, T., Kloepsch, R., Dühnen, S. and Winter, M. (2017). Lithium ion, lithium metal, and alternative rechargeable battery technologies: the odyssey for high energy density. Journal of Solid State Electrochemistry 21(7): 1939-1964.

Posada, J. O. G., Abdalla, A. H., Oseghale, C. I. and Hall, P. J. (2016). Multiple regression analysis in the development of NiFe cells as energy storage solutions for intermittent power sources such as wind or solar. International Journal of Hydrogen Energy 41(37): 16330-16337.

Posada, J. O. G. and Hall, P. J. (2016). Towards the development of safe and commercially viable nickel-iron batteries: improvements to coulombic efficiency at high iron sulphide electrode formulations. Applied Electrochemistry 46(4): 451-458.

Rajamathi, M., Kamath, P. V. and Seshadri, R. (2000). Polymorphism in nickel hydroxide: role of interstratification. Journal of Materials Chemistry 10(2): 503-506.

Reimer, L. (2013). Transmission electron microscopy: physics of image formation and microanalysis: Springer.

Riahi, K., Van Vuuren, D. P., Kriegler, E., Edmonds, J., O'neill, B. C., Fujimori, S., Bauer, N., Calvin, K., Dellink, R. and Fricko, O. (2017). The shared socioeconomic pathways and their energy, land use, and greenhouse gas emissions implications: an overview. Global Environmental Change 42: 153-168.

Rota, M., Comninellis, C., Moller, S., Holzer, F. and Haas, O. (1995). Bipolar Al/O_2 battery with planar electrodes in alkaline and acidic electrolytes. Applied Electrochemistry 25(2): 114-121.

Ruetschi, P. (2004). Aging mechanisms and service life of lead–acid batteries. Power Sources 127(1-2): 33-44.

Saakes, M., Woortmeijer, R. and Schmal, D. (2005). Bipolar lead–acid battery for hybrid vehicles. Power Sources 144(2): 536-545.

Sarbu, I. and Sebarchievici, C. (2018). A comprehensive review of thermal energy storage. Sustainability 10(1): 191.

Sarrias-Mena, R., Fernández-Ramírez, L. M., García-Vázquez, C. A. and Jurado, F. (2014). Improving grid integration of wind turbines by using secondary batteries. Renewable and Sustainable Energy Reviews 34: 194-207.

Schipper, F. and Aurbach, D. (2016). A brief review: past, present and future of lithium ion batteries. Russian Journal of Electrochemistry 52(12): 1095-1121.

Shanaj, B. and John, X. (2016). Effect of calcination time on structural, optical and antimicrobial properties of nickel oxide nanoparticles. Journal of Theoretical Computer Science 3(2).

Shangguan, E., Chang, Z., Tang, H., Yuan, X.-Z. and Wang, H. (2010). Synthesis and characterization of high-density non-spherical $Ni(OH)_2$ cathode material for Ni-MH batteries. International Journal of Hydrogen Energy 35(18): 9716-9724.

Shen, D. H. and Halpert, G. (1993). Design concepts of high power bipolar rechargeable lithium battery. Power Sources 43(1-3): 327-338.

Shinomiya, T., Gupta, V. and Miura, N. (2006). Effects of electrochemical-deposition method and microstructure on the capacitive characteristics of nano-sized manganese oxide. Journal of Electrochimica Acta 51(21): 4412-4419.

Shukla, A., Ravikumar, M. and Balasubramanian, T. (1994). Nickel/iron batteries. Power Sources 51(1-2): 29-36.

Sing, K. (2001). The use of nitrogen adsorption for the characterisation of porous materials. Colloids and Surfaces A: Physicochemical and Engineering Aspects 187: 3-9.

Su, Y.-Z., Xiao, K., Li, N., Liu, Z.-Q. and Qiao, S.-Z. (2014). Amorphous $Ni(OH)_2$ @ three-dimensional Ni core–shell nanostructures for high capacitance pseudocapacitors and asymmetric supercapacitors. Journal of Materials Chemistry A 2(34): 13845-13853.

Subbaraman, R., Tripkovic, D., Strmcnik, D., Chang, K.-C., Uchimura, M., Paulikas, A. P., Stamenkovic, V. and Markovic, N. M. (2011). Enhancing hydrogen evolution activity in water splitting by tailoring Li^+-$Ni(OH)_2$ - Pt interfaces. Science 334(6060): 1256-1260.

Sun, Z. and Lu, X. (2012). A solid-state reaction route to anchoring $Ni(OH)_2$ nanoparticles on reduced graphene oxide sheets for supercapacitors. Industrial and Engineering Chemistry Research 51(30): 9973-9979.

Suntivich, J., May, K. J., Gasteiger, H. A., Goodenough, J. B. and Shao-Horn, Y. (2011). A perovskite oxide optimized for oxygen evolution catalysis from molecular orbital principles. Science 334(6061): 1383-1385.

Tawonezvi, T. (2019). Development of a composite iron-matrix electrode for nickel-iron battery energy storage systems, Cape Peninsula University of Technology.

Tawonezvi, T., Bladergroen, B. J. and John, J. (2020). Development of $FeCu_x$/FeS/Graphite composite electrode materials for iron-based Alkaline batteries. Internatinal Journal of Electrochemical Science 15: 12428 – 12446.

Thackeray, M. M., Wolverton, C. and Isaacs, E. D. (2012). Electrical energy storage for transportation—approaching the limits of, and going beyond, lithium-ion batteries. Energy and Environmental Science 5(7): 7854-7863.

Thommes, M. and Cychosz, K. A. (2014). Physical adsorption characterization of nanoporous materials: progress and challenges. Adsorption 20(2-3): 233-250.

Thommes, M., Kaneko, K., Neimark, A. V., Olivier, J. P., Rodriguez-Reinoso, F., Rouquerol, J. and Sing, K. S. (2015). Physisorption of gases, with special reference to the evaluation of surface area and pore size distribution (IUPAC Technical Report). Pure and Applied Chemistry 87(9-10): 1051-1069.

Thurner, H. (2016). Battery storage systems for electricity technology, applications and economics of large projects in Central and Eastern Europe, Wien.

Tkalych, A. J., Yu, K. and Carter, E. A. (2015). Structural and electronic features of β-$Ni(OH)_2$ and β-NiOOH from first principles. The Journal of Physical Chemistry C 119(43): 24315-24322.

Tsais, P.-J. and Chan, L. (2013). Nickel-based batteries: Materials and chemistry. Electricity Transmission, Distribution and Storage Systems, Elsevier: 309-397.

Ullah, S., Amin Badshah, F. A., Raza, R., Altaf, A. A. and Hussain, R. (2011). Electrodeposited zinc electrodes for high current Zn/AgO bipolar batteries.

Wang, H., Lee, H.-W., Deng, Y., Lu, Z., Hsu, P.-C., Liu, Y., Lin, D. and Cui, Y. (2015). Bifunctional non-noble metal oxide nanoparticle electrocatalysts through lithium-induced conversion for overall water splitting. Journal of Nature Communications 6(1): 1-8.

Wang, H., Liang, Y., Gong, M., Li, Y., Chang, W., Mefford, T., Zhou, J., Wang, J., Regier, T. and Wei, F. (2012). An ultrafast nickel–iron battery from strongly coupled inorganic nanoparticle/nanocarbon hybrid materials. Journal of Nature Communications 3: 917.

Wang, X., Luo, H., Yang, H., Sebastian, P. and Gamboa, S. (2004). Oxygen catalytic evolution reaction on nickel hydroxide electrode modified by electroless cobalt coating. International Journal of Hydrogen Energy 29(9): 967-972.

Wang, X., Wan, L., Yu, T., Zhou, Y., Guan, J., Yu, Z., Li, Z. and Zou, Z. (2011). Non-basic solution eco-routes to nano-scale NiO with different shapes: Synthesis and application. Materials Chemistry and Physics 126(3): 494-499.

Warren, P. (2014). A review of demand-side management policy in the UK. Renewable and Sustainable Energy Reviews 29: 941-951.

Whitacre, J., Wiley, T., Shanbhag, S., Wenzhuo, Y., Mohamed, A., Chun, S., Weber, E., Blackwood, D., Lynch-Bell, E. and Gulakowski, J. (2012). An aqueous electrolyte, sodium ion functional, large format energy storage device for stationary applications. Power Sources 213: 255-264.

Wiston, B. R. and Ashok, M. (2019). Electrochemical performance of hydrothermally synthesized flower-like α-nickel hydroxide. Vacuum 160: 12-17.

Wu, H.-C., Lin, Y.-P., Lee, E., Lin, W.-T., Hu, J.-K., Chen, H.-C. and Wu, N.-L. (2009). High-performance carbon-based supercapacitors using Al current-collector with conformal carbon coating. Materials Chemistry and Physics 117(1): 294-300.

Xia, Q. X., San Hui, K., Hui, K. N., Kim, S. D., Lim, J. H., Choi, S. Y., Zhang, L. J., Mane, R. S., Yun, J. M. and Kim, K. H. (2015). Facile synthesis of manganese carbonate quantum dots/$Ni(HCO_3)_2$–$MnCO_3$ composites as advanced cathode materials for high energy density asymmetric supercapacitors. Journal of Materials Chemistry A 3(44): 22102-22117.

Xie, M., Duan, S., Shen, Y., Fang, K., Wang, Y., Lin, M. and Guo, X. (2016). In-situ-grown $Mg(OH)_2$-derived hybrid α-$Ni(OH)_2$ for highly stable supercapacitor. American Chemical Society: Energy Letters 1(4): 814-819.

Xu, W., Lan, R., Du, D., Humphreys, J., Walker, M., Wu, Z., Wang, H. and Tao, S. (2017). Directly growing hierarchical nickel-copper hydroxide nanowires on carbon fibre cloth for efficient electrooxidation of ammonia. Applied Catalysis B: Environmental 218: 470-479.

Yamada, Y., Usui, K., Sodeyama, K., Ko, S., Tateyama, Y. and Yamada, A. (2016). Hydrate-melt electrolytes for high-energy-density aqueous batteries. Nature Energy 1(10): 1-9.

Yan, J., Wang, Q., Wei, T. and Fan, Z. (2014). Recent advances in design and fabrication of electrochemical supercapacitors with high energy densities. Advanced Energy Materials 4(4): 1300816.

Yan, Z., Sun, H., Chen, X., Liu, H., Zhao, Y., Li, H., Xie, W., Cheng, F. and Chen, J. (2018). Anion insertion enhanced electrodeposition of robust metal hydroxide/oxide electrodes for oxygen evolution. Journal of Nature Communications 9(1): 1-9.

Yan, Z., Wang, E., Jiang, L. and Sun, G. (2015). Superior cycling stability and high rate capability of three-dimensional Zn/Cu foam electrodes for zinc-based alkaline batteries. Royal Society of Chemistry (RSC): Advances 5(102): 83781-83787.

Yang, G.-W., Xu, C.-L. and Li, H.-L. (2008). Electrodeposited nickel hydroxide on nickel foam with ultrahigh capacitance. Chemical Communications(48): 6537-6539.

Yang, L., Gao, X., Wu, Q., Zhu, H. and Pan, G. (2007). Phase distribution and electrochemical properties of Al-substituted nickel hydroxides. The Journal of Physical Chemistry C 111(12): 4614-4619.

Yeetsorn, R., Fowler, M. W. and Tzoganakis, C. (2011). A review of thermoplastic composites for bipolar plate materials in PEM fuel cells. Nanocomposites with unique properties and applications in medicine and industry: 317-344.

Yin, J., Zhou, G., Gao, X., Chen, J., Zhang, L., Xu, J., Zhao, P. and Gao, F. (2019). α-and β-Phase Ni-Mg hydroxide for high performance hybrid supercapacitors. Nanomaterials 9(12): 1686.

Yoshima, K., Harada, Y. and Takami, N. (2016). Thin hybrid electrolyte based on garnet-type lithium-ion conductor $Li7La_3Zr_2O_{12}$ for 12V-class bipolar batteries. Power Sources 302: 283-290.

Young, K.-H., Wang, L., Yan, S., Liao, X., Meng, T., Shen, H. and Mays, W. (2017). Fabrications of high-capacity alpha-$Ni(OH)_2$. Batteries 3(1): 6.

Young, K.-h. and Yasuoka, S. (2016). Capacity degradation mechanisms in nickel/metal hydride batteries. Batteries 2(1): 3.

Young, K., Wang, L., Mays, W., Reichman, B., Chao-Ian, H., Wong, D. and Nei, J. (2018). Nickel hydroxide positive electrode for alkaline rechargeable battery, Google Patents.

Yu, J., Pan, S., Zhang, Y., Liu, Q. and Li, B. (2019). Facile synthesis of monodispersed α-$Ni(OH)_2$ microspheres assembled by ultrathin nanosheets and its performance for oxygen evolution reduction. Frontiers in Materials 6: 124.

Yuan, S., Wang, X., Lu, C. and Chen, C.-M. (2016). The fine control of porous pompon-like Mg-incorporated α-$Ni(OH)_2$ for enhanced supercapacities. Functional Materials Letters 9(05): 1650057.

Zhai, Z., Liu, Q., Zhu, Y., Cao, J. and Shi, S. (2019). Synthesis of $Ni(OH)_2$/graphene composite with enhanced electrochemical property by stirring solvothermal method. Journal of Alloys and Compounds 775: 1316-1323.

Zhang, L., Huang, H., Zhang, W., Gan, Y. and Wang, C. (2008). Effects of conductive ceramic on the electrochemical performance of ZnO for Ni/Zn rechargeable battery. Journal of Electrochimica Acta 53(16): 5386-5390.

Zhang, Y., Chang, C.-R., Jia, X.-D., Cao, Y., Yan, J., Luo, H.-W., Gao, H.-L., Ru, Y., Mei, H.-X. and Zhang, A.-Q. (2020a). Influence of metallic oxide on the morphology and enhanced supercapacitive performance of $NiMoO_4$ electrode material. Inorganic Chemistry Communications 112: 107697.

Zhang, Y., Chang, C.-R., Jia, X.-D., Huo, Q.-Y., Gao, H.-L., Yan, J., Zhang, A.-Q., Ru, Y., Mei, H.-X. and Gao, K.-Z. (2020b). Morphology-dependent $NiMoO_4$/carbon composites for high performance supercapacitors. Inorganic Chemistry Communications 111: 107631.

Zhang, Y., Gao, H.-L., Jia, X.-D., Wang, S.-W., Yan, J., Luo, H.-W., Gao, K.-Z., Fang, H., Zhang, A.-Q. and Wang, L.-Z. (2018). $NiMoO_4$ nanorods supported on nickel foam for high-performance supercapacitor electrode materials. Journal of Renewable and Sustainable Energy 10(5): 054101.

Zhang, Y., Mei, H.-X., Cao, Y., Yan, X.-H., Yan, J., Gao, H.-L., Luo, H.-W., Wang, S.-W., Jia, X.-D. and Kachalova, L. (2021). Recent advances and challenges of electrode materials for flexible supercapacitors. Coordination Chemistry Reviews 438: 213910.

Zhang, Y., Mei, H.-X., Yang, J., Wang, S.-W., Gao, H.-L., Jia, X.-D., Yan, J., Cao, Y., Luo, H.-W. and Gao, K.-Z. (2020c). New $NiMoO_4$/$CoMoO_4$ composite electrodes for enhanced performance supercapacitors. Ionics 26(7): 3579-3590.

Zhang, Y., Yao, Q. Q., Gao, H. L., Zhang, L. S., Wang, L. Z., Zhang, A. Q., Song, Y. H. and Wang, L. X. (2015). Synthesis and electrochemical performance of MnO_2/BC composite as active materials for supercapacitors. Journal of Analytical and Applied Pyrolysis 111: 233-237.

Zhao, H., Wu, Q., Hu, S., Xu, H. and Rasmussen, C. N. (2015). Review of energy storage system for wind power integration support. Journal of Applied Energy 137: 545-553.

Zheng, Y., Zhu, B., Chen, H., You, W., Jiang, C. and Yu, J. (2017). Hierarchical flower-like nickel (II) oxide microspheres with high adsorption capacity of Congo red in water. Journal of Colloid and Interface Science 504: 688-696.

Zhong, Y., Xu, X., Liu, Y., Wang, W. and Shao, Z. (2018). Recent progress in metal–organic frameworks for lithium–sulfur batteries. Polyhedron 155: 464-484.

Zhong, Y., Xu, X., Veder, J.-P. and Shao, Z. (2020). Self-recovery chemistry and cobalt-catalyzed electrochemical deposition of cathode for boosting performance of aqueous zinc-ion batteries. Iscience 23(3): 100943.

Zhou, X., Peng, C. and Chen, G. Z. (2012). 20 V stack of aqueous supercapacitors with carbon (−), titanium bipolar plates and CNT-polypyrrole composite (+). AIChE Journal 58(3): 974-983.

Zide, D., Felix, C., Oosthuysen, T. and Bladergroen, B. J. (2020a). Electrochemical studies of the nickel-based hydroxide electrode for the oxygen evolution reaction and coulombic efficiency of the electrode. Electroanalysis 32(12): 2703-2712.

Zide, D., Felix, C., Oosthuysen, T. and Bladergroen, B. J. (2020b). The influence of copper and carbon black on electrochemical behavior of nickel positive electrode. Journal of Electroanalytical Chemistry 878: 114539.

Zide, D., Felix, C., Oosthuysen, T. and Bladergroen, B. J. (2021). Synthesis, structural characterization, and electrochemical properties of the Mg and Mn doped-Ni (OH) 2 for use as active cathode materials in NiFe batteries. Journal of Electroanalytical Chemistry 895: 115418.

Zimmerman, A. and Effa, P. (1984). Discharge kinetics of the nickel electrode. Journal of the Electrochemical Society 131(4): 709-713.

Ziv, B., Haik, O., Zinigrad, E., Levi, M. D., Aurbach, D. and Halalay, I. C. (2013). Investigation of graphite foil as current collector for positive electrodes of Li-ion batteries. Journal of the Electrochemical Society 160(4): A581.

Zuo, W., Li, R., Zhou, C., Li, Y., Xia, J. and Liu, J. (2017). Battery-supercapacitor hybrid devices: recent progress and future prospects. Advanced Science 4(7): 1600539.